GAS JET PROCESSING FOR LOCAL HEAT TREATMENT APPLICATIONS

By

IAN MITCHELL

A thesis submitted to the University of Birmingham for the degree of

DOCTOR OF ENGINEERING (ENGD)

School of Metallurgy and Materials

College of Engineering and Physical Sciences

University of Birmingham

June 2012

UNIVERSITY OF
BIRMINGHAM

University of Birmingham Research Archive

e-theses repository

This unpublished thesis/dissertation is copyright of the author and/or third parties. The intellectual property rights of the author or third parties in respect of this work are as defined by The Copyright Designs and Patents Act 1988 or as modified by any successor legislation.

Any use made of information contained in this thesis/dissertation must be in accordance with that legislation and must be properly acknowledged. Further distribution or reproduction in any format is prohibited without the permission of the copyright holder.

ABSTRACT

This research takes the principle of localised heat treatment using inert gas jets from concept to delivery of a working prototype system and its application on a specific component. Described is the development of this technology and proof of its thermal capabilities on a number of components and test pieces. Included are discussions on the atmospheric requirements of the system and the development of the system design to minimise the formation of significant oxidation and alpha case. Finally the later sections of this thesis detail the work carried out to understand the underlying principles of this technology and how this understanding can be read across to future applications. This is done in the form of process modelling; the output of this being boundary conditions which can be used to model this technology for a number of applications and geometries in the future.

ACKNOWLEDGEMENTS

I would particularly like to thank Dr Justin Burrows[*], Daniel Clark[*], Dr Stephen Tuppen[*], Dr Jean-Christophe Gebelin[†], Prof. Paul Bowen[‡], and Prof. Roger Reed[†], for their invaluable guidance and support during this doctoral research project. Thanks is also offered to Dr Paul Brown[*] for providing access to the modelling facilities at PRISM2. The support of my parents Kathy and Tony has been a constant source of inspiration, motivation and comfort.

I would like to thank the EPSRC and Rolls-Royce plc for proving funding and the opportunity to conduct industrially relevant work within the context of a high technology company.

Finally, I would also like to thank the following people for their technical support and advice; Jeffrey Bishop[*], Dr Steven Halliday[*], Dr Peter Ireland[*], Dr Mat Davies[*], Kevin Bolton[§], Len Price[§], and Dr Marios Christodoulou[**].

---

[*] Rolls-Royce plc

[†] Partnership for Research In the Simulation of Manufacturing and Matrials (PRISM2), The University of Birmingham

[‡] The University of Birmingham

[§] Stork Cooperheat (UK) Ltd

[**] Scitek consultants Ltd

INTELLECTUAL PROPERTY 1

PUBLISHED WORK AND AWARDS.....1

1 INTRODUCTION 2

1.1 Materials used in the gas turbine.....2

1.2 What is a blisk? 3

1.3 Business driver for blisk repair.....4

1.4 Blisk repair process overview 6

2 BACKGROUND INFORMATION AND REVIEW OF RELEVANT LITERATURE ...10

2.1 Foreign Object Damage (FOD).....10

2.2 The key repair processes 12

2.3 Titanium and its alloys 16

2.4 Microstructure of the deposited material.....20

2.5 Heat treatment of titanium 24

2.6 Atmosphere requirements for processing titanium 26

2.7 Stress relief heat treatment.....30

2.8 Heat treatment techniques.....35

2.9 Convection heating using impingement jets 38

2.10 Impinging jet heat transfer 38

2.11 Gas and material thermal properties 50

2.12 Technology development approach – the capability acquisition process 54

2.13 Summary of literature 57

3 ASSUMPTIONS 62

4 LOCAL HEAT TREATMENT DEVELOPMENT STRATEGY.....64

5 TEMPERATURE MEASUREMENT 66

6 EQUIPMENT – KEY SYSTEM ELEMENTS 68
6.1 The innovation – inert gas jet processing 68
6.2 Local heat treatment Equipment 69
7 EQUIPMENT - LOCALISED HEAT TREATMENT 74
7.1 Residual stress of repaired components 74
7.2 Localised heat treatment head unit development 84
7.3 Producing tailored jet arrays 90
7.4 Demonstration of head with integrated cooling pipes 99
8 EQUIPMENT - PROTOTYPE SYSTEM DEVELOPMENT 111
8.1 System design 111
8.2 Prototype System – Overview 112
8.3 Key system design features 114
8.4 Atmosphere study - alpha-case examination 120
9 PROCESS - HEAT TREATING OF A BLISK 128
9.1 Introduction – the component 128
9.2 The apparatus 130
9.3 Achieving the required temperature distribution 138
9.4 Tip heat treatment 140
9.5 Leading Edge (LE) Heat treatment 151
10 PROCESS – DEVELOPING UNDERSTANDING 161
10.1 Experimental introduction 161
10.2 Key process parameters 164
10.3 Positional sensitivity 171
10.4 General outcomes 176

11 MODELLING - COMPUTATIONAL FLUID DYNAMICS (CFD) ANALYSIS OF JET HEAT TRANSFER 177

11.1 CFD modelling strategy 177

11.2 Model configuration 180

11.3 Calculating heat transfer coefficient from modelling data 188

11.4 Results and discussion – single air jets 190

11.5 Conclusion – single air jets 193

11.6 Results and discussion – single jet argon 195

11.7 Results and discussion - multi-jet model (argon) 201

11.8 Flow visualisation of impinging jets 210

11.9 Key outcomes - validity of the multi-jet simulation 212

12 MODELLING - THE FINITE ELEMENT APPROACH 215

12.1 Experimental configuration for modelling validation 215

12.2 FE modelling strategy 216

12.3 Results of process model 230

12.4 Discussion and conclusion of the initial modelling exercise 235

12.5 Heat up rate assessment 236

12.6 Key outcomes 239

12.7 Using the process model 241

13 GENERAL DISCUSSION 246

13.1 General discussion : Equipment development 246

13.2 General discussion : Process validation 265

13.3 General DISCUSSION: Modelling 275

13.4 Future considerations 285

14 CONCLUSIONS 289

15 APPENDIX 1 – LOCAL HEAT TREATMENT (LHT) HEAD EVOLUTION ... 293

15.1 In-head hot spot 293

15.2 Head design and manufacture 296

16 APPENDIX 2 – KEY PROCESS PARAMETERS AND SENSITIVITY STUDY METHOD 299

17 REFERENCES 311

INTELLECTUAL PROPERTY

The principle of performing localised heat treatment using inert gas jet impingement is covered by patent US7759614B [1]. During the course of this research a further patent has been filed to facilitate the future commercial exploitation of this technology, EP2088212 / US2009173416 [2].

PUBLISHED WORK AND AWARDS

Due to the commercially sensitive nature of the work, extensive publication and dissemination of this work has been restricted. However, generic process and development and modelling activities have been presented at two international conferences.

- "Gearing up for the winds of change" - 25th ASM Heat treating society conference, September 14-17, 2009, Indiana Convention center, Indianapolis, IN, USA [3].
- Gas Turbines: High Temperature Coatings and Life Extension, 09 Dec 2009 - 10 Dec 2009, The Institute of Materials, Minerals and Mining, London, UK.

This work has been presented to members of Rolls-Royce senior management was awarded *runner-up in the Sir Henry Royce award for technical innovation in 2007*. It was part of the project awarded *runner-up in the Sir Henry Royce award for technical innovation in 2009*, highlighting the importance of this technology. *The local heat treatment concept and prototype system described here has been adopted by Rolls-Royce and is currently being developed further using the principles and tools outlined and detailed within this thesis*.

1 INTRODUCTION

1.1 MATERIALS USED IN THE GAS TURBINE

A modern jet engine utilises a range of technologies and novel materials in order to reduce weight whilst increasing operating temperatures to provide improved specific fuel consumption (SFC). Nickel alloys are used extensively in the high-pressure compressor (HPC) and turbine regions where high temperature strength and integrity required. Titanium alloys have found significant use in the lower temperature regions (Low to intermediate compressor) due to their elevated temperature strength (relative to materials such as aluminium or polymer matrix composites), high specific strength (relative to steel and nickel), and excellent corrosion resistance.

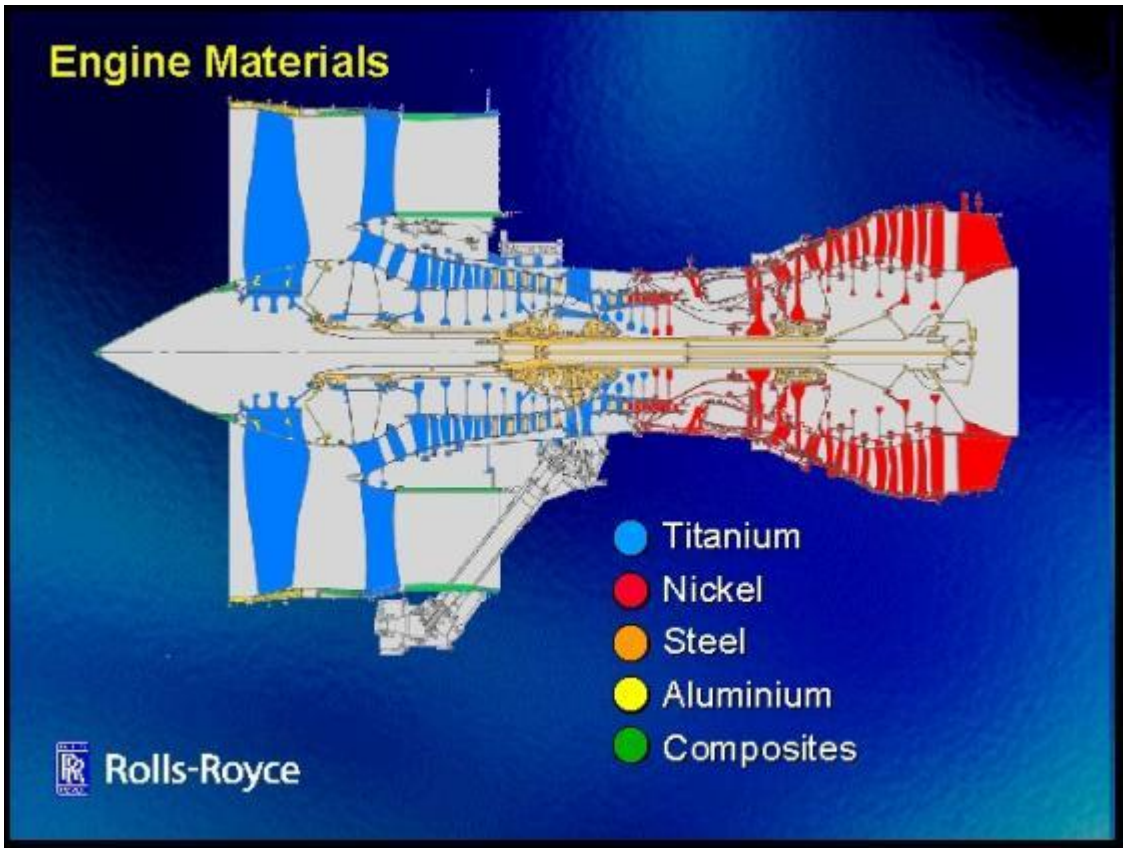


Figure 1-1 : Materials used in the gas turbine engine [4]

1.2 WHAT IS A BLISK?

Within an aero engine minimising of component weight is key in order to improved efficiency and thrust-to-weight ratios. Part of this drive has led to the development of components with integral parts joined using solid-state techniques. This reduces the requirement for heavy mechanical fasteners. A prime example of this is blisk (Bladed Disc) technology, where blades are permanently attached to the disc using a process called Linear Friction welding (LFW). This involves sliding the blade and disc against each other at high frequency in order to plastically deform the two components at the interface and produce a high integrity welded joint.

Blisk components provide significant advantages over conventional bladed disc assemblies. Over and above the aforementioned weight advantage, the removal of mechanical fasteners between the blade and the disc increases the stiffness [5]. Furthermore, removal of the join between the two components allows the designer to improve aerodynamic efficiency by smoothing these regions and blending the aerofoil into the disc rim [6]. This increase in aerodynamic efficiency can result in a significant improvement in specific fuel consumption making the engine a more desirable package for the customer.



Figure 1-2: Bladed disc (blisk)

Finally a blisk allows greater overall engine design flexibility by reducing the need for large sections on the rim to locate the locking features connecting blades to the disc. This increased weight at the rim, results in the disc itself being large to react the forces generated by the rotating mass. The use of a blisk removes the requirement for such a large rim section, thus allowing greater design flexibility, such as the use of less highly-specified bearings and shafts due to reduced loads during operation, increasing power-to-weight ratios.

1.3 BUSINESS DRIVER FOR BLISK REPAIR

Most aero-engine manufacturers supply engines to customers on a Total Care Agreement^{TM} (TCA) [7] basis, which involves the leasing of engines. Within this TCA the engine manufacturer is responsible for maintaining the engines and

providing any repairs required. Due to this business model more emphasis is placed on repair, especially in the case of expensive, lightweight components such as blisks. The manufacturing costs of blisks are very high due to the integral nature of the aerofoils and disc as well as the complex machining or welding operations required for manufacture. A simplified business case for blisk repair is given by Rabinovich [8].

As components become larger, more intricate and more expensive it becomes clear that in order to minimise the cost to the engine manufacturer these components have to be repairable. Previously if a mechanically attached blade became significantly damaged, due for example to Foreign Object Damage (FOD), it could be removed and replaced. In the case of a blisk this is no longer a viable option and a repair capability has to be developed.

1.4 BLISK REPAIR PROCESS OVERVIEW

Some minor component damage can be blended out, however such a repair may significantly alter the shape and hence affect performance. In this case a more sophisticated repair that restores the component back to its original form may be favourable.

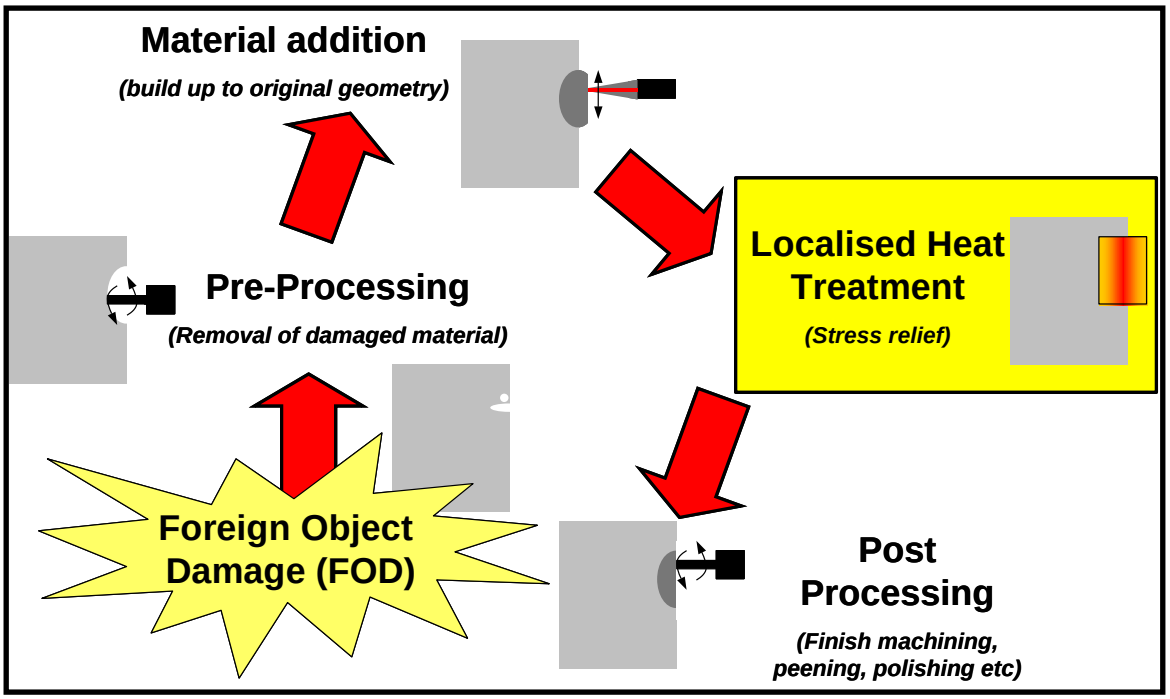


Figure 1-3 : Blisk repair process flow chart

One method of achieving this is to use a direct laser deposition (DLD) repair process that restores the component back to original design intent. Following DLD it is often the case that a stress relieving heat treatment is required to allow the component to enter back into service. This heat treatment may take many forms; it could be a stress relieving heat treatment in the case of welded titanium or a solution heat treatment in the case of nickel superalloys.

Figure 1-3 highlights the various steps in such a repair sequence. First is the incident leading to the requirement for repair (e.g. a FOD incident), next is a pre-processing stage, which includes material removal and preparation of the region ready for deposition. Following this there is a material addition phase where the component is built up back to the original geometry using a fusion welding technique, such as that described by Nowotny *et al* [9], Richter *et al* [10] and Tuppen *et al* [11]. Following the material addition stage the component goes through a number of post processing operations. These include a stress relieving heat treatment, machining of the deposition to restore aerofoil profile, and an etching process to remove oxidation formed during the previous processes. It may be that other processing steps such as shot peening are involved.

1.4.1 WHY LOCAL HEAT TREATMENT?

To maintain an acceptable fatigue life in the component such as a blisk, a stress relief heat treatment is required [12]. It is standard practice to heat treat titanium components in a vacuum furnace to provide effective stress relief. This is termed global heat treatment as the entire component is heated to the required temperature. The repair process for blisks contains a requirement for post deposition heat treatment, there are two main options for this; a localised heat treatment, or a global heat treatment requiring the entire blisk assembly to be placed in a hard vacuum furnace.

The application of global heat treatment would result in the entire component being stress relieved. However, these complex components often have regions of compressive stress deliberately introduced into the surface to increase fatigue life

[5]. The addition of compressive stress at the surface through processes such as shot peening, helps to resist fatigue crack initiation and growth [13]. If the component were globally processed, then these ‘useful’ residual stresses would also be relieved and have to be re-introduced. If one could not reintroduce these stresses then the component would suffer significant life reduction when entering back into service.

The application of a global heat treatment on titanium components would also mean the whole component would need to have the layer of alpha case resulting from the heat treatment removed, requiring a very complex machining process. This level of machining would be impractical and uneconomical; therefore a chemical removal technique would be required. It is likely that a service run blisk will be at the bottom geometrical tolerance level as they are designed to contain very little excess material.

Application of a local method may minimise the distortion experienced in the component. In service a blisk undergoes thermal and mechanical cycling due to the high temperatures and rotational loads it is subjected to. As a result it is highly likely there will be significant residual stress built up in the component. Subsequent heating in a furnace may result in these stresses relieving due to creep, which may result in significant change in form. The use of a localised heat treatment would limit this phenomenon to the aerofoil, specifically the repaired region. However, it is worth noting that the localised nature of this method may also actually act to introduce thermally induced stress into the component.

Finally, some aerofoil designs may utilise damping medium in the centre which degrades at temperatures above ~150°C [14]. Therefore putting these particular components in a furnace is not an option.

For localised features, such as high integrity DLD repairs, specialised local heat treatment allows significant regions of components to remain unaffected, retaining properties, life, and value [15]. Current methods such as radiant (thermal blanket), induction and power beam heaters cannot adequately control temperature across regions of complex geometry (e.g. thickness, positional, contour). A process is required that is compliant to variations in component geometry.

For alloys sensitive to oxidation such as titanium, an inert atmosphere must be employed. This thesis describes the development of a patented system [1] to process components locally using inert gas jets. The innovative system uses an electrical heater, which heats an inert process gas. This hot gas is directed onto the target area using patterned nozzle arrays. This is accomplished through low-cost box plenum structures with (typically) laser-cut jet plates. The argon accelerates through the nozzles as impingement jets, becoming turbulent on the component surface so as to maximise heat transfer. Independently heating the gas ensures that the component is protected from risks of extreme temperature.

2 BACKGROUND INFORMATION AND REVIEW OF RELEVANT LITERATURE

This literature review starts with a general overview of the repair process, beginning with the damage itself. The most commonly used material in blisk components is titanium 6-4, therefore a basic introduction to titanium and its alloys is included. This is followed by an introduction to the issues surrounding the heat treatment of titanium, including the generation of brittle phases and the requirement for stress relief. Finally an introduction to impingement jets and gas jet heating is provided.

2.1 FOREIGN OBJECT DAMAGE (FOD)



Figure 2-1 : FOD damage on the leading edge of an aerofoil

FOD (Figure 2-1) is most likely to occur during take-off or landing due to the existence of hard particles from the runway or low flying birds. Figure 2-2 shows the range of damage in different aircraft types and altitudes. Damage may also result from objects breaking off inside the engine (e.g. coatings); this is termed Domestic Object Damage (DOD). Titanium 6-4 fan and compressor blades by virtue of being located at the front of the engine suffer the majority of the impact leading to FOD, with the leading edges being common regions requiring repair. In terms of the size of the region requiring repair, Ruschau *et al* [16] noted that the “majority of FOD involves damage less than 2mm in depth”. Foreign Object Damage (FOD) is often in the form of deformation at the

edge of the aerofoil, often in the top half of the aerofoil towards the tip††. This deformation requires repair as it can result in a loss of aerodynamic efficiency, which may result in loss of thrust or increased fuel consumption, in some cases it can also result in engine in-balance. In its worst form it can significantly reduce fatigue life, a major concern on a critical rotating part such as a blisk [17]. Therefore this deformed material must be removed and replaced to return the aerofoil to its original form.

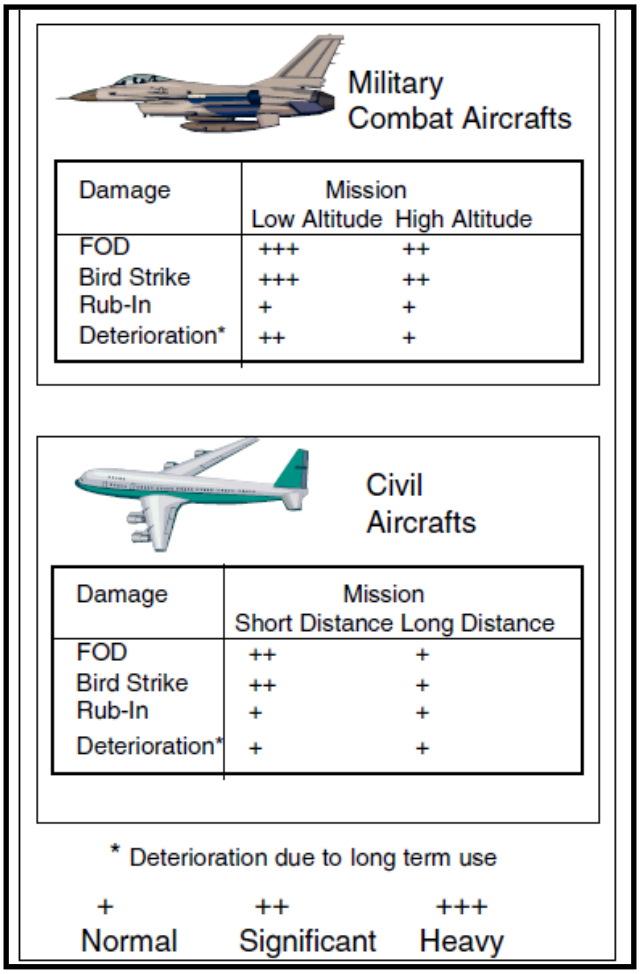


Figure 2-2 : Damage rate due to aircraft type and mission [18]

Ruschau *et al* [16] noted that the largest debit in fatigue life resulted from impacts not normal to the leading edge, normal impacts resulted in compressive stresses behind the crater from which failure initiated. In impact angles greater than 0°, tensile stresses were generated at the entrance to the FOD site and stress concentration features such as tears were noted. A further interesting point was that fatigue strength reduction could not be correlated to FOD depth alone

†† The reason for this is that objects tend to get thrown out to the tip of the aerofoil due to centripetal forces acting on the object.

due to the influence of irregular features such as tears or notches. As a result it is sensible to repair a region larger than the impact deformation resulting from the FOD incident to ensure any regions of residual stress or irregular features are fully removed.

2.2 THE KEY REPAIR PROCESSES

Yilman *et al* [19] describe a generic aerofoil repair process in which the initial component geometry is captured using 3D non-contact measurement capability, (e.g. GOM ATOS II-400). The damaged region is identified and the 3D model used to generate the tool paths of the machining and material addition (welding) processes. The 3D scanning technology can then be used throughout the repair process to capture any distortion due to the subsequent processing operations and modify the tools paths in an adaptive manner [19].

2.2.1 THE DEPOSITION PROCESSES



Figure 2-3 : Example of deposit for aerofoil repair [20]

After removal of the damaged material, an additive process is often used to re-build the aerofoil (see Figure 2-3). The welding process can take the form of conventional wire fed Tungsten Inert Gas (TIG) [21], or using a laser as the heating source and a wire or powder feed to introduce material into the melt pool [22].

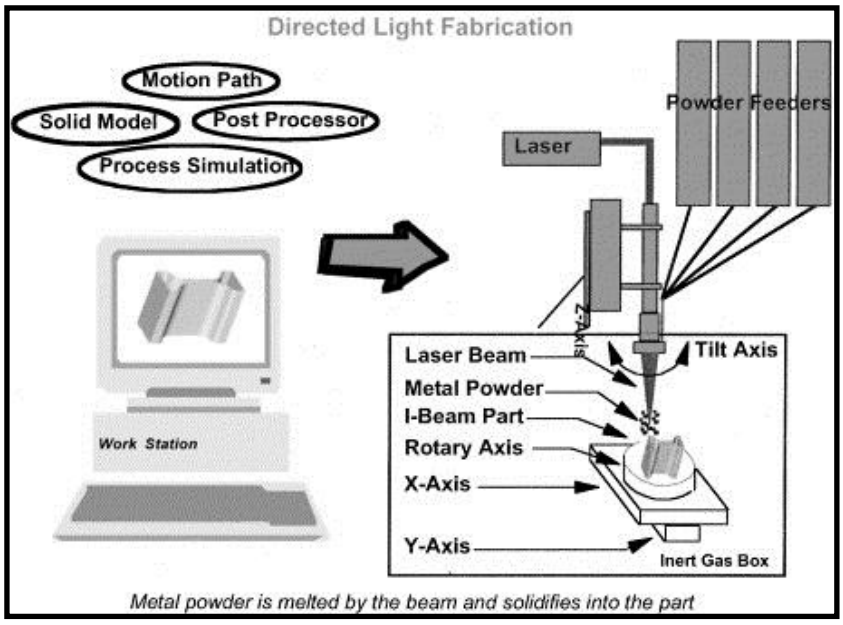


Figure 2-4 : Schematic description of additive process, from Lewis and Schlienger [23]

During the additive process a continuous supply of filler material (wire or powder) is fed into the laser (or welding torch/arc) focal zone where it is melted and re-solidifies in the wake of the molten pool. Figure 2-4, from Lewis and Schlienger [23] schematically describes the process in which a computer system is used to produce the CAD/CAM control for toolpath generation and to drive the hardware to deposit the material. Processing is typically performed in an inert gas environment to reduce oxygen levels when processing materials such as titanium alloys [23]. Deposition of multiple layers one on top of the other replaces the damaged material and restores the component geometry and integrity.

The benefit of using a laser deposition system for repair of aerospace components is the low heat input generated (when compared with conventional welding techniques), and the ability to produce thin walled depositions (0.3-2.5mm [23]). CNC control along with isotropic powder delivery to the melt pool through coaxial delivery nozzles allows multi-directional deposition onto complex shapes [24].

During the laser additive process a molten pool is created at the focal zone of the laser into which the filler material is introduced. The molten pool can vary from half to five times the diameter of the laser focal-spot depending on the power and velocity of the spot on the surface [23]. The pool is affected by the underlying heat sink of either the substrate or previous deposition layers. Controlling laser power and laser travel speed can compensate for the cooling effect of the underlying material.

2.2.1.1 Surface finished of deposited material

Lewis and Schlienger [23] quote a surface roughness of 12μm (comparable to investment casting) resulting from laser powder deposition, whereas a typical value of 0.5 μm [25] is required for aeroengine compressor aerofoils. This highlights the need for further finishing operations to restore aerodynamic performance. Ahsan *et al* [37] noted that the use of Plasma rotating Electrode Powder (PREP) in blown powder deposition as apposed to Gas Atomised (GA) powder resulted in lower surface roughness.

2.2.2 MACHINING OF THE REPAIRED REGION

Following restoration of the damaged region using an additive process, a machining technique such as 5-axis milling is applied. Machining to final shape is typically done after heat treatment in order to reduce the tendency for residual stresses arising from deposition to be relaxed through deformation during machining as described by Brinksmeier [26].

In terms of surface finish following final machining Ginting *et al* [27] quote achievable surface roughness values of 0.39 – 0.72µm following dry machining of Ti-6242. This allows the surface roughness of 12µm following the deposition process [23] to be brought closer to the 0.5µm [25] requirement quoted by Passey for aero engine applications. Further improvements in surface finish can be achieved through polishing.

2.3 TITANIUM AND ITS ALLOYS

Titanium alloys are used extensively in a variety of industrial applications. Around 50% of all titanium is used in the aerospace industry [28] due to its excellent strength to weight ratios. Titanium is also highly corrosion resistant due to its stable surface oxide and has a melting temperature of 1678°C, although this varies with alloy composition. At 882.5°C [28] pure titanium undergoes a microstructural change from low-temperature hexagonal close packed (alpha (α)) structure to a body-centred cubic (beta (β)) structure. This temperature is termed the β transus and varies with alloy composition. The crystallographic structure of titanium means it reacts with solid solution strengthening elements with a size factor within 20%.

The alloying of titanium is dominated by elements that stabilise the alpha or β phase of the material. Generally, elements with electron/atom ratios of <4 stabilise the alpha phase, those with ratios of 4 are neutral, and those with ratios >4 stabilise the β phase [28]. Titanium and its alloys are highly reactive with other elements at elevated temperature, particularly interstial elements such as oxygen, nitrogen and hydrogen. This has necessitated the development of non-conventional refining and processing techniques, often aimed at reducing the amount of small mobile atoms such as oxygen (causing oxidation) and hydrogen (leading to hydrogen embrittlement) at high temperature [29]. Titanium alloys are also highly ductile and can be machined and forged relatively easily [30].

2.3.1 ALPHA ALLOYS

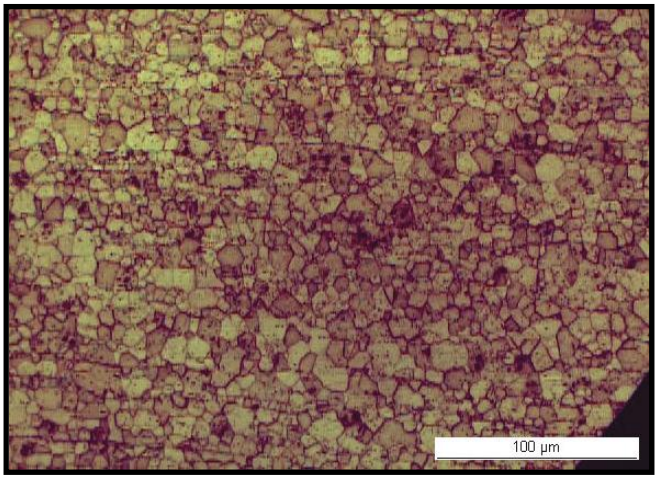


Figure 2-5: Commercially pure titanium microstructure shown through optical microscopy

Alpha alloys tend to have higher modulus, lower density, higher creep resistance [31], and diffusion rates at least 2 orders of magnitude lower than β alloys. The alloying elements used in α alloys generally dissolve in the α-phase; examples of such elements are aluminium, and oxygen, although the latter is generally regarded as an impurity and kept at low levels to avoid embrittlement. A general rule for α titanium alloys is that for every 1% of added element the tensile strength increases by 35-70MPa [28]. α alloys display excellent corrosion resistance but lower strength than α/β or β alloys and tend to find extensive use in the chemical industry for piping, valves and heat exchangers. Figure 2-5 shows the microstructure of a commercially pure titanium alloy, which is essentially a titanium-oxygen alloy containing no significant levels of β stabilisers. The main features of this microstructure are the equiaxed grains of single phase α and absence of β phase.

2.3.2 ALPHA/BETA ALLOYS

A limitation of α titanium alloys is the existence of an ordering reaction when the aluminium equivalency goes beyond 9%. α alloys are also difficult to hot forge leading to the development of α/β alloys containing both α and β stabilising

elements. These alloys retain more β after final heat treatment and can be strengthened by solution treatment and ageing. Solution treatment is generally performed in the α-β phase field with ageing performed at lower temperatures to precipitate α, and give a mixture of fine α in a β matrix [32]. Aluminium equivalent can be calculated by summing the weight percentages as follows;

Equation 2-1: Aluminium equivalency = $Al + \frac{1}{3}Sn + \frac{1}{6}Zr + 10(O + C + 2N)$ [28] ,

2.3.3 TITANIUM 6-4

α/β alloys possess relatively high tensile strength and improved formability (over α alloys), however they exhibit reduced creep strength above 400°C. Titanium 6-4 is an example of an α/β alloy, and contains around 6 weight percent aluminium (α stabiliser) and 4 weight percent Vanadium (β stabiliser). Titanium 6-4 is a very widely used alloy in the engineering sector and represents around 50% of titanium alloy sales in the U.S. and Europe [28].

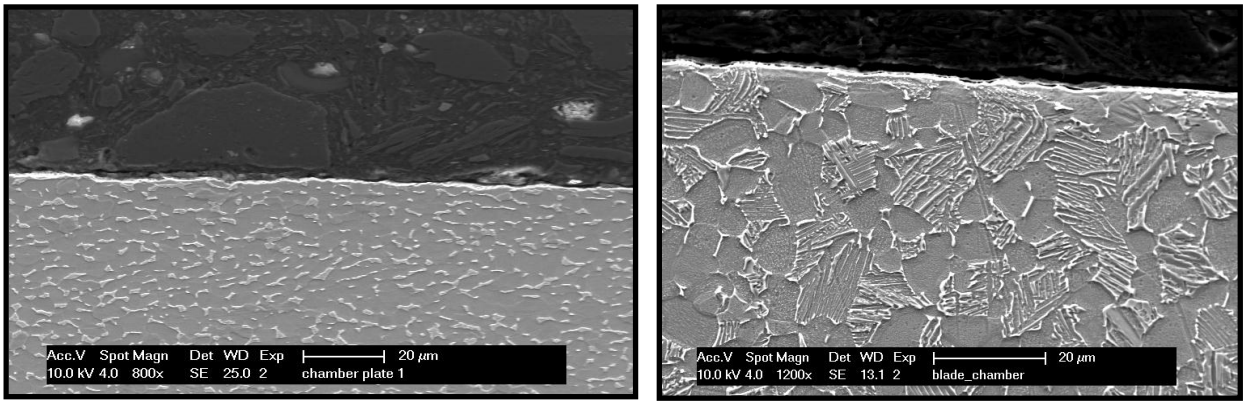


Figure 2-6 : Titanium 6-4 microstructure showing finely dispersed retained beta (left), and bi-modal microstructure (right)

Many texts offer descriptions of the microstructural properties available by careful processing of α+β titanium alloys, with those by Polmear [28], Porter and Easterling [33] and Lütjering [34] being the most accessible. There are two transformations of interest in titanium 6-4 alloy heat treatments. The first is the precipitation of α from β when cooling from above the β transus into the α+β phase field. On cooling Widmanstätten morphology is formed at all practical cooling rates, resulting in a microstructure of retained β layers between plates of Widmanstätten α. The second is the transformation of β into martensite (a supersaturated hcp α phase) by rapid cooling, such as water quenching. For titanium 6-4 the martensite finish temperature is above room temperature and the resulting martensite can be aged by heating. Ageing allows the decomposition of supersaturated α' by precipitation of β on martensite plate boundaries and dislocations [33].

When titanium 6-4 is used in engineering applications it is generally worked in the α+β or β phase field, this breaks up the structure to finely distribute it in the material. Following this the material is annealed at around 700ºC resulting in finely dispersed retained β producing a ductile material (with the presence of Widmanstätten α (Figure 2-6)). Additional strength is provided by a bi-modal microstructure (Figure 2-6) produced by further heating to the α+β field (~940ºC) in order to produce a large volume fraction of β before water quenching to produce α' martensite. This can then be heated to precipitation harden the martensite. If further strength is required the alloy is held at a lower temperature in the α+β phase field before quenching to produce a Vanadium rich β phase. If rich enough this depresses the martensite finish temperature to below room temperature,

therefore producing retained β on quenching [33]. Kubiak *et al* [35] also noted the larger the β-stabiliser content, the lower the martensite start and finish temperature.

2.3.4 BETA ALLOYS

If a higher proportion of β-stabilisers than α-stabilisers are present in the alloy then β alloys result. These alloys generally have a higher hardenability and display good forgability and formability in the solution treated form. High strength levels can be achieved through fine dispersion of α particles in the β phase. β alloys generally have higher densities and lower creep strength than α or α/β alloys. The fracture toughness of aged β is higher than that of an α/β alloy, however crack growth rates can be faster.

2.4 MICROSTRUCTURE OF THE DEPOSITED MATERIAL

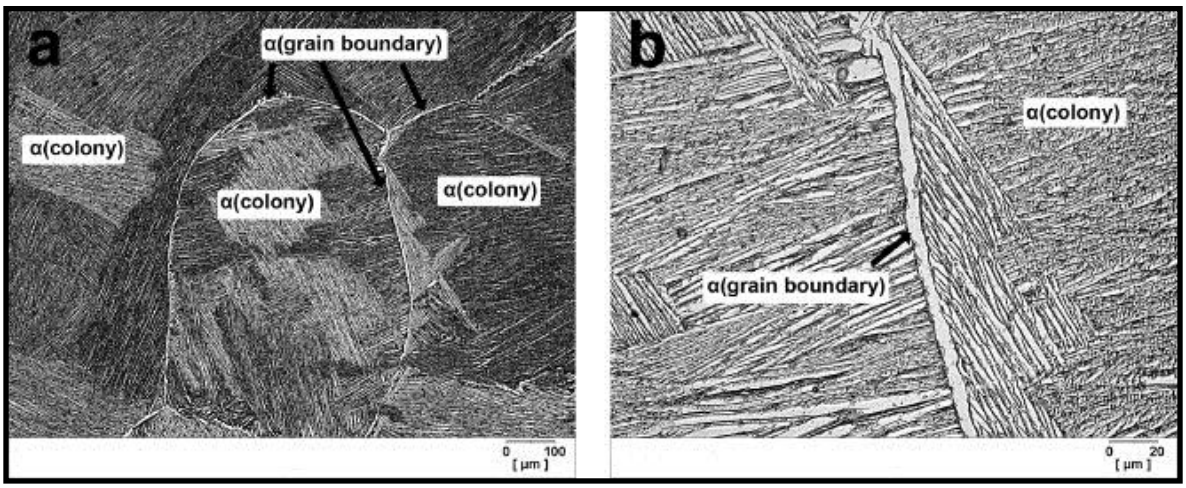


Figure 2-7 : Typical Ti-6Al-4V deposited microstructure resulting from laser additive manufacturing process, figure from Brandl *et al* [36]

The Ti-6Al-4V deposits produced from the additive processes are generally characterised by basketweave-like Widmansttaten α in large prior β grains [37, 36],

see Figure 2-7 (above). Lamellar spacing is influenced significantly by laser power, generally increasing linearly with laser power [37]. Ashan *et al* [37] note that microhardness decreases with increasing lamellar spacing. Baufeld *et al* [21] state that UTS decreases with increasing lamellar width and suggest that the lamellae width determines the active slip length. Higher heat input additive processes as Shaped Metal Deposition (SMD) produce deposits with significantly varying lamellar width from top to bottom of the deposit due to the repeated heat treatment of the subsequent layers [21]. Detailed understanding of the effect of parameters on resulting microstructure (and therefore mechanical properties) is critical to developing a repair with acceptable integrity for a given application.



Figure 2-8 : Typical Ti-6Al-4V laser deposit showing columnar grain growth and layer banding, figure from Ahsan *et al* [37]

The large retained β columnar grains that characterise additive process deposits grow perpendicular to the solid-to-liquid interface due the steep temperature gradient providing the maximum driving force for solidification. It is noted by Ahsan *et al* [37] that increasing laser power results in increased β grain size, a typical example is shown in Figure 2-8. The preferred crystallographic growth direction for these grains varies from alloy

to alloy (for example <100> for BCC β in Ti-6Al-4V). During solidification, grains that form with this direction aligned perpendicular to the maximum temperature gradient will displace other grains that do not [22]. This competitive growth leads to fewer, larger, highly textured grains towards the top of the deposit, as shown in Figure 2-8 (above). Also of note in Figure 2-8 (above) are the horizontal lines (banding) across the deposit showing evidence of the various layers, a refined microstructure characterises the boundary between layers as a portion of the previously deposited material is re-melted and re-solidifies.

The heat affected zone (HAZ) of Ti-6Al-4V deposited material is defined in detail by Brandl *et al* [22] as being made up of various 'zones' containing a graded microstructure from the bimodal microstructure of the forged base material to the basket weave structure characteristic of additive processes.

2.4.1 MECHANICAL PROPERTIES OF DEPOSITED MATERIAL

The literature is in general agreement that mechanical properties comparable to base material are achievable with laser additive deposition processes. Lewis and Schlienger [23] quote Ti-6Al-4V produced by Direct Laser Fabrication to display tensile strengths equivalent to wrought, but with elongations of 6% compared to 10% for wrought Ti-6Al-4V. Baufeld *et al* [21] quote a UTS of between 929MPa and 1014MPa for deposits made using Shaped Metal Deposition (SMD) depending on orientation and location in the deposit. These comparing these favourably with values of 930MPa for wrought material [21]. Higher values for strain at failure of between 9-21% (compared to 10% for wrought) are reported for SMD [21], showing that the higher heat input of this process compared to laser deposition techniques produces a coarser, more ductile microstructure. However it is noted

that the increased heat input may have a significant effect when it comes to distortion of repaired parts.

2.4.2 EFFECT OF MACHINING ON THE MICROSTRUCTURE OF TITANIUM ALLOYS

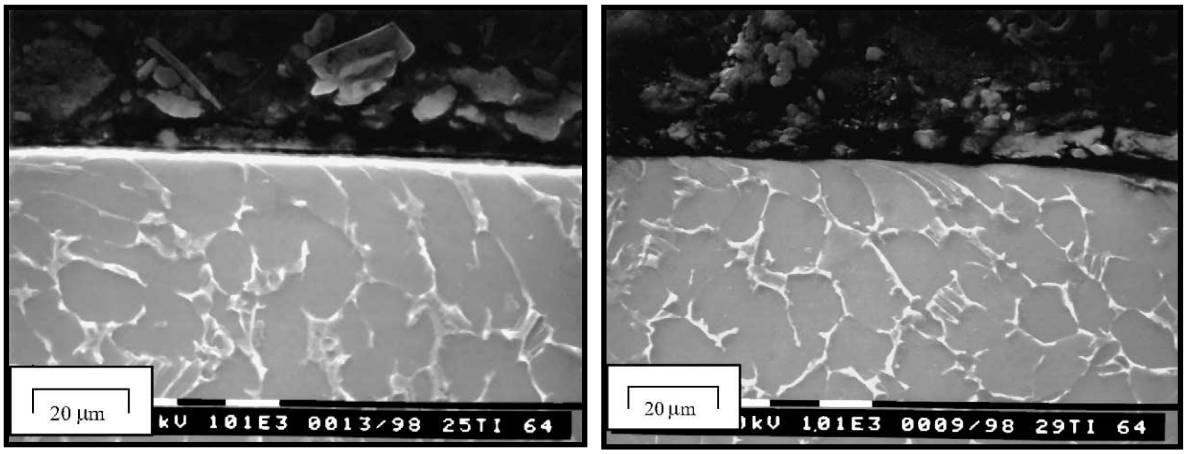


Figure 2-9 : Undesirable surface features during machining of titanium alloys, figures from C. H. Haron *et al* [40]

Ulutan *et al* [38] provide a detailed introduction to the machining of titanium and nickel alloys. Titanium alloys are prone to carbide cracking due to plucking and smearing of titanium carbides from the surface during machining [38]. These features act as initiation sites for cracks and can lead to a reduction in fatigue life in the finished component. The thermal properties of titanium alloys are such that conduction of heat away from the cutting surface is reduced in comparison to other alloys [38]. This can lead to overheating and significant plastic deformation resulting in the formation of a 'white layer' [38, 40, 39] visible through microscopy, extending 10-20µm into the surface [38], Figure 2-9 [40]. Machining with worn tools or poorly development machining parameters can lead to severe plastic deformation of the surface microstructure, see Figure 2-9 [40]. All of the above can be minimised (although not completely removed) by the selection of appropriate

feed rates and cutting speeds, as described elsewhere [27]. However there is always a balance to be struck between process time and cost.

2.5 HEAT TREATMENT OF TITANIUM

The heat treatment of titanium alloys is performed for a number of reasons. It can be to reduce residual stress developed during other manufacturing processes in order to produce the most acceptable combination of ductility, machinability and dimensional stability, or to increase strength by solution treating or aging [41]. One of the characteristics of titanium is its susceptibility to oxygen and nitrogen 'pickup' during heat treatment stabilising the α phase. Due to titanium's high affinity to oxygen, critical rotating titanium components must have their number of heat treatment cycles minimised [42].

2.5.1 LIMITING ALPHA CASE FORMATION

When temperatures exceed 480-530°C oxygen noticeably diffuses into the surface of titanium. At higher temperatures >760°C oxidation becomes more rapid and the elements in contact with its surface (i.e. those in furnace atmospheres such as oxygen, nitrogen, and hydrogen) diffuse into the metal causing a hardening effect at the surface and embrittlement [43]. The hexagonal close packed nature of titanium results in few slip planes, and interstitial elements entering the lattice act to block these slip planes causing dislocations to stack up. As a result, when cracks form the reduction in plasticity at the crack tip provides little resistance to crack propagation. The elements mentioned above not only form compounds at the surface but also enter the metal lattice causing a loss of ductility and toughness. This is a lifing issue, as the hard brittle surface layer and large α grain

size (known as alpha case when oxygen is the embrittling element), provides little resistance to crack propagation [44]. An example of alpha case is provided later in Figure 8-8 (a). Donachie [41] suggests that any heat treatment above 425°C should be performed in an inert atmosphere designed to minimise alpha case and scaling. Bache *et al* [45] noted that fatigue crack propagation in titanium 6-4 alloy is highly sensitive to both external atmosphere and internal oxygen concentration. They also noted that at relatively high oxygen content (above 4000ppm) there was a significant increase in the fatigue crack growth rates in comparison with alloys containing lower oxygen levels i.e. <2300ppm.

Donachie [41] states that at 955°C alpha case can extend 0.2 - 0.3mm beneath the surface, and notes that oxygen is a more potent alpha case former than nitrogen due to its higher absorption rate. The work of Jordan [46] presents a more quantitative and industrially relevant investigation into the levels of alpha case formed on titanium 6-4 test pieces processed in a vacuum furnace. Here, the deepest level of alpha case recorded was 10.2 microns after a vacuum furnace heat treatment at 1300°F (~700°C) for 30 minutes. In this test the vacuum had been maintained at $3x10^{-4}$ torr and the furnace door had been left open for three hours on a damp morning. The resulting surface was blue in colour and the sample had increased in weight by 0.0012g. The interesting point to note from this work is that when the same sample type was processed in an air furnace for 1 hour at 1300°F the test piece colour was grey/brown and alpha case visible only to a depth of 3.8microns. Although this may initially seem to be an unconventional result Jordan does note the existence of a thick (~0.5 microns) continuous grey oxide on the surface. Measurement of alpha case depth is not limited to visual

techniques, for example hardness profiles or the use of dispersive X-ray analysis (WDX) line scans are used [47].

Fukai *et al* [44] investigated the formation of oxygen enriched layers on two α/β alloys in both vacuum and argon atmospheres at the temperatures associated with super-plastic forming operations. They noted visibly detectable alpha case to a maximum depth of 20μm in Ti-4.5%Al-3%V-2%Fe-2%Mo when heated in argon at a temperature of 775°C for 6 hours, and 63 μm in Ti-6%Al-4%V in argon at 899°C for 3 hours. The argon gas oxygen content was 5ppm in both cases (typically bottled argon contains between <5ppm O2 [48]). Noteworthy is that the maximum depth of alpha case was observed in the titanium 6-4 alloy held at the higher temperature.

Clearly it is important to minimise the amount of reactive elements in the atmosphere when performing heat treatments. However it is not possible to entirely eliminate these elements (such as oxygen, nitrogen, hydrogen) and the high affinity of titanium to these at temperature. Hence, there is a requirement for post heat treatment processing to remove their effects [44]. This can take the form of etching or machining, however, Donachie [41] also notes significant reduction in tool life due to the abrasive nature of alpha case.

2.6 ATMOSPHERE REQUIREMENTS FOR PROCESSING TITANIUM

The previous section has dealt with some of the issues surrounding titanium at temperature; the options for a heat treatment atmosphere are; a vacuum, inert gas, carbon dioxide, or air. Air can be used but leads to the formation of significant alpha case on the components surface. This would require removal, which is

unfavourable given the tight tolerances found on aerospace components. A heat treatment method that limits the available oxygen within the system is required to minimise the alpha case. In the case of carbon dioxide, carbon also has a marked effect on titanium properties (specifically titanium 6Al-4V) [49], and oxygen contained within CO_2 has been shown to increase oxidation at temperatures of 675°C [50]. It is therefore not considered suitable for the heat treatment of titanium alloys.

2.6.1 VACUUM HEAT TREATMENT

The practicalities of maintaining a vacuum in a local region and having sufficient sealing on a component to achieve a reasonable vacuum standard is impractical. This is without considering a preferential oxygen sink in the form of a hotter metal "getter". In short, a vacuum is only applicable in a global heat treatment scenario.

2.6.2 INERT GAS ATMOSPHERES

The inert gases (such as helium and argon) do not diffuse through metals [51] and commonly used for furnace atmospheres, however helium has a significantly high unit cost. The lower cost of argon and the fact that most facilities have a shop supply, make it a common choice. When an argon atmosphere is used it is recognised that there is still up to 5ppm [48] of oxygen in the system [52]. As the purity of the gas supply is increased then the partial pressure of oxygen in the system decreases. Most production facilities have a bulk supply of argon (e.g. for weld shielding) although heat treatment systems use large quantities of gas leading to a requirement to re-circulate the gas and use argon scrubbers (oxygen and moisture sinks). Argon scrubbers can manifest themselves as large surface area pieces of hot titanium (i.e. above 500°C), which act to preferentially remove

oxygen before it comes into contact with the component. Argon gas purities vary from bottled gas (of varying purity levels) to liquefied argon; any system containing argon requires an oxygen analyser to monitor oxygen content. There is also the possibility that moisture could be contained within the gas (especially in the case of bottled gas), through leaks, or condensation in the pipe work. R. J. Fradette of Solar Manufacturing Inc. suggests [53] that for the most popular vacuum furnace operating on a humid day (70% relative humidity, and temperature of 90°F) 6.25 ounces of water could be contained within the insulation and other furnace materials.

2.6.3 HYDROGEN AND SURFACE CONTAMINATION

Hot titanium surfaces readily react with moisture, water vapour decomposes at high temperatures and the hydrogen enters the material in solid solution. This hydrogen acts to stabilise the transformed β phase, potentially leading to brittle hydride formation in regions of high stress intensity, for example at crack tips [54].

The solubility of oxygen and hydrogen is noticeably increased above 500°C, i.e. the heat treatment temperature. Any residual grease (or other contaminants) on the surface may also undergo the same process as that of moisture. Any level of surface roughness will act to trap contaminants on the surface as well as increase the surface area available for them to diffuse into. Aero-engine components being heat treated may have unknown levels of hydrogen (from Original Equipment Manufacture (OEM) and service) already within their structure. There is the possibility that when the heat treatment is applied locally, following Ficks 2nd Law, there will be diffusion of the hydrogen to the heat treatment area from other parts

of the component. Within the MA region the coarse grain structure results in a smaller number of grain boundary triple points (Figure 2-8, previsouly). When an even distribution of hydrogen is assumed then these points will become relatively more saturated.

2.6.4 HYDROGEN DEGAS?

It is possible to employ a hydrogen degas heat treatment involving heating the titanium component in a vacuum to 730°C [55]. This drives out much of the hydrogen held in solid solution. However, the impracticalities of providing sufficient sealing around the tight radius of an aerofoil leading edge preclude this from being a suitable process for this application. Localised heat treatment design should mitigate the risk of hydrogen ingress through the use of high purity inert gas and correct bake-out procedures to remove water, such as that defined in [53].

2.7 STRESS RELIEF HEAT TREATMENT

The repair to the leading edge of a blisk aerofoil is done by depositing material using processes closely akin to welding. As a result it is necessary to perform a stress relief heat treatment. In the case of titanium 6-4, this heat treatment is performed at well below the β transus temperature and therefore produces no significant microstructural change. Donachie [41], states that selection of the correct stress relief cycle to reduce stress levels in an economical timescale should use 'the maximum temperature consistent with limited change in microstructure'. Several authors detail the range of temperatures that produce the most effective level of stress relief in titanium 6-4. J.A. Burger *et al* [43] state a temperature of 550-700ºC for 1-2 hours is sufficient to significantly reduce residual stress levels in a Ti 6-4 MA DLD repaired test piece. P. Gupton [56], states a temperature of 1000 (538°C) to 1100°F (593°C), for a period of 1 to 12 hours is sufficient to stress relieve titanium 6-4. Wagner [57] also noted shot peened specimens exhibited the same stress curve after 1 hour at 500°C, as those in an unpeened condition, suggesting this time and temperature was sufficient to relieve all residual stresses present from the peening operation. Although cooling rate from the stress relieving temperature is not critical in titanium alloys, Donachie [41] warns that uniformity of cooling is; especially between 480 and 315°C as it may induce residual stress.

2.7.1 WHAT CAUSES RESIDUAL STRESSES?

Leggatt [59] suggests that the maximum tensile residual stress generated in a welded structure can be equal to the yield strength of the material if there is

restraint against the thermal contraction on cooling, and the thermal contraction strain on cooling is greater than the yield strength. Moat *et al* [24] describe a peak tensile residual stress of ~420MPa at the free surface on the top edge of walls built up in Waspaloy, and peak compressive stresses of –410MPa towards the bottom close to the substrate. It is suggested that these residual tensile stresses in the substrate are due to the bending moment produced in the specimen as a result of the thermal contraction of the last layer on cooling. Ding *et al* [58] also predicted using finite element modelling (validated with experimental data) tensile residuals at the top of a thin wall of deposited material balanced by compressive residuals in the base material close to the interface. Significant bending of the test piece was also noted when the stresses were redistributed after unclamping of the test piece, supporting the suggestions of Moat *et al*. Leggatt [59] also states that during multi-pass welding transverse shrinkage of the final weld passes results in tensile residuals generated near the upper surface, balanced by compression at the mid thickness. Liu *et al* [60] note high residual stresses in the overlapping regions of two adjacent layers and low residual stress in the interior regions of single passes of laser rapid formed Inconel 718 nickel based superalloy. This correlates with the suggestion that the restraint provided by the substrate acts to increase residual stress on cooling.

As a result of the material addition process used in repair there are local expansions and contractions of the material as the powder is melted and solidifies in the repair region. The surrounding material is put under strain from these effects as it attempts to resist the movements. The stresses induced as a result of these are termed residual stress. Welding typically produces large tensile stresses,

which are often close to the yield stress of the material. These are balanced by lower residual compressive stresses elsewhere in the component [59]. It is the tensile residual stresses that pose the most significant threat as these can increase the rate of fatigue induced failure and also cause distortion [61]. As stress relieving occurs through a process of diffusion, the stress relief mechanisms are time and temperature dependant. At low temperature it is elastic strain relieved by plasticity and at higher temperatures it is a creep driven mechanism [62]. This means there are a number of potential options for a heat treatment cycle. For example, one could hold at low temperature for a long period (this would be beneficial from the point of view of alpha case formation). Or a higher temperature for a shorter period (in this case the opposite may be true).

P.Prevey *et al* [63], describe the stress relaxation properties and mechanisms of titanium due to heat treatment. The paper is specifically interested in the reduction in residual stress (measured by x-ray diffraction) introduced due to surface enhancement techniques (such as shot peening and laser shock peening) at engine operating temperatures. The majority of the study is interested in temperatures at the lower end of the titanium heat treatment scale (325 - 425°C). Prevey's data showed 50% reduction in stress in 10 minutes, and distortion on stress relieving. Prevey [63] makes particular reference to a two stage effect of stress relaxation. In the primary stage stress relaxation is rapid, whereas the secondary stage is slower and is likely to be a diffusion lead phenomenon.

It is noted by Leggatt [59] that due to the high yield strength and low Young's modulus of Ti-6Al-4V, that the contraction strain is not sufficient to generate yield magnitude residual stresses during welding.

2.7.2 MACHINING INDUCED RESIDUAL STRESSES

Wyatt and Berry [64], describe the three main sources of residual stress generation during machining as; thermal deformation, mechanical deformation, combined thermal and plastic deformation. Thermal deformation is a result of heat accumulation (and potentially a resulting phase change) during the machining process due to poor parameter selection. This causes localised expansion or contraction, which is resisted by the bulk material below [26]. Mechanical deformation is induced by load on the surface from the machine tool and usually manifests itself as a compressive surface layer, similar to, but with a lower magnitude than that resulting from shot peening [39]. In the case of thermal and plastic deformation, the expansion due to the heat generated in the surface is relieved by plastic flow during the machining process, this results in the surface being placed in tension due to the restraint applied by the bulk material on cooling [39]. Surface tensile residual stresses are less favourable than compressive stresses as they can lead to significantly reduced fatigue life.

2.7.3 CHOOSING A STRESS RELIEF CYCLE

The Metals Handbook [65] suggests that a heat treatment at 620°C for 2 hours would result in >75% stress reduction. At a temperature of around 595°C, residual stresses in a titanium 6-4 test piece dropped off from 750MPa to below 150MPa in less than one hour [65]. The same work also provides a graph which highlights that above 480°C there is a marked reduction in residual stress between 0 and 10 minutes followed by little further change until after 1 hour, indicating the change from creep to plastic relax mechanisms. Li *et al* [66] discuss the stress relaxation

of titanium 6-4 between 500-900ºC noting that below 700°C the relaxation rate was slow, but increased with increasing temperature. Sridhar *et al* [67] noted a 90% relaxation in machining induced residual stresses in IMI834 when heat treated at 600°C. A further consideration is that titanium 6-4 may contain coherent Ti3Al particles to provide age hardening, the solvus of which is at 550°C. Heat treatment at 500°C will result in precipitation of these particles, therefore Lütjering [34] suggests that heat treating at 600°C or above will result in a stress relieving with little observable microstructure change.

Brandl *et al* [22] defines a temperature of T_{diss} (stated as 708°C) as the temperature at which the α phase dissolves into β under equilibrium heating conditions, stating that if material is heated to a temperature below Tdiss no microstructural change will occur. Majorell *et al* [68] state a temperature of 677°C (950 K) for the point at which the volume fraction of β increases (i.e. T_{diss}) in Ti-6Al-4V. In a second paper by Brandl *et al* [36] it is stated that no change in the microsturcture of layer additive deposited Ti-6Al-4V is observed after heat treatment at 600°C for 4 hours. However, a noticeably more homogeneous distribution of aluminium and vanadium is noted when EDX line scans across deposited samples are taken and compared pre and post heat treatment [36].

On the basis of information found in the literature 600°C for one hour and 600^{o}C ±15-20C for the ‘soak’ period is a good target for the equipment in this thesis.

2.8 HEAT TREATMENT TECHNIQUES

2.8.1 RADIANT HEATING

In radiant heating, a surface is raised to a temperature at which it begins to transfer energy through thermal radiation. The amount of energy or power transferred from the heating source to the substrate is a function of its emissivity and the temperature difference between emitter (heat source) and the receiver (substrate). The governing equation for heat transfer via radiation is;

Equation 2-2 : $q = \varepsilon A\sigma(T^4)$ [69]**,**

where q is energy emitted by the surface in Watts, A is the area of the emitting surface in m^2, σ is the Steffan-Boltzmann constant (5.67e-8 W m^{-2} K^{-4}), ε is the emissivity of the emitting surface, and T is the temperature of the emitting surface in Kelvin.

Radiant heating can be harsh in terms of energy input (Q in W mm^{-2}) and/or too susceptible to stand-off distance [70]. The severity of the heat flux is a source of risk in the case of processing variation, and slight geometric or positioning variation can lead to large overheating of the component. For example, for radiant heaters to be effective emitters for this application, as shown in modelling and confirmed in practice [70], the elements must be above 1000ºC. When these are in close proximity to a blade surface, which is to be held at 600ºC it creates a risk of localised over temperature. Titanium's comparatively low thermal conductivity (6.7W m^{-1} K^{-1} [71]) means that there could be a risk of surface temperature accumulation (hence rapid temperature rise).

2.8.2 INDUCTION HEATING

In induction heating an alternating current in a coil produces eddy currents in the work piece, which through internal resistive properties generate heat. Two effects are important when dealing with induction heating; the skin effect, and proximity effect.

Eddy currents induced in the work piece due to Faraday's law have opposite directions to those in the coil. Due to the alternating current the current flow induced in the conductor (work piece) is non-uniform through the section. There is a concentration of the current density at the surface adjacent to the coil, is termed the skin effect. The degree of skin effect depends on the frequency and penetration depth δ (in m) and is defined as;

Equation 2-3: $$\delta = 503\sqrt{\frac{\rho}{\mu_r F}}$$ [72],

where ρ is electrical resistively of the conductor in Ω.m, μ_r is relative magnetic permeability, and F is frequency (Hz). Thus showing that penetration depth is proportional to one over the square root of frequency. This is important where through thickness heating is required (as in the case of stress relief heat treatment of a repaired region), highlighting the need for a low frequency. It also follows that penetration depth is a function of temperature as electrical resistivity in some materials (such as carbon steel) varies significantly with temperature.

An effect perhaps more pertinent to the use of induction heating in this application is the proximity effect. The level of concentration of eddy currents and therefore current density in the workpiece is a function of the distance between it and the coil.

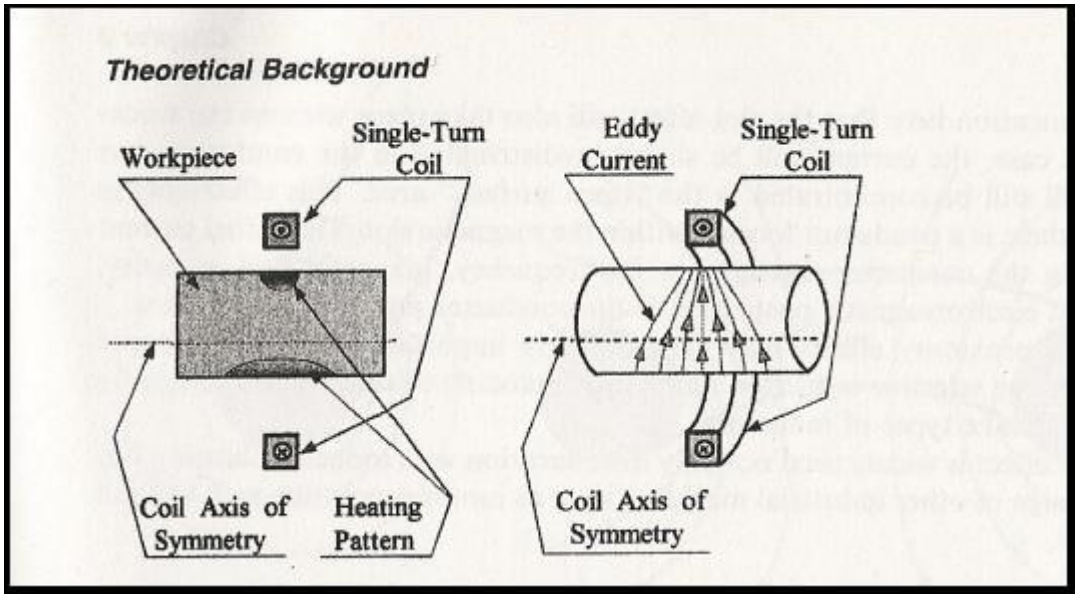


Figure 2-10 : Schematic representation of proximity effect taken from Rudnev *et al* [72].

Figure 2-10 shows the variation in heating pattern that can result from different coil stand-off distances. If the part is of constant cross section, rotation can help improve temperature uniformity. Davies and Simpson [73] show that the loss in power of the conductor falls off with the square of height h (i.e. the distance between conductor and coil).

The aforementioned observations show the sensitivity of induction heating to stand-off/depth relationship. The control of this is critical and is very difficult when dealing with components of complex and varying shape and topology (such as aerofoils).

2.9 CONVECTION HEATING USING IMPINGEMENT JETS

Convection heating in its simplest form is the transfer of heat energy to a component using gas. The gas is heated and then the energy in the gas is transferred to the work piece through conduction where the gas and component are in contact. There are techniques being developed for similar applications to one described in this thesis such as Patent no. US 2008/0099465 A1 [74], in this invention a localised shell is placed around a blisk aerofoil and heating is done by resistive heating elements.

Impingement jets are used extensively throughout industry to remove heat from the surface of a component due to the high heat transfer that can be achieved [75]. However in this application the reverse is being utilised, i.e. hot gas is impinging on the component surface to heat it. There are a number of advantages to the use of gas jets to provide heating for the component and these are summarised below.

2.10 IMPINGING JET HEAT TRANSFER

The field of impingement jet research has been extensively studied in the past due to the high heat transfer rates which can be achieved by careful design of the impingement system. Impinging jets are used for a variety of applications from annealing of metal and plastic sheets, drying of textiles and paper [76], as well as in ovens for cooking and food processing applications [77]. Jets that enter the same fluid or a more dense fluid are termed submerged jets, whereas free-surface jets enter a fluid of lower density. Confined jets are those whose jet flow is confined between the impingement plate and orifice (or jet) plate. In general, the impingement jets discussed in this document are defined as submerged and

confined. One could argue that in the case of an argon jet entering air, it would be classed as a free-jet, however the densities of the two gases (air = 1.23 kg m^{-3}, argon = 1.64 kg m^{-3}) are so similar that they have be termed them submerged. There is much literature in the public domain attempting to survey and review the field of impinging jet heat transfer. The most detailed text is that of Martin [76], which details much of the early work performed to understand the physical principles behind impinging jet heat transfer. More recently, papers by Wright [78], Sarkar *et al* [77], Jambunathan *et al* [79] and Goldstein *et al* [80] offer more concise and application focused reviews of the field. J. Livingood *et al* [81] provides a detailed review of the literature available in 1973 offering many empirically derived correlations, that can be used to calculate the heat transfer of an impinging jet with a range of boundary conditions. Finally Viskanta [82] presents a detailed review of the heat transfer characteristics of single and multiple isothermal turbulent jets.

2.10.1 WHAT IS AN IMPINGEMENT JET?

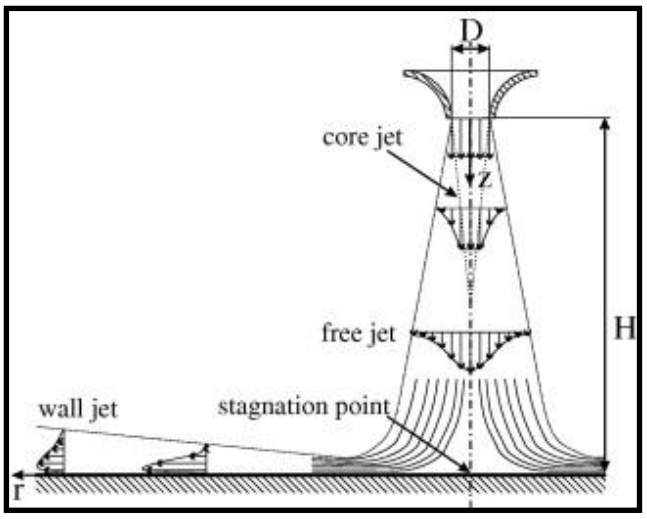


Figure 2-11 : Impinging jet morphology [83]

Figure 2-11 shows the varying velocity profiles that exist in an impingement jet emerging from an orifice of diameter D. The velocity profile at the orifice is assumed to be fairly linear with the average speed seen at the centre line (dotted) being present across the

majority of the jet diameter. This velocity can be calculated simply by dividing the flow rate of gas at this point by the cross sectional area of the jet orifice. As the jet moves further from the jet exit the velocity profile begins to take a more bell-shaped appearance and according to Martin [76] can be approximately described by a Gaussian function. This shape is formed as the jet becomes entrained in the surrounding fluid, generating friction, producing turbulence and therefore reducing the jet edge velocity. As the jet travels further from the exit, less of the central region of the jet is at the jet exit velocity due to increased interaction with the surrounding fluid. The region of the jet with the same velocity as the jet exit velocity is termed free jet. Gardon and Akrifat [84] noted through comparison of their own work with that of Corrsin [85] that the potential core was reduced towards the centre line up to a jet length of approximately five jet widths (in the case of slot jets).

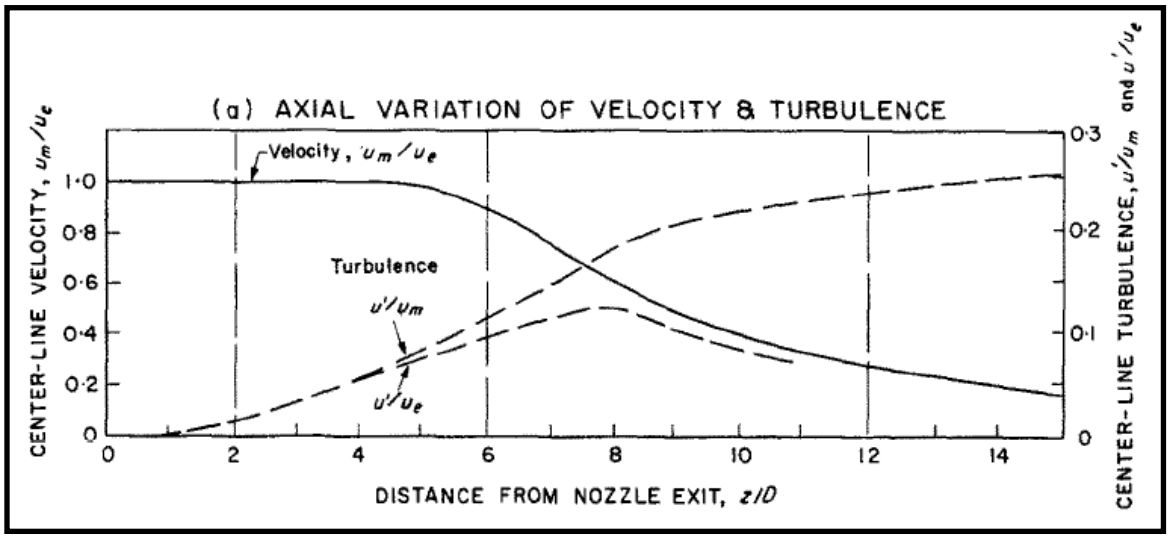


Figure 2-12 : Variation in velocity and turbulence with distance from the nozzle exit [84]

Figure 2-12 shows the inverse relationship which exists between the centre line velocity and turbulence for an axi-symmetric (round) jet. One can see here that the reduction of the centreline velocity begins to decay at around 4-5 times the nozzle

diameter. Noteworthy is that the centreline turbulence begins to increase from a distance of one jet diameter.

2.10.2 PARAMETERS AFFECTING HEAT TRANSFER

The focus of much of the literature is the interaction of jet exit Reynolds number, jet exit to plate spacing (H), jet diameter (D), and in the case of arrays, jet-to-jet spacing (S); and the effect of these parameters on local heat transfer at the base of the jet. It is detailed in many papers [86], [76], [79], that the localised heat transfer achieved by turbulent impinging jets depends strongly on both Reynolds number and stand-off distance. A Reynolds number of >2000 defines turbulent flow, where as <2000 defines laminar flow [75].

The Reynolds number (Re) is defined by the following equation;

Equation 2-4; $\mathrm{Re} = \frac{VD}{\upsilon} or \mathrm{Re} = \rho \frac{VD}{\mu}$ [75],

where, V is velocity in m s^{-1}, D is diameter in m, υ is kinematic viscosity in m^2 s^{-1}, is ρ density in k $gm^{-3,}$ μ is dynamic viscosity in kg m^{-1} s^{-1}.

The majority of authors choose to represent the effectiveness of an impinging gas jet in terms of Nusselt number (Nu). This is a dimensionless number used extensively in the field of thermo-fluids to describe the ratio between convective heat transfer coefficient and conductive heat transfer coefficient. In the case of an impinging jet, the convective element (the numerator) is the product of the hole diameter and heat transfer coefficient, and the denominator is the thermal

conductivity of the fluid. Nusselt number (Nu) is defined for an impinging jet by the following equation;

Equation 2-5: $Nu = \frac{hD}{k}$ [75],

where, *h* is heat transfer coefficient in W m^{-2} K^{-1}, *D* is jet diameter in m, and *k* is thermal conductivity of the fluid in W m^{-1} K^{-1}.

Many papers deal with the effects of Reynolds number, orifice geometry and jet length (i.e. distance between jet plate and impingement plate) on heat transfer characteristics. For example Lee *et al* [87] notes that increasing the nozzle diameter for the same Reynolds number (Re) increases stagnation point Nusselt number (Nu). Lee [87] conducted trials for a jet Reynolds number of 23,000 and a range of jet diameters from 1.36 - 3.4cm, as well as H/d ratios of 2-14, recording Nusselt numbers of 140, 130, and 125 for decreasing jet diameter.

The conclusions of Lee *et al* [87] are that the potential core length increases with increasing jet diameter for the same Re, stagnation point Nu increases with increasing diameter. However, Glynn *et al* [88], propose that the smaller the diameter for a given Reynolds number the higher the heat transfer. Glynn *et al* [88] attribute this to the higher velocities associated with the smaller jet diameters. All sources agree that heat transfer increases with increasing Reynolds number, with Glynn *et al* [88] reporting that Nu is proportional to $Re^{0.5-0.8}$.

The most common method for measuring heat transfer from an impinging jet is to use a thin metallic sheet, measuring the current and voltage drop across it as a result of heat being drawn out by the impinging jet [88, 89]. In order to measure

temperatures a thermal camera on the underside of the thin sheet can be used [88], or liquid crystals to plot the isotherms generated by jets impinging on a surface [89].

2.10.3 ARRAYS OF IMPINGING JETS

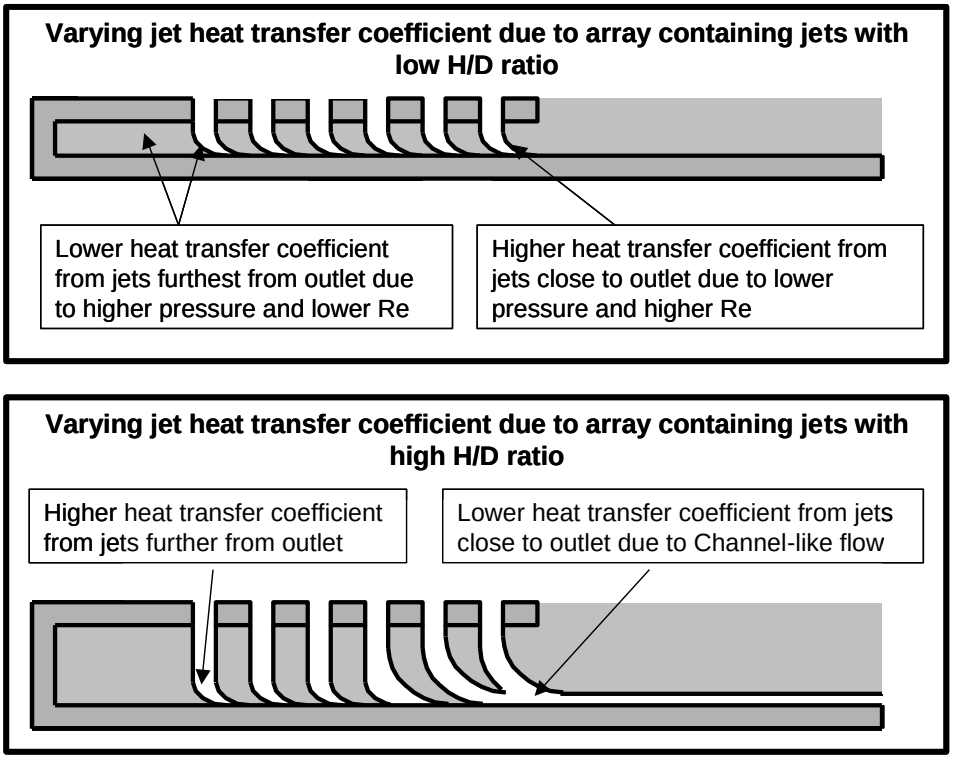


Figure 2-13 : Schematic diagram to describe the effect of H/D ratio on relative heat transfer coefficients of jets within an array, as described by Bailey *et al* [89]

The practical use of impinging jets requires an understanding of their behaviour when used in arrays. Arrays provide heat transfer over a large region. The work of Bailey *et al* [89] and Dano *et al* [90] deal with square in-line arrays of holes, comparing dense arrays and sparse arrays for high Reynolds numbers of 28,700-64,900. Again the Nusselt number was measured across numerous rows of impinging jets. In this experiment the impingement area is surrounded by walls on three sides with the fourth open to promote exhaust cross-flow in one direction.

Bailey *et al* [89] compared experimental results with simulated results from Florschuetz, concluding that for dense arrays with low h/d ratios (1.2),

'HTC is higher in the cross flow region where the flow is more akin to a simple fully developed turbulent channel flow' [89].

Jet Reynolds number is lowest due to the relatively higher pressure existing in the rows furthest from the outlet. Conversely the low pressure at the outlet increases Re and produces faster jets. As the h/d ratio increased Bailey *et al* [89] noted that heat transfer coefficient (HTC) was now maximum at the jets furthest from the exit (also noted by Goodro *et al* [91]) and the flow changes to a channel-like flow after jet row 3-4. This produces a diffuse flow addition effect due to the large stand-off and larger numbers of jets. Close to the exit most jets do not reach the surface and in-line stratification is apparent. Extended arrays like these are used to cool large areas. In the case of sparse arrays, jets behave independently with very little channel cross flow experienced [89].

General observations from Bailey *et al* [89] are that lower Re in each scenario results in a flatter profile of the Nu and Re values through the rows towards the outlet. Therefore it seems safe to suggest that a lower Re jet is likely to suffer less from this effect of generating channel cross-flow than a higher Re jet. This could be due to the relatively lower velocities and momentum involved.

A good general description of the role of impingement jets for cooling in gas turbine engines with some basic design rules are detailed by J. O'Grady [92]. Here O'Grady notes;

'The use of multiple jet impingement differs from single jet performance, where multiple jet configurations Nusselt number is largely dependent on the Reynolds number, due to inherent cross-flow between jets significantly effecting the velocity and viscosity of the stream'

This is in agreement with that found in the experiments of Bailey *et al* [89], however it is also noted by O'Grady [92], that cross-flow differs on curved aerofoils, resulting in varying heat transfer coefficients within the array. Han [93] notes that exhaust location is very important in the design of impinging jet arrays as creating a more open exhaust path reduces the effect of spent gas acting to deflect the jets away from the target surface. O'Grady [92] observed that jet orientation can increase the heat transfer overall by generating a constructive cross-flow pattern.

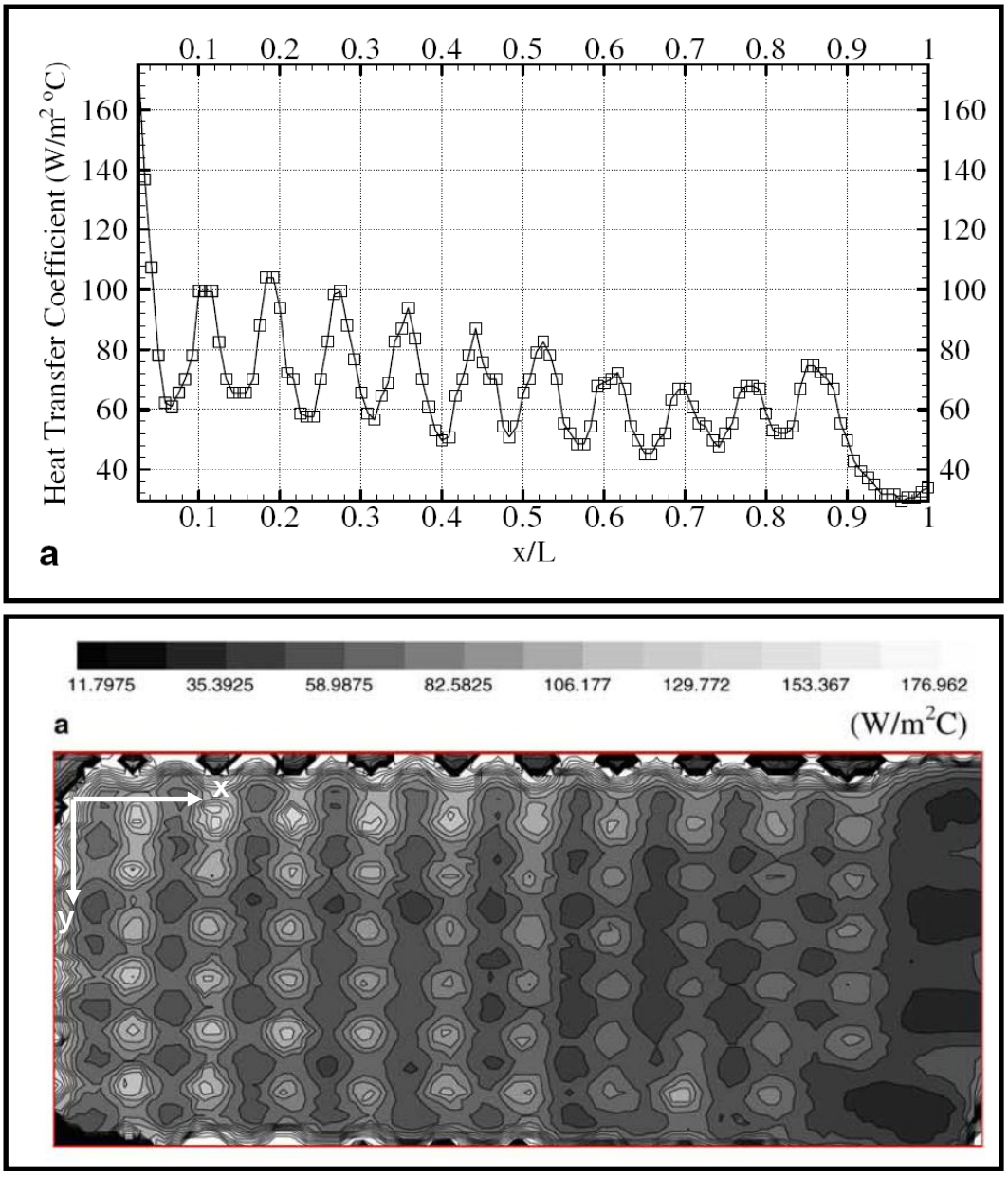


Figure 2-14 : Jet array interfacial heat transfer coefficients from Wang et al [94] presented as a plot through the centres of a line of jets (top), and a 2D contour map (bottom). (H/D = 6.35, S/D = 7.5 (x), 6.25 (y), Re = 1039)

The heat transfer under an array of jets is mostly presented in the literature as either an average value for the whole array, a maximum value (usually at the centre of the stagnation point), or by plotting the variation in heat transfer across the array. In the latter case, this can be done by taking a line of data through the centre point of a number of jets in an array as shown in Figure 2-14 (top), or by producing a contour map, Figure 2-14 (bottom). Wang [94] presents both

maximum and average values for heat transfer coefficient, for a jet array with a H/D ratio of 6.35, and a jet spacing (S/D) of 7.5 (x) and 6.25 (y) with jet Reynolds number of 1039, yielding an average heat transfer coefficient of 71.91W m-2 K-1. The effects of crossflow described previous by Bailey *et al* [89] are in evidence in Figure 2-14 with the heat transfer decreasing towards the outlet of the array (x direction).

2.10.4 MODELLING IMPINGEMENT JET HEAT TRANSFER

Much work has been performed to model the heat transfer and fluid flow characteristics of impinging jets using computational fluid dynamics (CFD) packages such as *Fluent*. Dahlquist [95] combined impingement jets with pin and film cooling using *Fluent 6.1*. L. Xianchang *et al* [96] compared Fluent 6 simulations with those of PHOENICS and compared the results with flow visualisation to check for variations due to the modelling codes used. L. Xianchang *et al* [96], investigated 2D laminar slot jets (Re 275-600) and noted the co-existence of two different flow patterns in the gas after impingement for Reynolds numbers between 275-400. In one case the gas flow broke away from the plate shortly after impingement, whereas in the other it was close and parallel to the plate. This observation was noted both in the CFD and in the flow visualisation analysis.

Heat transfer and fluid flow of impingement jets are turbulent and follow the turbulent time-averaged Navier-Stokes equations (continuity, Momentum, and Energy) for incompressible flows. Many methods exist to find solutions for these equations, two of the most popular are the k-ε [97], and the k-ω [98], these suggest

further equations to define turbulent kinetic energy (k), turbulent dissipation rate (ε), and specific dissipation, or dissipation per unit turbulent kinetic energy (ω).

Variations of these models have been used extensively for the modelling of impingement jets. The Low Re k-ε model is favoured by Koseoglu [99, 100] as it employs damping functions to reduce excessive kinetic energy production which can lead to over prediction of the stagnation region heat transfer when using the standard k-ε model, as reported elsewhere [101]. Angioletti et al [102] compared the k-ε Re-Normalised (RNG), k-ω Shear Stress Transport (SST), and Reynolds Stress Model (RSM) in Fluent CFD software to predict the heat transfer in submerged unconfined gaseous impingement jets comparing the results with Particle Image Velocimetry measurements. Figure 2-15 from Angioletti [102] shows the comparison between experimentally measured heat transfer and the computed data obtained with the different models for a jet with a Reynolds number of 1000 and H/D of 4.5. Angioletti *et al* [102] concluded that for lower Re jets the k-ω SST model provided the best correlation with experimental data, for both interfacial heat transfer and flow field morphology.

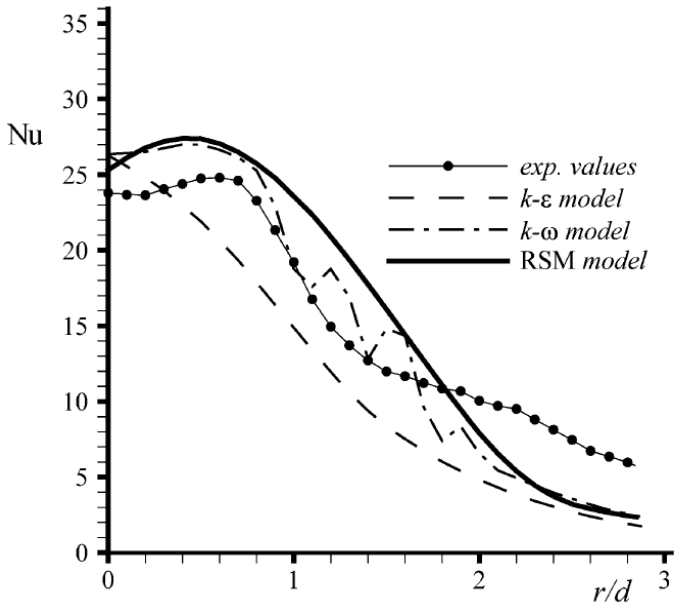


Figure 2-15 : Comparison between different turbulence models in Fluent and experimental data to predict variation in jet Nusselt number [102]

Sagot *et al* [103] also found good correlation between experimental data and the k-ω SST model for a turbulent hot air jet for 10,000 <Re <30,000 and H/D of 2-6. However for higher Re jets (1500-4000) Angioletti *et al* [102] found the k-ε RNG and RSM more closely matched the flow field measurements, however all models under estimated heat transfer. Funazaki and Hachiya [104] using CFX-4-4 software paid great attention to the turbulence model used concluding that low-Reynolds number k-ε models and particularly the k-ω models produced the best agreement with experimental data. The use of boundary layer mesh (i.e. finer mesh density close to the target plate) is widely employed in the field of impingement jet modelling [100, 102].

A number of flow visualisation techniques are used in impingment jet research to validate CFD modelling. Xianchange *et al* [96] and Carcasci [105] present the most commonly encountered method of using compressed air injected with smoke and a laser light sheet to illuminate the flow field for qualitative flow visualisation of the jets perpendicular to their centreline. Carcasci [105] commented the particular applicability of this method for laminar jets. Sarkar *et al* [106] used a similar method but seeding the air with helium filled bubbles, where as Dano et al [90] used a laser light sheet and air seeded with 2.5μm TiO_2 particles in to perform flow visualisation of a jet array from a plan view (this is discussed later in Figure 13-3).

2.11 GAS AND MATERIAL THERMAL PROPERTIES

The system developed in this research uses high temperature argon gas to heat a titanium component to a heat treatment temperature in the region of 550-650°C for stress relieving. A significant portion of the work undertaken in this research project involves modelling of the heat treatment system. Therefore it is important that good quality data characterising the thermal properties of the titanium 6-4 alloys in question are used. It is also important to include the variations in gas properties with temperature where possible.

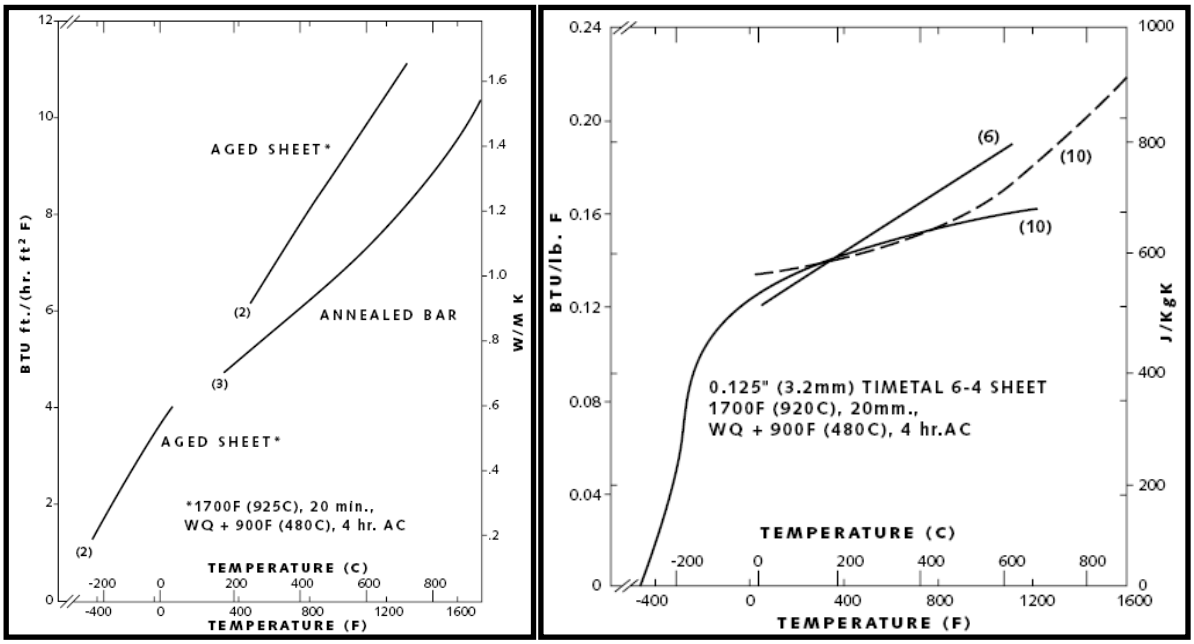


Figure 2-16 : Examples of public domain Ti 6-4 thermal data used for modelling. Thermal conductivity (left), specific heat (right) [131]

Titanium alloy data (particularly Ti-6-4) are available in the public domain, but the quality may vary from source to source. The value of thermal conductivity for titanium 6-4 at room temperature is quoted as ~6-7 W m^{-1} K^{-1} [107, 108, 30], and it varies with temperature [109].

The empirical law of conduction based on experimental data originates from Boit and is named after Joseph Fourier. It states that the rate of heat flow by conduction in a given direction is proportional to area normal to that direction and to the gradient of temperature in that direction. Heat flow in direction x (for example) is defined by the Fourier law given as:

Equation 2-6 : $$Q_x = -kA\frac{dT}{dx}$$ [110],

where, Q is heat in Watts, k is thermal conductivity in W m^{-1} K^{-1}, T is temperature in Kelvin, x is distance in metres, and A is area in m^2.

This low thermal conductivity (for comparison, stainless steel is 25 W m^{-1} K^{-1}, mild steel is 50 W m^{-1} K^{-1}, Inconel is 15 W m^{-1} K^{-1} [111]) could lead to non-uniform heating of the component and the formation of hotspots.

Within this thesis some computation fluid dynamics (CFD) modelling has been undertaken which required the input of density and viscosity of argon at elevated temperatures. In order to obtain these data the a number of sources were reviewed. Lemmon *et al* [112] present a set of equations for calculating viscosity and thermal conductivity for argon (as well as nitrogen, oxygen, air) and evaluate these against a large amount of data collected from an extensive literature survey (consisting of calculated and measured data). Focussing on argon the equations used generally represent a deviation of only 2% from the published values for argon thermal conductivity above 170K. However the quantity of data available at these elevated temperatures is significantly reduced. In terms of viscosity (the property of most interest) Lemmon *et al* quote deviations of only 1% at pressures

between 1-100MPa and temperatures between 270-300K. However, the graphs available show a significant scatter in results at temperatures above 300K. The focus of the research of Lemmon [112] was to evaluate equations derived, and the scattered data at higher temperatures was of less concern.

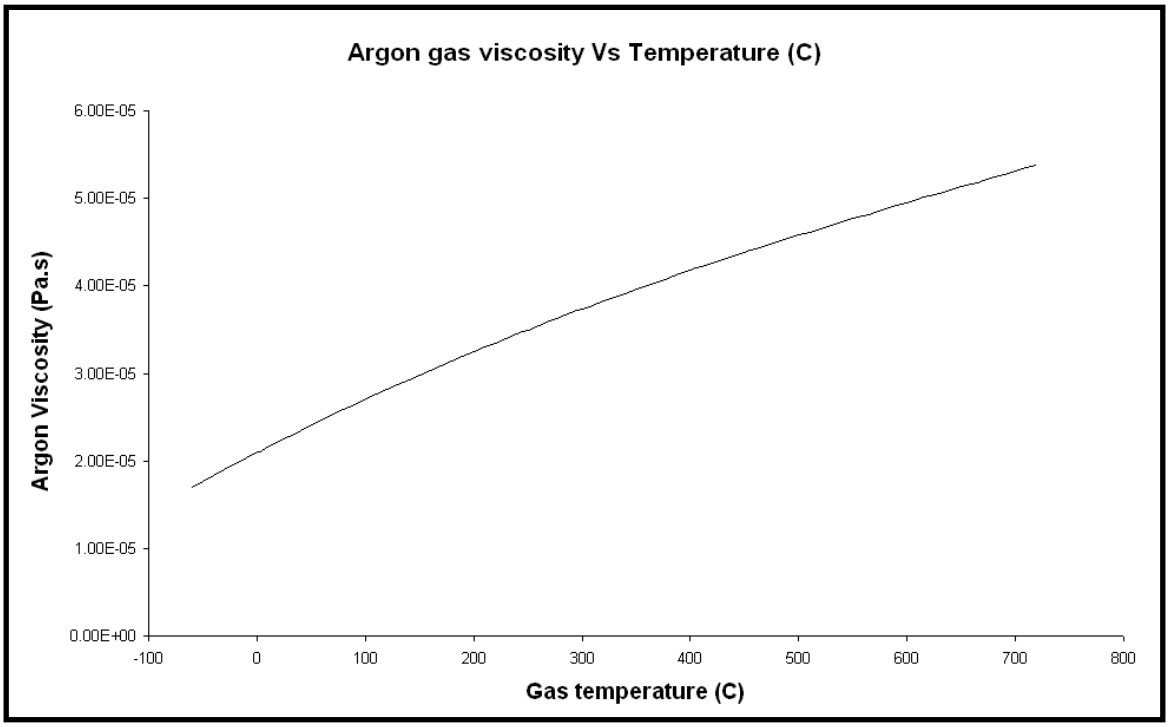


Figure 2-17 : Variation in argon viscosity with temperature [114]

Cook [113] and Din [114] reported an alternative source of data for argon at elevated temperatures. Cook provides tables containing the variation in volume of argon at various pressures (1-5000atm) from temperatures of 90K to 600K (-183 to 327°C). Using this and the molecular weight of argon (39.9 [113]) the variation of density with temperature can be calculated to use later.

Din [114] describes the viscosity of argon varying with temperature. The data obtained highlights that the properties of argon at atmospheric pressure vary significantly with temperature. The significance of this in the context of the local heat treatment system is that the heat transfer properties of the gas are likely to be

significantly different at higher temperatures. This is highlighted when the heat transfer coefficients of impinging jets are closely linked to their turbulence levels at the nozzle exit as discussed previously. The Reynolds number of the gas exiting the jet orifice has been shown previously to be a function of jet velocity, orifice size, gas density and gas viscosity. Therefore any significant changes in gas viscosity are likely to significantly change the Reynolds number at the jet exit orifice. The reader can appreciate that in order to fully evaluate the performance of the proposed gas jet impingement system one must understand the regime relevant to the problem.

For example, if;

A gas flow rate of 150 l min^{-1} is passing through 60 jets of diameter 1mm, to give a jet orifice velocity of 53.05 m s^{-1}. In this scenario, using the data above taken from Cook [113] and Din [114] would result in a Reynolds number of 2270 at a gas temperature of 23°C and a Reynolds number of 1134 at a gas temperature of 327°C. At a lower temperature the jet would be considered turbulent (i.e. Re>2000) and at the higher temperature laminar (i.e. Re<2000).

2.12 TECHNOLOGY DEVELOPMENT APPROACH – THE CAPABILITY ACQUISITION PROCESS

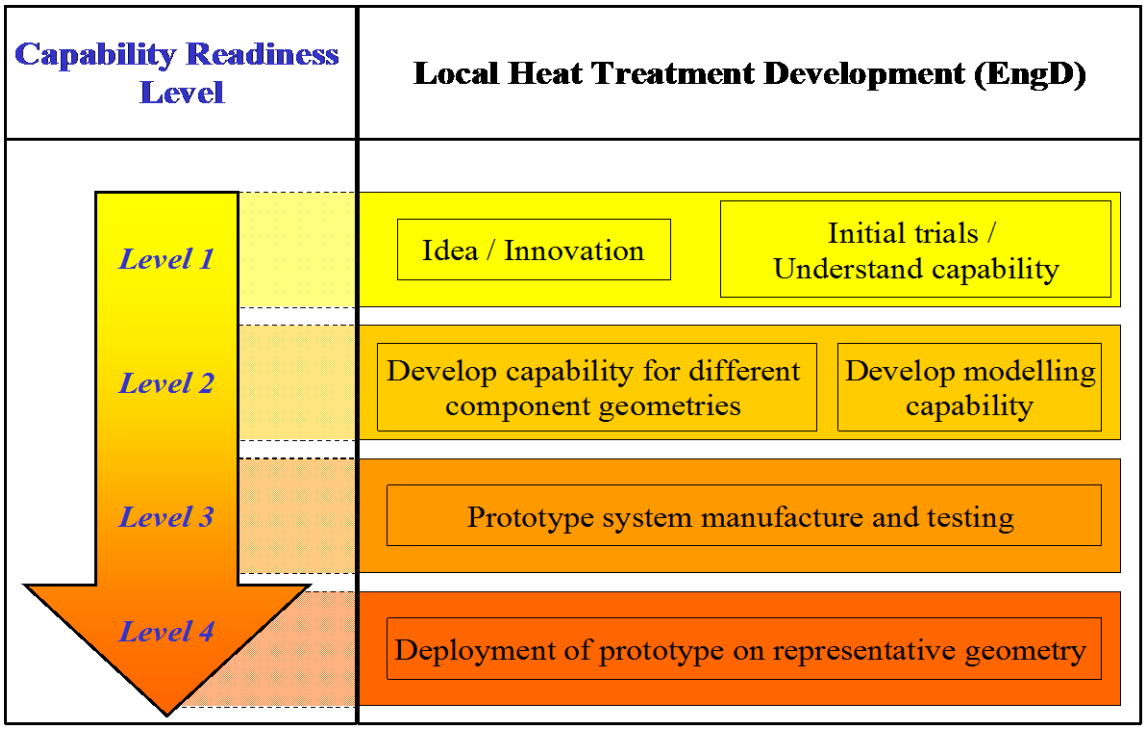


Figure 2-18 : Modified TRL process as used for gas jet process system development

John C. Mankins delivered a white paper on technology readiness in 1995, detailing the principle behind the NASA developed Technology Readiness Levels (TRLs). More recent papers on this by Mankins [115], [116] discuss the application of this process to define robust process delivery strategies. In the course of technology development many companies and institutions have adopted a model similar to that outlined by Mankins. In Figure 2-18 the development described in this thesis is compared to a modified version of Mankins' TRL's. Figure 2-18 details the process used for developing the gas jet processing capability. This involved a number of steps (or levels) from the initial idea and concept stage to the delivery of a prototype unit.

The following definitions are loosely based on the TRL process providing a structured and well-documented framework for technology development. Key to any development process, as highlighted by Mankins [115], is the need for regular peer review in order to ensure the approach taken and the decisions made are technically and commercially sound. Much of the data and results presented in this thesis has been reported to the internal[‡‡] and external[§§] customers for the technology. Each TRL is described as follows;

Level 1 - The concept is formulated and articulated to the technical experts within the development team. The idea is then explored and the relevant intellectual property protection is applied for (page 1). Intellectual property is likely to be generated at various stages of the process, however at level one this is mostly investigative work and 'blue skies thinking'. It is acknowledged at this stage that much of the key intellectual property regarding the process is generated. Understanding of the competitor's position with regards the particular technology development should be investigated see references [17, 9, 10, 15].

Level 2 - The results from the initial experimental investigations and literature reviews allows process development to start targeted at particular test pieces or component geometries. Process capability is demonstrated, however more specific and tailored development is required to deliver a solution. Component

[‡‡] Rolls-Royce technical specialists through the reports

[§§] External technical experts such as the Ministry of Defence (MoD) through project reviews, and the wider engineering community through conferences. The work has also been presented at a national and international conference.

specific issues may exist, which require more detailed examination and development activities (page 109). This is the stage when process understanding is developed and significant lessons are learned and recorded. In the case of the local heat treatment development, the modelling activities and gas flow visualisation allowed a greater understanding of the concepts and physical principles that under-pinned the process (page 177).

Level 3 – Here the lessons learnt are used to develop and manufacture a working prototype that can then be used for the purposes of testing the capability of the system (page 66). Here process sensitivity and key process variables are defined and tested (page 161). Aspects of the system at this stage become component and application specific and issues surrounding fixturing and manipulation become important (page 114). Some of the lessons learnt at this stage are component/test piece specific but the general principles developed here are often directly transferable.

Level 4 – At this stage the technology is deployed on a component (page 128) and the necessary testing is performed to ensure the required standards are achieved (page 265). This is very much a demonstration stage and provides the step before a pre-productionised solution can be specified and manufactured.

Beyond level 4 is where the technology moves from research into application and the information and underlying principles outlined in this thesis form the foundations upon which that process can take place.

2.13 SUMMARY OF LITERATURE

Titanium alloys are used extensively in aerospace applications particularly in compressors where high strength to weight ratios, excellent corrosion resistance and elevated temperature mechanical performance are required. Increasingly complex and expensive components require high integrity repairs to extend life and minimise life-cycle cost. These repairs often require innovative and robust solutions to the various stages involved in the repair. This work considers the development and deployment of a novel, localised heating technique for application on titanium blisk components. These components require tight temperature control over a small region on the leading edge, trailing edge and tip. The process must be reliable, controllable and minimise the potential for generating scrap due to process non-conformance.

2.13.1 MATERIAL INTEGRITY

The purpose of this heat treatment is to relieve residual stresses generated in the component due to the material addition process. It is well documented [34, 55, 61, 63, 65, 66] that titanium alloys (particularly titanium 6-4) respond favourably to stress relieving heat treatments. However, there is significant variation in the temperatures suggested for the most effective stress relief cycle. There is unanimous agreement that the higher the temperature (below the β transus) the faster stress relief occurs, although there is another factor effecting the heat treatment. The longer titanium 6-4 is held above 425ºC in the presence of oxygen (and at higher temperature), the faster the diffusion rate, and therefore the thicker the layer of alpha case formed. As a result, choosing the heat treatment cycle is a

compromise between minimising the amount of time and temperature a component is heat treated for and achieving sufficient stress relaxation. It is beyond the scope of this thesis to investigate the optimum heat treatment cycle as standards and specifications already exist both within the company and externally. The goal is to achieve temperatures representative of those used for the stress relief of titanium and provide sufficient evidence as to the capability of the system in achieving and maintaining that temperature locally. As a result, the temperatures of interest in this work are between 550°C and 700ºC and for soak times of 1 to 2 hours.

2.13.2 THE USE OF CONVECTION HEATING

The advantage of utilising impinging jets for heat transfer is that one can use a medium commonly employed to provide an inert atmosphere as the heat-carrier. Also, the gas temperature is only a few degrees above the target component temperature, which is beneficial when the component being heated is of varying geometry. This reduces the likelihood of hotspots being generated. However, due to the relatively thin section of the plates being heated in this work, a low intensity heating method is required to provide a diffuse heating pattern whilst reducing the likelihood of hotspots. In heating methods such as induction (eddy current), stand-off distance is critical in order not to generate hotspots. In the case of radiant heating, the source would be well above the melting temperature of the material being processed. This has the potential to cause significant issues in generating the required temperatures as well as to the materials required. If the material being processed were to come into contact with the heat source this would result in significant damage to the component. In the case of induction heating, the design

of the coil would be very complex and bespoke in order to maintain the stand-off if the component did not possess a regular cross-section.

2.13.3 HEAT TRANSFER FROM IMPINGING JETS

In order to provide high heat transfer coefficients from convective flows, the general trend has been towards highly turbulent gas jets utilising high flow rates of gas to generate maximum heat and mass transfer. The majority of the literature available on the subject of impinging gas jets focuses on the development of the optimum parameters required to attain the maximum heat transfer. However the optimum parameters defined in the literature may not necessarily be appropriate in the design of a real jet array for a local heat treatment application.

It is generally accepted that increasing Reynolds number gives one increasing Nusselt number (Nusselt number increases roughly with the square root of Reynolds number), however in a system where all the jet parameters are variable, this does not necessarily mean that the goal should be to maximise Reynolds number.

Consider Reynolds number; which is defined as the product of velocity, fluid density and hole diameter, divided by the fluid viscosity. When considering a single jet, increasing hole diameter will reduce velocity (for a given flow rate) by a square relationship and therefore reduce Reynolds number. This will then also decrease Nusselt number and therefore heat transfer coefficient.

Things are not quite so straightforward when dealing with an array. If one considers that a specific total flow rate is used to supply a jet array, and with some

parameters fixed (e.g. jet spacing must remain at 5 times the jet diameter). This allows one to take a given array area and define how many jet holes of a given size can be tolerated.

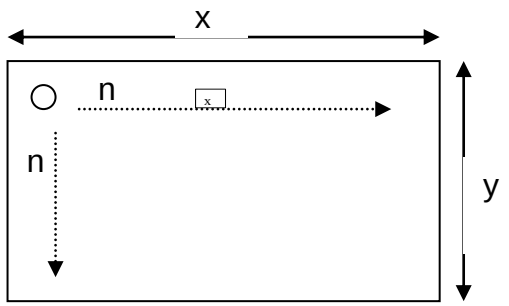


Figure 2-19 : Schematic of basic jet array

Consider a jet area of 90mm x 30mm (Figure 2-19), with n number of jets in directions x and y in a square array. Let us make the assumption that a square array is the most efficient [75], and that the optimum jet spacing is around 5 times the jet diameter [76]. Table 2-1 highlights the

Jet dia. (mm)	Spacing (mm)	Width (mm)	Depth (mm)	Number of jets	Hole area (m^2)	Flow rate per hole ($m^3\ s^{-1}$)	Jet average velocity ($m\ s^{-1}$)	Re	Nu	h
1	5	18	6	108	7.9E-07	7.7E-06	9.8	549	23.4	414.7
1.5	7.5	12	4	48	1.8E-06	1.7E-05	9.8	823	28.7	338.6
2	10	9	3	27	3.1E-06	3.1E-05	9.8	1098	33.1	293.3
3	15	6	2	12	7.1E-06	6.9E-05	9.8	1647	40.6	239.4

Table 2-1 : Table showing variation in heat transfer coefficient with diameter for a constant total flow rate

various values which can be calculated for a range of hole sizes from 1mm to 3mm assuming that $Nu = Re^{0.5}$ [88]. For each jet diameter, the velocity, Reynolds number (Re), Nusselt number (Nu) and then by re-arranging Equation 2-5 heat transfer coefficient (h), are calculated. It is clear from this that if one is looking for the highest heat transfer coefficient, then it is not simply the Reynolds number that one must optimise as this does not necessarily result in maximum heat transfer coefficient. In fact it appears from data presented in the table that the biggest effect on heat transfer coefficient is actually the jet diameter. Although Reynolds number increases by a factor of 3, the Nusselt number only increases by a factor

of 2 leaving the heat transfer coefficient around one half of that achieved for the smaller jet diameter.

This raises the question of what is the most appropriate jet size to use for this application. Early trials [117] suggested when comparing jet sizes of 1, 2 and 3mm that the best temperature distribution across the heated zone was as a result of using 1mm diameter jets. It is practically possible to produce 1mm diameter jets in metallic plates with laser cutting/drilling, however smaller holes become more difficult to achieve. The size of the heated area also affects the hole size chosen as one needs a good coverage of the heated region with jets in order to produce a uniform temperature distribution. The heat transfer across a jet displays a Gaussian distribution with its peak value at the centre [76]. Therefore, one large jet covering the heated area would produce a similar profile and an associated poor temperature distribution would exist.

3 ASSUMPTIONS

Early system development employed parameters found in the open literature to manufacture a system capable of heating a component in a localised manner. Apart from the physical parameters of the process one has to consider the engineering limitations of designing a system to utilise impinging jet heating. For example, there are limitations as to the manufacturing and operational costs, issues with the use of argon in this manner and limitations as to the constituents of the system and their capability. These limitations are discussed in context as follows:

- The impingement jet plates are to be manufactured using standard laser cutting techniques and therefore have a limited practicable jet diameter of 1 mm. This allows holes with good and repeatable surface finish to be produced on a standard shop-floor laser cutting facility.

- The maximum overall flow rate of the system is limited to 200 l min^{-1} (measured at room temperature) which is the maximum flow rate achievable with the digital flow controllers used. In order to calculate the exit velocity of each jet (v_j), the following formula has been derived;

  Equation 3-1 : $v_j = Q_t / (60000\ N_j\ \pi\ r_j^2)$,

  where, Q_t is the total system flow rate in $lmin^{-1}$, N_j is the number of jets in head unit, and r_j is the radius of the jet exit orifice in m. It is assumed that the pressure across the jet plate is uniform, therefore each jet will have the same flow rate.

- Under general operation, when heating an aerofoil test piece the pressure within the heating system and head unit is measured at 20-150mbar gauge pressure at a flow rate of 100-150 l min^{-1}.

- The fluid used in the system is argon, although much of the early tests were conducted in a two-phase environment with the heated argon interacting with a surrounding atmosphere fluid (air). The final system is contained within an argon atmosphere but to minimise the testing costs the system was evaluated experimentally in a two-phase environment.

- For the purpose of the modelling described later the gas temperature measured in the head unit is assumed to be equal to the temperature of the gas exiting the jet orifice.

4 LOCAL HEAT TREATMENT DEVELOPMENT STRATEGY

In order to deliver a Local Heat Treatment (LHT) system the work conducted during this doctoral research programme is presented in this thesis as three ‘themes of work’. These themes; equipment, processing, and modelling are shown below in Figure 4-1, and have culminated in the delivery of a validated localised heat treatment technique. These themes are described on the following page.

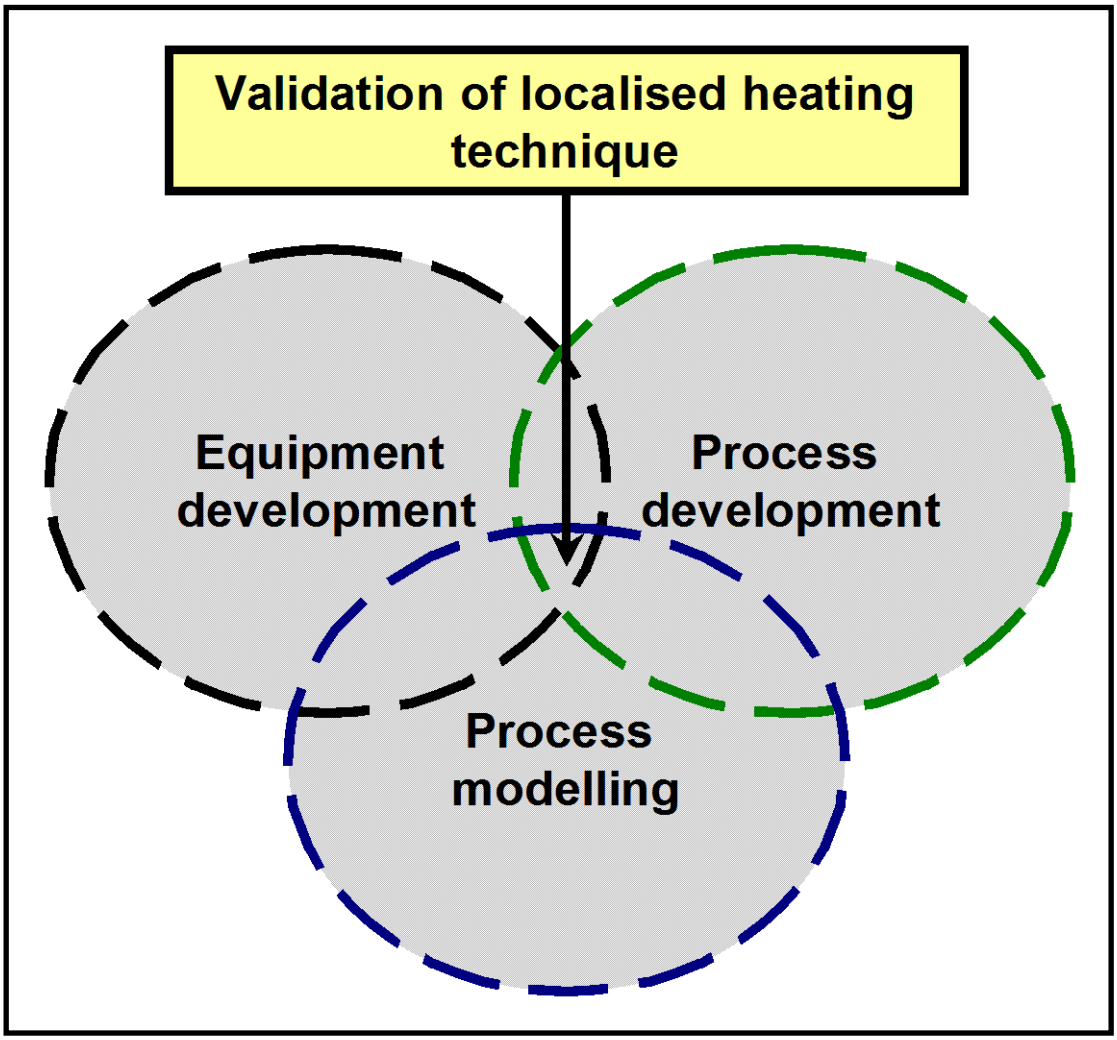


Figure 4-1 : Gas jet processing capability acquisition process split into three 'themes of work'

Equipment development – This comprises three chapters dealing with the development of the overall system including the head unit.

- Section 6, Equipment – Key system elements
- Section 7, Equipment - Localised Heat Treatment
- Section 8, Equipment - Prototype system development

Process development - This comprises two chapters, the first detailing the development and application of the system to a blisk component. The second describes the development of key process variable understanding.

- Section 9, Process - Heat treating of a blisk
- Section 10, Process – Developing understanding

Modelling development - This comprises two chapters, the first dealing with the development of a CFD model to determine the heat transfer characteristics of the gas jet process. The second describes the use of a finite element modelling approach, culminating in validation on a component.

- Section 11, Modelling - Computational Fluid Dynamics (CFD) analysis of jet heat transfer
- Section 12, Modelling - The finite element approach

Finally, the discussion section (section 13) details the validation of the localised heat treatment system and analysis of the overall development process and key system attributes.

5 TEMPERATURE MEASUREMENT

In the experimental work described in this thesis thermocouples are used as the main method of temperature measurement. A thermocouple is a simple and robust method for measurement of temperature. It consists of two dissimilar metal wires joined near the measurement point. The output voltage is measured between the two wires and compared to a reference voltage by the measurement device. There are several types of thermocouple, which can operate in different temperature ranges. For the experimental work described in this thesis, k-type thermocouples were used as they are suitable for use between 375C and 1000C.

Two different thermocouple types were used during this experimental work, Inconel Sheathed mineral insulated K-type, and K-type thermocouple wire supplied by Stork Cooperheat (UK) Ltd. The sheathed mineral insulated thermocouples were used for the control temperature measurement and measured the gas temperature in within the head unit. The nickel chrome/nickel aluminium thermocouple wire was resistance welded on the test pieces using a capacitor discharge welder.

Both the sheathed thermocouples and the thermocouples were class one, meaning they are supplied with a certificate of conformance stating an uncertainty of +/- 0.4%. Therefore the following equation can be used to define the maximum and minium level of variation at a given temperature;

Error = +/- 0.004 T, where T is the temperature.

So, at a temperature of 600°C, the error would be +/- 2.4°C or a range of between 597.6°C to 602.4°C.

Actual temperature (°C)	Measured output of calibrated thermocouple			Uncertainty of calibrated thermocouple	
		Error			
	μV	°C	μV	+/- °C	μV
401	16518	1.87	79	1	42
600.14	25002	2.13	91	1	43
400.8	16507	1.81	76	1	42

Table 5-1 : Calibration data from thermocouple wire used throughout the experimental work described in this thesis. Calibration performed by N.T.P.L Northern Temperature Primary Laboratory, Southport

In the case of the thermocouple wires welded to the surface of test pieces to measure test piece temperatures, the wire was calibrated [118]. This was done by providing a welded thermocouple on Ti-6-4 base material to The Northern Temperature Primary Laboratory (N. T. P. L). Table 5-1, shows the results of the calibration highlighting a maximum error of +2.13°C at a temperature of 600°C. Throughout this thesis temperature measurement values are given and the reader is encouraged to consider that these temperatures are subject to this potential maximum error of +2.13°C.

6 EQUIPMENT – KEY SYSTEM ELEMENTS

The following pages detail the basic design of the local heat treatment (LHT) system. Development was conducted through a number of prototype units culminating in one capable of processing a demonstration component.

6.1 THE INNOVATION – INERT GAS JET PROCESSING

Gas jets are currently used in turbine aerofoils and combustion chambers for cooling, here the reverse is true with the hot gas jets heating the component/substrate. Gas jets can provide a diffuse, moderate temperature, configurable heat source, able to accommodate complex component shapes. The basic structure of a head unit is introduced later (see Figure 7-7). The head unit is the part of the system where hot gas from the heater is directed onto the component as an array of jets. Hot gas enters the rear of the head unit before assign into plenum chambers intended to promote flow uniformity across the jet array. The gas then passes through the jet plates producing impinging jets to transfer heat from the gas to the target region.

6.2 LOCAL HEAT TREATMENT EQUIPMENT

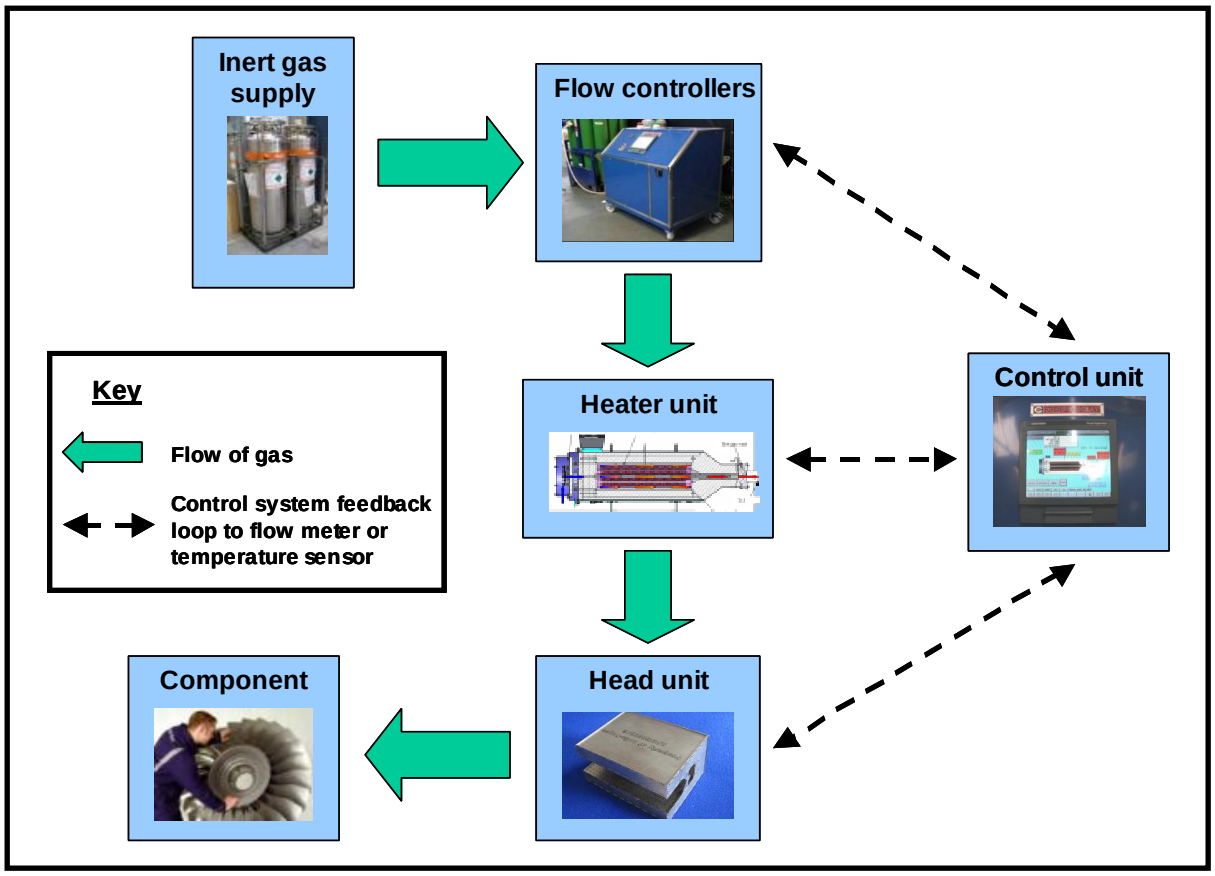


Figure 6-1 : Schematic representation of the gas jet processing system

To provide hot gas to the impingement plates with the head unit a number of elements of the localised heat treatment system are required. This section briefly details the equipment comprising the local heat treatment system (see Figure 6-1). The base unit and heater unit were manufactured by Stork Cooperheat (UK) Ltd based on the specification written by Mitchell [119].

Figure 6-1 is a schematic representation of the system used to heat treat the test pieces. Inert gas is supplied by a bank of cylinders (or tank) via digital flow controllers. The flow controllers allow predetermined flow, as specified by the

operator using the control unit, to be supplied to the heater unit and heated to the required temperature. Thermocouples positioned carefully [120] within the heater and head unit monitor gas temperature during the process. The desired gas temperature in the head unit is manually inputted to the control unit, and the feedback control loop provides the power necessary to the heater whilst monitoring the head (control) thermocouple temperature until the desired value is achieved. The heater power is controlled to maintain this target gas temperature. The heater element temperature is monitored using a heater thermocouple to ensure it does not overheat and fail. The main components of the system are described in more detail on the following pages.

6.2.1 CONTROL UNIT (PART NO. HES1266C)



Figure 6-2 : System control unit

The control unit supplies the heater with argon gas at the prescribed flow rate. It also contains the graphical user interface, through which the required control temperature and flow rate can be set. The user also determines the ramp rate required (in °C min^{-1}) to achieve the temperature and the required 'soak' time at this temperature. The control system has data logging capability, allowing all the process thermocouples, flow rates and up to six validation thermocouples to be monitored throughout the cycle.

6.2.2 HEATER UNIT

The heater is supplied with argon from the control unit and uses resistive element wires heat the gas up to a maximum of ~1000°C. The heater itself has undergone two major iterations in this project, both of which are described below:

6.2.3 FIRST GENERATION HEATER (HES1266)

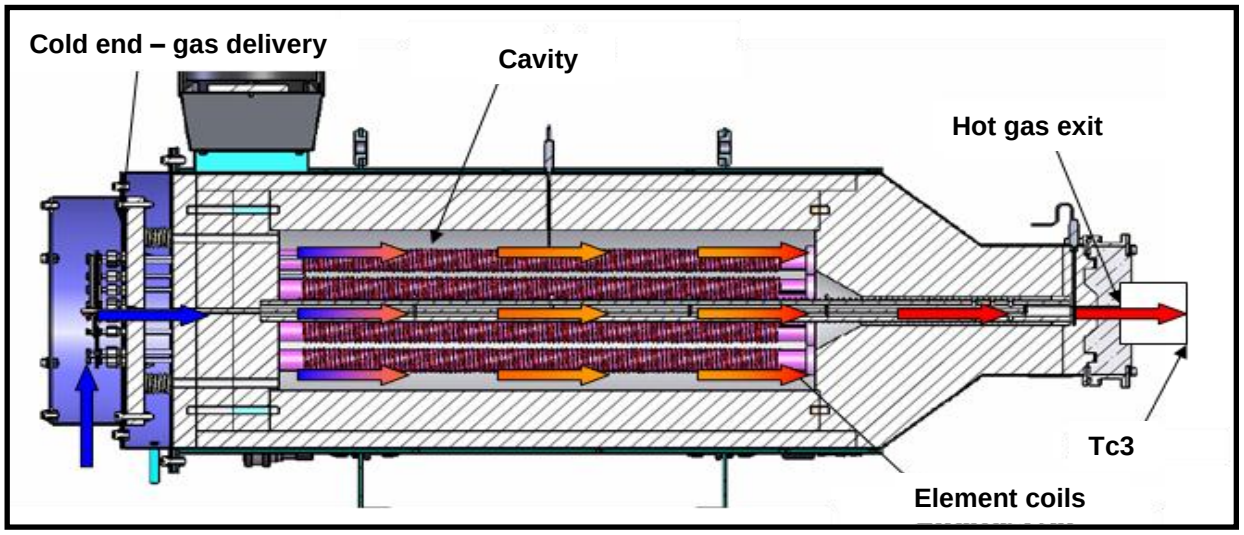


Figure 6-3 : Cross section of first generation heater

Figure 6-3 is a section view of the first generation heater showing the heating coils, central cavity and gas delivery and exit locations. The basic construction consists of a vacuum formed ceramic internal section encased in both ceramic wool and Monalite^{TM} machinable ceramic. The structure is held together using a steel case welded into a cylinder. A fan delivers cooling air between the steel case and a second steel skin to reduce the external temperature of the heater during operation. The arrows on the diagram show the gas path as it enters the heater, and heats up as it passes over the heating coils. The gas then exits the heater into the head unit. In this design the large cavity produces slow moving gas in proximity

to the heating coils to maximise contact time and heat transfer. The design of HES1266 has proved capable of delivering up to 200 l min^{-1} of gas at around 700-750°C to the head unit.

6.2.4 HIGHER POWER DENSITY HEATER (PART NO. CES-2690)

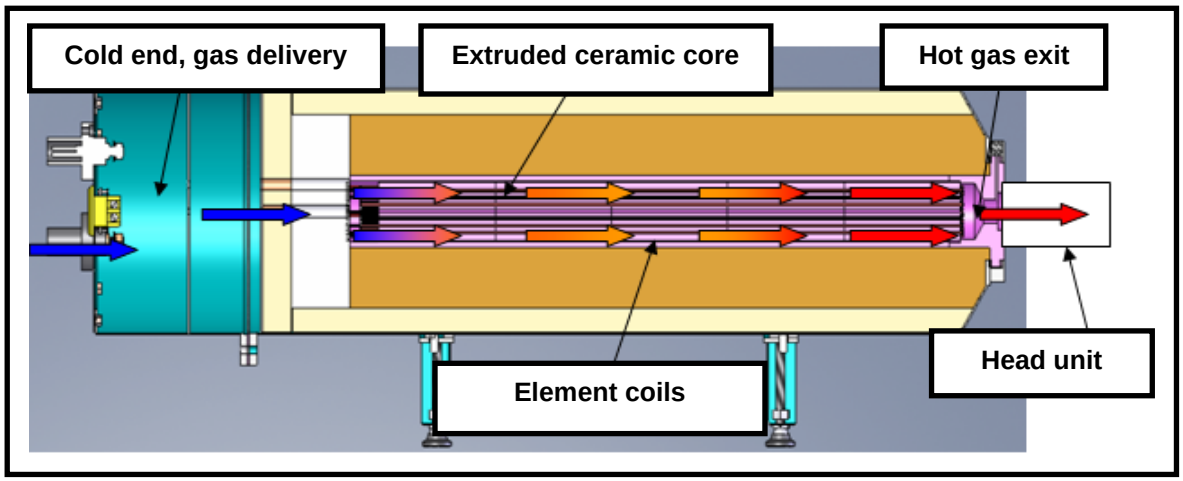


Figure 6-4 : Cross-section of second generation high power density heater

Figure 6-4, shows a cross-section view of the second generation heater (part no. CES-2690) developed during the course of this research. This higher power density heater contains an extruded ceramic core containing a number of holes running through its length. Each of these holes contains a resistance heating element wire. The argon gas enters the heater at the cold end and passes down the holes in the ceramic core. The larger element surface area in contact with the passing gas increases the energy density making the heater more effective at heating the gas. The resistance wires also run to a higher temperature than the previous example (up to 1300°C) making this heater able to achieve higher temperatures, approaching 850°C at the head unit.



Figure 6-5 : Size comparison between first and second generation heaters

The higher power density heater (CES-2690) has some major advantages over its predecessor aside from its increased temperature capabilities. The higher power density heater has smaller dimensions, measuring 700mm long by 200mm diameter, compared with 1200mm x 400mm for the first generation heater (Figure 6-5). This reduced size has two major advantages. Firstly, the heater is more manoeuvrable aiding manipulation of the heater to the correct position on the component. Secondly, the heater has a lower thermal mass. HES1266 has a large amount of insulation and this can take considerable time to heat up. As a result to achieve the desired heat treatment temperature a pre-heat cycle to soak the insulation was required. The smaller high power density heater unit (CES2690) reacts much more quickly and does not suffer from the same thermal lag.

CES2690 uses an extruded Mullite-based ($3Al_2O_3$ $2SiO_2$) ceramic in the core, compared with a porous vacuum formed ceramic used in HES1266. Use of a less porous material reduces the potential for trapped oxygen and moisture to transferred to the gas flow.

7 EQUIPMENT - LOCALISED HEAT TREATMENT

7.1 RESIDUAL STRESS OF REPAIRED COMPONENTS

As described previously (section 2.7.1), heat treatment of the repaired region is required in order to reduce the effect of residual stresses built up during the repair. Fusion welding processes such as those used in blisk repair are known to induce residual stresses [24, 59]. An understanding of the residual stress field generated in repairs of the type to be heat treated using the gas jet process developed in this thesis is key to aiding initial development of a local heat treatment process and the associated stress relieving parameters. The success of the resultant repair process (including the effectiveness of the local heat treatment) was determined directly by fatigue (i.e. vibration testing) of aerofoil test pieces containing repairs which have undergone gas jet heat treatment (section 13.2.3). However, residual stress measurements were made on representative repairs pre and post heat treatment to support development of the gas jet system and confirm the suitability of the temperatures documented within this thesis. The location of these residual stresses within the repair is also important to determine the extent to which the localised heat treatment region should cover the component.

7.1.1 TEST METHODOLOGY

A large number of both destructive and non-destructive residual stress measurement techniques exist, a detailed review of various techniques is given by Wyatt and Barry [64]. The most popular are hole drilling (destructive method), X-ray diffraction (non-destructive, although etching of layers is often used to produce

residual stress profiles making it destructive [64], Synchrotron (high energy X-ray) (non-destructive), and Neutron diffraction (non-destructive).

It is acknowledged that significant uncertainties exist in the measurement and interpretation of the most common residual stress measurement techniques. As a result repeat measurements must be taken. Incremental centre hole drilling was selected to undertake the residual stress measurements and Stresscraft Ltd, were contracted to undertake this work. The selection of hole-drilling was due to a number of factors, one of which is the relative low sensitivity to microstructure. As discussed in the literature review, the grain size and morphology varies considerably between the repaired region, HAZ, and base material. There are however limitations of the hole drilling method, such as poor spatial resolution, limited drill depths up to 1,6 mm, and the fact that stresses are averaged over a relatively large area (the orbital drilling diameter is 2 mm).

Hole drilling is used extensively in the aerospace and heavy manufacturing industry for the purposes of component lifing from condition of supply. The technique produces a two dimensional profile of residual stresses at discrete locations on a test piece (or component) at a range of depths. In these measurements a three-element strain gauge rosette is applied to the surface and the strain relief associated with incremental drill cuts is measured. The measured strains are then converted into stresses by multiplying by the Young's modulus. The data provided from Stresscraft Ltd and are discussed below.

7.1.2 TEST PIECES MEASURED

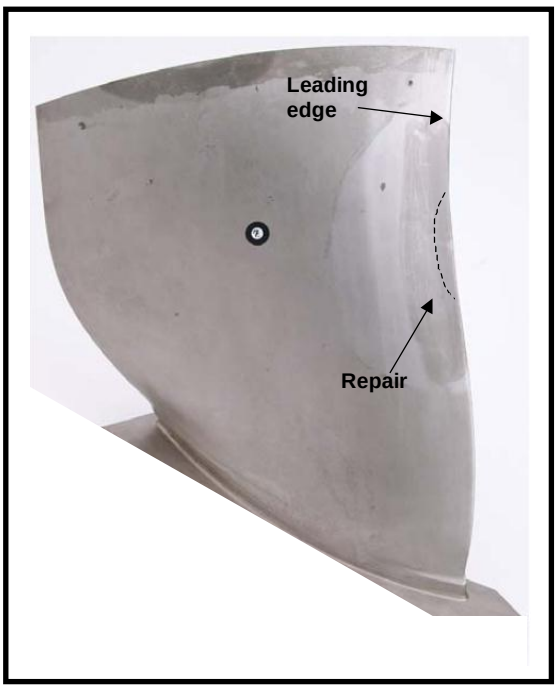


Figure 7-1 : Ti 6-4 test pieces used for residual stress measurements

Seven Ti 6-4 component test pieces (Figure 7-1) were provided for these trials containing repairs*** representative of those requiring heat treatment with the local heat treatment equipment. The gauges (rosettes) are applied following degreasing of the surface and bonded in position using Loctite® (see Figure 7-2 for gauge positions). The component is positioned on an angle plate and drilling rig for alignment with a miniature, 3-axis PC-controlled drilling machine. Incremental orbital drilling is performed at each gauge, the gauges record the relaxed strains at numerous drilling depth increments (between 0.064mm and 0.70mm). The heat treatment was performed in a production vacuum furnace at Bodycote Heat Treatment Services (Stockport, UK). The furnace was evacuated to 6.67 x 10-4 millibar or better, prior to and after the heat treatment and the test pieces were cleaned and immersion etched within a production environment. The composition and cycle times for the etch is considered commercially sensitive, however descaling was performed using Turco 4316 solution, and etching was

*** The details of the repair are considered commercially sensitive but the geometry of the repair is similar to that show in Figure 7-2 below, and is representative of those described in the literature review generated using a laser based deposition process.

performed using a hydrofluorosilicic acid plus Nitric acid solution. After etching the test pieces were rinsed with cold water, then acetone and finally dried in warm air.

7.1.3 POSITION OF RESIDUAL STRESS MEASUREMENTS

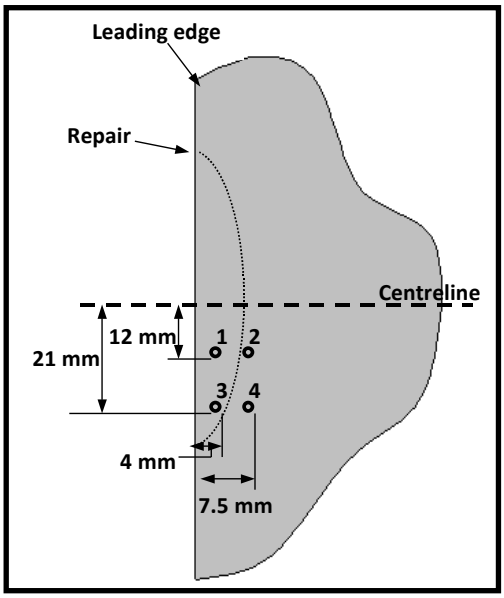


Figure 7-2 : Diagram of the residual stress measurement positions (small circles), (1) repair, (2) HAZ, (3) repair edge, (4) base material

Figure 7-2 shows the location of the residual stress measurement positions relative to the repair region on a repair of the type to be heat treated by the system being developed. These positions (numbered 1-4) represent the key regions of interest, giving an indication as to the level of residual stress present in; the repair, the repair edge, the heat affected zone (HAZ), and the base material. The dimensions show the position of the hole drilling measurements relative to the leading edge of the aerofoil.

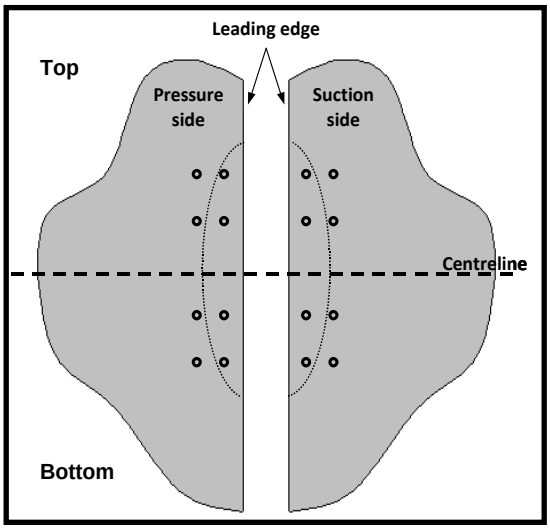


Figure 7-3 : Schematic showing the various regions of the repair where residual stress measurements were taken for this study

The repair was split into four equally sized regions, two on the pressure side and two on the suction side. Figure 7-3 shows schematically these regions of the repaired area. Splitting the repair in this manner allows each repair to yield four regions for measurement at various

stages of the process. Once hole drilling has been performed that region is no longer suitable for further measurement due to the destructive nature of the measurement technique.

7.1.4 AS-REPAIRED RESIDUAL STRESS

Figure 7-4 shows the results of hole drilling measurements in the as-repaired condition. The values are taken at the maximum drilling depth increment of 0.51mm, this was chosen in order to minimise any surface effects and provide a value consummate with the bulk residual stresses of the repaired region. These values were all measured in the radial direction (i.e. root to tip of the aerofoil) as these were consistently significantly higher than those measured in the chordwise direction. Due to the additive layer process used in this repair, the longer direction for material contraction is in the radial direction on the aerofoil. As a result one would expect a larger amount of thermal contraction and thus higher residual stresses to be generated in this direction. The data presented in Figure 7-4 represent an average of all seven measured aerofoils. These were measured in the top suction side region of the repair (see Figure 7-3) for consistency. As a cross check one blade was measured in the top suction, bottom suction, and top pressure regions (Figure 7-3) and the measurements taken in all four positions (Figure 7-2) fell within the spread of data measured across the seven represented in Figure 7-4.

The residual stress values in Figure 7-4 are presented as a percentage of the UTS of the deposited material[†††] (in this case titanium 6-4) and show significantly higher values in the repaired region than in the substrate or HAZ. The values are very low in the base material at less than 5% of the UTS, whereas in the repair, values of 30% are observed. The actual values of residual stresses measured varied by up to 200MPa in the worst case, highlighting the limitations of this method. It is also noted that the data presented do not necessarily constitute the maximum level of residual stress in the repair region. Hole drilling measures at discrete locations in the repair and may not capture the peak value in the repaired region.

The residual stresses measured were typically tensile as shown in Figure 7-4. However, when the profiles for each hole were reviewed, some compressive residual stresses were seen at the surface to depths of less than 250 microns. These quickly became tensile with depth and are likely due to the 5-axis machining operation post deposition as described by Griffiths [39]. Leggatt [59] describes large tensile residual stresses approaching yield within welds. While the values measured are not close to yield they represent significant stresses which could contribute to premature fatigue failure, as described by Radaj [61]. Liu *et al* [60] noted significantly higher residual stresses close to adjacent layers similar to the repair edge measurements described here where the relatively cooler base material provides restraint.

[†††] This percentage was calculated by taking the actual measured value and dividing by a typical UTS of deposited Ti-6-4material from the open literature.

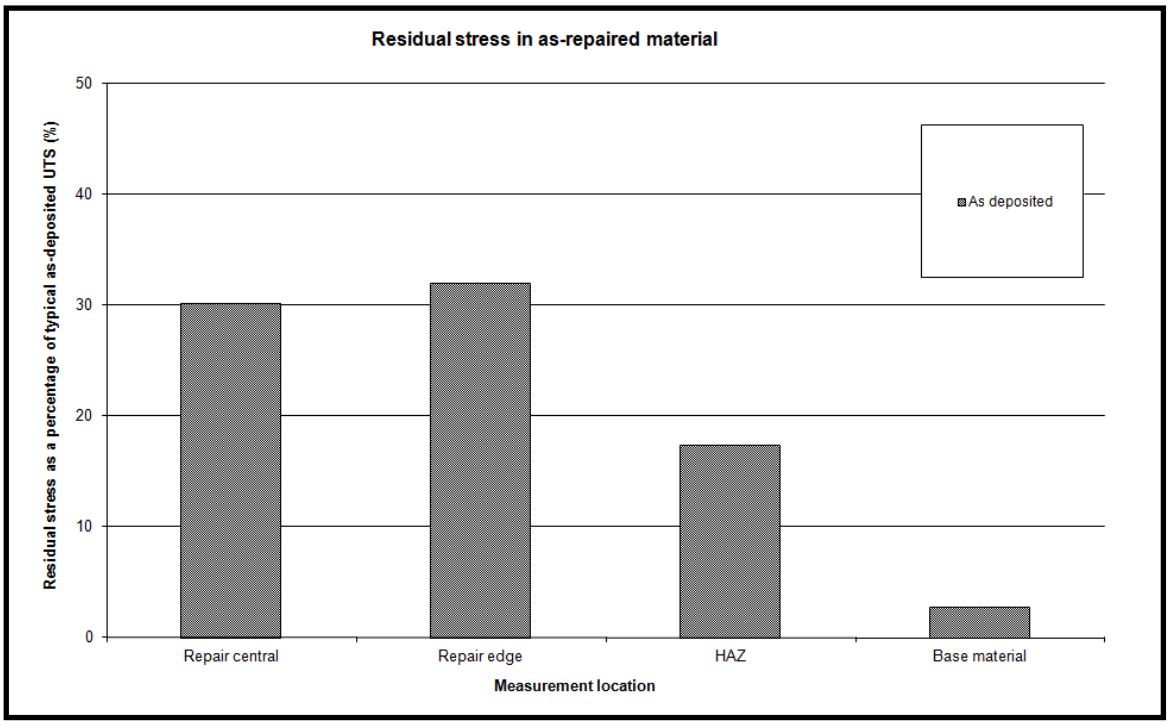


Figure 7-4 : Residual stress in as-repaired condition

7.1.5 EFFECT OF HEAT TREATMENT ON RESIDUAL STRESS

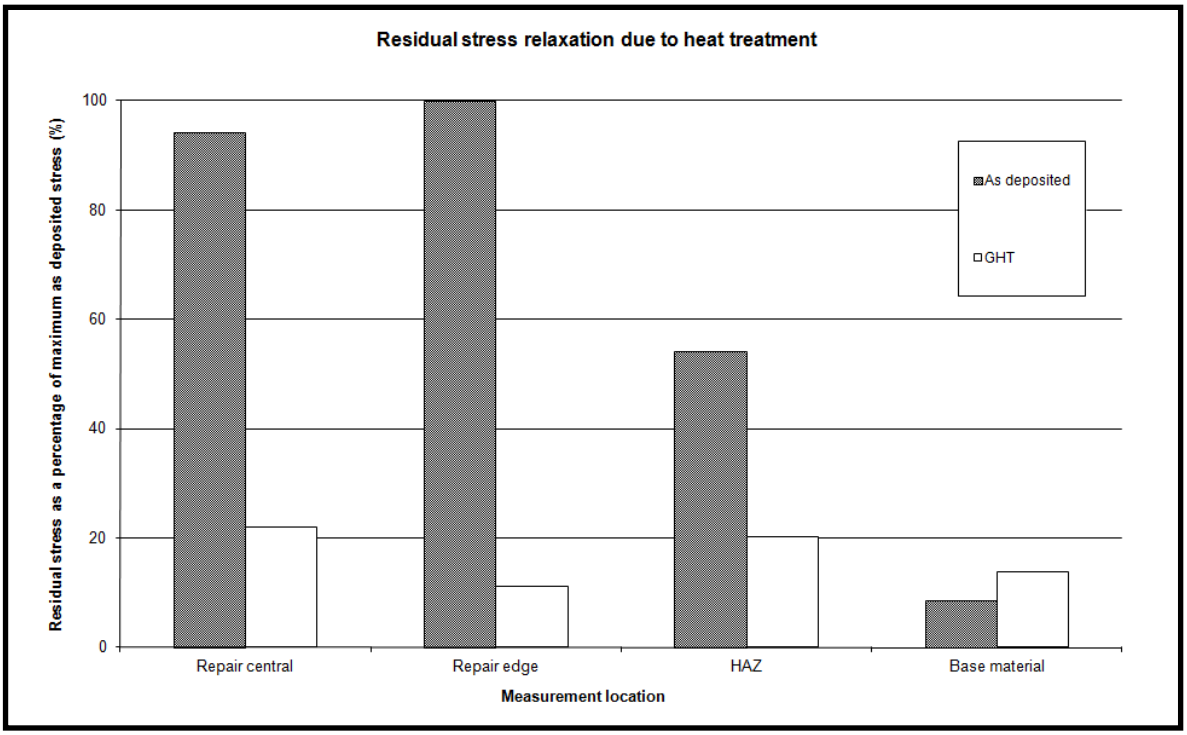


Figure 7-5: Residual stress in as-repaired, and repaired and globally (Vacuum furnace) heat treated condition

Figure 7-5 shows the effect of heat treatment on the level of residual stress after heat treatment of the whole component in a vacuum furnace (termed Global Heat Treatment (GHT)). Significant reduction in residual stress is noted in all locations, with all residual stress levels being less than ~20%. The data represent a residual stress reduction of between 63-76% from the as-deposited condition, which is in agreement with that reported elsewhere [65,67]. This highlights the effectiveness of heat treatment in the temperature range being used for the development of the local heat treatment process in this thesis. Note worthy is that the average residual stress appears to increase in the base material following heat treatment. However,

the measurement uncertainty presented in the following section is very similar in magnitude to the residual stress levels measured in the base material location.

7.1.6 RESIDUAL STRESS MEASUREMENT ACCURACY/UNCERTAINTY

The data presented in this section provide trends as to the level of residual stress that requires relief by the local heat treatment system. Measurement accuracy and uncertainty can have a significant effect on the results achieved using the hole drilling method and these should be considered. Factors that contribute to stress measurement uncertainty include; surface condition, material properties, drilling factors (including drill bit shape, condition and depth control), and strain gauge factors such as bond and installation. A random strain uncertainty for this application is stated as +/- 6Mpa at a hole depth of 0.26mm and increasing to +/- 12Mpa at positions close to the surface (i.e. ~0.03mm) and at full hole depth (~0.51mm) based on observed residual stress and data reported by Grant *et al* [121]. In addition the measurement supplier estimates the combined uncertainty due to the remaining factors at 8%. Therefore for any given value of stress measured (x) the total uncertainty would be expressed as follows;

Equation 7-1: xMPa +/- (12+x*0.08) Mpa [118]

Given the maximum level of residual stress in laser deposits reported by Moat *et al* [24] of 420MPa, this would result in an uncertainty of +/- 45.6 MPa.

7.1.6.1 VARIATION IN MEASURED DATA

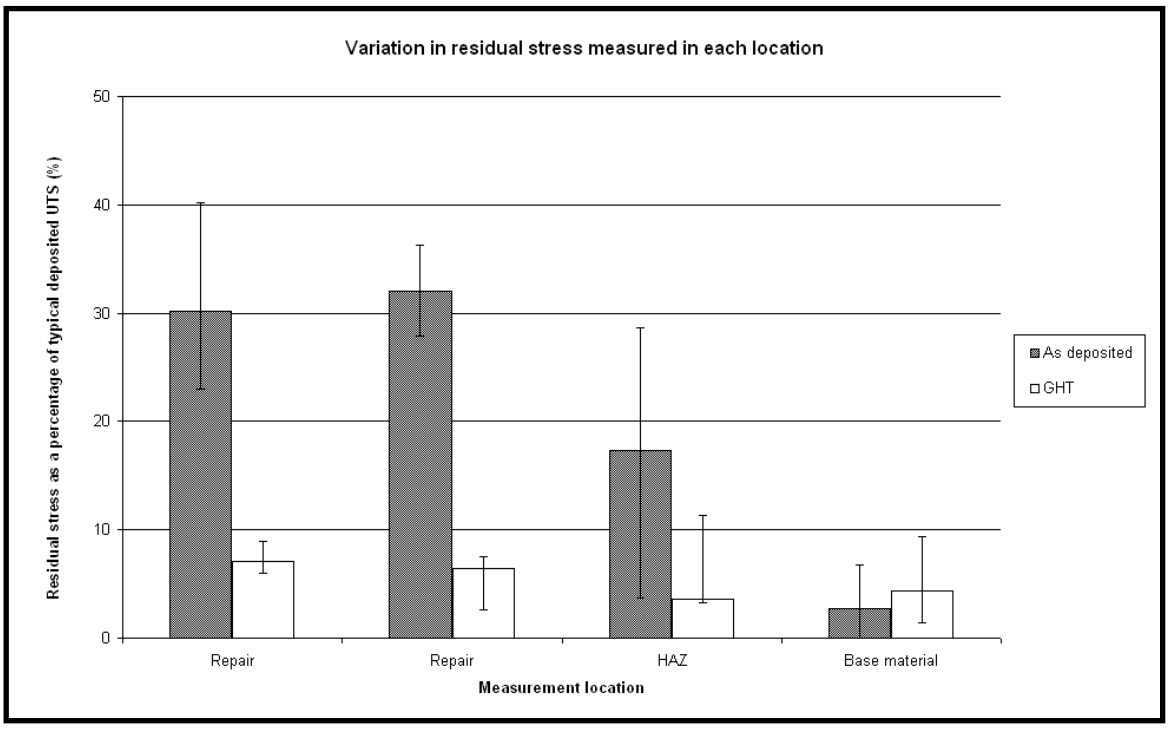


Figure 7-6 : Graph highlighting the variation in residual stress measurements both as deposited and post heat treatment for the various repair locations

Figure 7-6 shows the variation in residual stress measurements across the test pieces and locations measured, highlighting the large variations when using this measurement technique. The error bars represent the maximum and minimum values of residual stress measured in the test pieces. The heat affected zone shows the largest variation. The HAZ is small in size (of the order of 0.5mm) and has a relatively steep stress gradient across it. Both these factors mean that slight differences in the positioning of the residual stress measurement equipment relative the heat-affected zone could yield significantly different results. This again highlights a limitation of this technique as only discrete locations are measured.

7.2 LOCALISED HEAT TREATMENT HEAD UNIT DEVELOPMENT

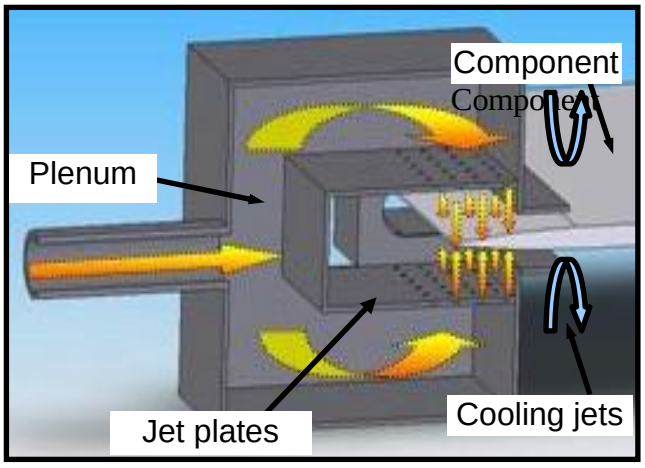


Figure 7-7 : Schematic section view of typical heat unit structure

In order to produce a localised stress relief of the repair geometry shown in Figure 7-2 hot argon impingement jets were used. Gas is heated using the equipment described in section 6 and delivered to a head unit (Figure 7-7) which directs pre-heated inert gas onto the target component zone using patterned nozzle arrays (impingement jet arrays). The gas enters a plenum chamber at the rear of the unit slowing the flow to promote uniformity across the jet plates. The gas then accelerates through the jet plates as impingement jets which impact on the component to provide heating.

A number of different head units have been designed and tested to determine the most appropriate design methodology. Having previously described the basic system operation, this section details the work to understand the specific issues surrounding locally heating a component and the head development to achieve this. An overview of evolution of the head design is given in Appendix 1 – Local Heat Treatment (LHT) head evolution.

7.2.1 LOCALLY HEATED REGION MORPHOLOGY

When heat treating locally there is a characteristic heat treatment zone shape (when applying a rectangular head unit), which is shown in Figure 7-8. The images

show the shape of the heated zone achieved during thermal paint trials. The use of air as the process gas‡‡‡ was required in this instance as the colour change in the thermal paints is associated with an oxidation reaction. Although the flow rates were set to be equivalent to those used for heating components, the heat transfer characteristics of air are markedly different to the intended process gas (argon). As a result of the tests being conducted on square plate test pieces with no heat sinks or large section changes, the conduction away from the heated region was largely uniform. This produced isotherms within the heated zone that were symmetrical around their centreline.

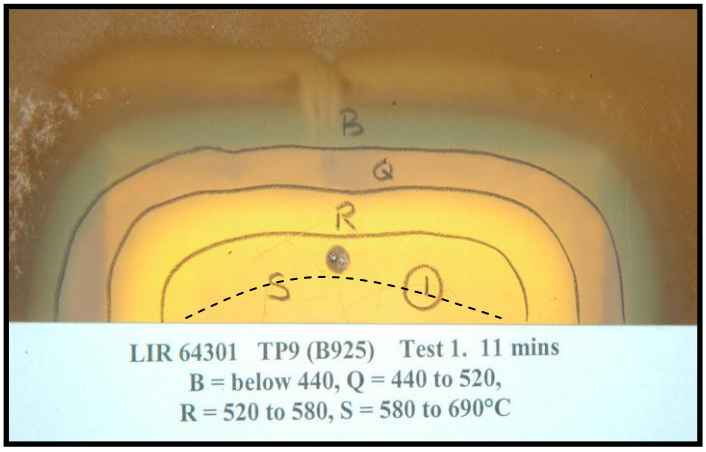


Figure 7-8 : Thermally painted test pieces showing isotherm morphology due to the application of the gas jet processing head unit. The dotted line represents a typical repair location and size.

‡‡‡ The Rolls-Royce plc proprietary thermal paints rely on an oxidation reaction to produce the colour change shown in the pictures. These colour changes are calibrated to occur in a known temperature range, but require an oxygen rich atmosphere and are not calibrated for use in argon.

7.2.2 THE CONTROL THERMOCOUPLE

During the heat treatment of a repaired component, attachment of temperature measuring devices (such as welded thermocouples) is not permitted. This practise would cause surface damage to the component and could have a detrimental effect on the microstructure adjacent to where the thermocouple was attached. In order to monitor the temperature during heat treatment of the repaired region a 'control thermocouple' is placed in the gas flow close to the leading edge. This monitors temperature in close proximity to the test piece and is used to ensure the component remains within the defined temperature limits during the cycle. The control thermocouple enters the heat treatment zone along the edge, with the thermocouple positioned only a few millimetres from the test piece. This proximity allows measurement of temperatures representative of that seen by the

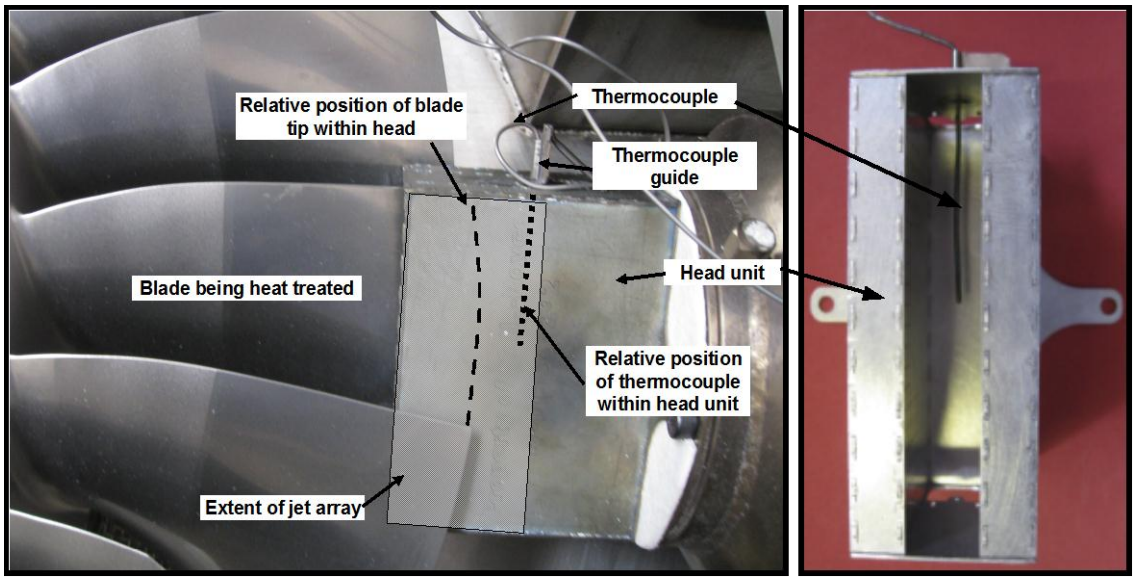


Figure 7-9 : Images showing the position of the control thermocouples in a head unit used to heat treat the tip of an aerofoil (as used later in section 9.4). Note the relative positions of the thermocouple, jet array, and tip (image left). In the case of a leading edge heat treatment the thermocouple and blade edge have the same relative positions. The right hand image is taken with the head removed from the system and looking directly into the blade cavity along what would be the stacking axis of the blade.

component. Control thermocouple measurements show gas temperatures 20-50°C higher than the component (depending on gas flow rate). Testing is required to establish this ‘offset’ before processing any demonstration component. The offset is defined as the difference between the gas temperature and average thermocouple temperatures.

7.2.3 EFFECT OF HEAT SINKS

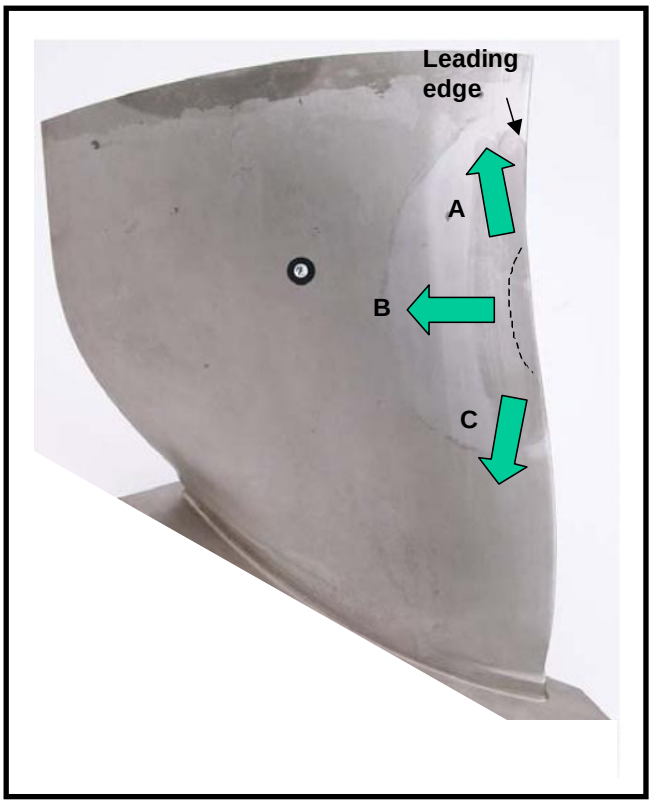


Figure 7-10 : Typical large titanium test piece with arrows showing direction of heat loss from heated zone (top), and the shape of the heated zone due to their affects (bottom).

One of the main challenges when applying local heat treatment is the effect of conduction of heat away from the heated zone.

Figure 7-10 highlights a typical scenario for an aerospace component being heated locally. In this image three main affects are highlighted, A, B and C

A - The large mass (heat sink) associated with this region requires significant energy to raise its temperature. It remains relatively cool as the thinner sections heat up, creating a large ΔT and therefore a significant driving force for conduction. Although the heat sink effect is significant, the cross sectional area restriction due to the thin blade helps to counter some of the effects generated by the large mass in this application.

B - The application of cooling gas in this region is required to maintain the integrity of a temperature sensitive material within the blade core. An example of a temperature sensitive region may be a soft, damping core. Polymer damping cores

are being investigated by Sheffield University for use in fan blade applications [14]. The edge of temperature sensitive regions are often located close to the leading edge and cooling needs to be applied to these regions to maintain integrity.

C – Heat conducts away from the heated region as a result of heat lost through convection from the surface of the component. The aerofoil is positioned in a vertical orientation, providing the maximum level of convective heat loss. The removal of this heat reduces the temperature of the aerofoil increasing the ΔT between this region of the aerofoil and the locally heated region. This increases the driving force for conduction.

7.3 PRODUCING TAILORED JET ARRAYS

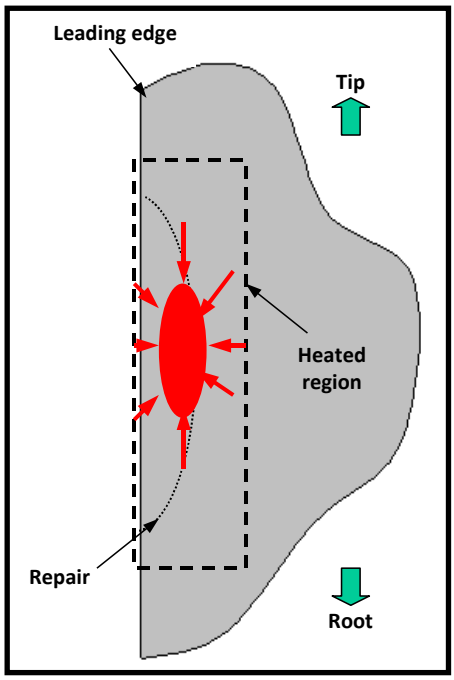


Figure 7-11 : Location of hot spot in current unit design

Early trials using square arrays of jets covering the whole repair region highlighted the presence of a hotspot in the centre of the heated region. The red region in the centre of Figure 7-11 represents the area where the majority of the heat is focused in such a scenrio. The surrounding arrows represent the heat coming into the region from elsewhere. The red region is heated not only by the jets directly above it but through conduction of heat from the surrounding material. At the centre of the heat treatment region is where the majority of the heat within the component is concentrated.

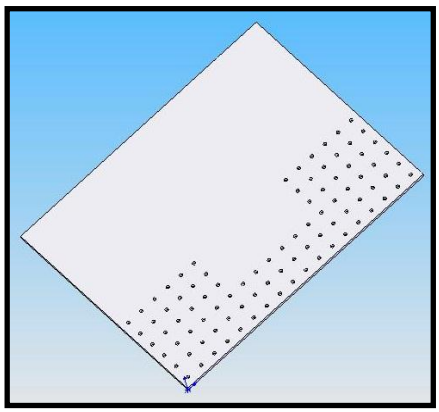


Figure 7-12 : Tailored jet plate array with central holes blocked

In order to provide an acceptable temperature distribution across the heated region the difference between the maximum and minimum temperatures must be as close to the specified temperature tolerance as possible. A target for the heat treatment tolerance was defined as 600ºC +/- 10ºC, thus the ΔT should be ~20ºC, making the minimum temperature 590ºC, and the maximum temperature 610°C.

Early tests indicated that the blocking of holes in the jet plate to produce a tailored array (Figure 7-12, above) has the desired effect of reducing the temperature

distribution across the repair region. This is achieved through heating the central region primarily through conduction from the surrounding regions. It is noteworthy that some heating from hot gases within this region still exists but not through direct impingement. As a result of more gas being directed through the jets surrounding the central region, the flow rates through these holes will be greater (for the same overall flow rate). The resulting higher velocities enable greater heat transfer. These combined effects reduce the heating in the central region whilst simultaneously increasing heating in the outer regions.

7.3.1 TEST SETUP AND PROCEDURE TO INVESTIGATE THE CONCEPT OF TAILORED JET PLATES

Trials were conducted in order to establish the effectiveness of blocking holes to reduce the hotspot and improve temperature distribution.

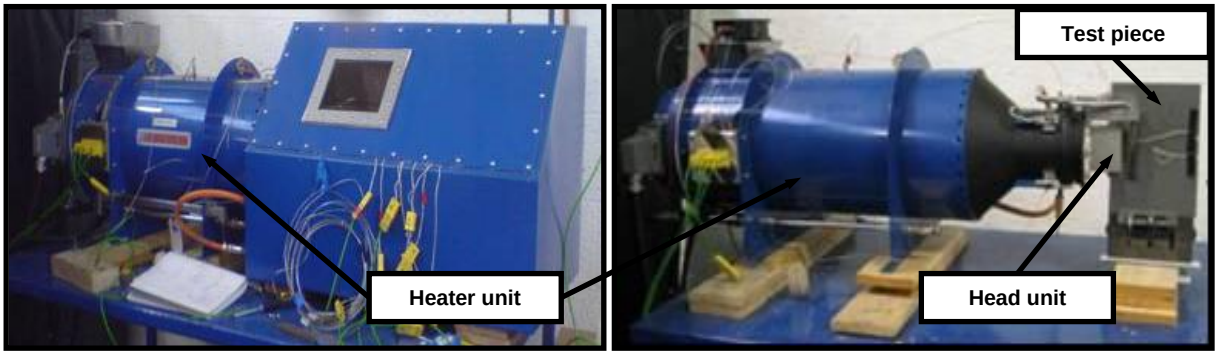


Figure 7-13 : Photographs of test setup during head development trials. Note localised chamber in left hand image.

Figure 7-13 shows the test setup used, in total, five tests were conducted (1, 2, a, b, and c). In tests 1 and 2 a jet array of 6 x 18 1mm holes with a 5mm spacing was used (see head unit in Figure 7-15, below). In tests a, b, and c holes were blocked with Resbond 920^{TM} high temperature adhesive as shown in Figure 7-14.

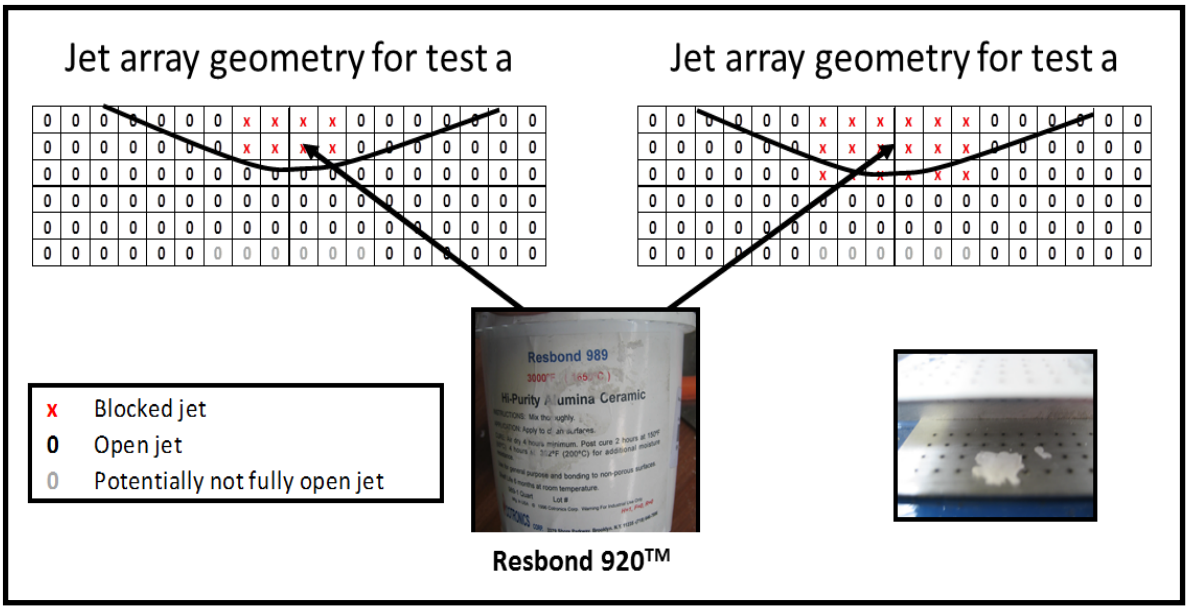


Figure 7-14 : Diagrams to show the method and pattern for hole blockage used to assess the effects of the hot spot generated with the standard hole array. Resbond 920^{TM} high temperature adhesive is used to block individual holes (inset image right).

The diagrams at the top of Figure 7-14 represent the jet arrays in the head unit, showing two different stages for blocking jets. The intention was to block the holes as shown in the geometry for test a to see if this was sufficient to alter the temperature distribution and then, move onto geometry b to further reduce the temperature difference as required.



Figure 7-15 : Head unit (RPDG000195) used for hole blocking trials

7.3.2 IN-HEAD TEMPERATURE DISTRIBUTION

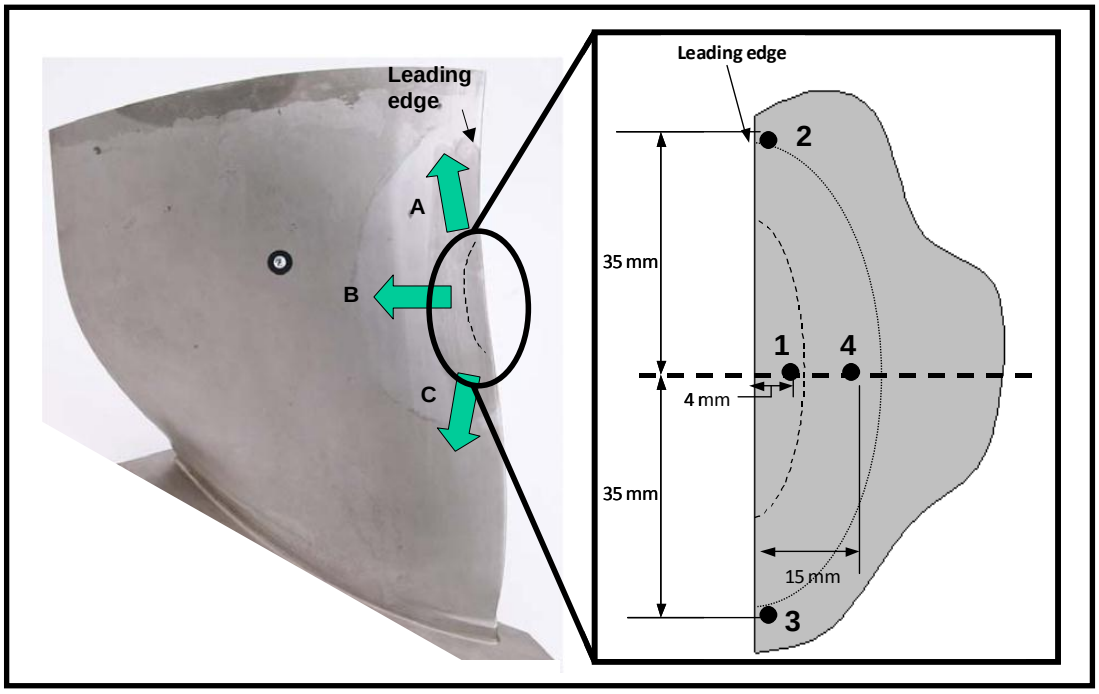


Figure 7-16 : Schematic representation of the heated region (right) and relative position on the aerofoil (left)

Figure 7-16 highlights four main regions of interest within the heated zone; numbers 2, 3, and 4 are influenced by the factors described previously. Region 1 is the hottest region, with central jets impinging upon it and surrounded by hot material. Conductive losses are minimal while ΔT to the surrounding material is low. Convective losses are minimised due to the hot gases above. (Regions 1-4 in Figure 7-16 will be referred to in the following discussion.) K-type welded thermocouples were positioned in locations corresponding to loctions 1-4 in Figure 7-16.

To develop understanding of head design and gas jet process deployment, early work focused on heating the leading edge of the testpiece in Figure 7-10 (above).

The objective was to heat a representative repair region (i.e. the containing thermocouples 1-4, and regions designated repair, HAZ, and repair edge in Figure 7-2) to 600ºC. The target is to achieve a tolerance of +/- 10°C, at this temperature.

7.3.3 EXPERIMENTAL ASSESSMENT OF HOLE BLOCKING TECHNIQUE

Figure 7-17, Figure 7-18 and Figure 7-19 highlight the effect of blocking central jets. Tests 1 and 2 were completed using a head unit with a standard square array. Test a had 8 jets blocked and tests b and c had 18 holes blocked. Between tests 1 and 2 the head unit was realigned to a more central position on the repair region (defined by thermocouples placed at positions 1, 2, 3 and 4 from Figure 7-16). This produced the effect of minimising the temperature differences in the thermocouples, especially those located at the extremities of the repair. The reason for this improvement originates from the morphology of the isotherms generated in the case of a head unit symmetrical around its centre line. The heat

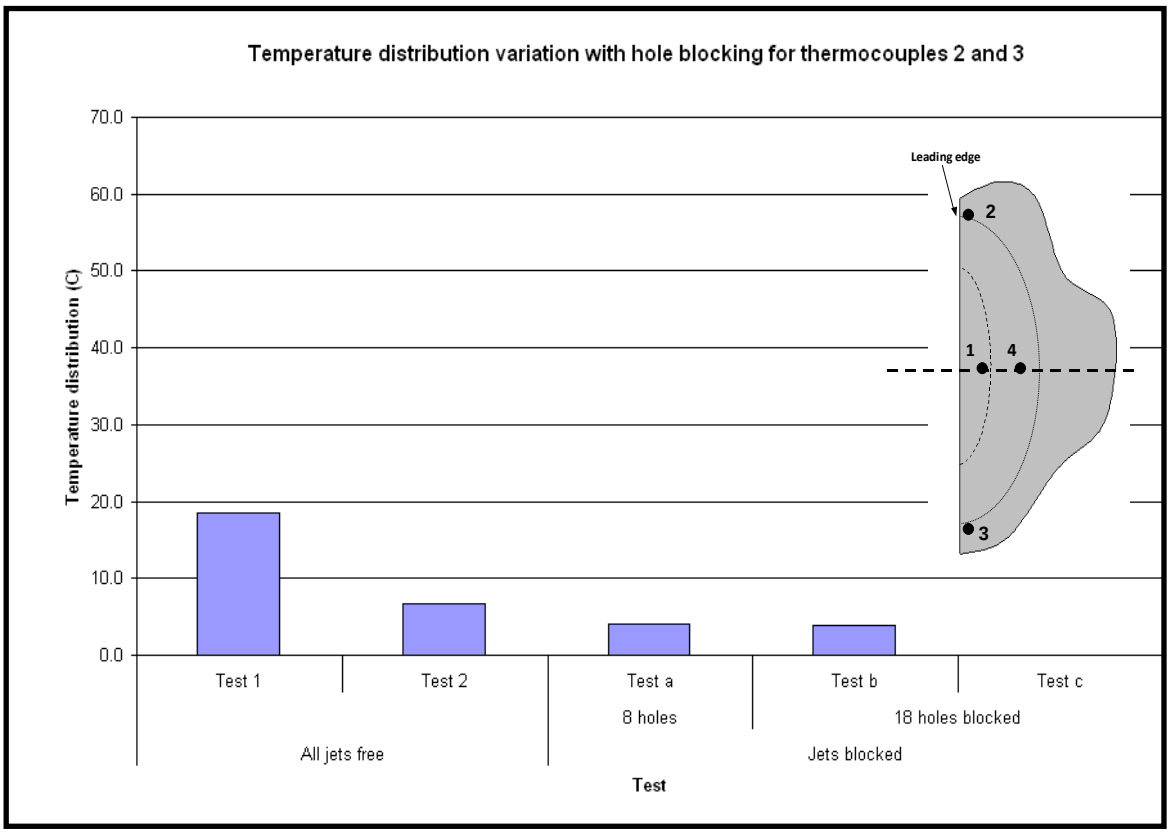


Figure 7-17 : Temperature distribution due to blocking of holes on thermocouples 2 and 3 (Gas flow rate = 120 l min^{-1}, Gas control temperature = 620 °C)

treatment zone will also be symmetrical around the centre thermocouple.

All the blocked holes in this experiment were in the central location as shown previously in Figure 7-14. In the first graph (Figure 7-17) the difference between the top and bottom of the heated zone is shown (regions 2 and 3). This remains fairly constant through tests 2, a, b and c at a value well below 10°C (the reduction in temperature distribution between tests 1 and 2 is due to head realignment). The temperature drop through these tests, particularly between test 2 and tests a, b and c is due to the redirection of gases to the holes located at the outer regions of the head unit. This leads to increased velocity and therefore increased heat transfer.

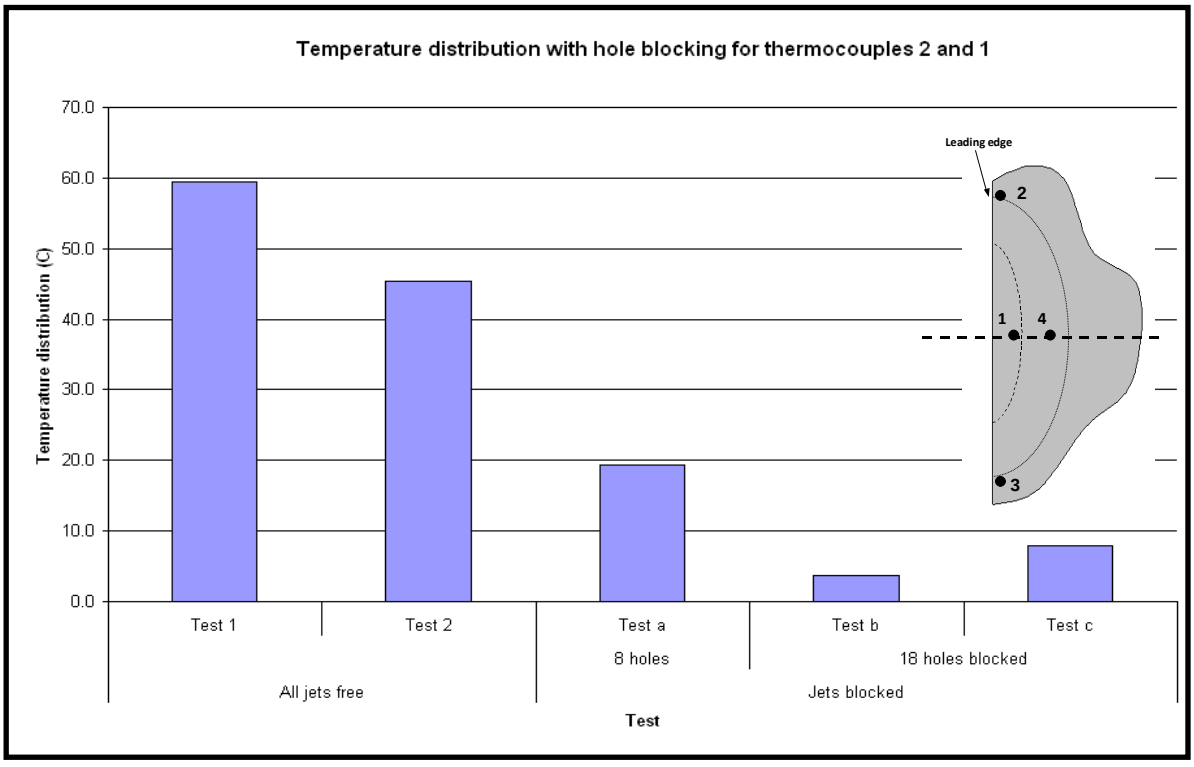


Figure 7-18 : Temperature distribution due to blocking of holes on thermocouples 1 and 2 (Gas flow rate = 120 l min^{-1}, Gas temperature = 620 °C)

Figure 7-18 highlights the effect of blocking the central holes on the temperature difference between zones 1 and 2. This confirmed that blocking holes above the central region reduced the heat input. This region is now primarily heated through conduction through the material and less through convection as in the rest of the heated area. The reduction in ΔT between zones 2 and 1 is clearly evident in Figure 7-18 and shows a significant trend to suggest this is a good methodology for reducing the temperature of the central region.

Figure 7-19 shows the effect of blocking central holes on the ΔT between the central 'hot' zone 1 and the 'coolest' zone 4. Zone 4 also benefits from the increased velocity of the gas jets over it. However, this region is usually the lowest temperature due to the large amount of surrounding material increasing

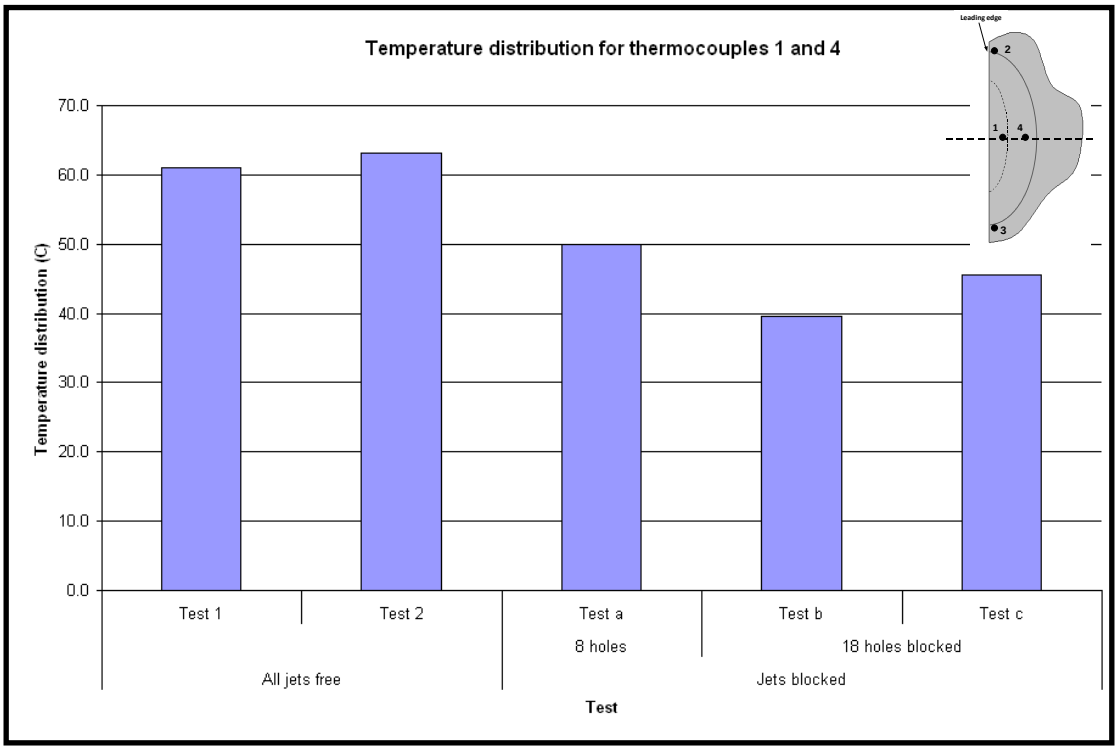


Figure 7-19 : Temperature distribution due to blocking of holes on thermocouples 1 and 4 (Gas flow rate = 120 l min^{-1}, Gas temperature = 620 °C)

conduction of heat away from this area. Although there is a clear reduction in temperature difference through these trials, the temperature difference is still reasonably high at around 40°C.

The information detailed above provides evidence of the highly tunable nature of this system and suggests that it is possible to tailor jet plates to a specific application. The use of tailored jet plates allows one to direct the jets at the regions of the component that require the highest heat input.

7.4 DEMONSTRATION OF HEAD WITH INTEGRATED COOLING PIPES

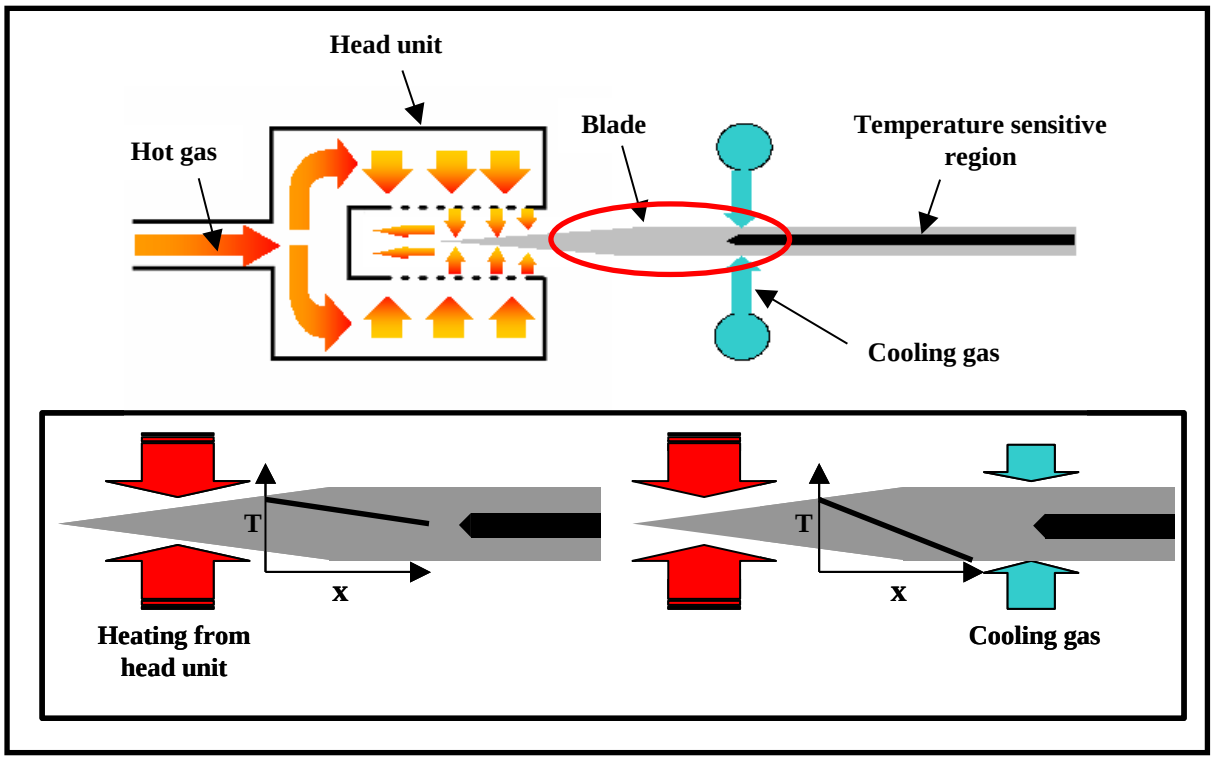


Figure 7-20 : Heat treatment setup with head unit, cooling gas and temperature sensitive region

In some applications requiring localised heat treatment, regions close to the heated area require cooling to minimise the area at heat treatment temperature. Figure 7-20 shows a schematic diagram illustrating a cross sectional view of a head unit with cooling gas. In the centre of the blade (grey) in the diagram there is a temperature sensitive region (black), which must kept cool. In order to achieve this cooling pipes are used deliver jets of cool gas onto the surface. At the bottom of Figure 7-20 are sketches of two graphs describing the temperature gradient which exists through the component (temperature on the y-axis, distance on the x-axis), between the heated and cooled regions. When force cooling is applied the gradient is much steeper. This results in a large ΔT and significant driving force for

conduction of heat away from the heated zone. This diagram highlights the challenge posed when forced cooling is required in tandem with localised heating. The following section details the experimental trials conducted to develop an appropriate method of simultaneously heating and cooling adjacent regions of a component.

7.4.1.1 HEAD WITH INTEGRATED COOLING – THE TEST PIECE

The test piece used in the following trials was a large blade component (similar to that seen previously in Figure 7-16) containing a hollow cavity. The target was for the leading edge of this component to be heated whilst maintaining the temperature of the cavity below 150°C.

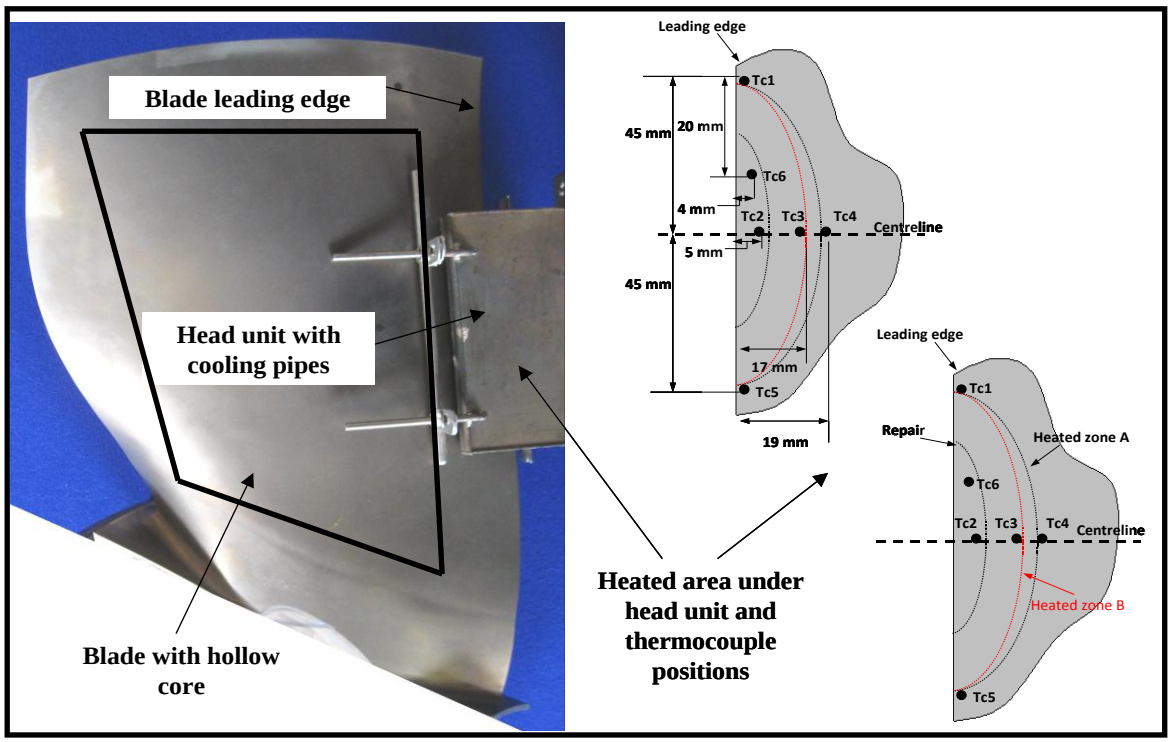


Figure 7-21 : Test piece used in trials with cavity location shown by the solid black line (left), heated region and thermocouple locations (right).

The edge of the hollow cavity (signified by the solid line in the left of Figure 7-21) within the test piece is 50mm from the leading edge. A k-type mineral insulated thermocouple was placed in the cavity to monitor the temperature. The target for this work was to maintain the temperature sensitive region below 150°C, whilst achieving the required heat treatment temperature. The test piece was x-rayed to

confirm the location of the thermocouple in relation to the leading edge and was held in place with adhesive.

Resistance welded k-type thermocouples monitored the region shown on the left of Figure 7-21. Thermocouples were placed in the locations shown, corresponding to those expected to yield the maximum and minimum temperatures seen in the repair region during heat treatment. It is the magnitude of the temperature difference that is being investigated in this section; therefore the reader can assume (unless otherwise stated in the text) that the temperature differences quoted are around the target temperature of 600°C.

7.4.1.2 HEAD UNIT WITH INTEGRATED COOLING

The region defined in Figure 7-21 is to be heated to 550-700ºC to provide sufficient stress relief for a Ti 6-4 repair [43]. Current commercial practise for local heat treatment requires temperatures above 500ºC to be controlled to within +/-10ºC. This has therefore been set as the target for this localised region.

Previous trials demonstrated that the required region could be heat treated to 600ºC +/- 10ºC using head unit RPDG000195 (Figure 7-15) by tailoring the jet plate as described previously. Head unit RPDG000194 (Figure 7-22) was manufactured for these trials. It contained a simple square jet array (1mm diameter holes, 5mm spacing), with external dimensions measuring 140mm x 45mm x 80mm. The reason for the increase in head size was to provide a larger heated region. As described in section 7.3 the central holes were blocked to reduce the central hotspot. Due to the larger head unit compared with that shown in Figure

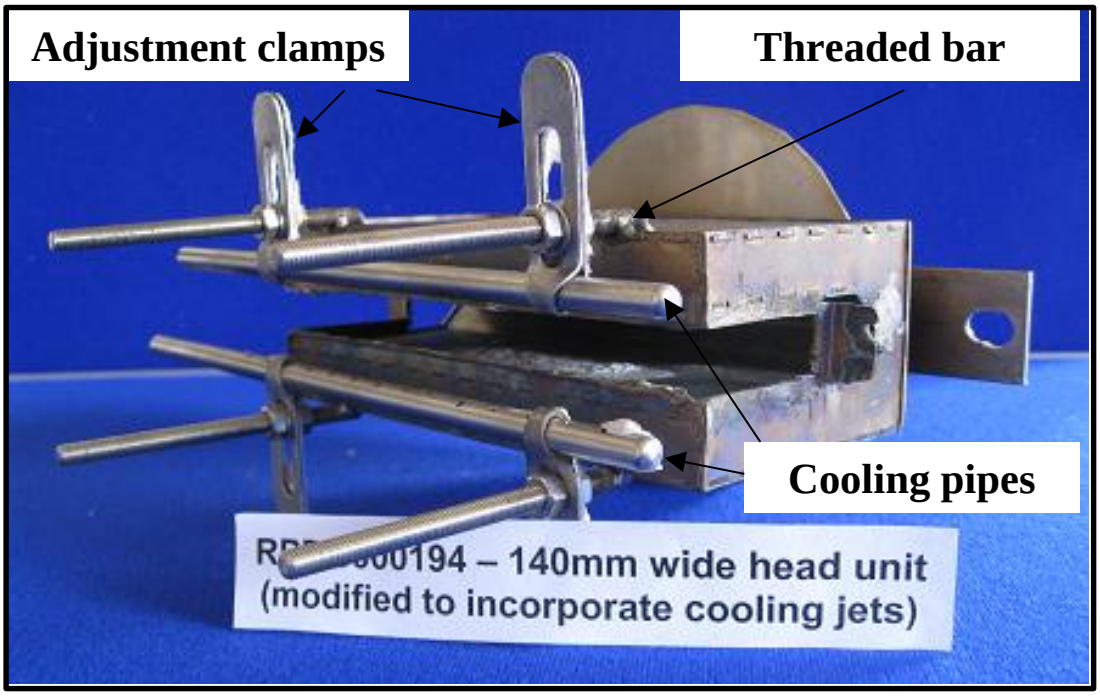


Figure 7-22: Head unit RPDG000194 with integrated cooling

7-15 a flow rate of 150 l min^{-1} was used in these trials, with a control temperature of 650°C.

7.4.1.3 COOLING JETS AND THERMAL BARRIER

A further addition to head unit RPDG000194 was an arrangement for providing cooling to adjacent regions of the test piece. Threaded bar was welded to the top and bottom surfaces to provide support for slotted clamps which held cooling pipes. The cooling pipes, have 1mm holes (again with a 5mm spacing) drilled into them for the delivery of ambient temperature argon to the work piece. These clamps allow the cooling pipes to be adjusted for height from the test piece surface and distance from the head front. This allowed targeted positioning of the cooling pipes in order to maintain the temperature of the cavity thermocouple below the 150ºC target value.

Once the initial testing was underway, it became apparent that cooling gas flowing across the surface into the head unit, reducing the temperature of the heated region.

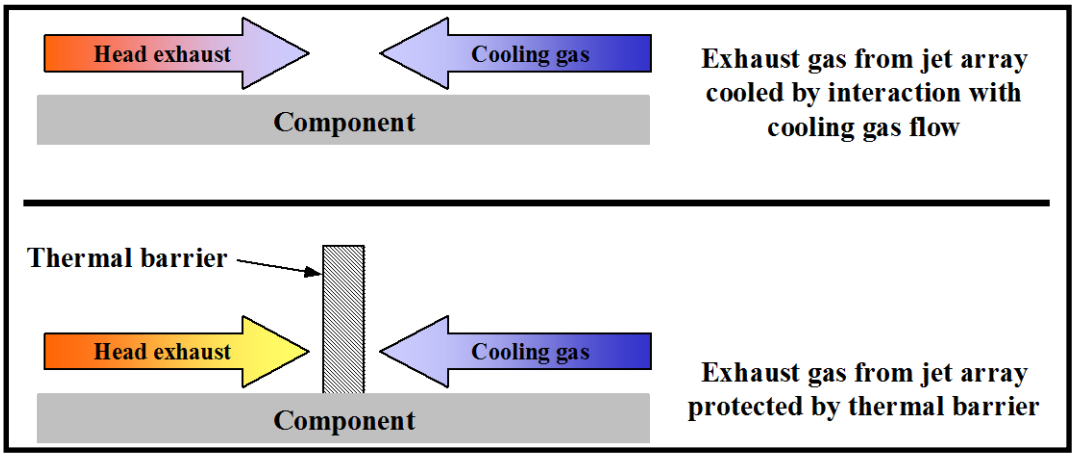


Figure 7-23 : Diagram highlighting the influence of the cooling gas on head exhaust temperature and therefore component temperature (top), and the use of a thermal barrier to reduce the interaction.

Initially, some tests were conducted to observe the effect of providing a physical barrier between the cooling gas flow and the exhaust flow from the head unit (shown schematically in Figure 7-23). The first attempt was to place some insulation material between the head unit and the cooling gas in the proximity of the central thermocouple. Once it was established that this had the desired effect then a larger piece of material was cut to stand along the whole length of the head unit. Cut-outs were made in the barrier to allow the thermocouple wires to pass out

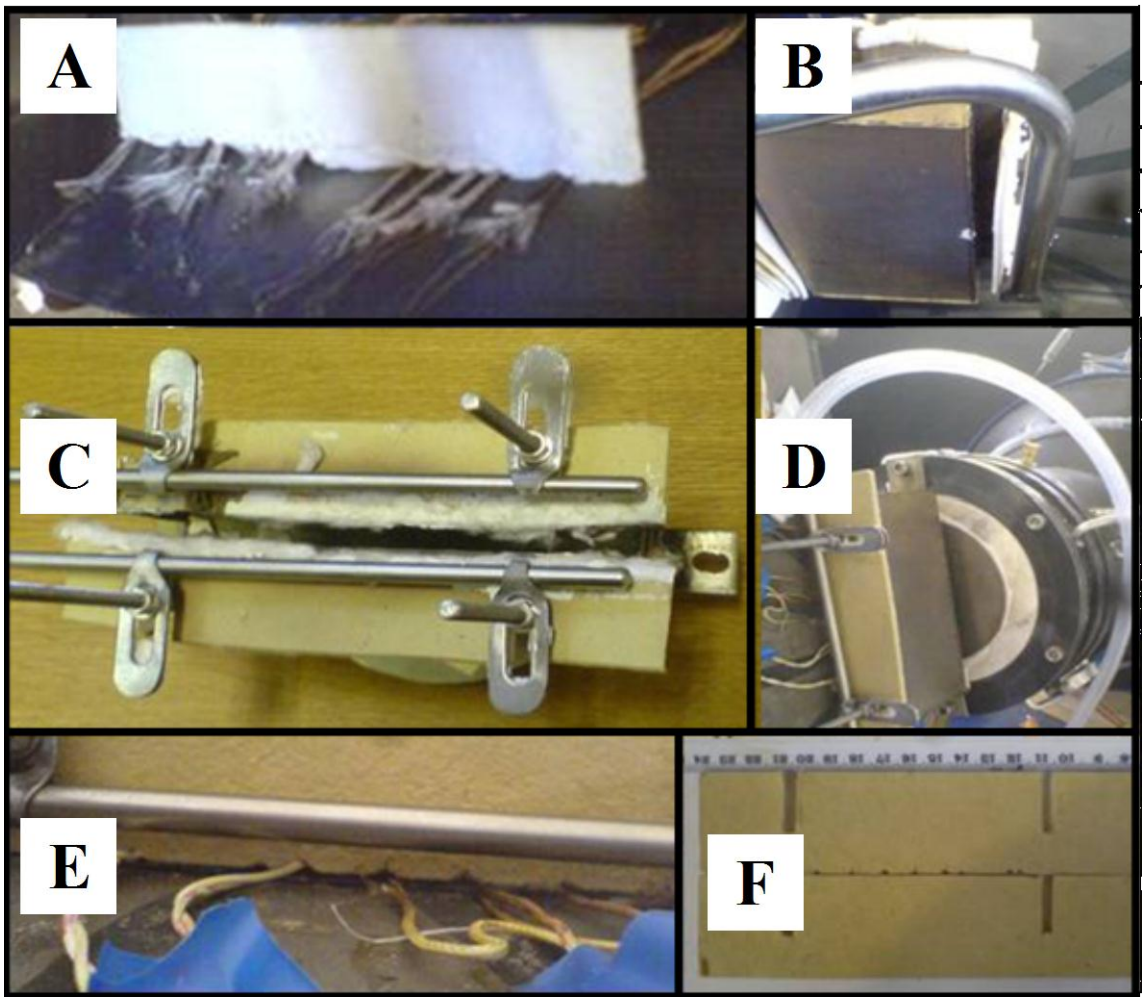


Figure 7-24 : Various methods of cooling gas blocking, A-B are pieces of insulation material cut and stuck into position on the blade. C-F are high temperature, high density fibre board cut to shape and held in position on the cooling fixture. *Note: Oxidation on surface due to tests not being conducted in an inert atmosphere as would be the case in a final local heat treatment solution.*

of the heated zone.

This trial proved the principle and allowed further testing to be conducted providing a more robust solution. Figure 7-24 (above) shows the various configurations with used in an attempt to block the cooling gas flow. Photographs A and B show a piece of insulation bonded to the test piece to provide the best possible seal around the thermocouples. This proved to be successful although it is not a sustainable solution as bonding to an actual part is unacceptable. Photographs C-F show an alternative solution involving the use of high density fibre board to prevent the cooling gas-flow entering the head unit. Photographs E and F show the small cut-outs in the board to allow the thermocouple wires to exit the head unit and lay along the test piece surface. This method proved effective but required accurate alignment of the board and the thermocouple wires. Photograph C shows the use of a softer insulation material attached to the base of the fibreboard to provide close fitment to the wires by conforming to the changing surface geometry. This had the added benefit of providing a soft surface to prevent damage to the test piece surface. Another trial involved re-routing the thermocouple wires along the leading edge of the test piece so as to not interfere with the blocking piece. This provided similar results to the solution shown in photograph C.

7.4.1.4 EXPERIMENTAL RESULTS

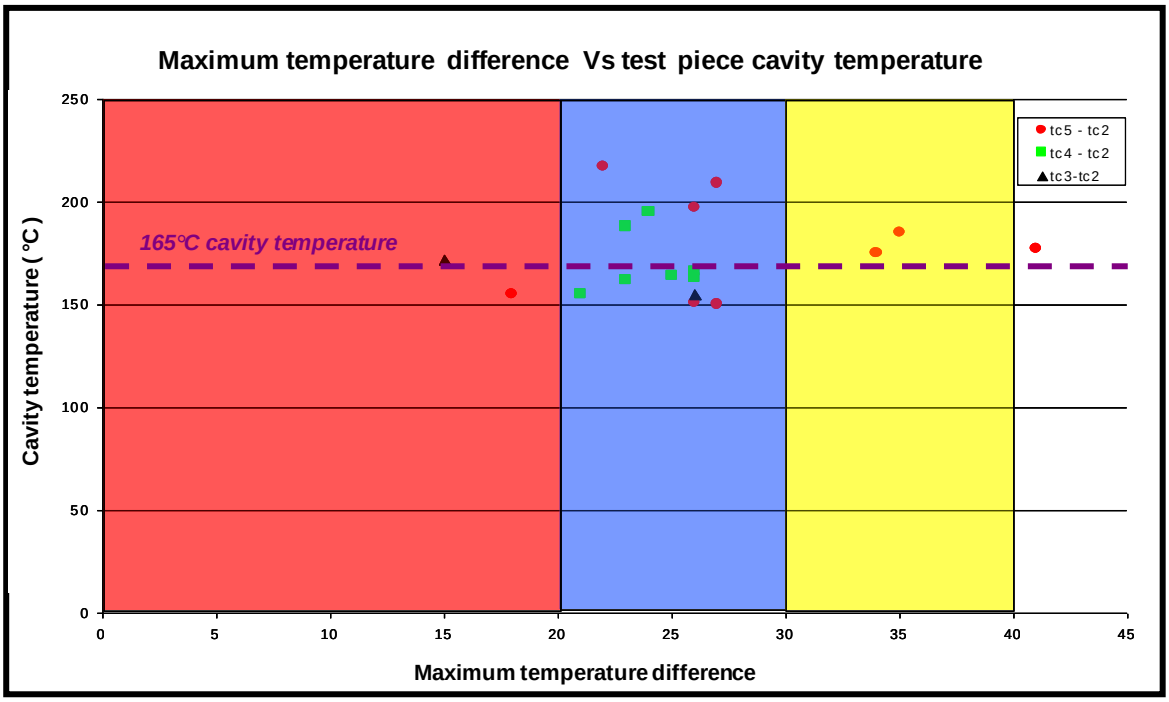


Figure 7-25 : Temperature difference (magnitude) Vs cavity temperature

This section presents the results of the trials conducted on the test piece shown previously in Figure 7-21 containing a thermocouple in its central cavity. Figure 7-21 also shows the relative positions of the welded thermocouples used to monitor the heated region.

Figure 7-25 above highlights the relationship between blade cavity temperature and the temperature difference within the heated zone. The graph details the maximum temperature difference recorded during the soak period of the heat treatment trial. During the tests the highest temperature was located at Tc2. The different colours and shapes of the points in Figure 7-25 represent the different thermocouples that recorded the lowest temperatures (and therefore resulted in the largest distribution) during the tests. Solid red circles represent the heat treatments where tc5 was the lowest temperature, and black triangles where tc3

was the lowest value. It has been stated previously that a conventional furnace (e.g. a vacuum furnace) should be controlled to within +/- 10ºC at temperatures above 500ºC (for titanium). This would allow a 20ºC temperature difference to exist across the heat treatment zone (signified by the red region in the graph).

Generally thermocouples tc5 and tc4 show the lowest temperatures. Tc 5 is located at the bottom of the heated region and is significantly affected by the heat sink effect of the large mass located at the base of the test piece. The large spread of data is due to the various combinations of jet hole blocking, heat treatment head unit positioning, and development of the cross-flow inhibitor. The purpose of these trials has been to determine what is achievable in relation to test piece cavity temperature and heat treatment temperature distribution.

The points representing a cavity temperature less than 165ºC are observed clustered around 18-28ºC for the temperature distribution. These are the values obtained with the optimum setup and show that a value of 18ºC is achievable with a cavity temperature of around 155ºC. However, it is very difficult to achieve this situation and the data suggest increasing the temperature limits to +/-15-20ºC would allow the heat treatment of the desired region whilst the cavity remained at around 150ºC. There appears to be an anomalous result showing a temperature distribution above 40°C, this was due to a positioning inaccuracy between the test piece and head unit were re-introduced.

Figure 7-26 was generated from a number of tests to assess the effect of cooling gas flow rate (blue line) on cavity temperature (solid black line) and highlights the

strong relationship between the two. Reducing cavity temperature increases the temperature gradient to the heated region.

The fluctuation observed in Figure 7-26 is due to the flow rate being altered throughout the tests. In order to provide more validity to the effects seen due to flow rate fluctuations, the flow rate was not increased in a steady manner. Instead when the flow rate was increased (and an associated reduction in test piece cavity temperature noted), the flow was dropped again to prove that the core temperature would then rise once more.

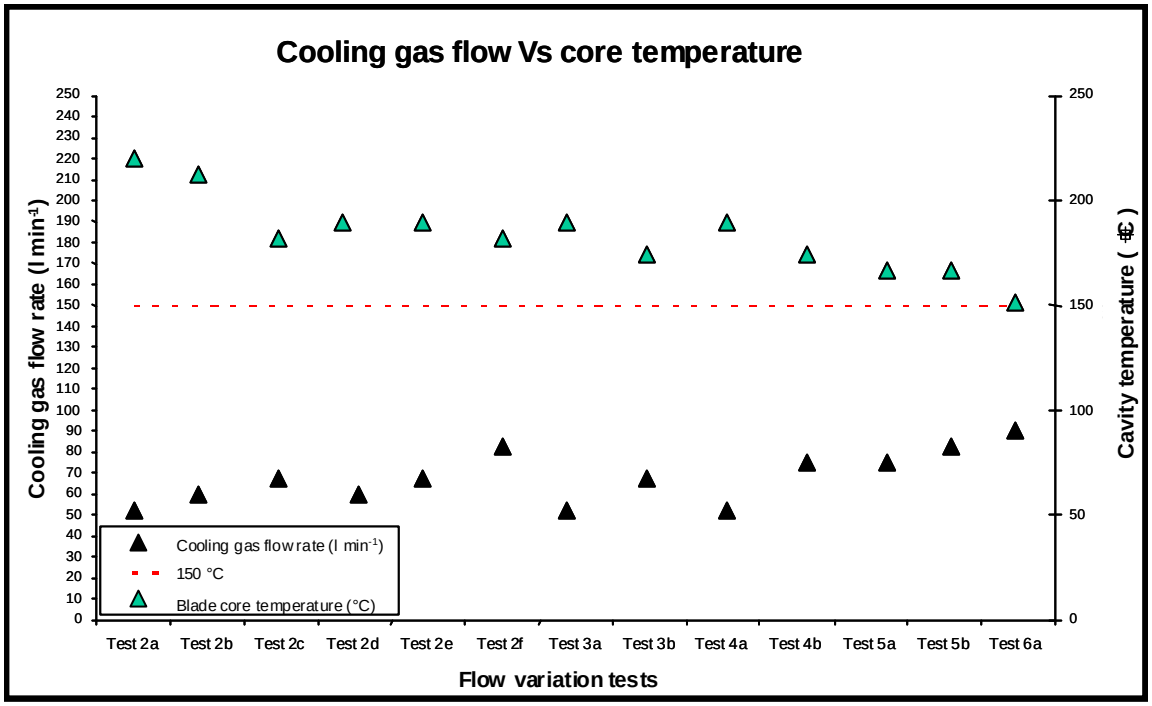


Figure 7-26 : Cooling gas Vs cavity temperature

7.4.1.5 DISCUSSION AND CONCLUDING COMMENTS

The outcome of this feasibility study is that it is possible to locally heat treat a large test piece containing a temperature sensitive region to 600ºC while maintaining the cavity at ~150ºC. Many low weight, high strength rotating components in aero-

engines are likely to contain cavities with polymer-based damping materials that are limited to temperatures between 150-200°C.

With the setup described in this section, 600ºC +/-10ºC is achievable, but not in the whole under-head region (defined as region A in Figure 7-21). The data presented here suggest a small region (shown as region B in Figure 7-21) could be held at 600+/-10ºC whilst maintaining the cavity temperature at around 150°C with appropriate cooling. However as Figure 7-25 shows this is not achievable repeatedly. If one could relax the temperature limits then a larger region (region A) could be heated to a temperature of 600C +/-15-20ºC with a high level of repeatability. Closer control of the alignment between the head unit and repair region would also help to eliminate the points that lie outside the +/- 20C region of Figure 7-25.

8 EQUIPMENT - PROTOTYPE SYSTEM DEVELOPMENT

The elements described previously in section 6 were built into a demonstration rig for controllable and repeatable heat treatment of a demonstration component (section 9) for the validation trials (section 13.2).

8.1 SYSTEM DESIGN

Any component requiring heat treatment will have different manipulation requirements in terms of loading, unloading and presentation of the heater and head to the appropriate position. The concept of the prototype demonstration rig was to keep manipulation simple so as to mitigate the risk of contact with the test piece (potentially causing damage and an associated reduction in fatigue life). This prototype system also allowed assessment of the feasibility of manufacturing a simple argon box structure to reduce the oxygen levels within the vicinity of the component.

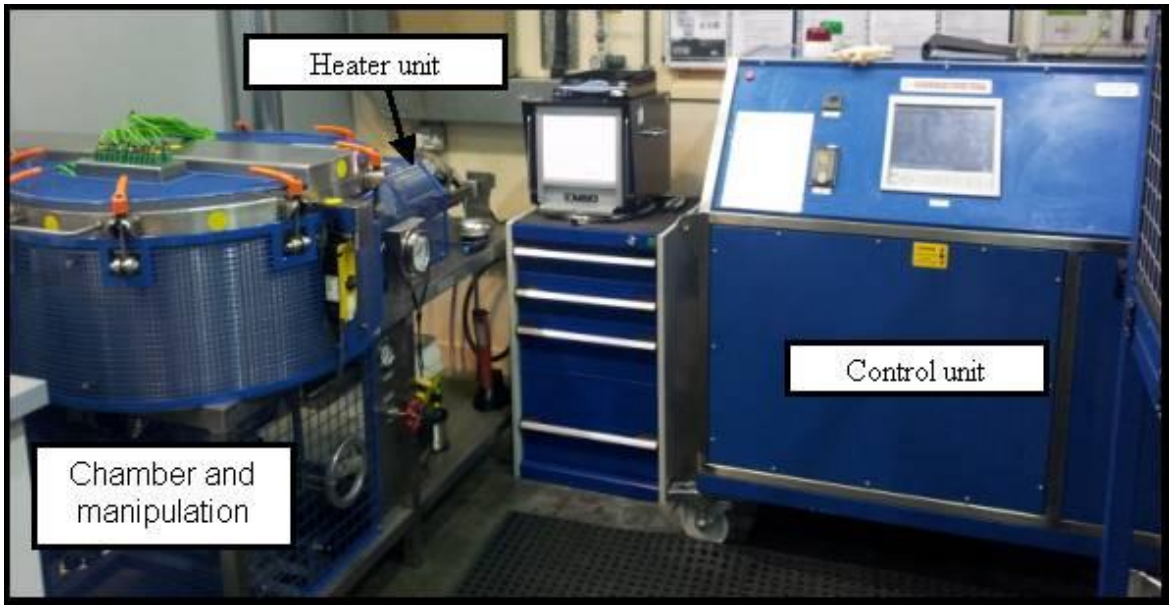


Figure 8-1 : Photograph showing all the elements of the localised heat treatment system together as used for experimental work detailed within this thesis

8.2 PROTOTYPE SYSTEM – OVERVIEW

Figure 8-2 shows the development rig incorporating a chamber to minimise oxidation and alpha case formation during heat treatment of titanium alloys. The system also allows one to process individual test pieces and has the capability to reach the tip and leading edge of a blisk. The manipulation principle involves rotation to move the component through each of the test piece positions (movement A on Figure 8-2). The heater and head unit can then be moved on and off the blades in the axis parallel to the stacking axis of the blade (movement B in Figure 8-2). The basic principle to move from one blade to another is to slide the heater and head unit off, then rotate to the next test piece. This can be done without removing the lid and thus negating a further purge of the system with argon.

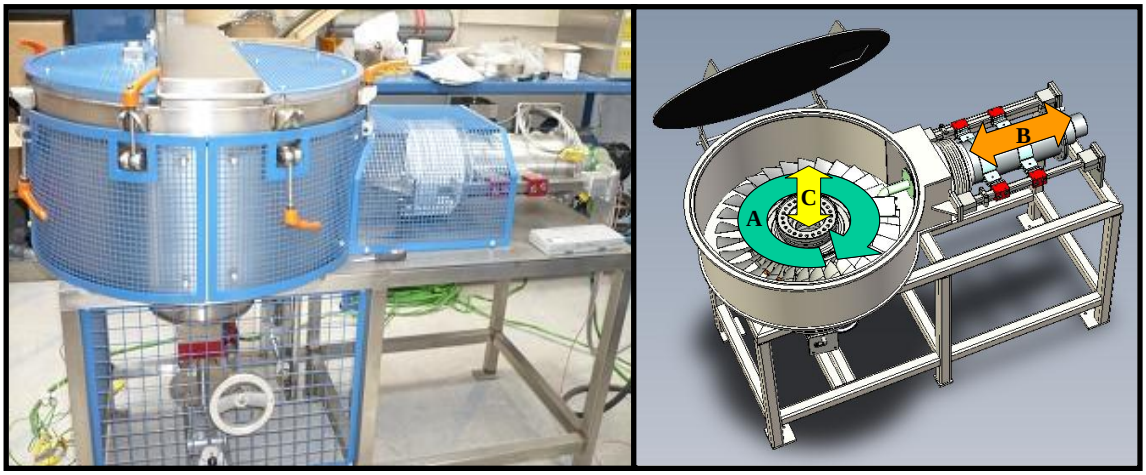


Figure 8-2 : Prototype local heat treatment system, with manipulation axes shown (right)

The use of this approach allows all geometric relationships between the heater, head unit and the aerofoil to be defined and finalised in the optimised design. Moving the heater in one horizontal plane and incremental rotational movement of the test component means that every individual leading edge (or tip, depending

upon head unit) can be heat treated with only one initial system setup. The blisk only needs to be loaded into the system once, minimising the risk of handling damage and reducing the potential for contamination.

The chamber itself generates a reduced ppm of oxygen in comparison to processing in air. The use of a high throughput of hot argon gas is a key departure from conventional heat treatment processing. The actual ppm of oxygen was observed throughout testing to be between 10-100ppm[§§§] and the component will need to undergo a precautionary alpha case removal process as though it has been processed in air. The cost and complexity of producing a chamber with the parts per million oxygen levels similar to those found in a conventional vacuum furnace precludes its use in this project. The objective of building this system is to allow assessment of the capability of the local heat treatment system with respect to applying it to the components in a repeatable manner.

[§§§] Operating the system with no heat or component within the chamber, and after calibration of the oxygen analyser, a measurement of 10ppm of oxygen was recorded.

8.3 KEY SYSTEM DESIGN FEATURES

A number of aspects of the system were designed using best practice principles wherever possible, with the intention of reducing the oxygen level within the localised atmosphere. The following points detail the main system design aspects;

8.3.1 ROTATION AND MANIPULATION EXTERNAL TO THE CHAMBER

The manipulation of the heater is via guide rails and a heater support structure. This allows the heater to be moved along its central axis on and off the aerofoil between heat treatments (movement B in Figure 8-2). The second manipulation is rotational through the axis running down the centre of the Component (movement A in Figure 8-2). This rotational movement allows the component to be incremented from test piece to test piece. Movement is performed through the use of a gearbox acting on a shaft into the chamber. The shaft is attached to the base of the rotation plate which in turn has the component fixture bolted on to it. The

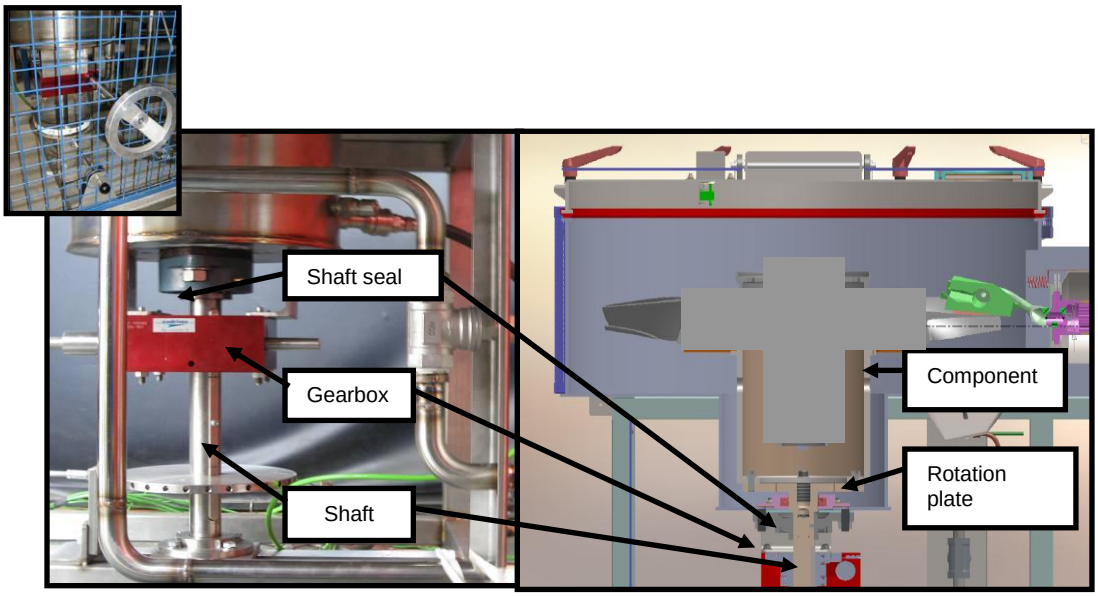


Figure 8-3 : Prototype manipulation system

shaft runs inside a lip seal that helps to reduce the passage of oxygen into the chamber. A slight positive pressure (10-15mbar) within the chamber helps to keep this seal in contact with the shaft during system operation.

The gearbox and associated interface are located external to the chamber in order to reduce the number of components within the reduced oxygen atmosphere, sealing is around the shaft. The location of this rotational manipulation external to the chamber allows the heat treatment to be applied to adjacent test pieces without the requirement to open the chamber lid.

8.3.2 BESPOKE BELLOWS ARRANGEMENT TO SEAL AROUND HEATER

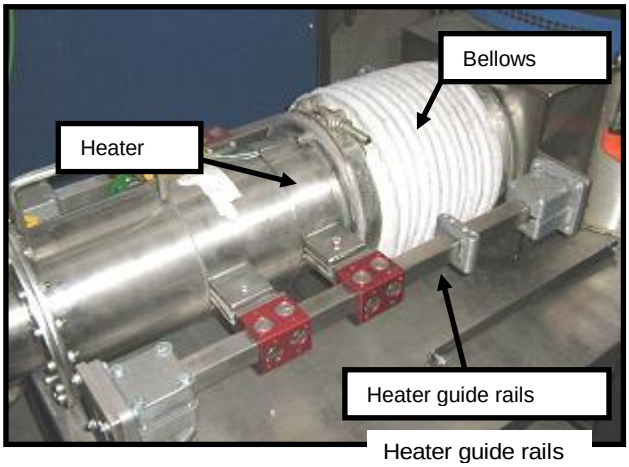


Figure 8-4 : Heater guide rails and bellows

Included within the system are flexible bellows between the heater and the walls of the chamber/manipulation cell. These bellows are required in order to maintain a seal between the heater and the chamber whilst allowing the heater to move along its axis and place the head unit on and off the test piece. This bellows arrangement locates on a machined surface on the chamber and a machined flange on the outside of the heater unit. The machined surfaces maintain the best possible seal to prevent oxygen ingress. The bellows are a fabric construction coated in silicone rubber making it gas and moisture tight.

There are limitations surrounding the use of bellows in this particular application, the convoluted shape of the bellows is required in order to allow sufficient extension. However it provides potential sources for trapping oxygen during the gas down phase. This effect could be significantly reduced by actuating the heater in and out of the chamber during the gas-down phase to aid mixing and thus displacement of the air from these trapped regions. A trickle feed of argon gas could be introduced in to the vicinity of the bellows to further displace any air trapped within this region. Finally, the temperature limitations of using silicon rubber mean that this part of the system must be positioned far enough from the hot gas exhaust to prevent thermal damage.

8.3.3 PRESSURE REGULATOR AND EXHAUST SYSTEM

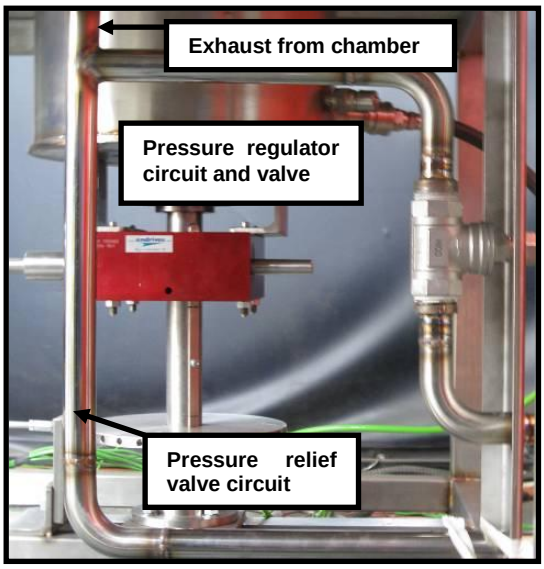


Figure 8-5 : Chamber exhaust system

The exhaust of gas from this system is through an external pipe network located at the base of the main chamber. The exhaust gas passes through a pressure regulator as it exists the chamber. This valve can be manually adjusted to maintain 10-15mbar of pressure. A small positive pressure is required in the system to prevent air ingress. Also, it allows one to maintain a low operating pressure when flow rates are significantly changed. For example, it could be favourable to have the gas down portion of the cycle at a high flow rate, so as to allow a quicker gas down and a larger throughput of argon in a shorter time. This transition from high flow rate (in the gas down) to lower flow rate (for processing) may result in a pressure change. This could be detrimental to the effectiveness of the sealing arrangement. Manual adjustment of the pressure regulator acts to mitigate this. Although argon his a higher density than air (see Table 11-1 and Table 11-3 later), the larger throughput of argon (~150 l min^{-1}) during operation means that it is unlikely to settle out with the air resting at the top. In future O_2 measurements should be made in various regions of the chamber during heat treatment in order to confirm that O_2 levels in the chamber are consistent.

8.3.4 THERMOCOUPLE TERMINAL POINTS

A number of thermocouples are required within the system for validation purposes. A gas-tight termination point is required for these thermocouples and is achieved by using an olive connection to produce a gas tight seal around the wires exiting the chamber. Passing all the wires out together within one group minimises the number of holes in the chamber.

8.3.5 OTHER KEY SYSTEM FEATURES

Gas down sequence - Generally, when processing components in this system it was purged for a total of one hour, at a total flow rate of 125 l min^{-1}. This represents a total argon volume of around 10 times the volume of the chamber in order to achieve a depleted oxygen level within the system.

Lid clamping - The circular lid has equally spaced clamps around the circumference (Figure 8-6). These clamps are hand tightened using a ratchet mechanism within the handle.

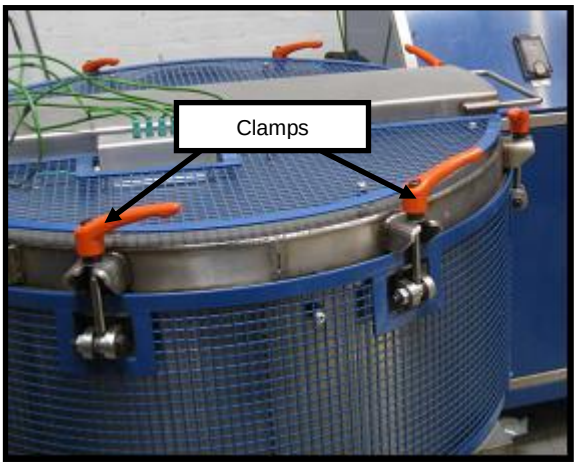


Figure 8-6 : Lid clamping

Oxygen analyser – The system uses a Cambridge Sensotec Radipox 3100 oxygen analyser, to monitor the levels of oxygen present during processing. Currently the oxygen analyser takes a feed of gas from the exhaust region, positioned directly below the head unit. The intention

is that this should be representative of the oxygen level within the head unit (and thus the oxygen level experienced by the test piece).

8.4 ATMOSPHERE STUDY - ALPHA-CASE EXAMINATION

As described previously the formation of a brittle oxygen enriched alpha phase can result after heating titanium in the presence of oxygen. However, the specific temperature at which alpha case forms is unclear. Temperatures above 470°C (in air) produce observable levels of alpha case on titanium 6-4 [122]. Oxygen enrichment of the surface is a diffusion-based process affected by time, temperature, and availability of oxygen. The majority of data regarding alpha case depths presented in the literature (section 2.5) was conducted at higher temperatures and for longer time periods than would be used for a titanium 6-4 stress relief heat treatment cycle (typically 1-2 hours at temperatures of between 550-700ºC). The following study assesses the microstructures of test pieces heat treated using the gas jet impingement system desribed in secion 8.

8.4.1 TESTING PROCEDURE

Two different test pieces were heat treated to 600ºC for 1 hour. The heat treatment cycle was very similar to that shown in Figure 9-15 and the oxygen levels recorded during the heat treatments were 50 and 10ppm for a titanium 6-4 plate (Figure 8-9 a) and titanium 6-4 aerofoil test piece (Figure 8-9 b) respectively. After heat treatment the test pieces were sectioned using a Brilliant precision cut-off saw. Flood coolant was employed to prevent test piece overheating. Sections were taken for a number of positions with care taken to section through areas of significant surface discoloration (oxide). Standard titanium metallographic preparation procedures were used to produce polished micro-sections. Automatic grinding and polishing wheels were used to provide even pressure when removing

material. Careful inspection of the micro-section was performed in order to detect any evidence of alpha-case or surface micro-cracking. The samples were then viewed using optical and scanning electron microscopy (SEM) with backscatter facility to assess the extent of any alpha case present.

8.4.2 LOW TEMPERATURE (<200°C) REGIONS

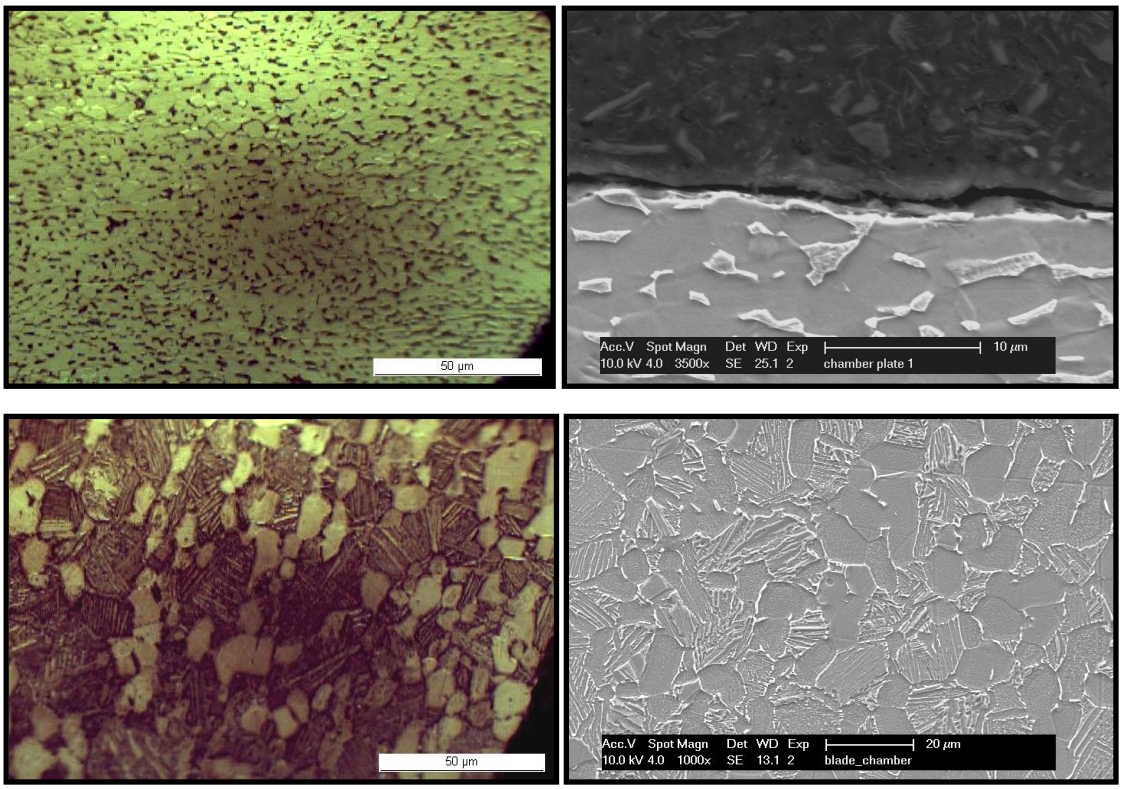


Figure 8-7 : Micrographs showing microstructures of titanium 6-4 plate (top) and component (bottom)

Figure 8-7 shows the microstructures of two test pieces. These images are taken from regions which saw only moderate temperature (<200ºC, measured with thermocouples welded onto the surface of the test piece) and which experienced no visible discoloration of the surface due to oxidation.

The top images in Figure 8-7 are characteristic of those that have undergone hot-working followed by annealing to create a microstructure consisting mainly of α with a fine dispersion of retained β and Widmanstätten α (darker phase). Evidence of the structure of the Widmanstätten α can be seen within the whiter phases on the SEM image on the right. Some directionality is also evident due to the rolling operations used to form the sheet.

The bottom mages in Figure 8-7 are characteristic of material that has undergone hot-working and annealing followed by heating to the $\alpha+\beta$ field (~940ºC) to produce large a volume fraction of β before water quenching to produce α' martensite. This is then followed by a further rise in temperature to precipitate equiaxed primary alpha grains (white regions). The smaller α grains and martensite structure help to reduce crack propagation rates [45] whilst the high level of retained β provides higher strength.

8.4.3 HEAT TREATED REGIONS

Walker in the commercially restricted report [123] defined an equation for the depth of alpha case penetration in IMI834 forged material by demonstrating experimentally that oxide growth follows a parabolic growth mechanism. Walker also noted its applicability to any commercial titanium alloy.

Using the equation in [123] for a one-hour heat treatment in air at 620ºC yields an oxide depth of 1.2µm, representing a worst-case scenario in terms of alpha-case depth for these test pieces. The image below (Figure 8-8 (a)) shows a test piece that has undergone heat treatment in air; one can see the continuous alpha case layer present at the edge of the test piece. Figure 8-8 (b) shows a test piece following heat treatment in a vacuum furnace and has no evidence of alpha case formation on the surface.

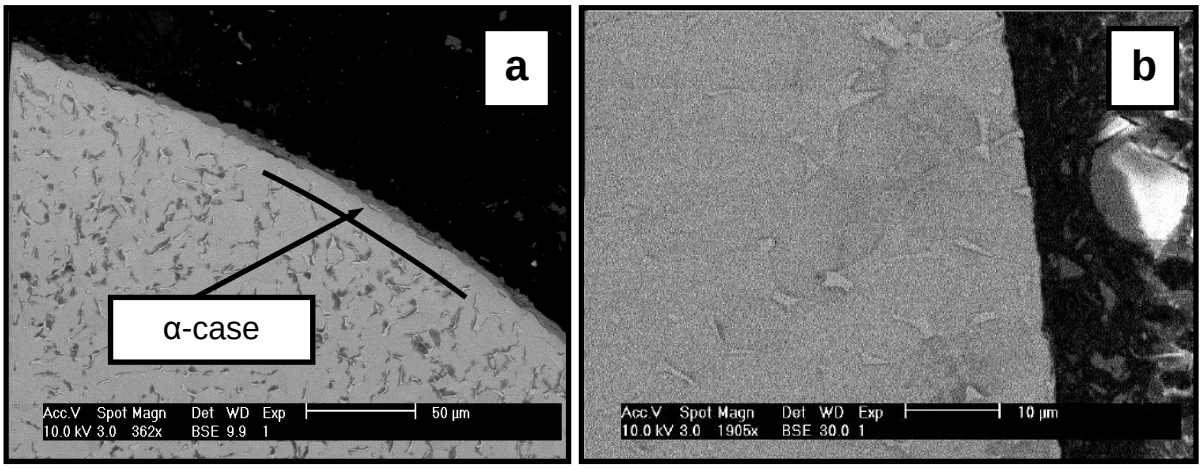


Figure 8-8 : Micrographs showing air furnace test piece with alpha case at the surface (a) and vacuum heat treated component with no alpha case (b)

The local heat treatment system uses argon as a process gas and the oxygen levels are monitored and maintained at low levels during processing. Therefore, the alpha-case levels one would expect to see on the component would be somewhere between those in Figure 8-8. However due to the relatively low temperature and short time that the material is heated it is considered unlikely that significant alpha case (i.e. comparable to that seen in air) would be found on the test pieces (air contains 20% oxygen, whereas argon gas <5ppm oxygen [48]).

Figure 8-9 shows two test pieces after heat treatment, the titanium 6-4 plate and the aerofoil test piece. Note the differences in appearance of the two test pieces post heat treatment. There is a well defined jet pattern on the plate, whereas the blade has a consistent bluing across the heated region.

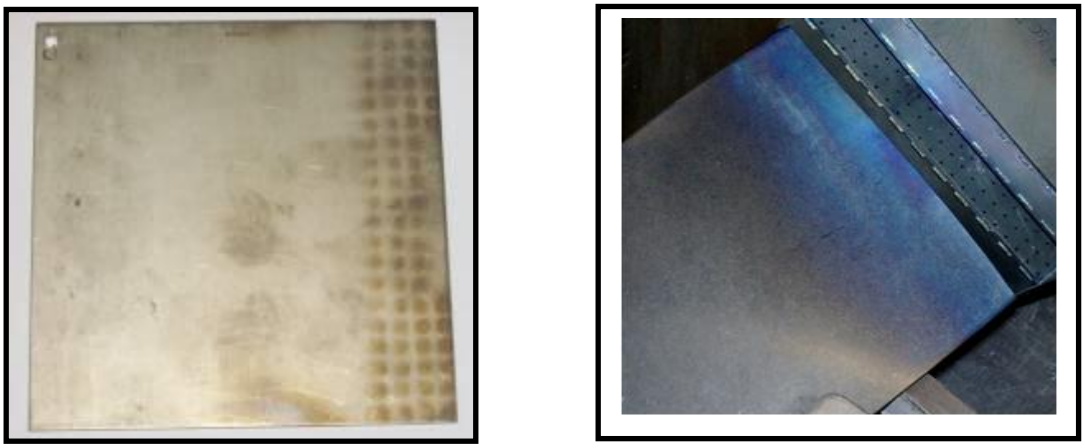


Figure 8-9 : Alpha case test pieces, plate (left) and component (right). Both processed with head RPDG000292, at a flow rate of 120 l min^{-1}

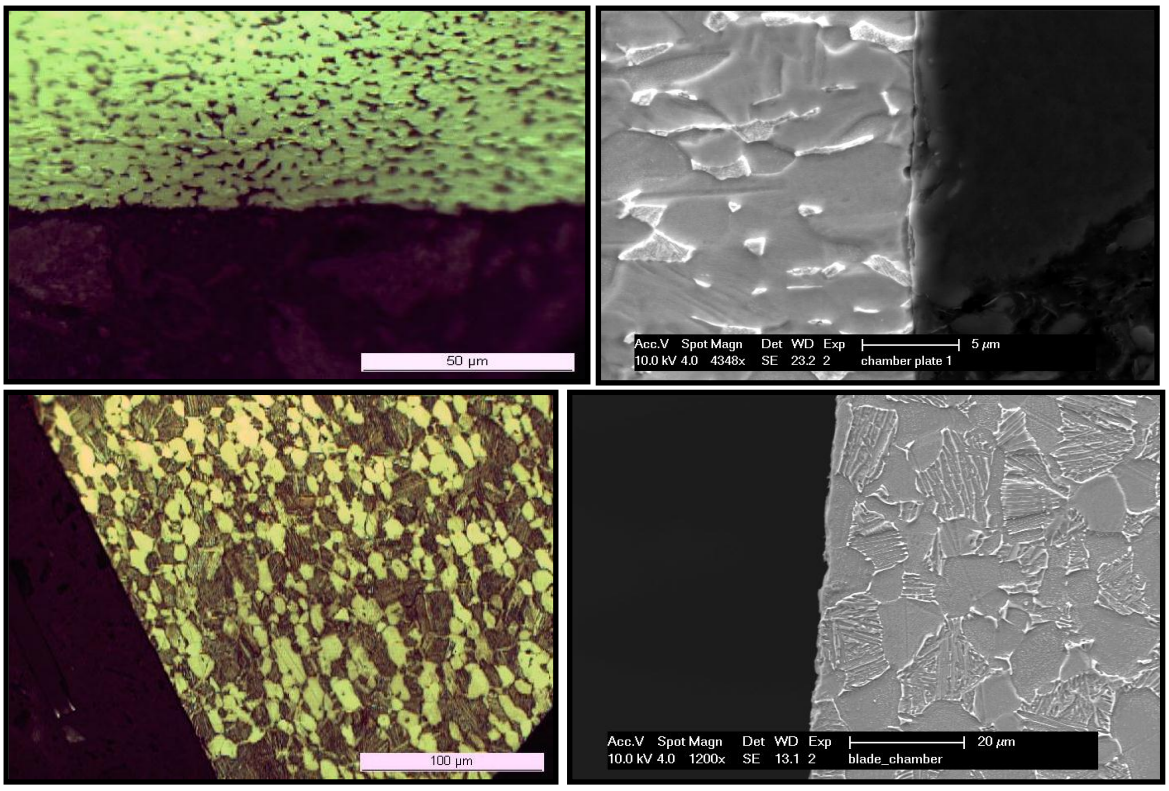


Figure 8-10 : Micrographs showing the post heat treatment microstructures of the plate (top) and component (bottom)

Figure 8-10 presents micrographs of the test piece edges in the regions which saw the highest temperatures and most significant oxidation. These images are representative of what was seen across all the test piece micro-sections and shows no evidence of alpha case present on the sample. Particularly of note is the retained β present right out to the edges of the test piece in both cases with no signs of a continuous band of alpha case or interlinked alpha grains along the surface. The general appearance of the microstructure also appears to be unchanged when compared with the images in Figure 8-7.

Although no alpha case has been detected on these samples it does not mean that there is conclusively no alpha case present on the surfaces, only that any

present is below the levels resolvable through microscopy. There are other methods of detecting oxygen absorption in titanium (as used by Dong *et al* [124]), such as microhardness profiling and measuring of weight differences in samples pre and post heat treatment. However, these methods are more appropriate to samples where the oxygen enriched layer is visible to a significant depth (i.e. >100μm in the case of microhardness). Whereas in the case of weighing the samples this measures the total oxygen pick-up not necessarily the depth of alpha case found in the component.

8.4.4 ALPHA CASE FORMATION DUE TO LOCALISED HEAT TREATMENT

The results of this investigation suggest that the prototype argon chamber provides a sufficiently reduced oxygen atmosphere to prevent significant alpha case formation on components during a typical stress relief heat treatment cycle for a titanium 6-4 alloy component.

9 PROCESS - HEAT TREATING OF A BLISK

This section takes the basic concepts and apparatus presented in the preceding sections to develop and then demonstrate the process on representative component geometry. The target for this study was to heat the leading edge and tip of the component without over heating the root region. This work culminated in the heat treatment of the test pieces used for the component validation work detailed in section 13.2.3.

9.1 INTRODUCTION – THE COMPONENT

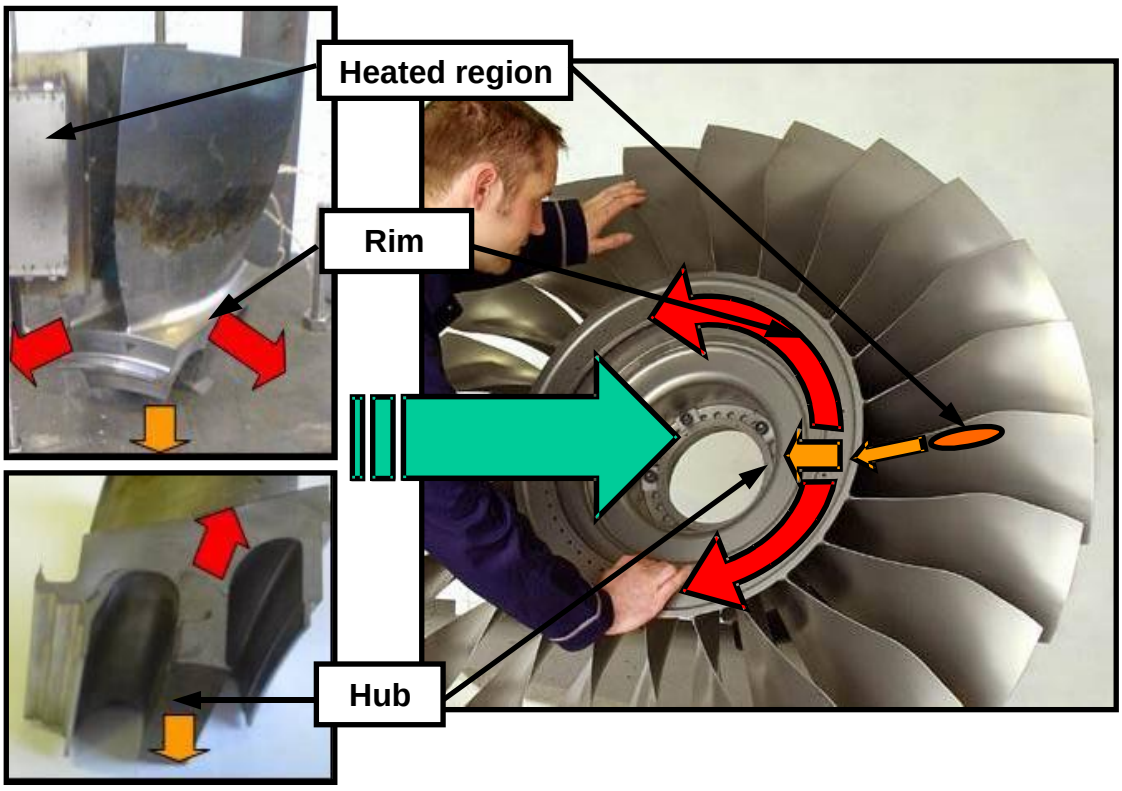


Figure 9-1 : Heat flow from the blade

Components such as those shown in Figure 9-1 are the target application of this technology. Previously the issues surrounding the effect of a heat sink attached to

the base of a test piece were highlighted (Figure 7-16). For these trials a component containing a heat sink was used to establish how much of an effect it has on achieving the desired heat treatment temperature. Figure 9-1 shows the aerofoil test pieces used, highlighting the various heat sink effects. Two regions (highlighted by the various arrows) provide heat loss from the blade through conduction; the largest cross sectional area is in the rim section (most noticeable in the bottom left image of Figure 9-1). A smaller area is evident towards the hub section (orange arrows).



Figure 9-2 : Test piece with limited heat sink, note exposed rim section

Due to limited component availability for these trials a test piece (see Figure 9-2) contained a disc section. However, most of the aerofoils and rim section had been removed. Therefore, the only conduction path to the disc heat sink is following the direction of the orange arrows through the hub.

The effect of these heat sinks is likely to be less pronounced when the tip of the test piece is heated, as this region is located furthest from the heat sink. The heated region is located approximately equidistant from the root of the aerofoil meaning the entire heated region will be acted upon by the heat sink in a relatively uniform manner. In the case of the leading edge repair the bottom of the heated region is positioned much closer to the root than the top of the heated region. Therefore any heat sink affect will manifest as an increase in the temperature difference across the heated zone.

9.2 THE APPARATUS

Figure 9-3 shows the experimental setup for the development trials detailed in this section. The main picture shows the common system elements and the insert picture highlights the slight configuration change in order to access the tip of the component.

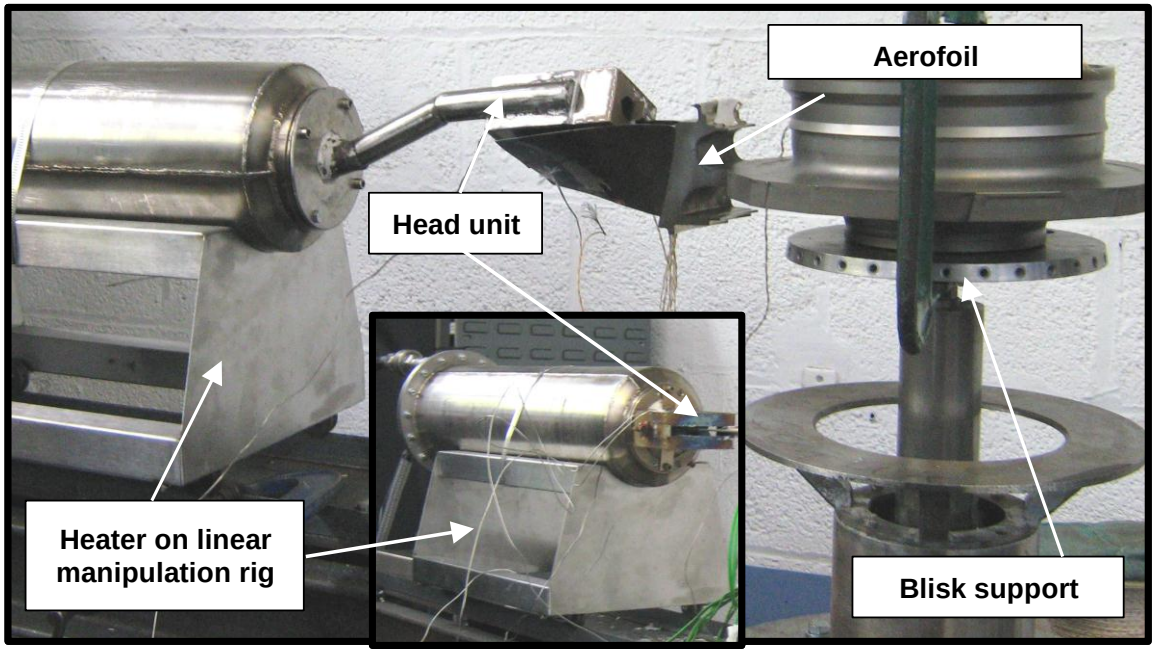


Figure 9-3 : Apparatus for the leading edge and tip head development trials, tip configuration inset.

9.2.1 QUANTIFYING THE HEAT SINK EFFECT

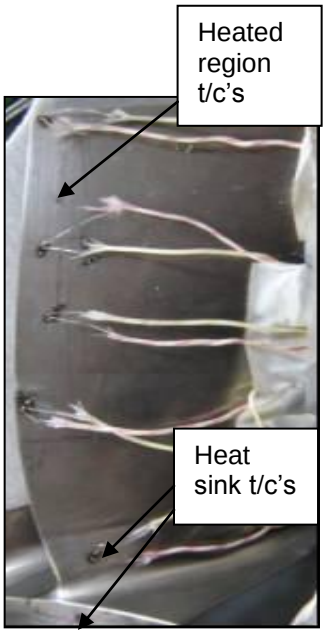


Figure 9-4 : Heated zone thermocouples

Ultimately in order to heat treat the aerofoils for validation, the final component will have all aerofoils and rim in position. However, to understand how representative the test piece in the form shown in Figure 9-2 is, a number of tests were performed. Firstly, the component was heated in the form shown in Figure 9-2 (i.e. with no extra heat sink attached), then with a large mass of steel clamped to the side of the rim (Figure 9-5). The temperatures were then measured close to the root of the test piece to assess the effect of attaching the heat sink (see bottom thermocouples in Figure 9-4). Two thermocouples were used, one on the test piece just above the annulus (in the thin section of the test piece) and a second on the rim of the component in the region of larger cross-section (heat sink). It is this temperature gradient, which will drive any conduction away from the aerofoil and reduce the temperatures in the heated region. Therefore, if these temperatures remain fairly constant and the difference between them does not increase significantly it is highly likely that the effect of an increased heat sink (e.g. a complete component) will not adversely affect the temperatures achieved in the subsequent trials.

The heat sink used was steel, which has a higher thermal conductivity than titanium. The two contact faces were flat and the clamp shown in Figure 9-5 was tightly applied to deform any significant asperities that may act to reduce contact area.

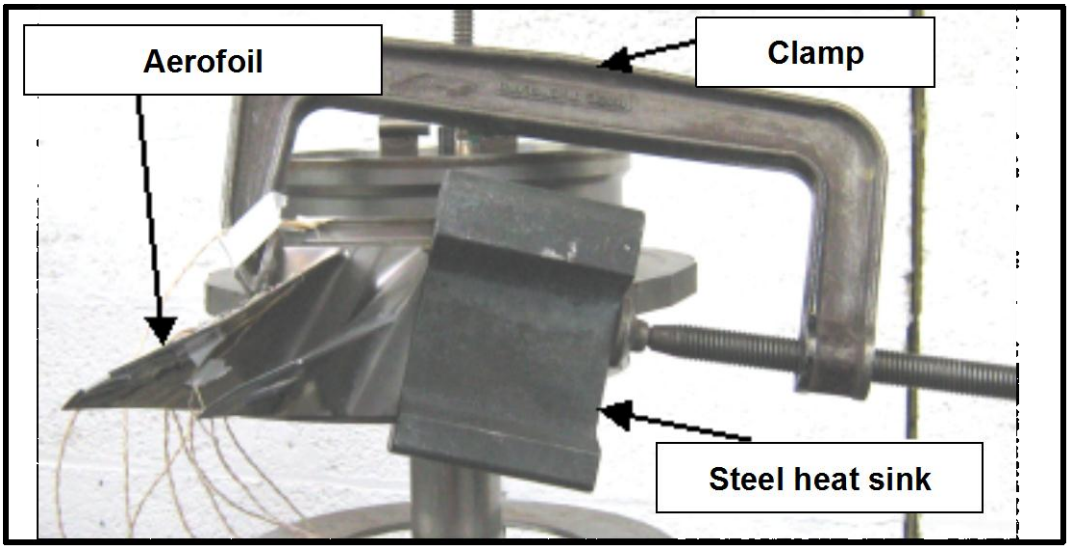


Figure 9-5 : Test apparatus used to test heat sink effect

9.2.2 HEAT SINK EFFECT - TRIAL SETUP

The position of the thermocouples welded onto the test piece is shown in Figure 9-4. Figure 9-5 shows the experimental set-up with the higher power density heater located on a track (linear manipulation rig). This provides lateral movement whilst maintaining the vertical position of the head unit relative to the test pieces. The component is located on a fixture to maintain its position relative to the heater and head unit. This setup allows the repeatable manipulation of the system with only lateral movement to position the heater.

In order to perform these trials, the flow rate and control temperature were kept constant. The following bullet points correlate with the legend in Figure 9-6 (below).

- **T1** – was a setup test and is therefore not included in the results.
- **T2** – This is the reference test completed with no heat sink attached.
- **T3** – Test with heat sink attached all other variables (flow rate, control temperature, apparatus relative positions) kept constant.
- **T4** – As T3 but the head unit had been moved to provide a slightly increased gap between the head unit and the test piece to minimise contact during heat treatment.

9.2.3 HEAT SINK EFFECT - RESULTS/DISCUSSION

Figure 9-6 presents the temperatures achieved with the setup described above at the two critical thermocouple locations (heat sink tc's in Figure 9-4). The grey bars represent the temperatures achieved just above the root radius of the aerofoil, and the white bars the thermocouple located in the rim of the test piece. T2 represents the temperatures with no heat sink and T3 and T4 are subsequent tests after the heat sink had been attached. These temperatures represent those seen in the soak region of the heating cycle, i.e. after the component had heated up and maintained a constant temperature in these regions. The error bars show the temperature variation in the soak portion of the cycle. This variation is due to

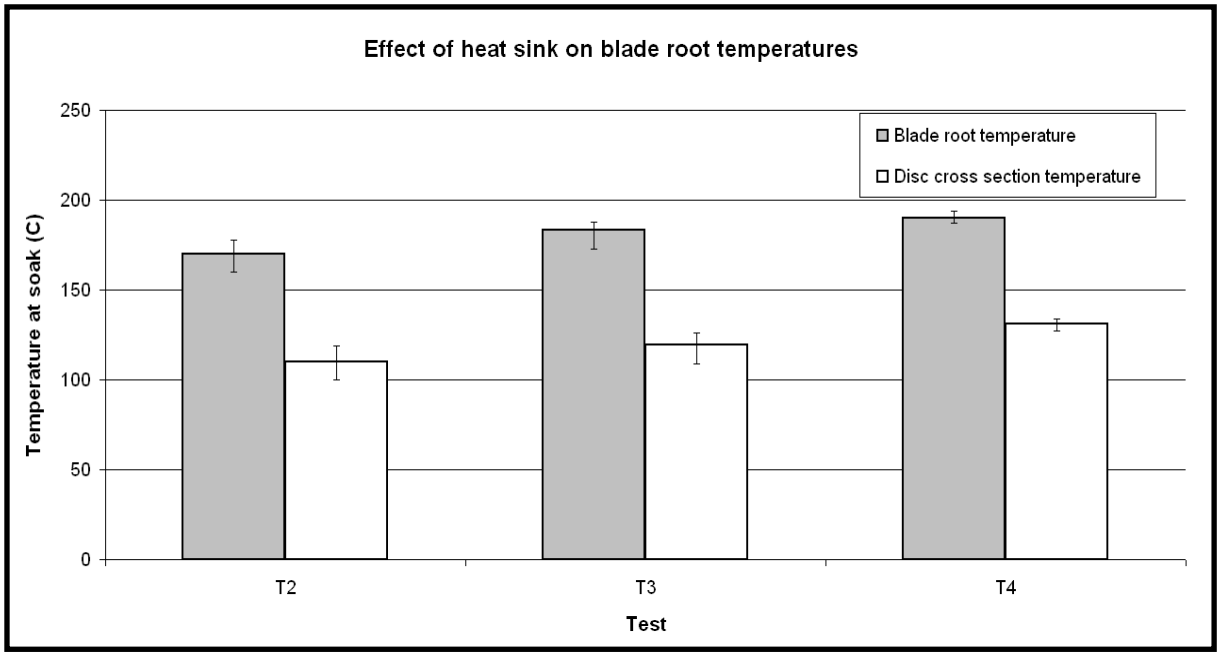


Figure 9-6 : Effect of heat sink on blade thermocouple temperatures

fluctuations in the gas temperature and that the heater was turned on and off by the control system to control the temperature at the value set.

The data presented in Figure 9-6 show no correlation between the addition of a heat sink and a significant reduction in temperature, or the difference in temperature between the two thermocouple locations. The temperatures actually rise between the tests due to the accumulation of heat in the system from the previous test. The temperature difference experienced between the two thermocouples varied from 59°C in T4 to 63°C in T3 showing that the temperature difference (the driving force for conduction from the aerofoil) does not change significantly with the addition of a heat sink. The temperatures presented in Figure 9-6 were measured close to the root of the test piece, and are in the range 100-200°C. However, it is worth noting that the temperature in the heated region had achieved 600°C (an appropriate heat stress relief temperature for titanium alloys).

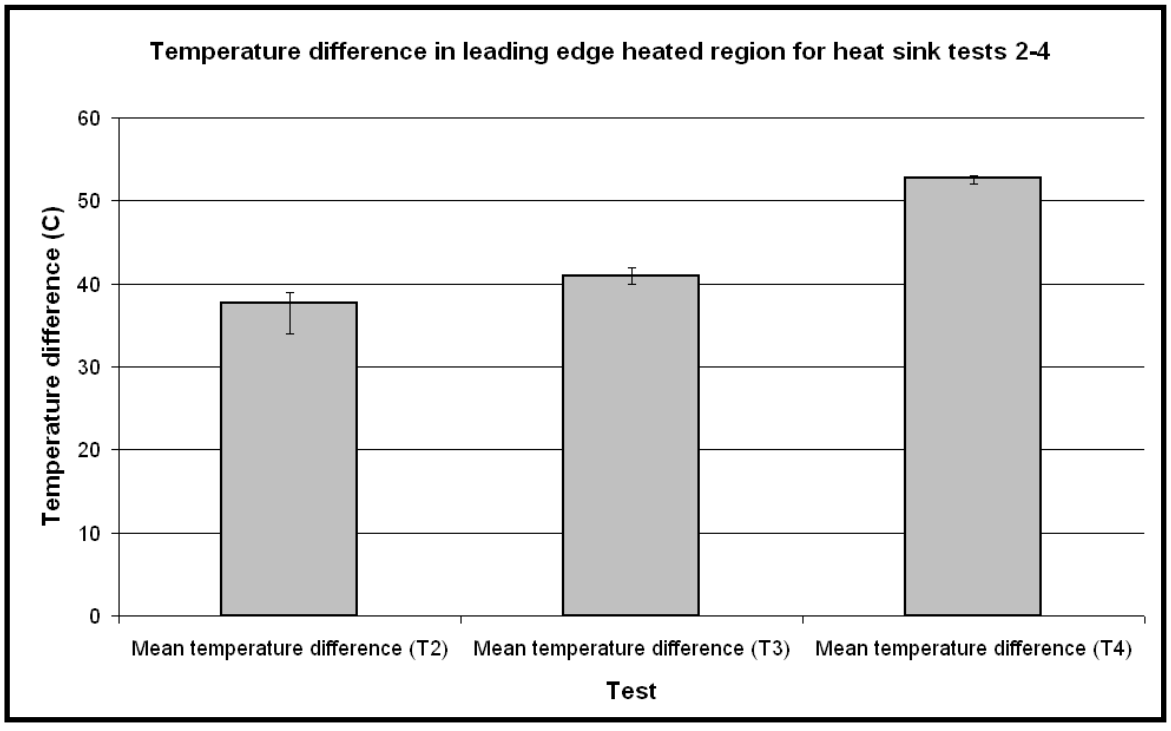


Figure 9-7 : Temperature difference variations due to heat sink attachment

Figure 9-7, highlights the temperature differences across the heated region (top four thermocouples in Figure 9-4) during the heat sink trials. One would expect adding a heat sink would significantly increase the temperature difference across the heated region. A slight increase was observed between tests 2 and 3, although this is only a few degrees and is more likely to be as a result of the retained heat in the tip from the previous trial. The tests demonstrated the highest temperature difference was in test 4, however this is due to the movement of the head unit between tests [****]. The temperature differences in Figure 9-7 are greater than the goal of +/-15°C. However, at this stage the temperature distribution in the heated region had not yet been optimised and these trials were purely to assess the effect of the heat sink.

9.2.4 HEAT SINK EFFECT – KEY OUTCOMES

The result of this experimental investigation provided evidence that when the leading edge of this test piece is being heated the effect of the disc section on the achieved temperatures is negligible. Therefore it is acceptable to use a component in the form shown in Figure 9-2 in order to develop the process, rather than having to use a rare and expensive complete component. The main conclusions from the experimental assessment into the effect of the disc heat sink on the heated region are as follows;

[****] Note the effect of head position on heated region temperature described in section 10.

- Root temperatures increased from tests 2 to 4 from 170°C to 190°C (Figure 9-6). This is due to the increased build up of residual heat in the component after each test.

- Test piece temperature distribution increased slightly with each trial (test 2-4). The increase between tests 2 and 3 was of the order of a few degrees. The larger difference between test 3 and 4 is as a result of the changing of head position between trials.

- A less pronounced heat sink effect than that anticipated was observed, as the cross section of the aerofoil is very thin. It is this cross-sectional area that governs the rate at which conduction can occur to the disc.

- Any heat sink effect is less pronounced than the effect of heat build up over time due to multiple heat treatments.

- Temperature distribution in the heated region is sensitive to head position.

9.3 ACHIEVING THE REQUIRED TEMPERATURE DISTRIBUTION

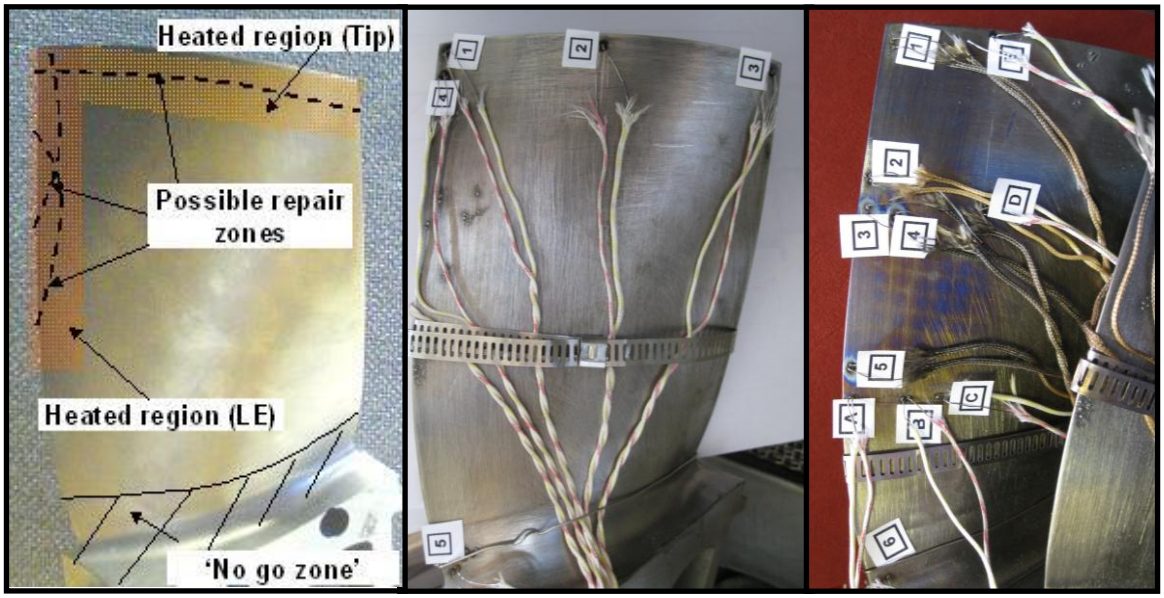


Figure 9-8 : Heated zones (left), tip thermocouples (centre), leading edge thermocouples (right)

Figure 9-8 shows the test piece to be used in the following trials. This section deals with the development of head unit configurations to achieve acceptable temperature distributions across the test piece in the tip and leading edge locations (show in the left of Figure 9-8). The location of these thermocouples is also shown in Figure 9-8, the tip in the centre photograph, and the leading edge is in the photograph on the right.

9.3.1 THERMOCOUPLE LOCATIONS AND THE REPAIR SIZE

Some of the thermocouples used for temperature measurement were outside the extremities of the repair, for example thermocouple 4 in Figure 9-8 was 2mm outside the repair. The heat-affected zones expected from the repair process are likely to be of the order of 0.5mm. It was necessary to ensure that the heated region from the process fully encapsulates the repair and that the system could allow for any distortion from subsequent processes. As a result, the size of the heated region (i.e. that defined as being within the target temperature +/-15°C) must be significantly larger than that of the repair to tolerate any variation from the intended geometry.

The positions of the thermocouples shown in Figure 9-8 define the extent of the region heated to a given temperature with a given temperature distribution. Thermocouple 6 in Figure 9-8 was used to monitor the temperature at the root of the test piece during heat treatment. The temperature attained by this thermocouple is primarily as a result of heating through conduction, however the effect of the hot exhaust gas from the head unit may be a factor. The temperature of thermocouple 6 gave a good indication for the root of the test piece and in the hub. However, although a much lower temperature was expected in the hub due to the significantly larger mass of this region (as demonstrated in Figure 9-6).

The following section details the specific challenges of heating the tip and leading edge locations of this component. The challenges surrounding the tip are

described first, followed by the leading edge. The issues of temperature distribution, repeatability, and head design are detailed.

9.4 TIP HEAT TREATMENT

The local heat treatment of the tip of the test piece presented the most significant technical challenge when attempting to limit the temperature distribution across the heated region. This was due to the thin section of the aerofoil tip, and the non-uniform nature of the cross section.

9.4.1 TIP HEAT TREATMENT - BLOCKED JETS



Figure 9-9 : Tip jet pattern

As discussed previously, blocking of the central jets in the head unit was necessary to reduce hotspots. In the case of the tip head it was determined through a process of hole blocking using ceramic adhesive (Figure 7-14). The result of this exercise was that the central 24 holes on both the top and bottom jet plate were blocked. Figure 9-10 (below) shows the temperature distribution that was achieved with this jet array. These data were taken from the soak period of the heating trial, and the experimental setup is the same as that shown in Figure 9-5. Tests 1, 2 and 3 on the graph were conducted to establish the repeatability of the temperature differences measured. In order to repeat the trials the head was removed and repositioned in order to simulate the operation of loading and unloading the component.

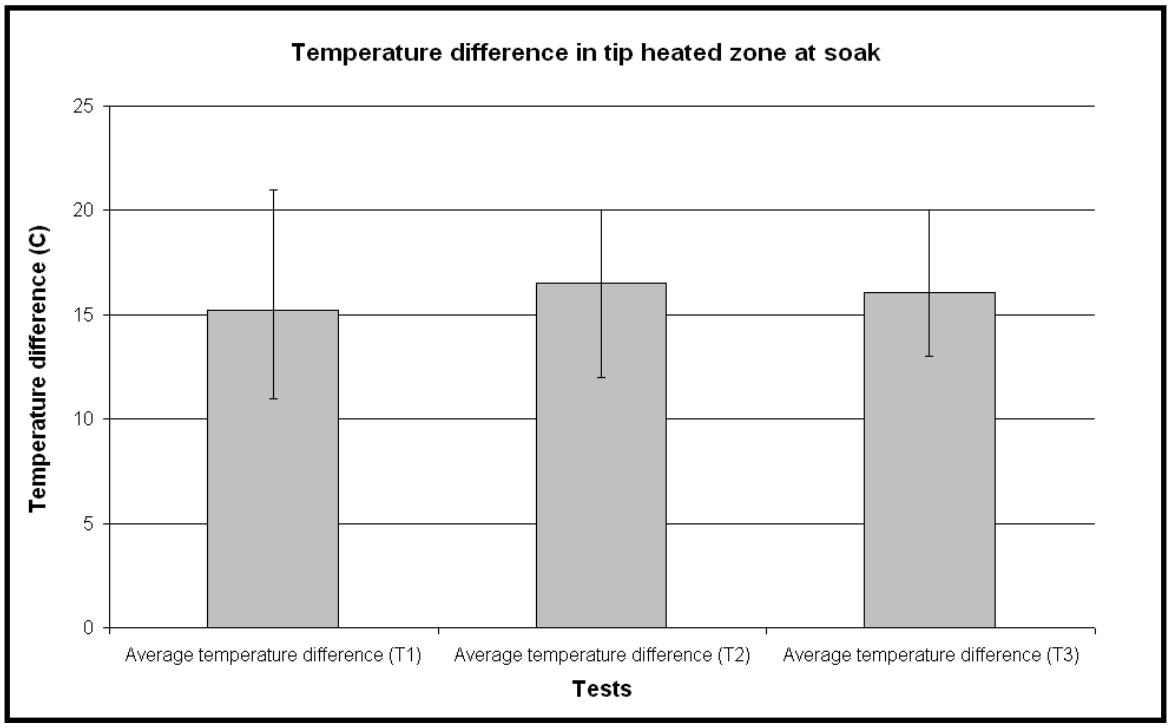


Figure 9-10 : Tip temperature distribution, all tests had a control temperature of 620°C and a flow rate 110 l min^{-1}

9.4.2 TIP HEAT TREATMENT - HEAD UNIT

In the design and manufacture of a head unit to heat treat the tip there were a number of factors that needed to be addressed and various improvements that were made in order to produce an optimised solution. The photographs below (Figure 9-11) show the comparison between the original tip head unit RPDG000195 (left) and the optimised design RPDG000292 (right). The main differences are described and discussed in the following paragraphs;

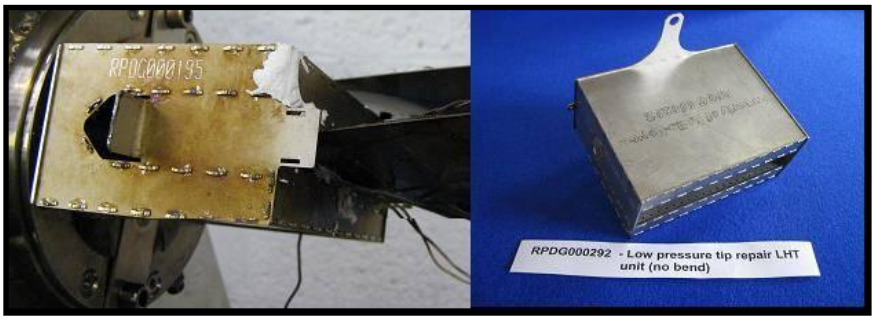


Figure 9-11 : Original tip head unit – RPDG000195 (left), optimised design RPDG000292 (right)

Baffle plate – The adoption of the improved baffle arrangement as described in section 15, was incorporated in this iteration of the head unit.

Larger mouth aperture – In RPDG000195 the distance between the jet plates was approximately 20mm, however the aperture at the front was closer to 10mm increasing the risk of collision the test piece. In order to mitigate this risk the mouth section in RPDG000292 was opened out to approximately 18mm. This represents the maximum allowable size without making the material around the rivet holes too thin and compromising strength. Although this increased aperture size is of great benefit to the system, it means that a larger degree of misalignment may be tolerated. This could have subsequent effects upon the component temperature (see section 10).

Head height – The overall height of the head unit was reduced to provide more space between the head unit and the adjacent blades. This provided two advantages; the first is that it further reduced the risk of contact between the head and the adjacent blades, and the second is that by increasing the gap, the temperature of the neighbouring blades would be minimised.

Thermocouple location - The addition of thermocouple location tabs on the side of the head units allowed the control thermocouple to be positioned centrally and repeatability within the head unit. These tabs provided a good positioning function, although there was still a requirement to attach a guide piece to the outside. This provided sufficient support to the thermocouple and prevented any movement during processing.

9.4.3 TIP HEAT TREATMENT - CAPABILITY

This section details the achievable temperature distribution and discusses the results of some of the key process variable (KPV) and sensitivity trials that have been conducted. The development work has been performed on a test piece shown in Figure 9-3 with thermocouples resistance welded onto their surface (Figure 9-8) and using equipment shown in Figure 8-2. However, when a heat treatment cycle is to be performed on an actual component there will be no way of directly monitoring component temperature. The temperature will be controlled by the gas temperature measured by a control thermocouple in the head unit close to the edge of the aerofoil. As a result, it is important to understand how the temperature recorded at this control thermocouple translates to the required heat treatment temperature on the component. The temperature and flow rate of the gas jet system that provides the best and most repeatable temperature distribution must also be understood.

From the data recorded during early trials to assess the optimum system parameters for the tip local heat treatment, it was apparent that the offset from the gas temperature to the component had a very strong correlation (this can be seen clearly in Figure 9-14). This correlation was consistent, even when the gas temperature was increased. For example, if during testing the control temperature were 600°C, giving a mean heated region temperature (thermocouples 1-4 in Figure 9-8) of 570°C, then increasing the gas temperature by 30°C to 630°C would result in a mean heated region temperature of 600°C.

9.4.4 TIP HEAT TREATMENT - KEY PROCESS VARIABLES (KPV) AND SENSITIVITY STUDY

There is significant risk to achieving a repeatable temperature distribution across the aerofoil caused by the positioning of the test piece within the head unit. However, it is important to make the distinction between varying stand-off distance in the sense of conventional local heat treatment techniques (such as radiant heating), and variations in standoff causing differing flow characteristics in impinging jets. In the case of a radiant heating source the temperature offset (between the component and the heat source) is significantly higher than in the case of a convection based system. For example up to 500°C for radiant heating and typically <50°C for a convective based process. Therefore although the efficiency of the jets may depend strongly on Reynolds number and jet length (controlled by aerofoil position, i.e. stand-off), the possibility of significant hotspots being generated is much lower in the case of a forced convection system. However, it may be that misalignment, whilst not causing a significant risk of over temperature, may provide a risk of the heat treatment falling outside the limits of +/- 15°C intended for the soak portion of the cycle.

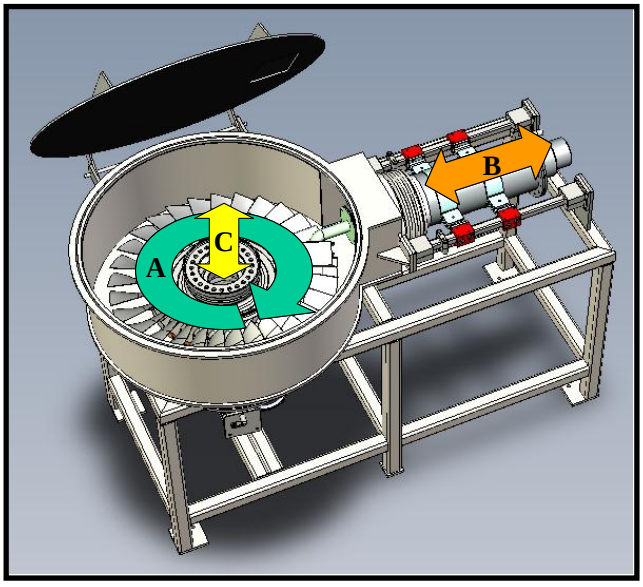


Figure 9-12 : Prototype system with manipulation axes shown

To mitigate this risk a set of sensitivity trials to quantify the effect of the test piece being out of position were performed. A description of the trials and the different positions tested is given in section 15. During the positional sensitivity trials, in order to test the variations likely to exist due to blade misalignment, three planes of movement were defined, shown in Figure 9-12 (above). The heater was moved axially (movement B) in order to heat treat further down (or up) the leading edge, the whole component was rotated (movement A) around its central axis (clockwise and anticlockwise), and finally the height of the component (movement C) within the head unit was changed. For each of these positions a maximum and minimum was defined and this was used to determine the test matrix. The maximum positions were defined as the maximum amount the component/heater could be manipulated before contact occurred between the test piece and the head unit.

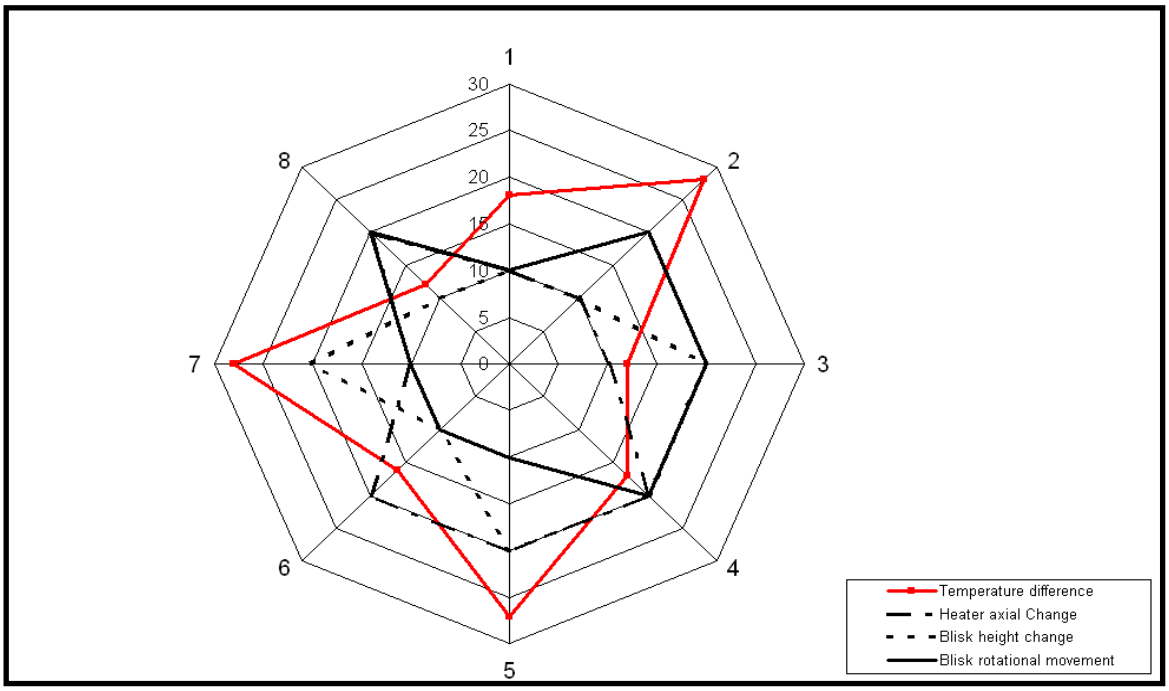


Figure 9-13 : Positional sensitivity trial results. Trial numbers are signified by each of the axes 1-8. Maximum and minimum positional variations are normalised, giving 10 (minimum) and 20 (maximum)

This established the maximum variation that could exist from test piece misalignments.

Therefore, if these maximum positional variations represent the greatest level of misalignment possible in the systems operation, then Figure 9-13 shows the relationship between the test piece position and the achieved temperature distribution during the trial. The trial numbers are signified by each of the axes (i.e. 1-8).

The graph is intended to highlight any relationship between a positional movement and the temperature distribution. The maximum and minimum positional variations are normalised, giving 10 (minimum) and 20 (maximum), to allow them to be shown on the same scale as the temperature differences measured. The red line on the plot shows the temperature difference in each test. For example in test one all the black lines go through 10 and the red line crosses at 18°C. This means that the positions were at their minimum values (10) and the temperature difference achieved was 18°C.

The graph above does not suggest that any one specific positional variation has the most significant affect on the temperature distribution. However, even with the most significant positional misalignment, the temperature distribution is less than 30°C (or +/- 15°C). This investigation further highlights the relatively flexible nature of the system with respect to standoff distance.

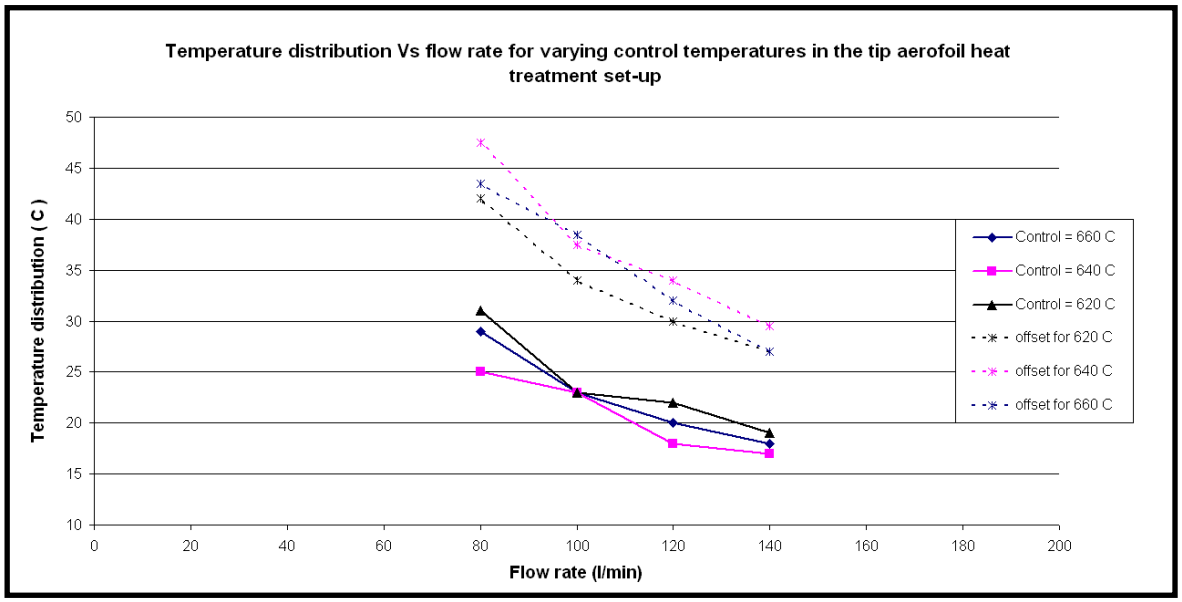


Figure 9-14 : Temperature distribution Vs flow rate for tip

Figure 9-14 contains the results of a KPV study to examine the effect of varying flow rate and control temperature on the temperature distribution achieved across the heated region of the test piece tip. The graph details a strong correlation between the temperature distribution across the heated region (thermocouples 1-4 in Figure 9-8) and the flow rate at different control (gas) temperatures. The relationship suggests that the magnitude of the distribution reduces with increasing flow rate for all temperatures. This is a result of the increased velocity of the gas jets, and therefore higher heat transfer due to the increased flow rates. The most significant effect is at the edges of the heated region where the driving force for conduction away from the hot zone is at its highest. Increasing the heat input in these regions will increase the size of the heated area and have the effect of spreading the more tightly packed isotherms further from the thermocouples positioned at the edge of the heated zone. The data show that by choosing a relatively high flow rate and using a low control temperature the component temperature will be fairly stable, even if there is a fluctuation in flow rate during

processing. Another effect observed is that as the flow rate increases, so the offset (difference between gas and component temperature) decreases (dotted lines on the graph). As a result of this investigation, the flow rate to be used for actual processing of aerofoils was increased from 110 l min^{-1} to 120 l min^{-1} and a control temperature of 630°C was chosen for the tip heat treatments. This was then verified by running the cycle shown in Figure 9-15. The flow rate chosen represents a compromise between using the minimum flow to improve the efficiency of the system whilst minimising the temperature distribution.

9.4.5 TIP HEAT TREATMENT – KEY OUTPUT

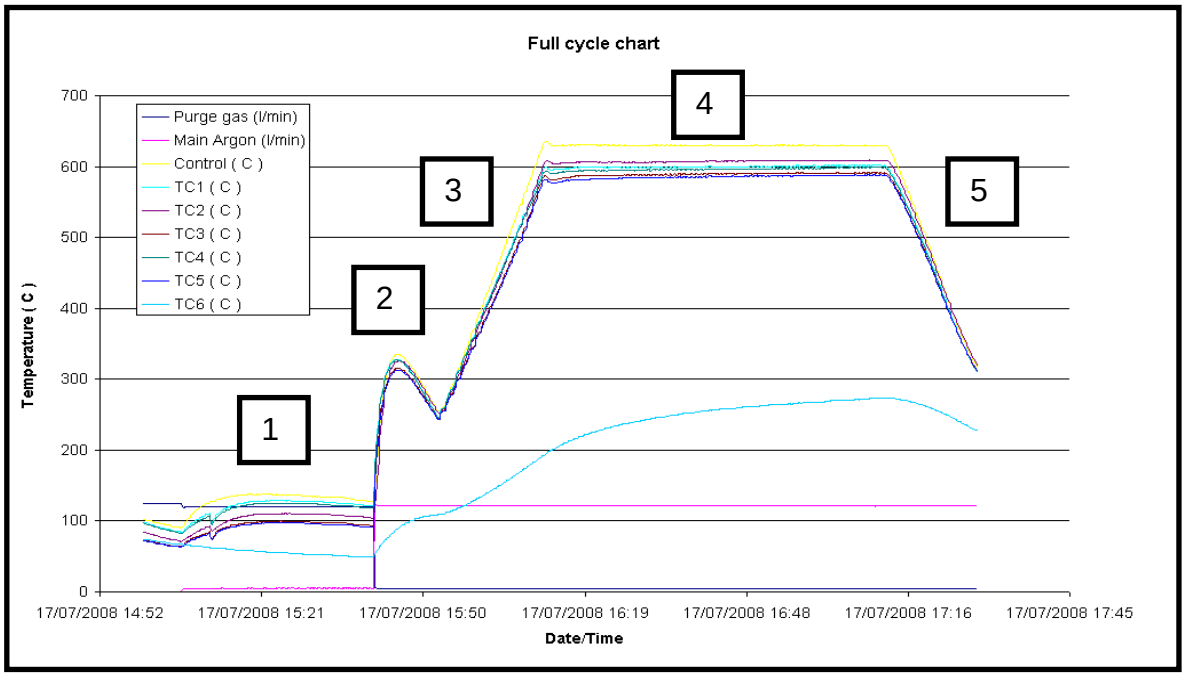


Figure 9-15 : Tip heat treatment cycle

Figure 9-15 was generated following the development described in this section and was performed as a validation exercise for the application of the local heat treatment onto a component. The graph shows the way in which the cycle is run

for both the tip and leading edge positions. The same basic setup was applied, however the control temperature is different for each of the positions. The temperature difference during soak, that is the difference between the maximum and minimum temperatures in the heated region, was observed to vary slightly. From a value of ~21°C to ~17°C over the course of the soak period. This is due to the transient nature of heating such a small section. If one were to hold at this temperature for an infinite time period it may even reduce. The temperatures seen in the soak region for thermocouples 1-4 also drift slightly, from an initial value of 597 +/- 10°C at the beginning of the soak, to 600 +/- 9°C after only 20 minutes at soak. These values and slight fluctuation is a result of a small overshoot at the beginning of the soak portion of the cycle.

As a result of this work it can be stated that a heat treatment temperature of 600°C +/- 15°C is achievable over the tip during the processing of repaired components. However, it is worth noting that for the majority of the cycle the value is likely to be closer to +/- 10°C.

The graph in Figure 9-15 is numbered 1-5, signifying the different sections of the local heat treatment cycle; described below. The basic shape of the graphs will remain largely the same for both the tip and leading edge heat treatment locations.

- **Section 1** – In this region the system was being purged with argon to reduce the level of oxygen within the system. It is a general rule of thumb to put a total of 10 times the chamber volume through the system; therefore the system was flushed through for one hour at 125 l min^{-1} to achieve this. In order to ensure the system is filled uniformly the heater has a constant

supply of 60 l min^{-1} moving through it and the chamber is filled from the bottom, through the component support fixture at a rate of 65 l min^{-1}. (N.B. In Figure 9-15 the ratio of gas entering the system from the chamber and the heater is 120 : 5 l min^{-1}, however this was changed later to allow more gas through the heater.)

- **Section 2** – In this region the gas flow is increased and the residual system heat from the previous cycle is transferred to the gas and heats the component, this is the reason for the initial peak in the temperatures. One of the reasons for the change mentioned above is to reduce this peak in the actual cycle.

- **Section 3** – At this point the ramp up to temperature is more controlled as the system control unit progressively increases the heater temperature in order to increase the gas temperature (and therefore component temperature).

- **Section 4** – This is the soak portion of the cycle. For the tip heat treatment the control temperature will be set at 630°C for a flow rate of 120 l min^{-1}. For the leading edge heat treatment a value of 620°C and a flow rate of 120 l min^{-1} is used.

- **Section 5** – This section is the cool down region of the cycle. At this point the heater turned off and the component cools slowly, at a rate of close to 20 °C min^{-1}. The flow through the heater was maintained at 120 l min^{-1} during this cooling phase in order to prevent any oxygen finding its way back into the system.

9.5 LEADING EDGE (LE) HEAT TREATMENT

The requirements of heat treating the leading edge were similar to that of the tip. Development of a head unit for locally heat treating the leading edge of larger test pieces is presented in section 7. The first point to highlight is that a straight head unit was used for the leading edge; this was due to the simplicity of manufacture and also the fairly straight nature of the test piece leading edge. It is worth noting that the test piece does begin to curve significantly along its chord, however the heated region extends only ~15mm into the test piece from the leading edge. Over these distances, the curvature seen in the test piece is not significant; making a flat aperture acceptable.

9.5.1 LE HEAT TREATMENT - BLOCKED JETS



Figure 9-16 : Leading edge jet plate

As described previously there is a requirement to block the central jets in the head unit in order to reduce the size of the hotspot towards the centre of the heated region. Figure 9-16 shows the actual jet plate used in the leading edge head unit. The blocked region is 8 x 3 (in terms of jets blocked) but is positioned off-centre, biased towards the root of the test piece. The reason for this is that the tip sits around 5mm inside the head unit. Figure 9-17 (overleaf) shows the results of the trials to establish the number and position of the jets to be blocked in order to produce an acceptable heated region temperature distribution. The data on the left represents the temperature distribution (across the thermocouples 1-5 in Figure 9-8) with the central 12 (6 x 2) holes blocked with

a temperature distribution across the heated region around 30°C. The data in the right hand side of the graph represents 24 (8 x 3) holes blocked to produce the off-centre pattern that can be seen in Figure 9-16. The result of this was a drop in temperature distribution to between 12-15°C as shown in the graph. Again, data presented in Figure 9-17 are a mean of the temperatures over a period of time (a minimum of 3 minutes) at steady state (i.e. once the system is in soak), the error bars represent the maximum and minimum temperatures in the heated region during the soak period measured.

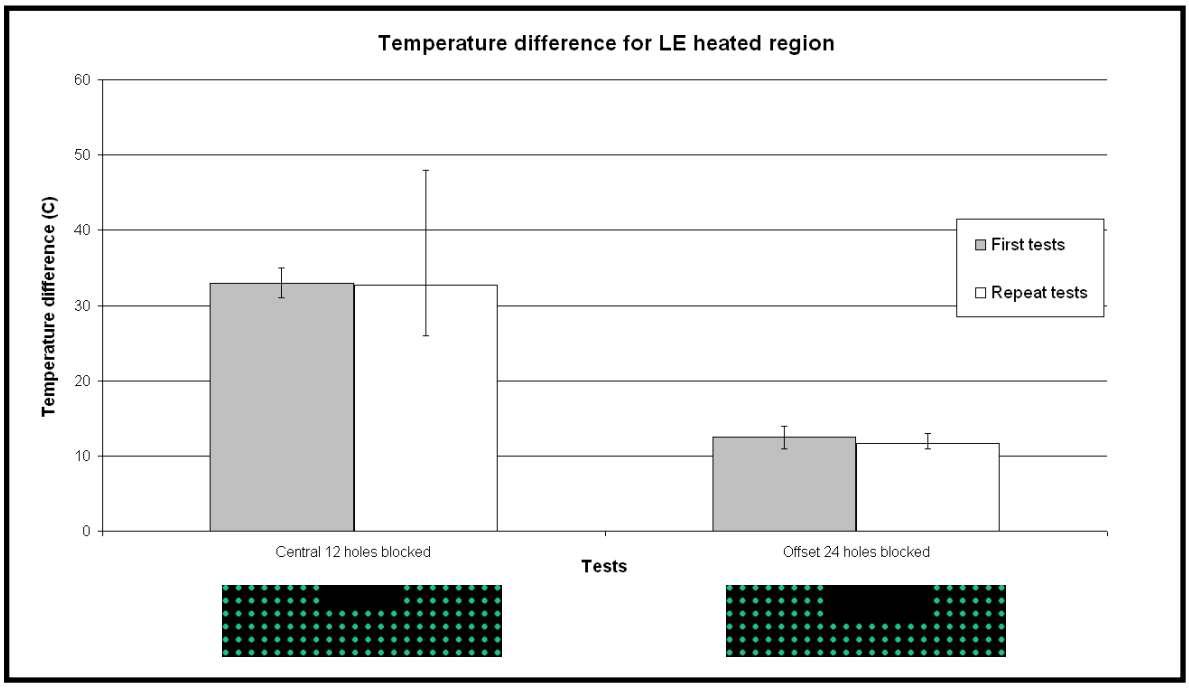


Figure 9-17 : Leading edge temperature distribution, bottom images show jet array configurations

9.5.2 LE HEAT TREATMENT - HEAD UNIT

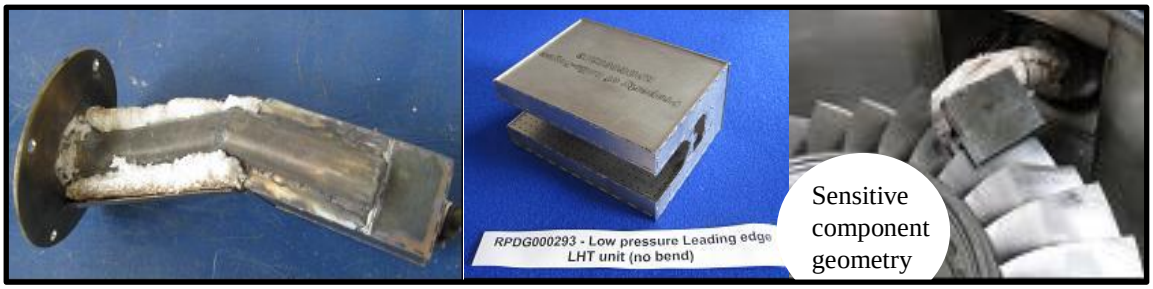


Figure 9-18 : Leading edge head unit

The design used for the leading edge head unit was similar to that described above. Also the reduction of the head height, increased head aperture size, and thermocouple location technique were included. In order to allow the system to be positioned on the leading edge whilst only moving the heater in one plane (i.e. not requiring vertical or rotational movement) and maintaining the blisk stationary, the head unit was mounted on an extended inlet pipe (Figure 9-18, far left image). The position of the head unit on the test piece can be seen in the photograph on the far right of Figure 9-18.

9.5.3 LE HEAT TREATMENT - CAPABILITY

As with the tip KPV and process sensitivity, experiments were completed to establish the capability of the leading edge heat treatment. The same trials were conducted to assess the sensitivity of the system with respect to the position of the test piece within the head unit. The axes of movement (a, b and c) defined in Figure 9-12 were used again for the leading edge trials. However in the KPV study the control temperatures tested were centred around 600°C (not 620°C as in the tip trials), as this is the control temperature that proved most appropriate during development.

9.5.4 LE HEAT TREATMENT - KEY PROCESS VARIABLES (KPVS) AND SENSITIVITY STUDY

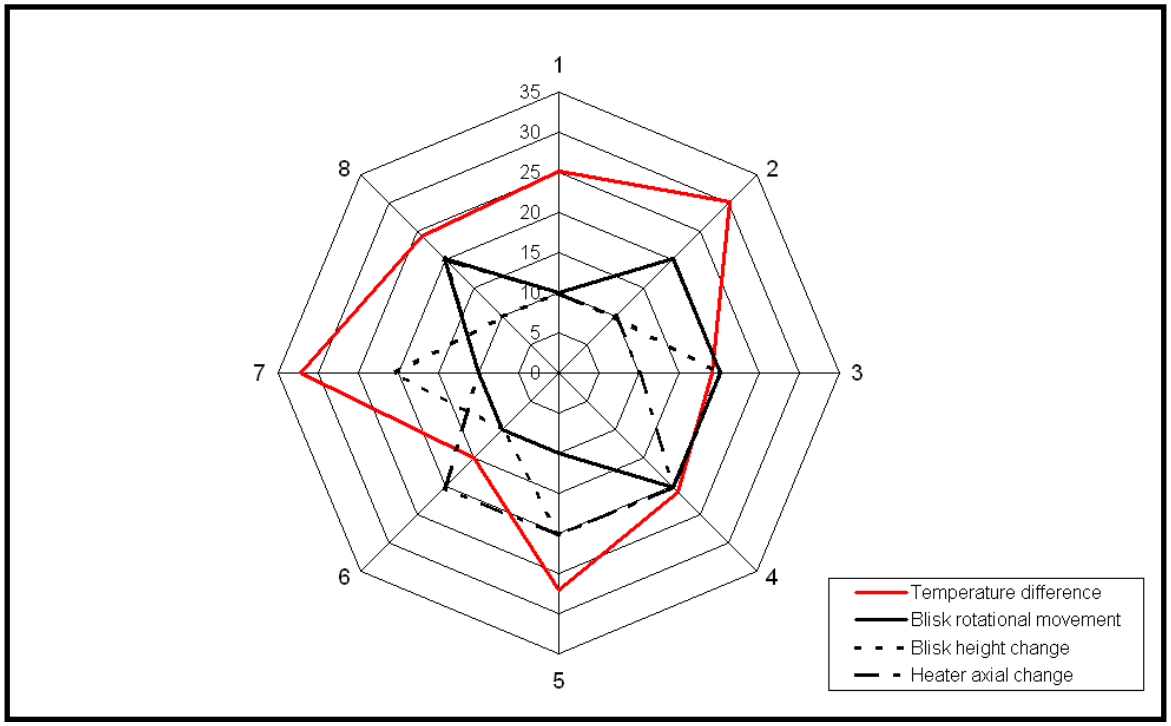


Figure 9-19 : Leading edge positional sensitivity results

Figure 9-19 shows the effect of varying the position of the aerofoil within the head unit during the sensitivity trials. As with the tip graph the positional variations have been normalised to allow them to be shown on the same graph as the temperature distribution. It can be seen that the general temperature distribution is higher than in the case of the tip. However the minimum value of 15°C for test 6 and the value of 20°C for tests 3 and 4 are still considered very low values. These data suggest that although narrower temperature distributions than for the tip heat treatment are achievable, variations in positional accuracy can cause the distribution to change significantly, up to a value of 30-35°C. The temperature distribution (solid red line) varies in a very similar pattern to that of the component height variation (black

dotted line). Whether these two are linked is unclear from these data, however it is possible that it is this variation that will most significantly affect temperature distribution in the heated region. A change in component height will directly result in a change in standoff and therefore a variation in temperature distribution. As a result of this and also the fact that it is easier to control the axial movement and component rotational movement in the final system, it was decided a method of using shims should be applied to ensure the position of the test piece within the head unit is kept central.

Figure 9-20 displays the results of the KPV studies where the flow rate and control temperature were varied and the resulting temperature distributions plotted. The graph shows similar trends to those seen in the case of the tip KPV study in that the general trends are for the temperature distribution and offset between gas and component temperature to reduce with increasing flow rate. It is noticeable that in the case of the temperature offset the values are much closer. In the case of the 580°C and 600°C control temperature the values appear to be the same. There appears to be a plateau in the control results between 120 and 140 l min^{-1} flow rate. Although it is worth noting (as with the tip, but to a lesser extent) it would be scientifically unsound to draw too many conclusions from the data set as it is so small. Also significant is that over a range of flow rates from 100 and 140 l min^{-1} the temperature distribution only reduced by 3°C. Whilst over the same flow rate range (and 40°C control temperature range) the offset between aerofoil and component only changes by 6°C. When compared with the variations seen due to the positional sensitivity trials it appears that the system is very stable and

insensitive to variations in flow rate and control temperature, in leading edge configuration.

As a result of the trials described above a control temperature of 620°C and a flow rate of 120 l min^{-1} was selected for the heat treatment cycle. Given the information in Figure 9-20 this should result in a heated region temperature of around 600°C with a temperature distribution of 18°C. However, whether or not the actual heat treatment temperature will achieve that value is reliant on to the position of the aerofoil within the head unit as demonstrated by the sensitivity study.

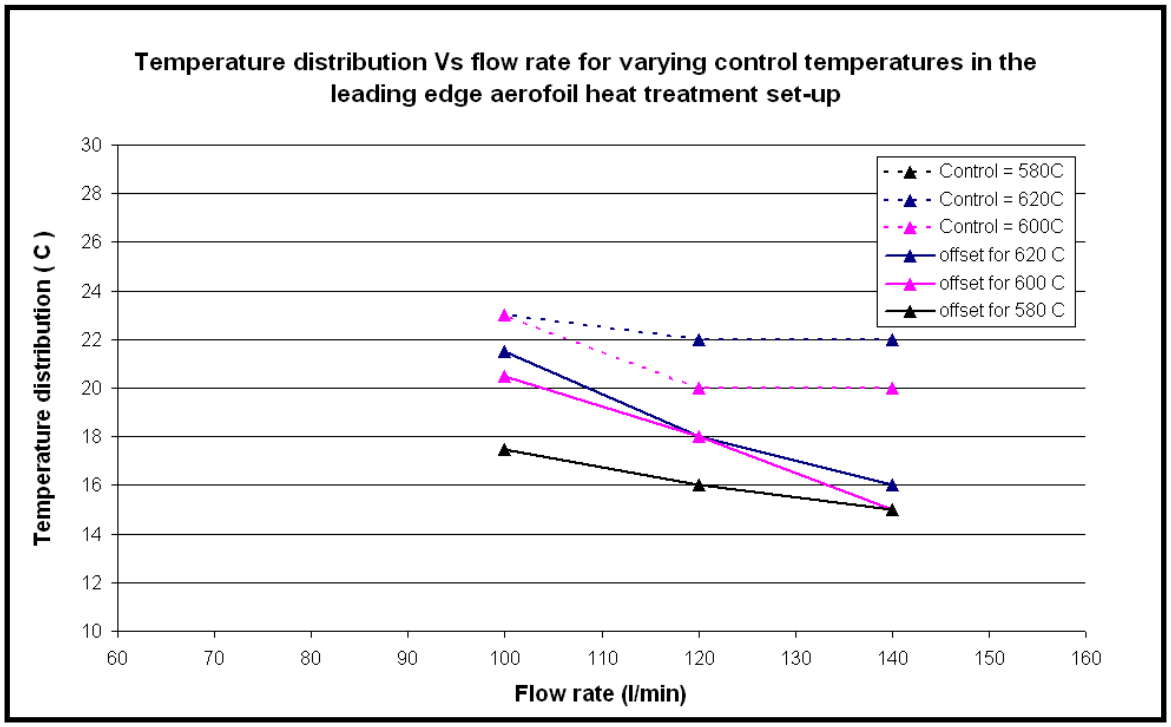


Figure 9-20 : Leading edge flow rate Vs temperature distribution

9.5.5 LE HEAT TREATMENT - USING THE SENSITIVITY DATA

The data described previously gave an insight into system sensitivity. An expedient method of assessing the location of the head unit on the test piece was developed. Flow rate and control temperature are monitored by the system, therefore any discrepancies are easily seen from the charts and data produced during heat treatment. However, the effect of positional variation is significant (Figure 9-13 and Figure 9-19) and this is more difficult to detect. To establish the position of the test piece within the head unit, two methods are used; the first was to cover the head unit in a soft protective cardboard skin, which was also covered in chalk. This was used to protect the test piece from damage in the unlikely event of contact occurring and when the head unit was slid onto the component. If any contact did occur then a chalk mark would be left on the aerofoil. The second method was the use of plastic shims (shown in Figure 9-21) to establish how close the test piece was to the head unit at critical points. For example, in the case of the leading edge head unit a total of six 0.5mm shims were used to check the gap between the suction and/or pressure surfaces of the test piece and the head unit at the closest point. Also, the gap between the tip and leading edge corner of the test piece and the jet plate within the head unit was checked. The final check was to use a shim containing a cut out (Figure 9-21, far right image), to measure the



Figure 9-21 : Shims used to check head to test piece clearance

depth of the head unit along the leading edge. A further shim containing a similar cut out was used to measure the distance of the head unit stretched into the chord width of the test piece.

These shims demonstrated that the blade was positioned centrally within the aperture of the head unit allowing good control of temperature distribution. The shims also ensured the head unit extended the required distance down the test piece and into the chord to ensure the whole target region was heated. This approach was employed on the component used for the validation trials described in section 13.2.

9.5.6 LE HEAT TREATMENT – KEY OUTPUT

Figure 9-22 is a short run up to temperature performed to check the temperature distribution on the leading edge of the test piece (the shim technique described previously was used to position the test piece correctly). The cycle was not run for the full hour to minimise gas usage and because the main purpose was to check that the temperature distribution was acceptable. Figure 9-22 shows that at the soak temperature the distribution was around 16-17°C. This correlates well with that seen in the KPV study discussed. Furthermore, the offset value from this graph is 22°C, which again correlates well with the values shown in the graph from the KPV studies (Figure 9-20). This confirms that for leading edge heat treatment the process is stable and controlled.

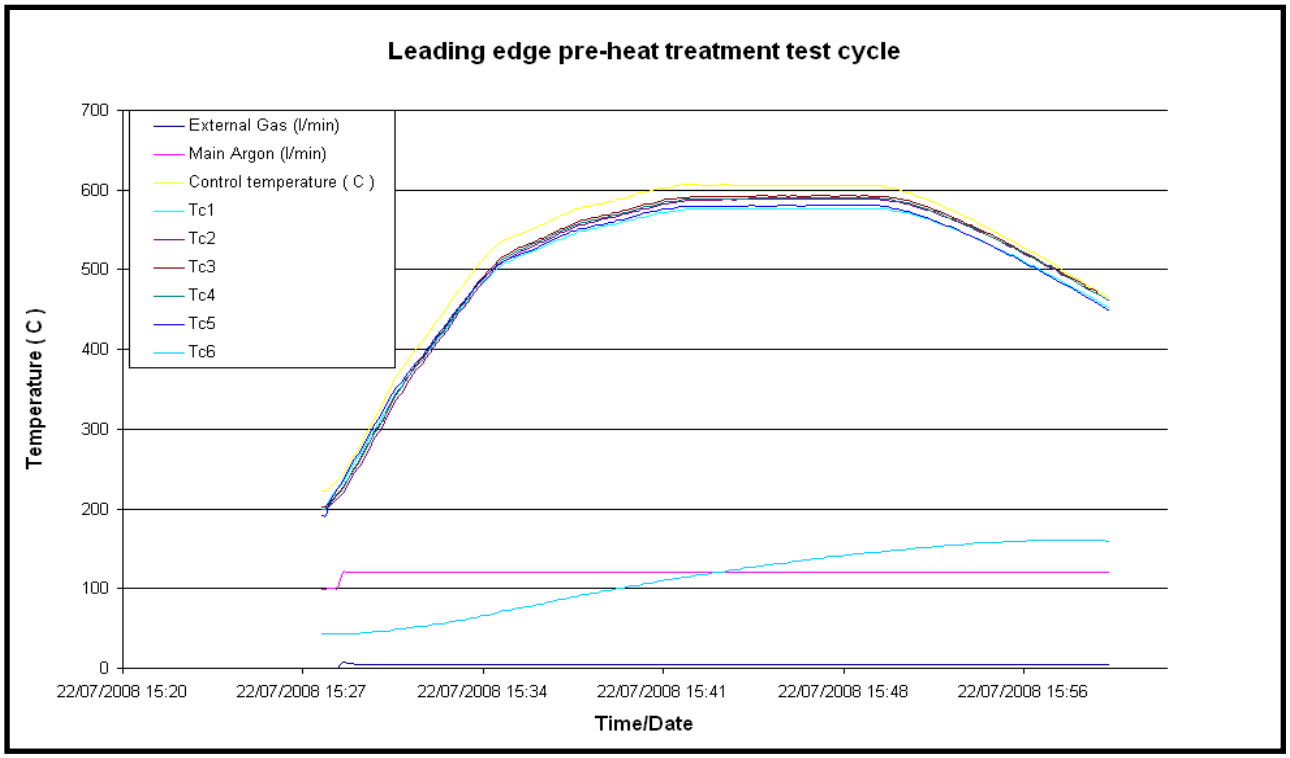


Figure 9-22 : Leading edge heat treatment cycle

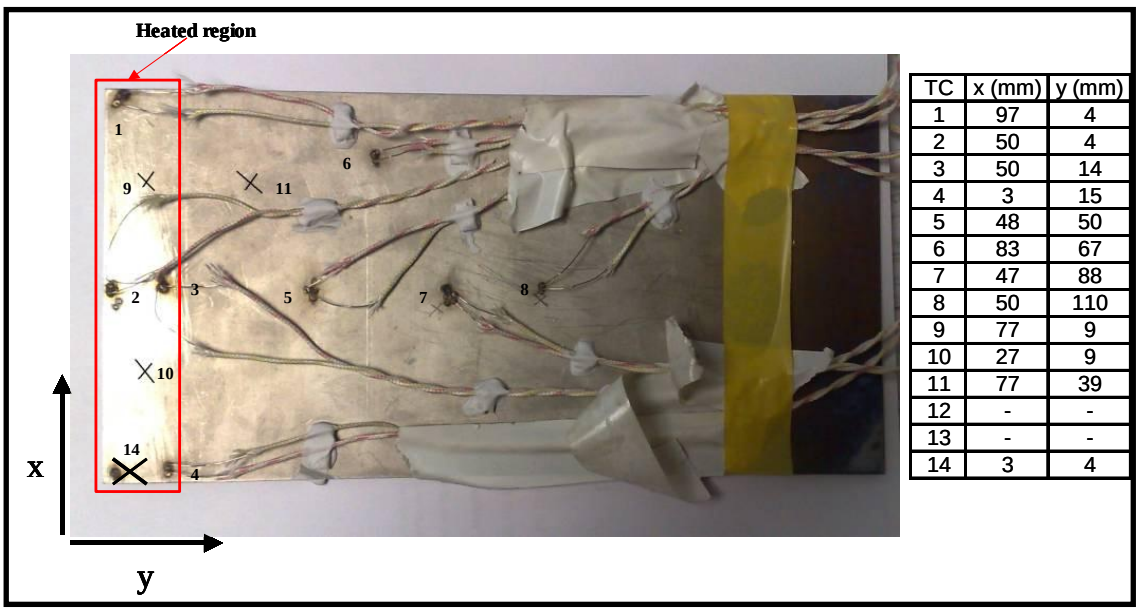
It was observed that the temperature recorded at thermocouple 6 was not quite at steady state during the heat treatment process. However it has been stated previously that it is the hub that must be kept below the critical 350-400°C at which alpha case begins to form in titanium 6-4. To monitor this situation a thermocouple was resistance welded onto the rim of the component in order to monitor the temperature attained by this region during the processing of these components. The maximum value for the rim-mounted thermocouple is approximately 160°C and the addition of this thermocouple is to assess the cumulative effects of performing several heat treatments sequentially.

10 PROCESS – DEVELOPING UNDERSTANDING

The earlier sections have dealt with the building and development of a system to locally heat treat test pieces to temperatures representative of stress relief cycles for titanium alloys. In this section thin section plate test pieces are used to investigate the repeatability of the temperatures achieved with respect to flow rate and positional variation.

10.1 EXPERIMENTAL INTRODUCTION

In order to investigate system repeatability, a number of tests were carried out. In the tests, a plate containing 11 randomly positioned k-type resistance welded thermocouples was used (Figure 10-1). The thermocouples also had a spot of ceramic glue to take the weight of the wires. This reduces the load on the welded joint by minimising the movement of the wire and maintaining positional consistency between tests.



TC	x (mm)	y (mm)
1	97	4
2	50	4
3	50	14
4	3	15
5	48	50
6	83	67
7	47	88
8	50	110
9	77	9
10	27	9
11	77	39
12	-	-
13	-	-
14	3	4

Figure 10-1 : Plate thermocouple locations, and positions measured in millimetres from the datum corner in the bottom left-hand corner of the image.

10.1.1 TEST MATRIX - KEY PROCESS PARAMETERS

The test strategy was to vary the flow rate of gas through the system between the limits allowed by the flow controllers. This resulted in a variation between 50-200 l min^{-1}. The gas temperature was measured within the head, close to the plate and was varied between 560°C and 660°C. The inert gas used in these experiments had a low specific heat capacity. As a result it was difficult to transport the gas over large distances at temperature without losing significant heat. The lower flow rate 50 l min^{-1} was chosen as anything lower would fail to achieve a gas temperature of 660°C at the head unit. The temperature range selected is within the range that one might expect to heat treat metallic components, particularly titanium alloys.

10.1.2 TEST MATRIX – POSITIONAL SENSITIVITY

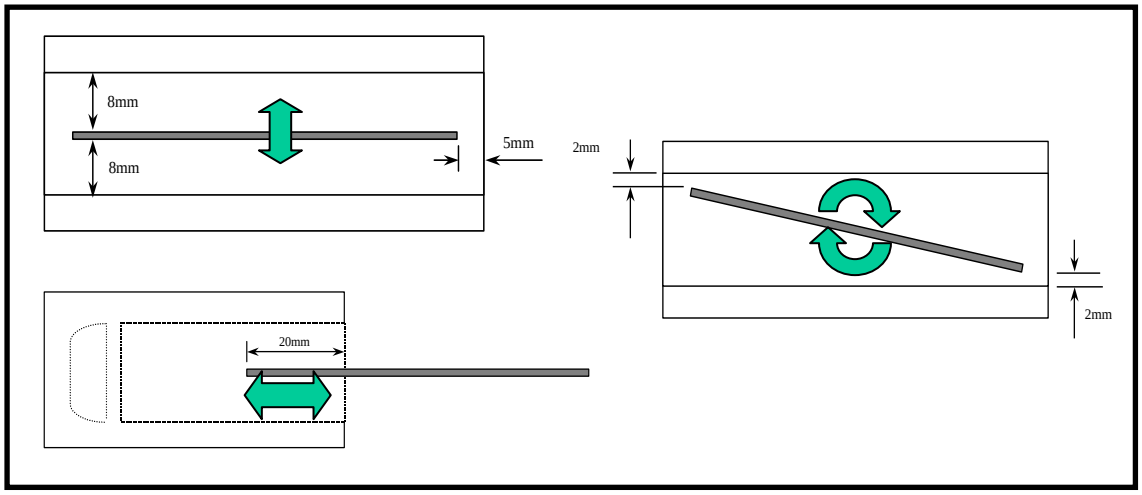


Figure 10-2 : Plate positional variation movements, the grey rectangle represents the test piece within the head unit

In order to conduct these tests the plates were placed in a positioning jig to achieve a 'neutral' position. This neutral position represented the point at which the plate was positioned centrally in the head unit with its top surface parallel to the head aperture with the tip of the plate 20mm into the head unit (neutral position

shown in Figure 10-2). From this position, the plate was moved to a maximum and minimum position in the following three axes of movement (all shown with green arrows on Figure 10-2); rotational, in-and-out of the head unit, and up and down (closer to each jet plate). For each axis of movement, three positions were defined (i.e. maximum and minimum rotation and the neutral position). A full factorial test matrix was defined to test each position, which produced a total of 27 trials. The table of tests and the key as to the numbers and letters is given below in Figure 10-3. The maximum and minimum rotation is defined as the maximum allowable rotation before the plate touches the head unit. In the case of the height and length movements, the plate was moved 2mm from the neutral position in each axis.

Tip	Max clockwise	Central	Max anticlockwise
Rotational (around plate axis)	A	B	C

Tip	+2mm	Optimal	-2mm
Along plate length	1	2	3

Tip	+2mm	Central	-2mm
Height in mouth	1	2	3

Test number	Rotational	Length	Height
1	A	1	1
2	A	1	2
3	A	1	3
4	A	2	1
5	A	2	2
6	A	2	3
7	A	3	1
8	A	3	2
9	A	3	3
10	B	1	1
11	B	1	2
12	B	1	3
13	B	2	1
14	B	2	2

Test number	Rotational	Length	Height
15	B	2	3
16	B	3	1
17	B	3	2
18	B	3	3
19	C	1	1
20	C	1	2
21	C	1	3
22	C	2	1
23	C	2	2
24	C	2	3
25	C	3	1
26	C	3	2
27	C	3	3

Figure 10-3 : Test matrix for positional variation trials

10.2 KEY PROCESS PARAMETERS

10.2.1.1 RESULTS - AVERAGE TEMPERATURE VS FLOW RATE

In the following graphs the thermocouples in the under head region are used to establish the temperature distribution and average heated zone temperature. The thermocouples cover the central section of the tip and extend to a depth of 14mm into the plate. The relationship between flow rate and average plate temperature[††††] in the heated zone is shown in Figure 10-4. A range of gas temperatures was used (i.e. from 560°C-660°C) and in some cases a number of

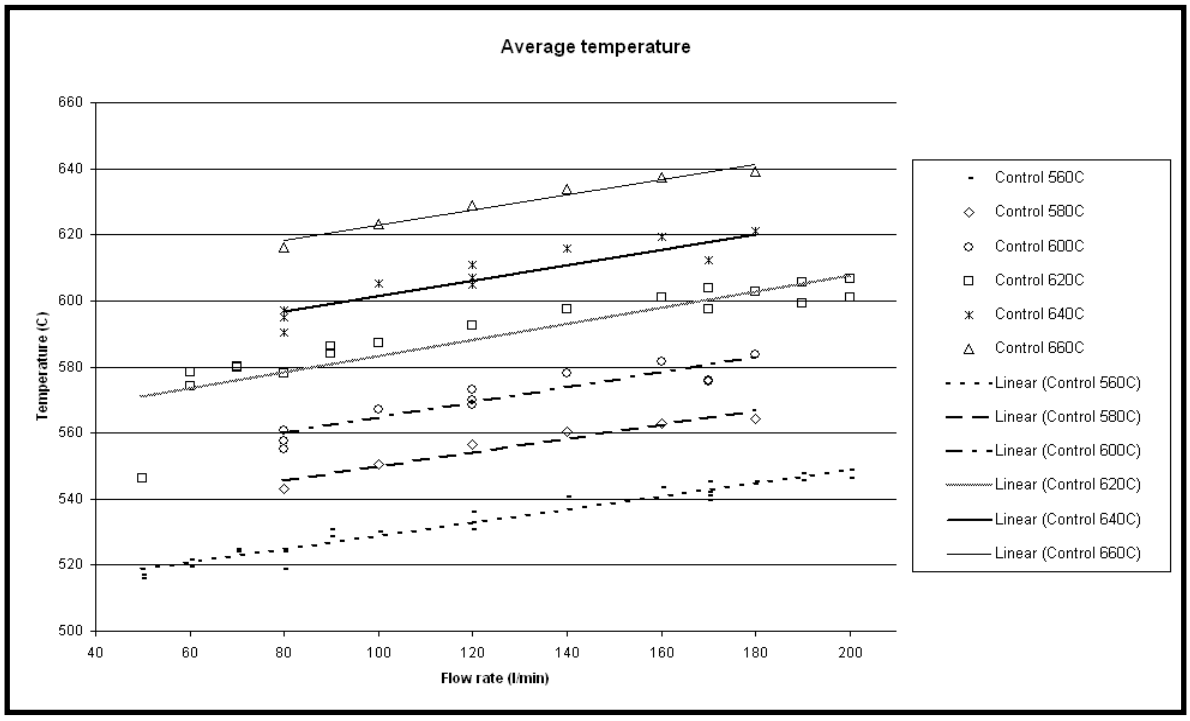


Figure 10-4 : Tip - average temperature of heated region thermocouples

[††††] Average plate temperature was calculated by taking the arithmetic mean of the thermocouples within the heated zone of the test piece.

test runs were performed to generate data. In some of the repeat tests the test piece and control thermocouple were replaced several times in order to capture the variations in set-up that may result during the use of this equipment. In the graphs, shapes are used to represent a data set for a given gas (control) temperature and linear best fit lines are used to show the trend of the data points in each set.

10.2.2 RESULTS - TEMPERATURE DISTRIBUTION VS FLOW RATE

Figure 10-5 highlights the relationship between flow rate and temperature difference across thermocouples positioned within the heated region for the range of gas temperatures detailed. The general trend in the graphs highlight that the temperature difference across all gas temperatures was below 25°C between flow rates 50 l min^{-1} and 200 l min^{-1}. Linear best fit lines describe the trends seen in the data. The trends for gas temperatures 560, 620, 600 and 640°C showed a general

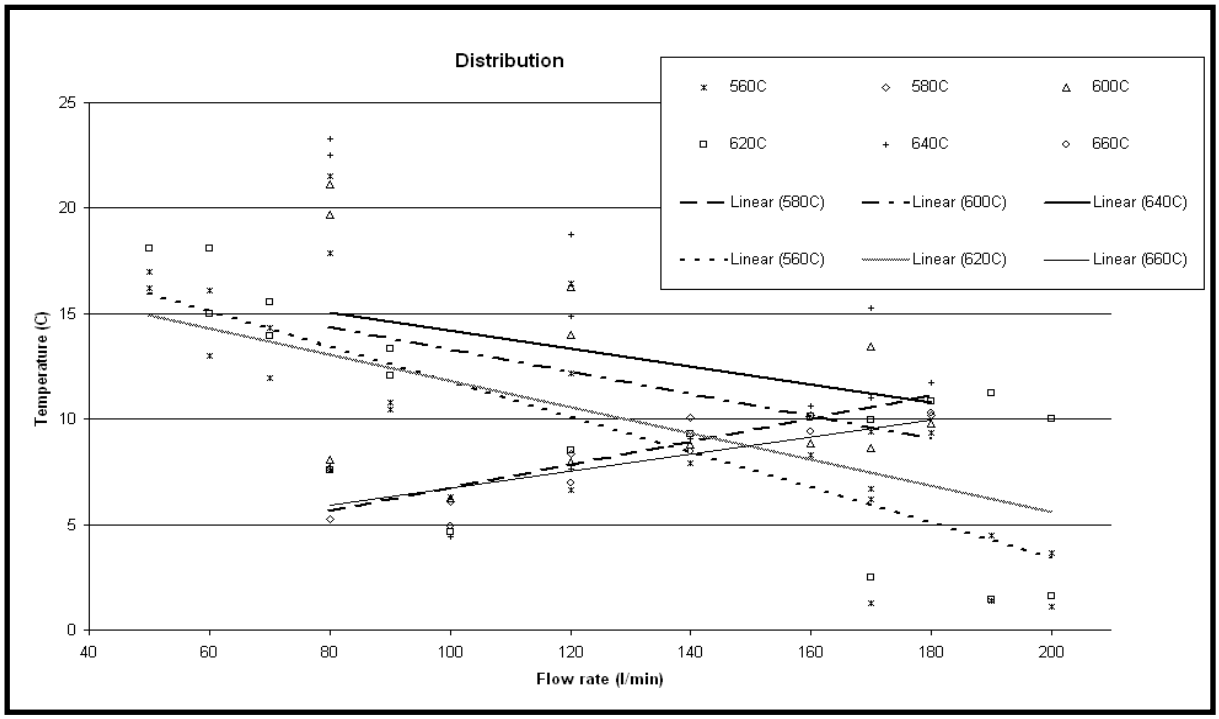


Figure 10-5 : Tip - temperature distribution of heated region thermocouples

decrease in temperature difference with increasing flow rate, however the data spread is high for all the temperatures tested. Noteworthy is that the best fit lines for the data sets representing 580°C and 660°C actually showed a slight increase in temperature distribution for increasing flow rate.

10.2.3 RESULTS - TEMPERATURE OFFSET VS FLOW RATE

Finally Figure 10-6 highlights the relationship between flow rate and the offset between the gas temperature (measured at the control thermocouple) and the average heated region plate temperature. The relationship between gas temperature and component temperature is an important one to understand. It is one of the goals of this technology development work to minimise (or remove) the requirement for temperature measurement devices (such as thermocouples) to be physically attached to the test pieces being heated. Therefore the relationship

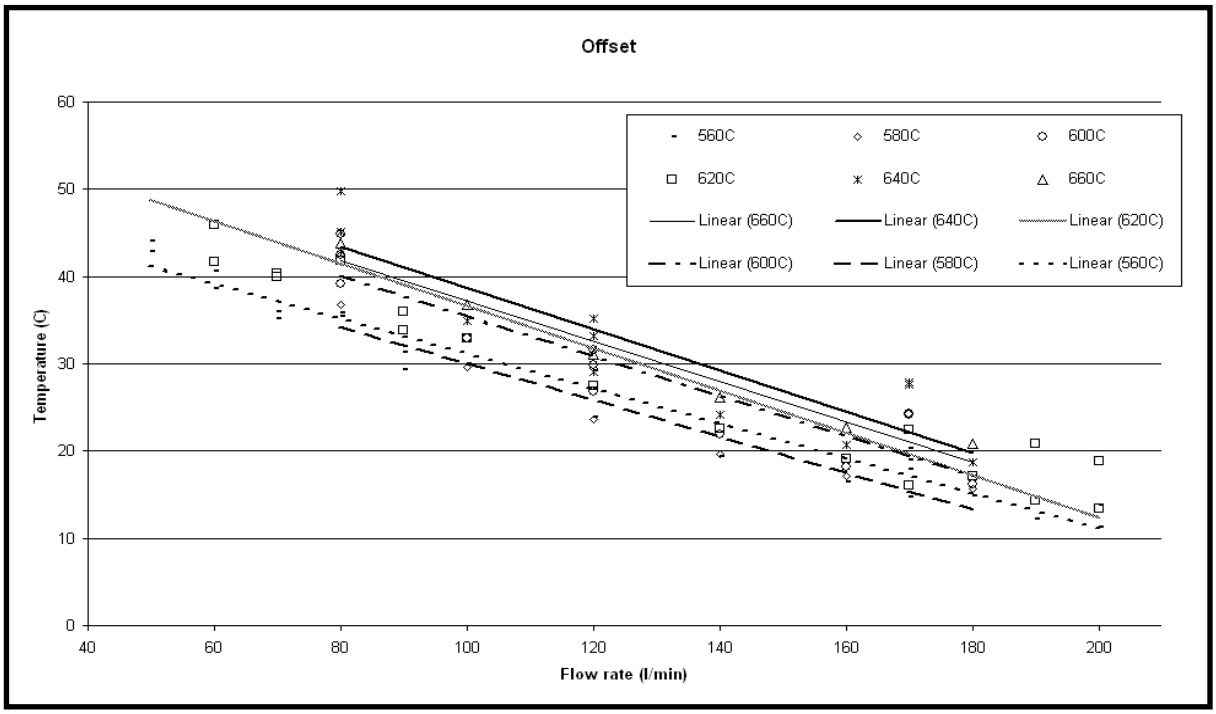


Figure 10-6 : Tip – Offset temperature, i.e. the difference between the average heated region temperature and the control temperature

between gas temperature and component temperature has to be both measurable and controllable. Figure 10-6 illustrates the strong correlation that exists between the gas temperature, flow rate and average heated zone temperature. It also shows that although this offset decreases significantly over the range of flow rates studied, this relationship appears to be very repeatable and stable across a range of gas temperatures.

10.2.4 DISCUSSION - AVERAGE TEMPERATURE

Data for the average hot zone temperature, show there is a very strong correlation between flow rate and average plate temperature. There are also distinct steps in data observed between each gas temperature tested. These data highlight that even for large variations in gas temperature (100°C), the relationship between flow rate and plate temperature is very consistent. Originally trials were conducted between flow rates of 80 and 180 l min^{-1}. However, to generate data beyond these flow rates further tests were conducted with flows of between 50 and 200 l min^{-1} at gas temperatures of 560 and 620°C. The tests at these two temperatures were also repeated a number of times to establish a level of repeatability from the results.

The data in Figure 10-4 allows one to confidently predict the plate temperature for a given flow rate and gas temperature. This is a useful relationship, particularly if different processing parameters are required. It also makes it possible to establish how the process can be optimised in terms of gas usage. For example, if one were trying to achieve a temperature of 560°C, these data would suggest that the lower flow rate of 90 l min^{-1} would achieve this value with a gas temperature of 600°C.

10.2.5 DISCUSSION - TEMPERATURE DISTRIBUTION

The data presented to highlight the hot zone temperature distribution have a significant spread and it is difficult to establish consistent trends. The main reason for this is that a number of tests were carried out to generate this data and the test apparatus was moved and replaced between each test. As a result the variations in test set-up are shown to have had a significant effect on the repeatability of the results. However it is important to put this variation in to context. In the case of the data for a gas temperature of 620ºC (which displays one of the largest spreads) the difference between the highest and lowest temperature distribution is 11ºC, between values of 19ºC and 2ºC. This highlights that although the temperature distribution varied with test set-up, the actual magnitude of the variations was small and within the limits one would expect to heat treat a localised region of a component (a temperature tolerance of 20ºC is not uncommon in repair applications [125]).

One potential source for the variation in temperature distribution seen in the graph is that one of the thermocouples used to generate the data was positioned on the outer regions of the heated zone. As described previously there exists a strong thermal gradient at the edges of the heated zone, and any slight misalignment could result in thermocouples in these positions registering a significantly different temperature.

The general trend of the data suggests that as one increases the flow rate there is an associated decrease in temperature distribution. This could be due to the fact that increasing the flow rate will cause a small rise in pressure in the plenum

chamber of the head unit. This slight increase in pressure behind the jet plate will act to help distribute the flow across the holes in a more uniform manner. At lower flow rates, the holes positioned at the edges of the jet plate (closest to the plenum walls) will have an associated lower pressure and therefore low jet flow rate. This will ultimately manifest itself as a lower jet exit velocity, Reynolds number and therefore heat transfer coefficient. This could be substantiated by computational fluid dynamics modelling of the head, however this is beyond the scope of the present study.

10.2.6 DISCUSSION - OFFSET

The relationship between gas temperature and average test piece hot zone temperature is strong, highlighting that as one increases the flow rate this difference reduces. Impingement jet theory outlined in the literature review is in general agreement that heat transfer coefficient is closely linked to jet velocity (and therefore flow rate) through Reynolds number for jets of the same size. As heat transfer coefficient increases, one would expect the target temperature to achieve a value closer to that of the gas. One of the main advantages of this method of heating components is that the difference between target heat treatment temperature and heat source temperature is low, therefore minimising the potential for overheating the component and compromising material integrity.

10.2.7 KEY OUTCOMES

The graphs in this section present a useful relationship between the gas temperature, flow rate, component temperature and distribution. For example, if the gas temperature was 620°C and the flow rate 120l min^{-1}, then one could

estimate that the average plate temperature would be ~590°C, giving an offset of 30°C, and a temperature range of 584 - 596°C. These graphs represent the basis for process control curves, although a more extensive data set would be required to present a more detailed analysis of any trends that exist.

The main area where the data appear inclusive is the temperature distribution. In Figure 10-5 there is a large spread of data. In particular gas temperatures of 580 and 660°C show the temperature distribution increasing with increased flow rate. Also at 620°C, the data appear to be very inconsistent at higher flow rates. This is most likely to be due to variations in the positioning of the plates between tests. The tightly packed nature of the isotherms due to the localised heating suggests that even for fairly small variations in position, fluctuations in temperature may occur. Temperature distribution in this case is measured as the difference between the maximum and minimum temperatures measured in the heated zone. Therefore, slight misalignment of the head unit could place a thermocouple on the edge of the heated region in a significantly colder region than in a previous test. Hence the need for accurate positioning jigs when processing components using this technique.

10.3 POSITIONAL SENSITIVITY

The following graphs (Figure 10-7 - Figure 10-11) display the results of the positional sensitivity trials. The positions are shown on the vertical axis as a number (1, 2 or 3) as shown in Figure 10-3. The temperatures (average or distribution) have been normalised to fit on this axis also, therefore the maximum value is denoted as 3 and the minimum 1. These plots allow one to establish if there are any patterns suggesting strong links between the positional variation of the plate and the temperatures achieved in the heated region. Each set of graphs plots the temperature data along with the variations in the axis of movement. Throughout all the positional sensitivity tests the temperature distribution varied between 6°C and 17°C, and the average plate temperature between 588°C and 602°C.

10.3.1 RESULTS - LENGTH POSITION EFFECTS

In Figure 10-7 the dashed black line represents the temperature data (left hand image is temperature distribution, and the right hand image is mean heated zone temperature). There is a very good correlation between the positional movement of the plate in the length axis of movement and the temperature distribution variations. The average hot zone temperature appears to also be related to the length positional movement. In this instance the high average heated zone temperatures correlate with the lowest length positions, where the head unit is covering the smallest region of the plate. Conversely, the lowest average heated zone temperatures are related to the highest length position values.

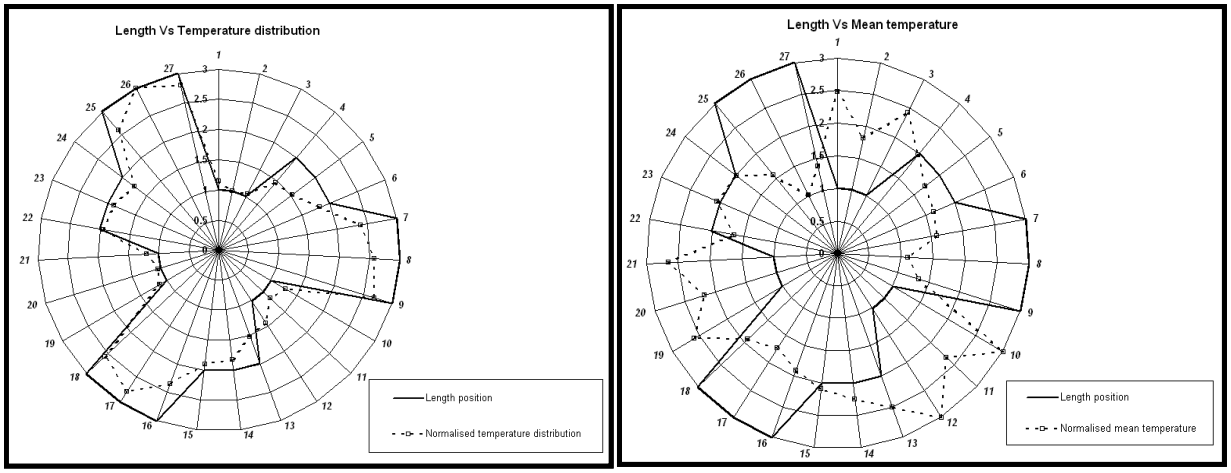


Figure 10-7 : Effect of varying length position on heated region temperature distribution (left), and heated region mean temperature (right)

10.3.2 RESULTS - HEIGHT POSITION EFFECTS

The effect of varying the height of the plate within the head unit aperture is shown in the graphs below (Figure 10-8). Height position appears to be independent of variations in temperature distribution and average plate temperature.

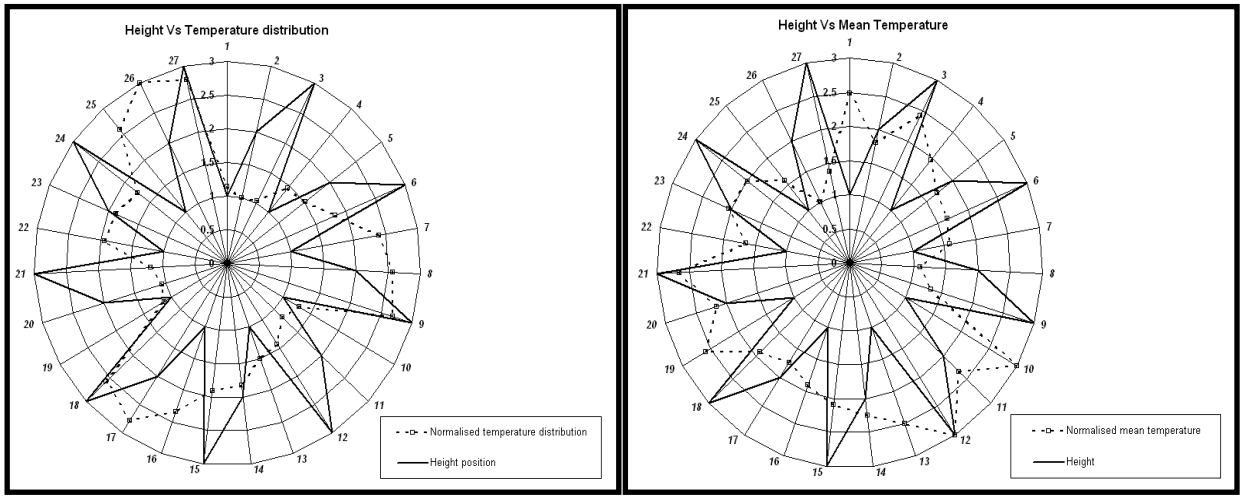


Figure 10-8 : Effect of varying height position on heated region temperature distribution (left), and heated region mean temperature (right)

10.3.3 RESULTS - ROTATIONAL POSITION EFFECTS

The effect of varying the rotational position of the plate within the head unit aperture is shown in the graphs below (Figure 10-9). Positional rotation appears to be independent of variations in temperature distribution and average plate temperature.

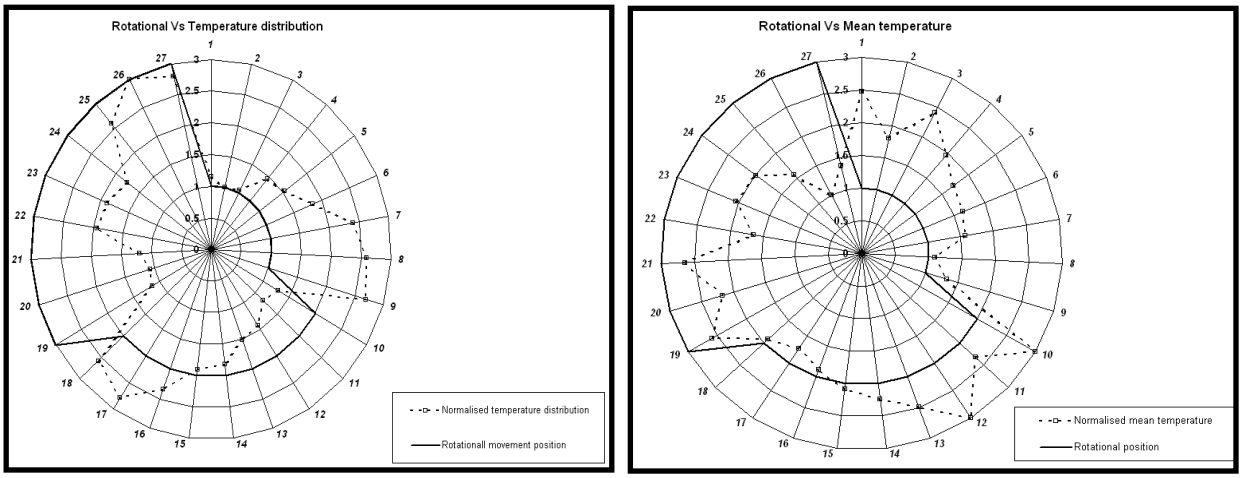


Figure 10-9 : Tip - Effect of varying rotational position on heated region temperature distribution (left), and heated region mean temperature (right)

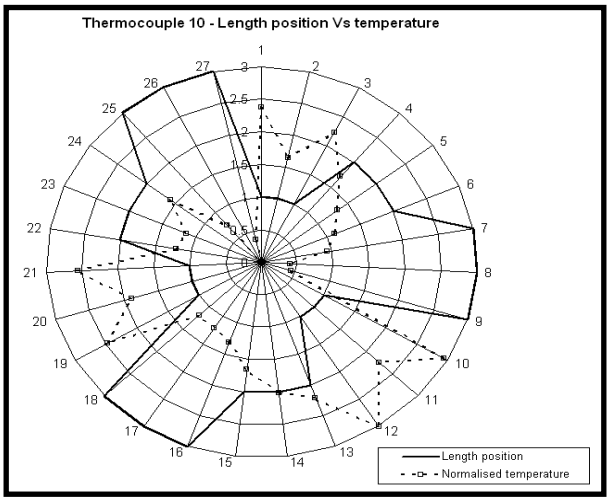


Figure 10-10 : Tip - length positional variation at thermocouple 10

10.3.4 DISCUSSION – POSITIONAL SENSITIVITY

The only significant trend from these summary graphs is that length position is closely linked to temperature distribution. This is due to the fact that varying the length position of the head unit on the plate effects the amount of plate being heated. This coupled with

the fact that isotherms are tightly packed at the edges of the heated zone and length movements will result in some of the thermocouples being positioned closer to the edges of the heated zone.

This phenomenon was investigated further by plotting the thermocouple temperatures against height, length and rotational position for all 27 tests and all thermocouples positioned within the heated region. Not all the data are presented here, however for the majority of the thermocouples the temperatures achieved in each test closely correlated with the length positional movement (see Figure 10-10). However, it is worth noting that the correlation is actually an inverse one in that where the length position is at its highest the temperatures are generally at their lowest. The highest length position is related to the smallest amount of plate being heated and the lowest temperature in the heated zone temperatures. This is because as one moves the plate out of the head unit the thermocouples move from the hottest region in the head unit to cooler region. Also a large driving force for conduction away from the hot region reduces the maximum temperature of a smaller region more than a larger one.

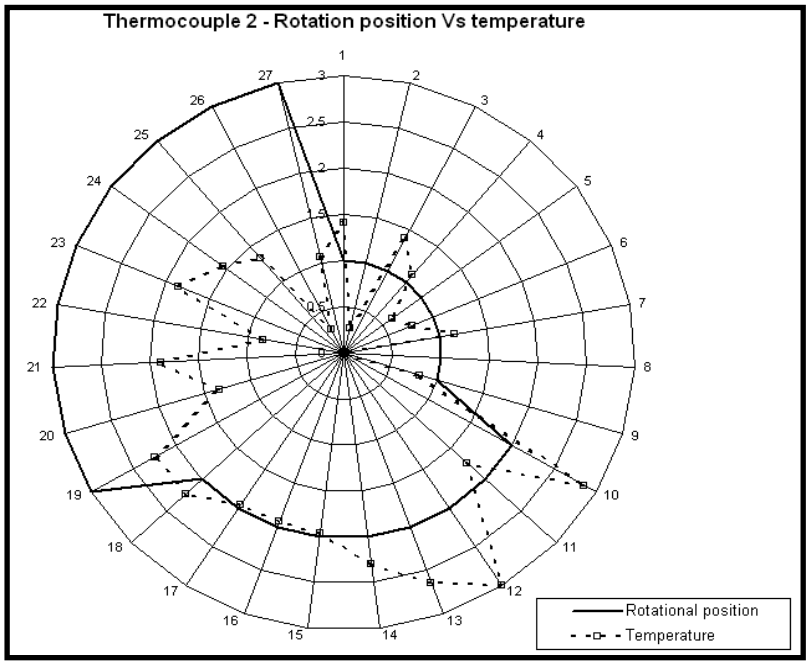


Figure 10-11 : Tip - rotation positional variation at thermocouple 2

The temperature of thermocouple 2 correlated with variations in rotational movement for all 27 tests completed (Figure 10-11). In the case of the temperatures achieved by thermocouple 2 in these tests, the maximum value was achieved with the plate in its neutral position, however as one rotates the plate (clockwise or anticlockwise) the temperature reduces. The reason for this correlation is in the efficiency of the jets acting across the plate. When the plate is centrally positioned within the head unit, jets of equal length are impinging perpendicularly on each side, therefore the heat transfer from these jets is even. As the plate is rotated the length of these jets and their angle of impingement varies from side to side, such that different levels of heat transfer are experienced on each side. As the heat transfer from a jet does not change proportionally with jet length [84], and reduces with angles less than 90°[126], then the overall heat flux into the plate due to two different length jets acting on each side is unlikely to be the same as if they were the same length. A noteworthy point is that the relationship between plate rotation and thermocouple temperature shows no significant trend for the other thermocouples positioned within the heated zone.

10.3.5 KEY OUTCOMES – POSITIONAL SENSITIVITY

The positional data described above suggest that length movement has the largest effect on plate maximum temperature and heat zone distribution. This is due to the fact that changing the length position of the head unit on the plate acts to reduce the size of the heated region. Also, the tightly packed isotherms present at the edges of the heated zone act to dramatically reduce the temperature of thermocouples positioned within this region.

10.4 GENERAL OUTCOMES

The data presented in this section highlight the significance of placing any region requiring heat treatment well within the jet region and oversizing the head unit to fully encapsulate the repair and some parent material. It is also important going forward with the development of this system to investigate the use of more thermally stable materials in the inlet pipe to reduce movement at higher temperatures.

However, the data presented do highlight that strong trends exist between average temperature, temperature distribution, temperature offset and flow rate. The positional data also highlight that as long as the region requiring heating is contained within the head unit, that positional variation does not significantly affect the temperatures observed in the under head region. This demonstrates within the limits tested in this work the gas jet impingement system is not particularly susceptible to stand-off variations. This is a desirable quality when dealing with components requiring repair after damage in service.

11 MODELLING - COMPUTATIONAL FLUID DYNAMICS (CFD) ANALYSIS OF JET HEAT TRANSFER

Computational fluid dynamics (CFD) was used to determine the heat transfer of the argon jets at the particular flow rates used in the gas jet impingement local heat treatment system. Fluent 6 (later updated to Fluent 12) was used with Gambit as a pre-processor to produce a number of models to gain a better understanding of the heat transfer of argon impingement jets with morphologies similar to those used in this system.

11.1 CFD MODELLING STRATEGY

Within the field of impingement jet research the general trend has been towards highly turbulent gas jets utilising high flow rates to generate maximum heat transfer. In the system presented here, laminar gas jets are used to heat thin sections. In the case of the local heat treatment system, there are a number of limitations when designing a jet array capable of heating the required region. Firstly, one must ensure that the region to be heated is sufficiently covered by the jet array. If coverage is insufficient then the regions close to the edge of the heated zone will display positional sensitivity (see section 10). Secondly, the mass flow rates available to the designer are limited by the economics of using an inert gas from a shop or bottle supply.

The optimum parameters defined in the literature may not necessarily be appropriate in the design of such a system. The majority of the literature focuses on jets with an exit Reynolds number of >2000, hence turbulent flow. Gardon and

Akrifat [84] give basic correlations between laminar flow and local heat transfer, but do not determine any significant relationships. However in the case of this localised heating method, jet exit Reynolds numbers of between 300-1000 are typical. An attempt is made here to develop understanding in this area and determine the capability of these argon jets operating in a laminar regime at the nozzle exit.

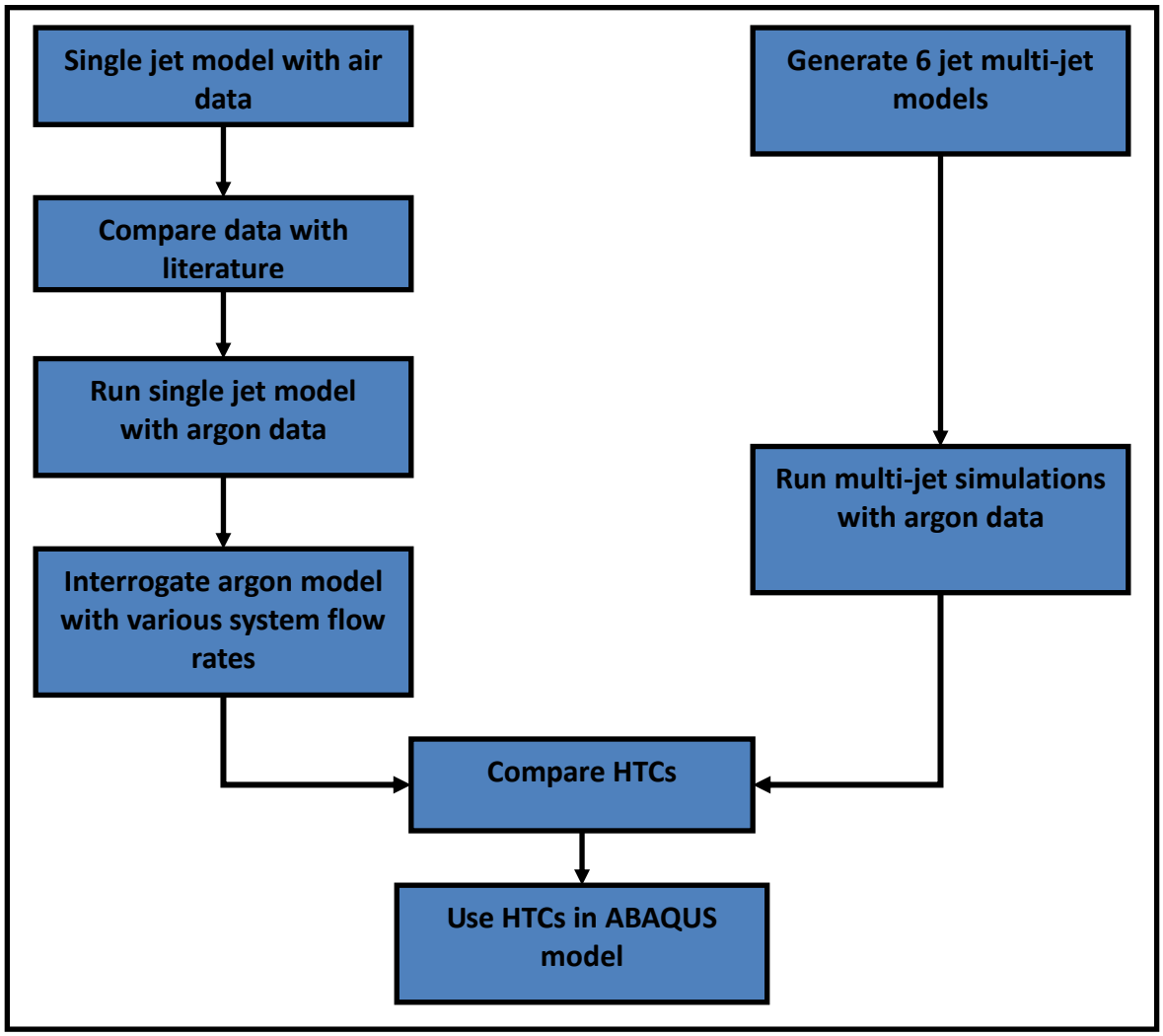


Figure 11-1 : CFD modelling strategy

Figure 11-1 shows the methodology used. Two strands are explored investigating both individual jet modelling and multi-jet modelling. Single submerged air jets with turbulent flow at the jet exit were simulated in 3D. The resulting heat transfer coefficients generated from these can be compared with the available literature. Argon data was then used in the model to run simulations at various system representative flow rates[‡‡‡‡]. In order to ensure the discrete jet was representative of a jet within a head unit like that shown in Figure 7-7 a unit cell approach was used. This unit cell can be modified by altering the boundary conditions to represent different regions of the head unit array (see Figure 11-4). A multi-jet model was then produced, simulating a single row of 6 jets in order to understand the effects of jet-to-jet interaction on the heat transfer achieved. The focus of these investigations was the under-jet region, which are validated against the literature. Regions outside the head unit are not discussed in this section. The heat transfer coefficients produced from the single jet and multi-jet models are compared to check cross-correlation of the values produced.

Due to the prohibitive run-time of a full head model incorporating component geometry, the CFD was limited to these simplified arrays. However the heat transfer coefficients produced by the CFD were used as starting points for the boundary conditions used in the ABAQUS finite element simulations for application to ‘real’ components.

[‡‡‡‡] System representative flow rates are those used in experimental testing shown to produce the required level of heating in the part.

11.2 MODEL CONFIGURATION

11.2.1 SINGLE JET IMPINGEMENT MODELLING – AIR

A single jet model was constructed with air as the fluid operating in a turbulent regime. To obtain the most accurate heat transfer coefficients the cell size within the mesh was kept low (at around 0.1mm or less). Both the k-epsilon and k-omega two-equation turbulence models [104,126] were tested for these simulations, with the best correlation obtained from the k-omega model with SST corrections. The selection of the k-omega model was also due to the previously reported superior performance in resolving boundary layer flows and near-wall conditions [127, 104]. As heat transfer data was calculated from this model it was considered important that the model be accurate close to the wall. It was difficult to obtain a converged solution with the k-epsilon model. The models were run as steady state simulations and the solutions were considered converged when the residuals of the velocities, turbulence and continuity equations had reached values below 10^{-3}. The energy equation was considered converged when its residual reached a value of 10^{-6}.

Density	1.225 kgm^{-3}
Viscosity	1.7894e-5 $kgm^{-1}s^{-1}$
Heat capacity	1006.43 $Jkg^{-1}K^{-1}$
Thermal conductivity	0.0242 $Wm^{-1}K^{-1}$

Table 11-1 : Air property data [114]

The flow rate used in this simulation was 0.0001513 kg s^{-1} and the data in Table 11-1 were used to characterise the properties of the fluid. The mesh used in the simulations is shown in Figure 11-2. During initial set up trials three mesh sizes were tested (varying from 1e-4 m to 5e-5 m) to check for any signs of mesh sensitivity. Although the two fine mesh sizes showed little variation in the

results observed, the smallest was chosen to reduce the likelihood of meshing errors in subsequent tests.

Black portions of the mesh in Figure 11-2 are the jet plate and substrate (target) whilst the small blue region shows the inlet at the jet entrance. The red region was designated as an outflow region with a gauge pressure set at 0MPa in order to allow the flow to leave the jet unit cell. In reality the exhaust flow from the head unit enters a chamber which is at atmospheric pressure. The yellow regions were assigned symmetry conditions to simulate the effect of having adjacent jets on all four sides. The final region of the model is the boundary layer mesh located at the

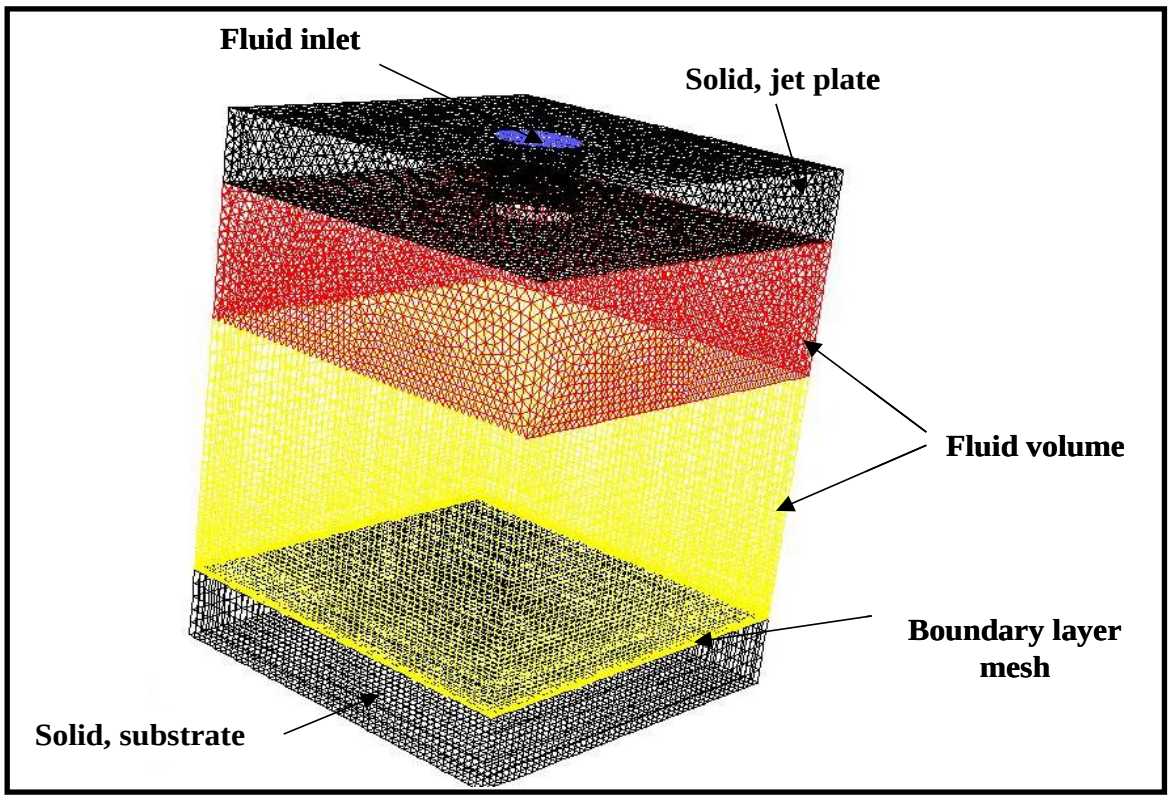


Figure 11-2 : Unit cell mesh (medium mesh size shown), heat transfer was calculated at the plane between the fluid volume and the solid substrate. Each of the red and yellow planes on the faces of the unit cell could be set in the wall, symmetry or outflow boundary condition depending on the position of the jet in the array being modelled. The solid substrate was set at a constant temperature of 600 K.

base of the yellow region close to the black region. This is where the heat transfer is calculated and therefore the resolution of the mesh must be high in this region.

Two unit cells were used for this modelling exercise, both of 5mm width and length. However the jet heights (H) of the two unit cells are 5 and 8mm (see Figure 11-3), the reason for this is that the system in its current configuration has head units manufactured giving a jet length of 8mm. However, the addition of a second smaller jet allowed a level of understanding to be obtained as to how this variation affected the heat transfer coefficients. Also, due to the curved nature of the components being heat treated and the straight nature of the current jet plates a 3mm variation is similar to what one would expect to see in the system due to component/test piece misalignment.

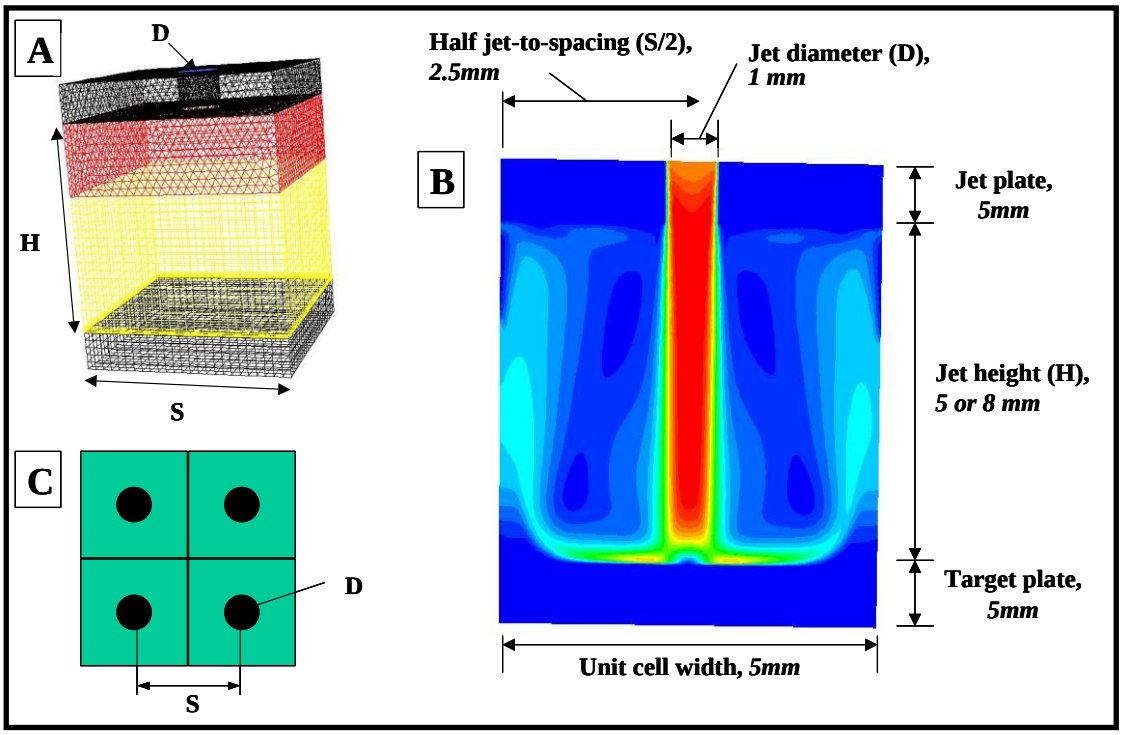


Figure 11-3 : Dimensions and regions of unit cell used in Fluent modelling of single jet. Image A shows the 3D view of the mesh, image B is a cross section through the model highlighting the characteristic impinging jet, image C shows plan view of a jet array of 4 unit cell jets.

The use of a unit cell model allows one to impose wall or symmetry boundary conditions. The effect of the position of an individual jet within a larger array can be assessed. Figure 11-4 highlights the various ways in which a symmetry boundary condition (red line) can be used to simulate the various positions within a larger array.

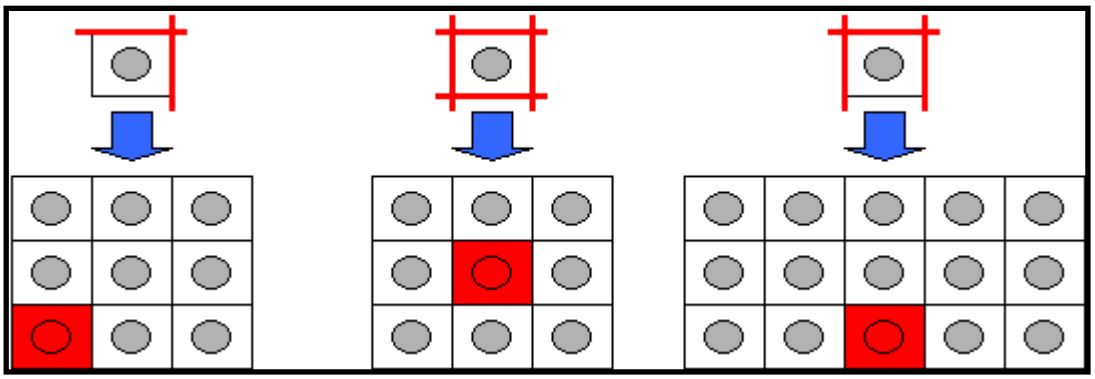


Figure 11-4: Schematic representation of how the unit cells could be used to simulate the effect on an individual jet of being positioned in a larger array. From left to right, corner jet position, centre jet position, front jet position.

11.2.2 BOUNDARY CONDITIONS

In all unit cell models the boundary conditions defined in Table 11-2 (below) were used. Figure 11-5 and Figure 11-6 show the model geometry and location of boundary conditions along with some specific mesh details.

Boundaries	Colour in figures	Boundary conditions
Outflow	Red	Pressure is atmospheric (0MPa gauge pressure), 300K, no turbulence
Symmetry	Orange	
Inlet	Blue	Mass flow inlet
Wall	Green, grey	Heat flux of 0
Gas contact	not visible	Coupled (Thermal), perfect conduction between gas and plate assumed

Table 11-2 : Boundary conditions used in CFD modelling, colours correlate to Figure 11-2, Figure 11-3, Figure 11-5, and Figure 11-6

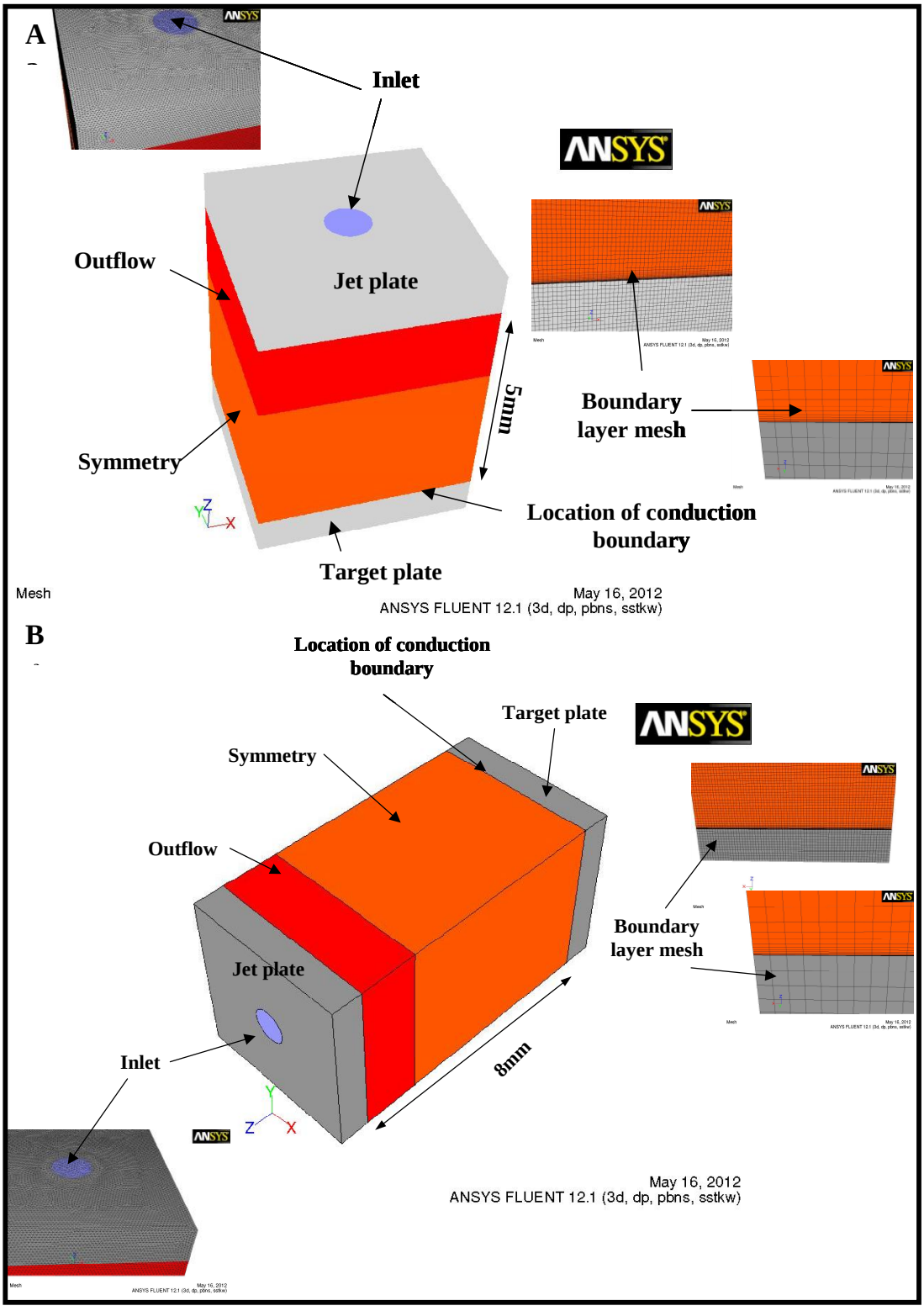


Figure 11-5 : 5mm (A), and 8mm (B) unit cell geometries with boundary conditions, grey for wall, orange for symmetry, blue for inlet flow, red for outflow . Note mesh details, including inlet and boundary layer meshes

11.2.3 SINGLE JET IMPINGEMENT MODELLING – ARGON

Density	1.64 / 0.55 kg m^{-3}
Viscosity	= 2.39e-7 + 8.84e-8x - 5.02e-11x^2 + 1.56e-14x^3 kg m^{-1} s^{-1} where x = Temperature (K)
Heat capacity	520.6 J kg^{-1} K^{-1}
Thermal conductivity	= 1.74e-4 + 6.75e-5x - 3.47e-8x^2 + 9.63e-12x^3 W m^{-1} K^{-1} where x = Temperature (K)

Table 11-3 : Argon data [114]

The same basic model set-up as that described above was used in the argon single jet model. The argon data in Table 11-3 were used to characterise the properties of the fluid, polynomials were used to describe the viscosity and thermal conductivity of the fluid with temperature and these were derived by fitting curves to the data provided by Din [114]. Also, the density of argon varies with temperature and therefore two different values are given, one at room temperature, 1.64 kg m^{-3} and one at the processing temperature 0.55 kg m^{-3}. The reason for using two densities is to assess the effect of variation on the heat transfer coefficient. It is important to note at this point that within the system the flow rate is measured with the gas at approximately room temperature. Therefore the mass flow rate used in the simulation is calculated using the density of argon at room temperature. The effects of density on heat transfer are discussed later.

Secondly, the system is intended to run within an argon atmosphere, from which any significant levels of air are removed before the process is started. Finally the model is run as a single-phase simulation due to the fact that the under head

region very quickly becomes predominately argon as the air is expelled (see Figure 11-21 and Figure 13-12 taken less than 1 second after the gas was been turned on).

11.2.4 MULTI-JET MODELLING – ARGON

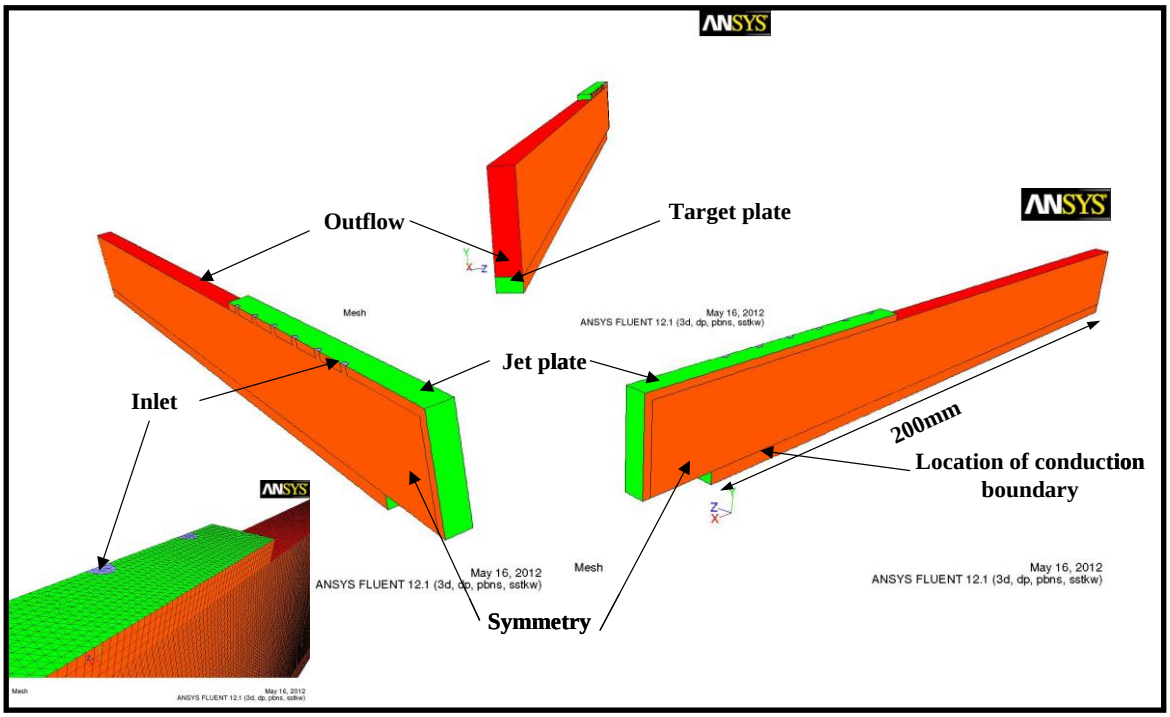


Figure 11-6: Multi-jet mesh, similar colours as in unit cell model to denote boundary conditions. Green for wall, orange for symmetry, blue for inlet flow, red for outflow

The same basic model set-up as that described above was used in the argon 3D multi-jet model. Only the top half of the head unit and a single row of jets was modelled to reduce run time. To obtain the most accurate heat transfer coefficients the cell size within the mesh was kept low (at 0.25mm), Figure 11-6 shows a close-up of a portion of the mesh (inset bottom left). Again both the k-epsilon and k-omega turbulence models were assessed for these simulations. The models were again run as steady state simulations and the solutions were considered

converged when the residuals of the velocities, turbulence and continuity equations had reached values of below 10^{-3}. The energy equation was considered converged when its residual reached a suitably small value of 10^{-6}. In these simulations as with previous unit cell models the substrate was maintained at a constant temperature of 600K in order to allow heat transfer calculations to be conducted.

11.3 CALCULATING HEAT TRANSFER COEFFICIENT FROM MODELLING DATA

In order to calculate the heat transfer coefficient for the jets, the total heat flux in each mesh cell on the target plate was extracted from the software. This could then be used to calculate the heat transfer coefficients for analysis. Given that convective heat transfer is defined by the following formula;

Equation 11-1: $Q = Ah\Delta T$ [75],

where Q is heat flow due to convective exchange (in Watts), A is the exchange area (in m^2), h is the heat transfer coefficient ($W\ m^{-2}\ K^{-1}$) and ΔT is the temperature difference between the target plate and the fluid.

Equation 11-2: $q' = h\Delta T$,

Heat flux (q') is defined as heat flow (in Watts) per unit area (m^2), giving;

or

Equation 11-3: $h = q'/\Delta T$**,**

ΔT is calculated following convention for impingement jet heat transfer literature [75] by using the difference between the jet exit gas temperature and the plate temperature (imposed to remain constant at a value of 300K (unit cell) or 600K (multi jet) in the model to allow calculation of the heat transfer). This assumes that the jet exit temperature is in thermal equilibrium with the ambient and not equal to the plate temperature. A value of heat flux (q') is obtained from the CFD modelling in each cell.

Therefore by using Equation 11-3 values of the heat transfer coefficient in each mesh cell can be calculated. As mentioned previously in the literature review, the convention within impingement jet research is to use the dimensionless Nusselt number (Nu) as the measure for impingement jet heat transfer. Therefore in order to calculate the Nusselt number for each of these cells Equation 2-5 from page 42 is used. Here d (the characteristic length, see Figure 11-3) is taken as the jet diameter for impingement jet analysis, and k is the thermal conductivity of the fluid (W m^{-1} K^{-1}). The use of d as the characteristic length for a round nozzle is in agreement with authors such as Viskanta [82], Martin [76], and Incropera [75]. It may be appropriate to express the jet averaged Nusselt number, which is carried out by calculating the Nu for each individual cell in the target plate of the model and finding the arithmetic mean of all these values. This uses the following formula;

Equation 11-4:
$$\overline{Nu} = \frac{d}{kn}\sum_{i=1}^{n} h_i$$

Once these calculations were completed one can plot the variation in heat transfer coefficient across the centre line of the jet or calculate the jet average heat transfer using the method described.

11.4 RESULTS AND DISCUSSION – SINGLE AIR JETS

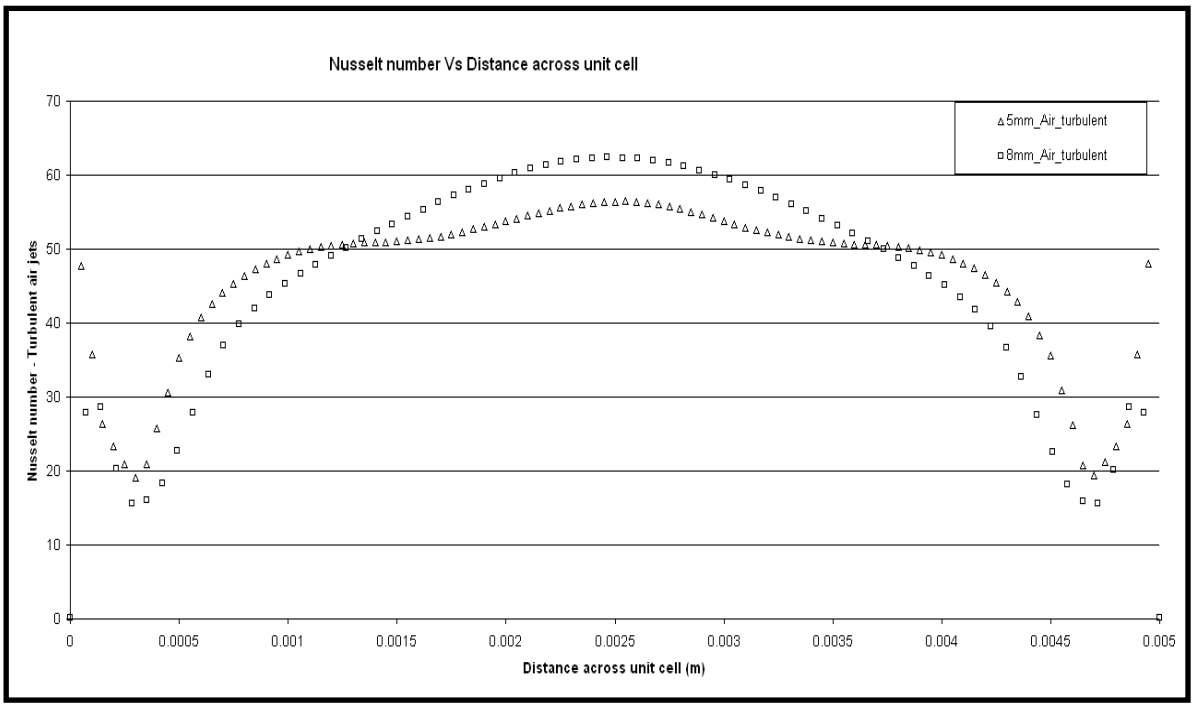


Figure 11-7 : Nusselt number plots across 8mm and 5mm turbulent air jets

Figure 11-7 above shows a plot of Nusselt number against distance across the unit cell (through the centre of the stagnation zone) for turbulent air jets with a jet length of 8mm and 5mm. The peak Nusselt numbers are 62 and 57 for the 8 and 5mm jets respectively. However, the 5mm jet gives a more uniform (but lower) heat transfer across the central portion of the jet. The Nusselt number reduces with radial distance from the stagnation point but then increases again in the wall jet interaction zone at the edges of the unit cell, as wall jets from adjacent jets interact.

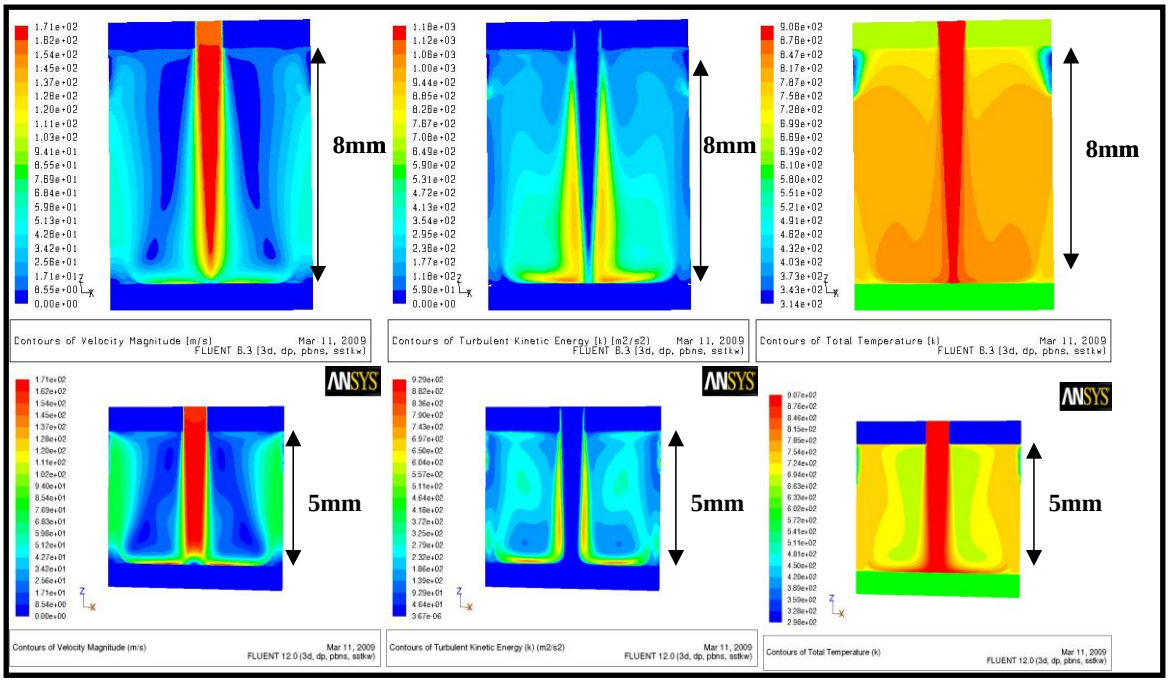


Figure 11-8 : Velocity, turbulence and temperature plots for 8mm jets (top), and 5mm jets (bottom)

Figure 11-8 shows the velocity magnitude and turbulent kinetic energy plots for the results of the single jet air models. Noteworthy were the higher velocities present in the interaction regions of 5mm jets, also the potential core (region of constant velocity) was wider than that for the 8mm jet. A further observation was that the turbulent region of the 8mm jet crossed the whole jet at the point which it interacted with the target plate. In the case of the 5mm jet, the potential core (seen as the blue region with zero turbulent kinetic energy) was still in existence as the jet came into contact with the wall. This was the reason for the higher peak heat transfer coefficients seen in the graphs in Figure 11-7.

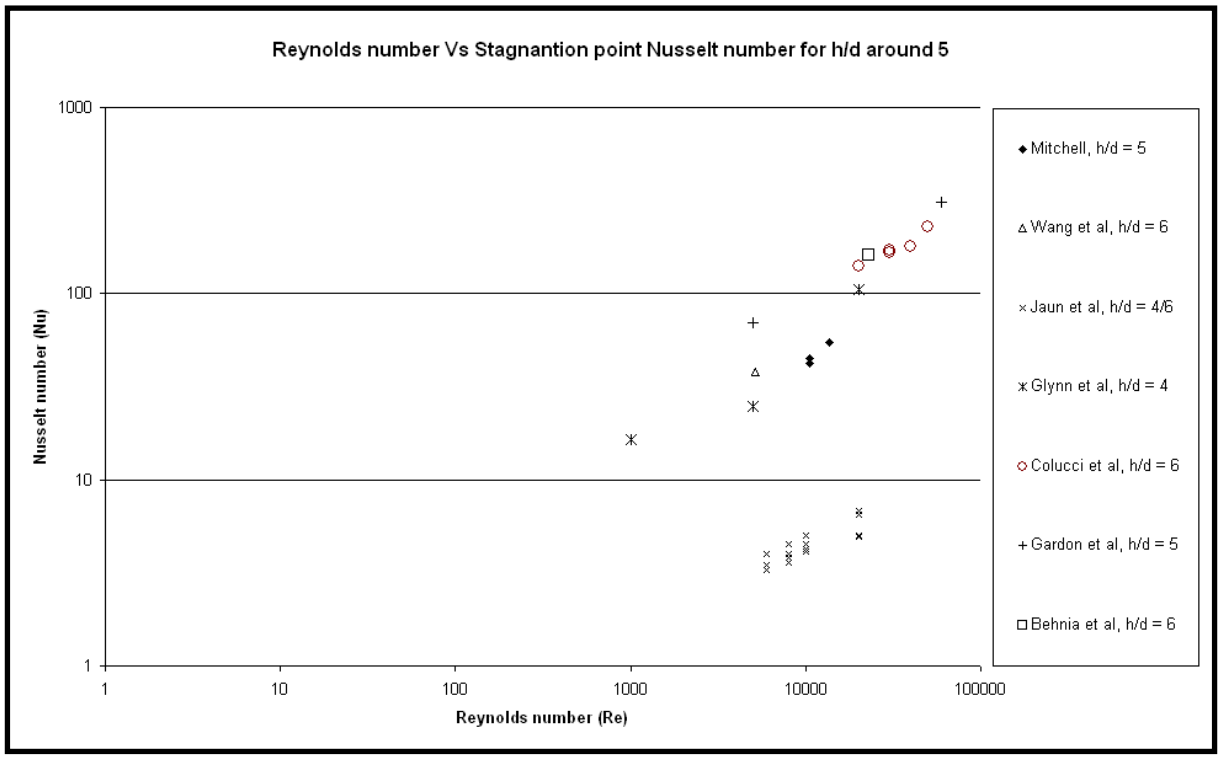


Figure 11-9 : Reynolds number Vs stagnation point Nusselt number from a range of sources for h/d ratios of around 5. Modelled values from this thesis circled in red.

As mentioned previously the most commonly used figure for comparing heat transfer due to impinging jets is that of the Nusselt number (Nu). Figure 11-9 shows a range of data from the literature for various jet geometries, with Nu plotted against Reynolds number. The data from the single air jets described in this section had also been plotted on the same graph to show correlation with the published data. A significant amount of the literature available on the subject uses a height to diameter ratio (S/D) of 5. Figure 11-9 plots data from the literature survey for jets with an S/D ratio of 5 or 6 along with the data presented in this thesis where S/D is 5. It is important to note at this juncture that the Nusselt numbers plotted on these graphs are stagnation point values and represent the peak heat transfer across an impingement jet. However, Gordan and Akfirat note that the peak heat transfer for an impinging jet is not always at the centre of the

stagnation point. In fact secondary peaks are sometimes found, particularly in those jets where the potential core is still intact on impingement with the target.

11.5 CONCLUSION – SINGLE AIR JETS

The correlation with the published data is good and shows that the heat transfer generated in the Fluent simulation using the k-omega model with SST corrections turbulence model to be a good approximation of the problem. This provides sufficient confidence for one to pursue the use of this method in order to establish the heat transfer coefficient for the local heat treatment system, which was then used in the ABAQUS modelling activity, described later.

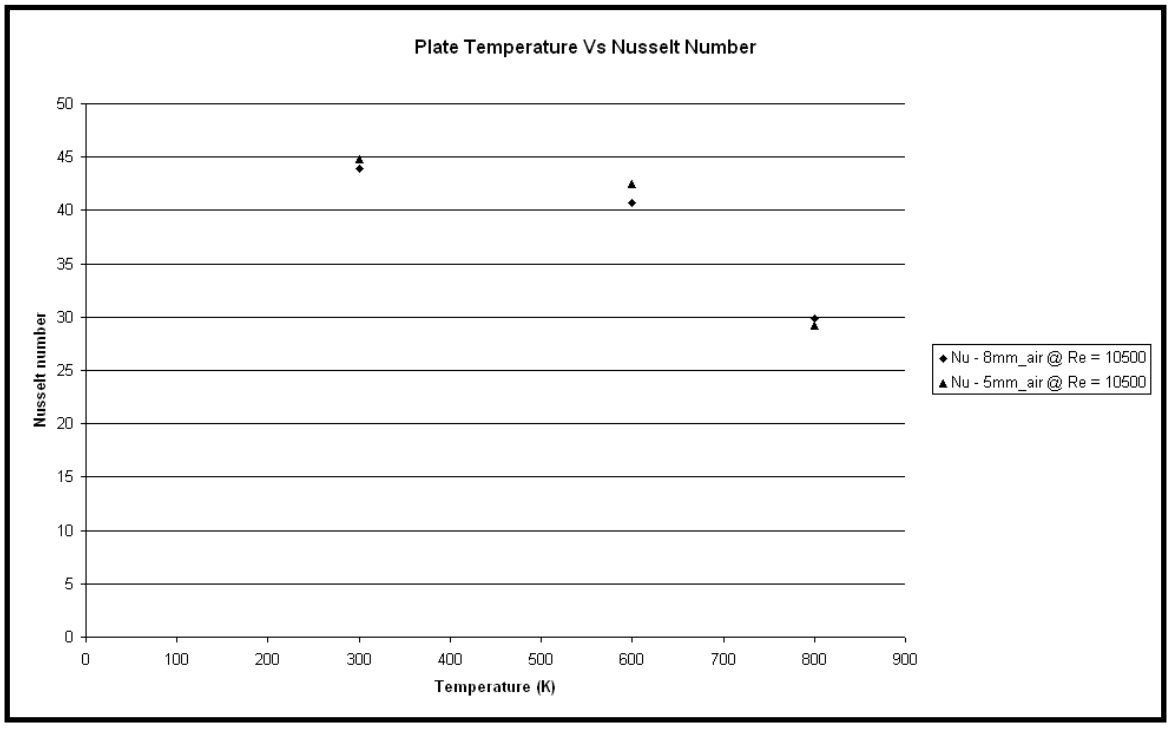


Figure 11-10 : Graph highlighting the variation in Nusselt number with substrate (plate) temperature in turbulent single jet unit cell models with jet diameters of 1mm and jet heights of 5 and 8mm.

The substrate material that the jets impinge upon in the following simulations was maintained at a constant temperature (300K for the single jets and 600K for the multi-jets). Figure 11-10, highlights the variation in Nusselt number (and therefore heat transfer coefficient) as a result of varying substrate temperature for a turbulent submerged unit cell air jet for two different jet lengths. As the substrate approaches the gas temperature (in this case 893K) the heat transfer coefficient reduces (due to a reduced ΔT).

One can see that the variation in Nu was relatively small between a substrate temperature of 300K and 600K before it dropped off significantly towards the gas temperature. This is the reason for choosing values of 300K and 600K for the single and multi-jet steady state simulations were selected.

11.6 RESULTS AND DISCUSSION – SINGLE JET ARGON

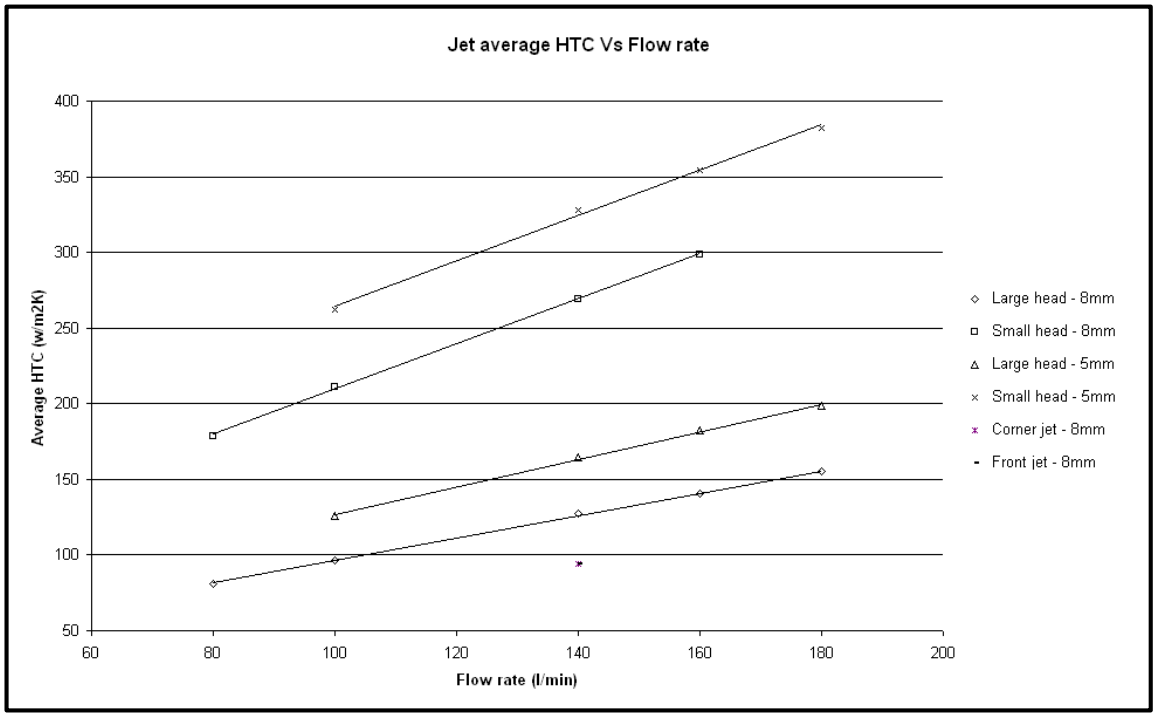


Figure 11-11 : Jet average heat transfer coefficients for system representative flow rates. (See Figure 11-4 for reference to unit cell locations given in graph legend)

Figure 11-11 shows the relationship between jet averaged heat transfer coefficient and flow rate for single 5 and 8mm argon gas jets for the range of flow rates used in the system. Here the jet average heat transfer coefficient was calculated by taking the arithmetic mean of all the heat transfer coefficients calculated for each cell on the target plate. The heat transfer coefficients were calculated as described previously.

Although the total flow rate is shown on the graph for reference, the actual flow rate used in the model was calculated by dividing the total flow by the number of holes in a given head unit and using that individual jet flow rate in the model. Two different head units are represented in these data with different numbers of jets producing different flow rates per hole. The large head unit by virtue of covering a

larger area of the test piece has a larger number of holes, which makes the flow per hole lower than that of the small head unit for a given total flow rate. The flow controllers limit the maximum total flow rate to 200 l min^{-1}, and the data in section 10 highlight that below 80 $l.min^{-1}$ the system is ineffective at heating the required region (especially in the case of the leading edge heat treatment).

The data in Figure 11-11 shows a strong trend towards increasing heat transfer coefficients with increasing flow rate. In both the large and small head configurations the higher heat transfer coefficients are shown for the smaller head unit with an overall maximum of 382 W m^{-2} K^{-1} for a flow rate of 180l min^{-1}. The 5mm jets achieve the highest jet averaged heat transfer coefficient for a given flow rate than the 8mm jets in both the large and small head units.

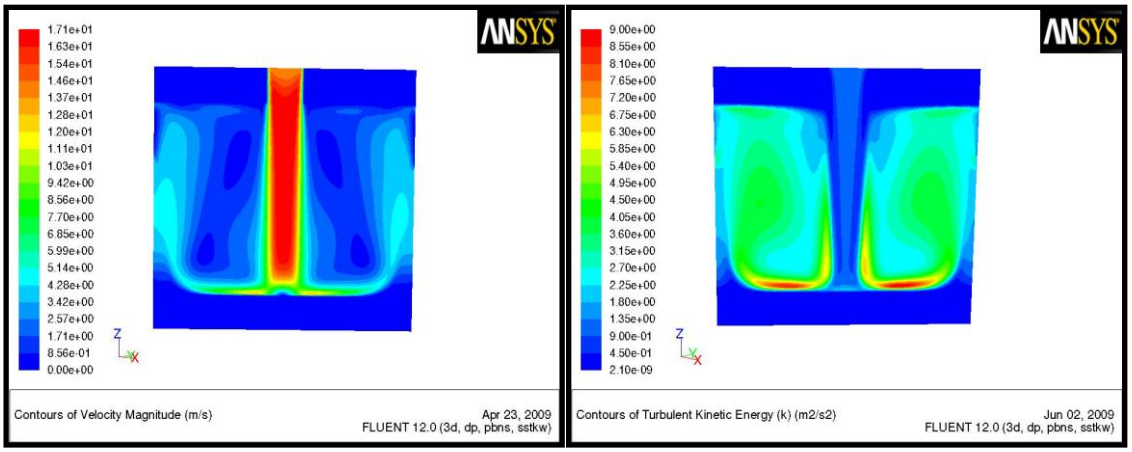


Figure 11-12 : 5mm argon gas jet morphology

The two plots in Figure 11-12 show the velocity (left) and turbulent kinetic energy (right) distributions in the 5mm argon jet within the large head at a total system flow rate of 140 l min^{-1}. The maximum velocity shown in the model is 17.1 m s^{-1} achieved in the core of the jet close to the jet exit. However, this value increases from the initial value of 13.7-14.6 m s^{-1} at the beginning of the jet nozzle. The

potential core of the jet is again present all the way to the target plate as in the turbulent air jet presented previously. In the case of the turbulent kinetic energy plot, the regions of largest turbulence (i.e. between the jet and the surrounding gas) begin much lower down the length of the jet than in the turbulent air jet. The magnitude of the turbulent kinetic energy is low due to the jet being characterised as laminar by the Reynolds number at the jet exit. There is also some evidence of turbulence in the core of the j*et al*ong its entire length although this is such a low value that it would be unwise to draw any significant conclusions from these values. Of significance are the plots shown in Figure 11-8, these show that at larger jet lengths the turbulence effects not only act to reduce the potential core region but also to reduce the velocity in the centre of the jet. This increased level of turbulence also reduced the temperature of the jet at the edges and resulted in a smaller region of the jet being at the in-head gas temperature when it reached the target plate.

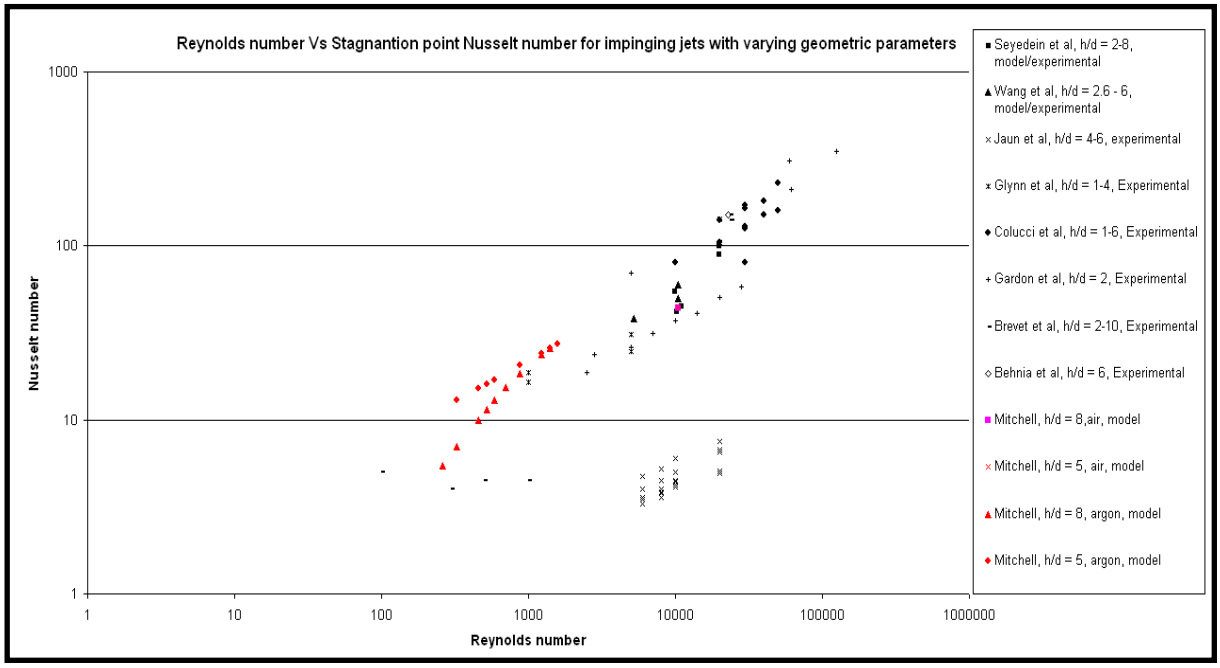


Figure 11-13 : Argon gas jet data plotted against literature data, for Stagnation point Nusselt number

Figure 11-13 (above) shows the data for argon jets at system representative flow rates plotted with the experimental data from the literature. There are less data within the literature dealing with laminar gas jets, such as those used in this work. However the data fit well with the overall proportional relationship between Reynolds number and Nusselt number. Although the literature deals generally with air jets, the use of dimensionless parameters such as Reynolds number and Nusselt number that account for gas properties (such as viscosity, density and thermal conductivity) enable such comparisons to be made.

As mentioned in the literature review all sources agree that Nusselt number increases with increasing Reynolds number, Glyn *et al* [88] suggests that stagnation point Nu is proportional to $Re^{0.5-0.8}$. In the case of Stagnation point heat transfer the relationships generated from the modelling data were as follows (note these are for argon not air);

Equation 11-5: $Nu_{5mm} = 0.8544*Re^{0.4698}$

Equation 11-6: $Nu_{8mm} = 0.0346*Re^{0.922}$

These values fall outside that suggested by Glyn *et al* [88], however it is important to note that these jets are laminar not turbulent as in the case of those described by Glyn. In the case of laminar jets the profile of the Nusselt number through the jet centreline has a more pronounced peak, due to the variations in velocity. In the case of a turbulent jet, the velocity is largely constant through its core (the definition of a potential core). As a result it is hypothesised that this more pronounced peak value explains why the relationship for the 8mm jet falls outside the values from the literature. In the case of the 5mm jet the potential core spreads

across most of the jet as it comes into contact with the target plate (as seen in Figure 11-8).

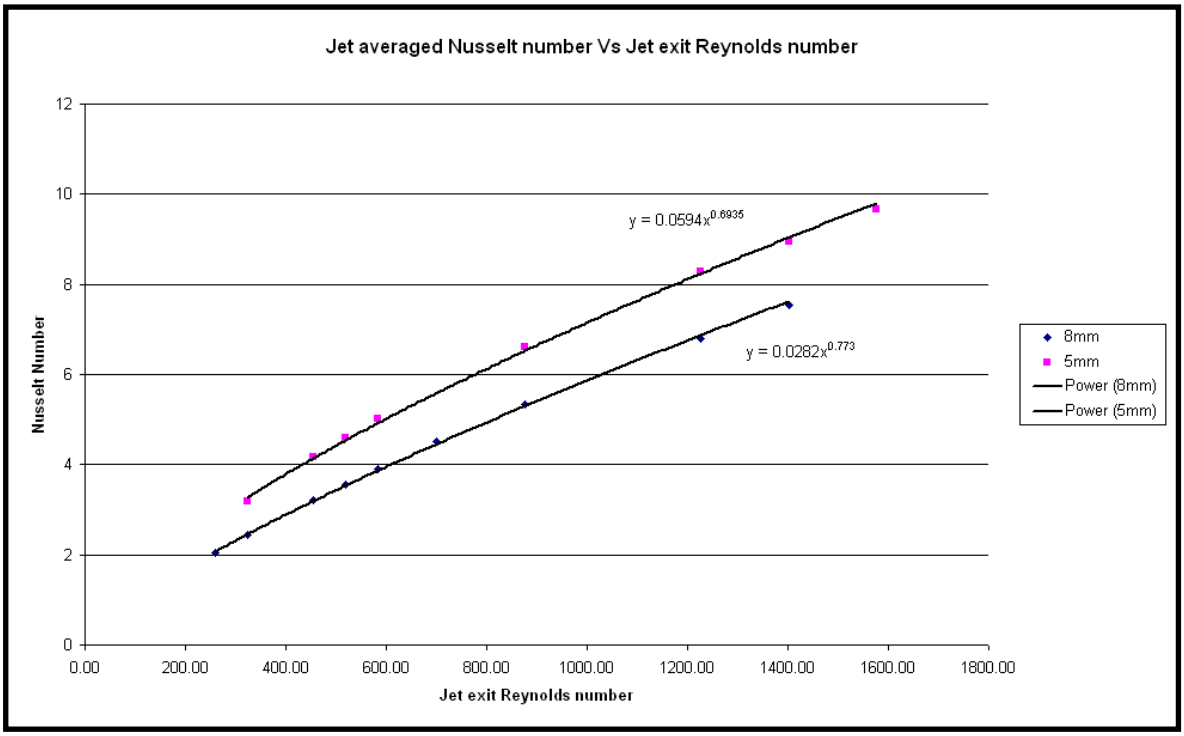


Figure 11-14 : Nusselt number Vs Reynolds for laminar argon jets (s/d ratios of 5 and 8)

Figure 11-14 is a plot of the data generated for the gas jet processing system and shows the relationship between jet average Nusselt number and Reynolds number. The jet averaged Nusselt number is the most useful description of the heat transfer as it describes the overall affect of the jet on the transfer of heat from (or to) the target plate. The relationships generated from the modelling for jet averaged Nusselt number were as follows (note these were for argon not air);

Equation 11-7: $Nu_{5mm} = 0.0594*Re^{0.6935}$

Equation 11-8: $Nu_{8mm} = 0.0282*Re^{0.773}$

These equations reflect the observations of Glyn *et al* [88] and provide a useful relationship between the jet average heat transfer of laminar argon jets and the Reynolds number.

11.7 RESULTS AND DISCUSSION - MULTI-JET MODEL (ARGON)

11.7.1 6-JET MODEL

The images below (Figure 11-15) show the results of *Fluent* simulations for a head unit containing a row of six jets. The top two images show the velocity plots and the bottom two images the temperature profiles for the same model set up apart from the fact that the density has been changed between each simulation. The two images on the left have an argon density of 1.64 kg $m^{-3,}$ whereas the right hand images have a density of 0.55 kg m^{-3}. The reason for assessing the affect of two

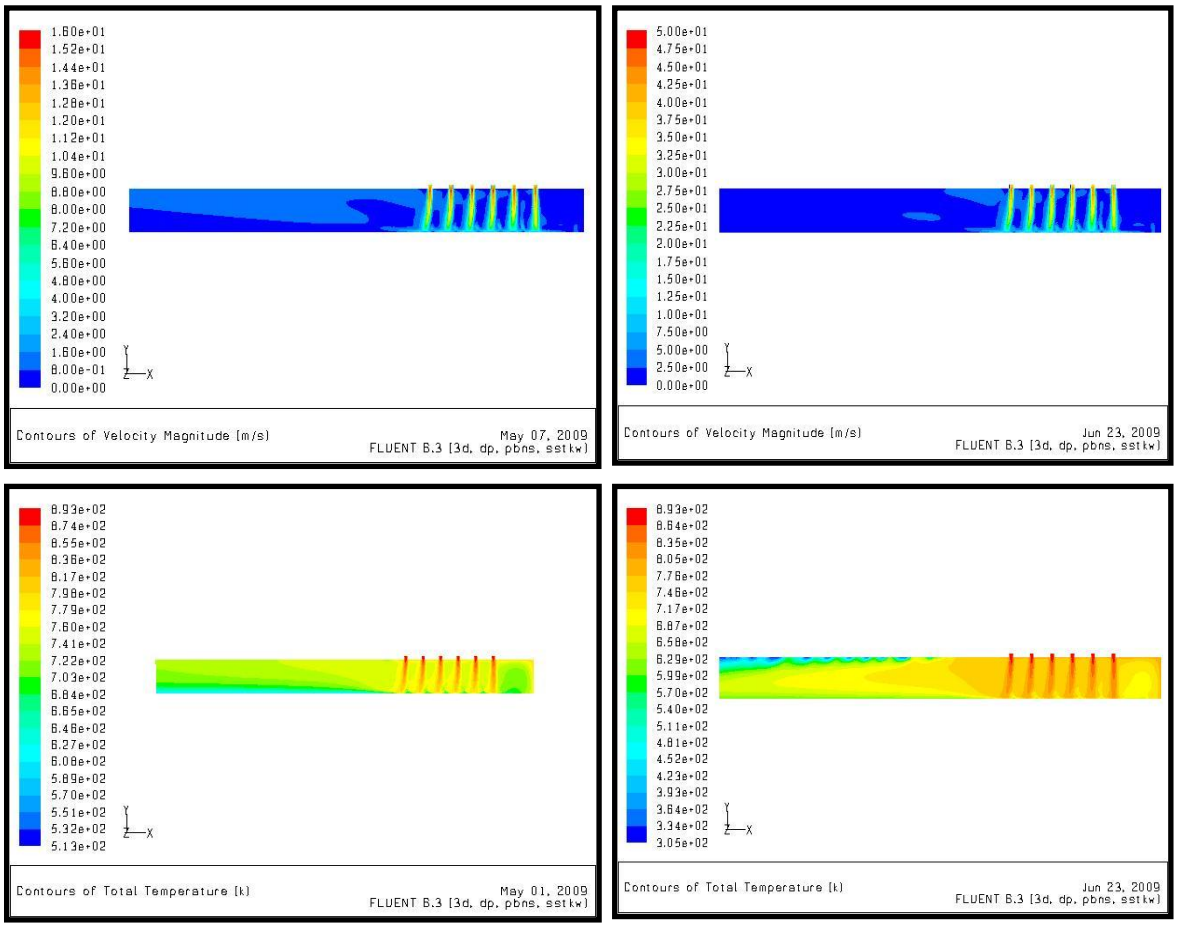


Figure 11-15 : Velocity (top) and temperature (bottom) plots for multi-jet model with room temperature (left) and high temperature (right) argon data

different densities on the model is that it was unclear at which density the gas existed in the system. In reality the volume flow rate is measured and controlled, whilst the argon gas was at room temperature before it entered the heater. Under ideal gas conditions, one would expect the gas to either increase in volume or pressure following Boyle's law. In this situation the gas stream is constrained by the jet exit orifice. However once the gas leaves the head unit the pressure is converted to velocity as the gas becomes free to expand. The high temperature of the gas in the head unit made measuring the pressure at these high temperatures very difficult. Therefore the effect of varying this gas density within the model was investigated to see what effect it has on the results. In these simulations the viscosity and thermal conductivity of the argon was assumed to follow the polynomial relationship defined previously in Table 11-3.

Figure 11-15 also shows the velocity magnitude plot generated using *Fluent* simulations. The velocity of 16 m s^{-1} at the jets exit is slightly above the value of 11.8 m s^{-1} calculated as an average velocity across the jet exit. This was calculated by taking the overall flow rate, dividing by the number of holes and then by the cross-sectional area. However, this is an average value whereas the value shown as red in the Fluent simulation is a maximum value. The images show that the velocity increases due to the reduced density of the gas and the same mass flow rate being used in both simulations. This is a valid input as it is measured and controlled throughout the cycle at the cold end of the system. It is assumed that there was no leaking of the gas during the cycle meaning flow rate was conserved. As a result of this any increase in the volume of the gas (due to a decrease in density at temperature) will have an associated increase in velocity. The velocity

increased from 18 to 50 m s^{-1}, an increase of almost 3 times, associated with a similar magnitude reduction in gas density. The temperature of the gas shown in the bottom images in Figure 11-15 highlight significant differences in the temperature of the gas.

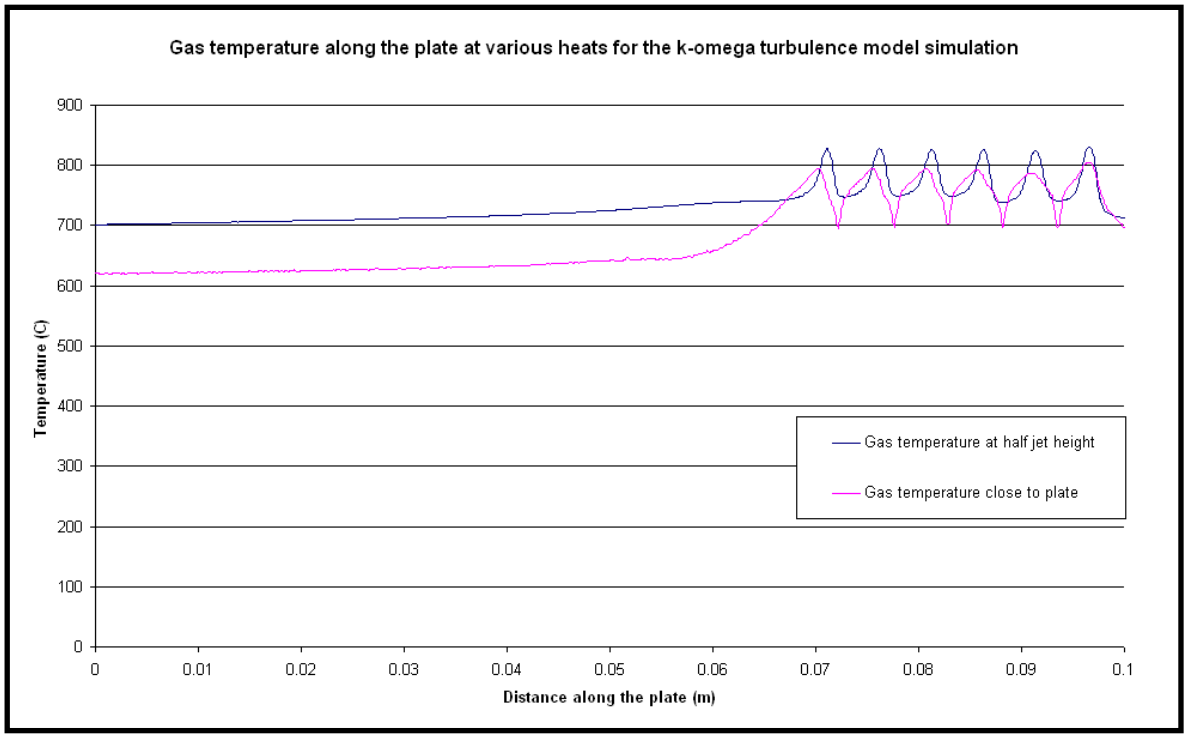


Figure 11-16 : Temperature profiles taken from Fluent simulations

Figure 11-16 shows the temperature contours generated by the Fluent simulations. The gas temperature at the base of the jet is ~800K, slightly lower than the 873K temperature achieved by the plate in this particular set-up during experimental trials. A steady state simulation with the plate maintained at 600K was used in order to allow heat transfer coefficients to be calculated along the plate. This will have acted to reduce the temperature of the gas. Viskanta *et al* [82] noted the importance of using a temperature representative of the gas temperature when calculating the heat transfer coefficient of impinging jets. Figure 11-16 shows the variation in gas temperature with distance along the plate at two different heights

from the plate. The blue line represents the gas temperatures at 4mm from the jet plate (half the jet height), whereas the red line details the temperatures on the upper surface of the plate. As is to be expected, the gas closest to the plate is at a temperature close to that value (600K) due to its cooling effect on the gas. Another interesting point to note on this graph is the slight offset in the peaks on this graph due to the curvature in the jet closest to the exhaust region. The effect of jet deflection due to the cross-flow of the gas is noted in papers by Bailey [89] and Glyn [88], however their jets were at much higher Reynolds number.

11.7.2 IDEAL GAS LAW FOR DENSITY

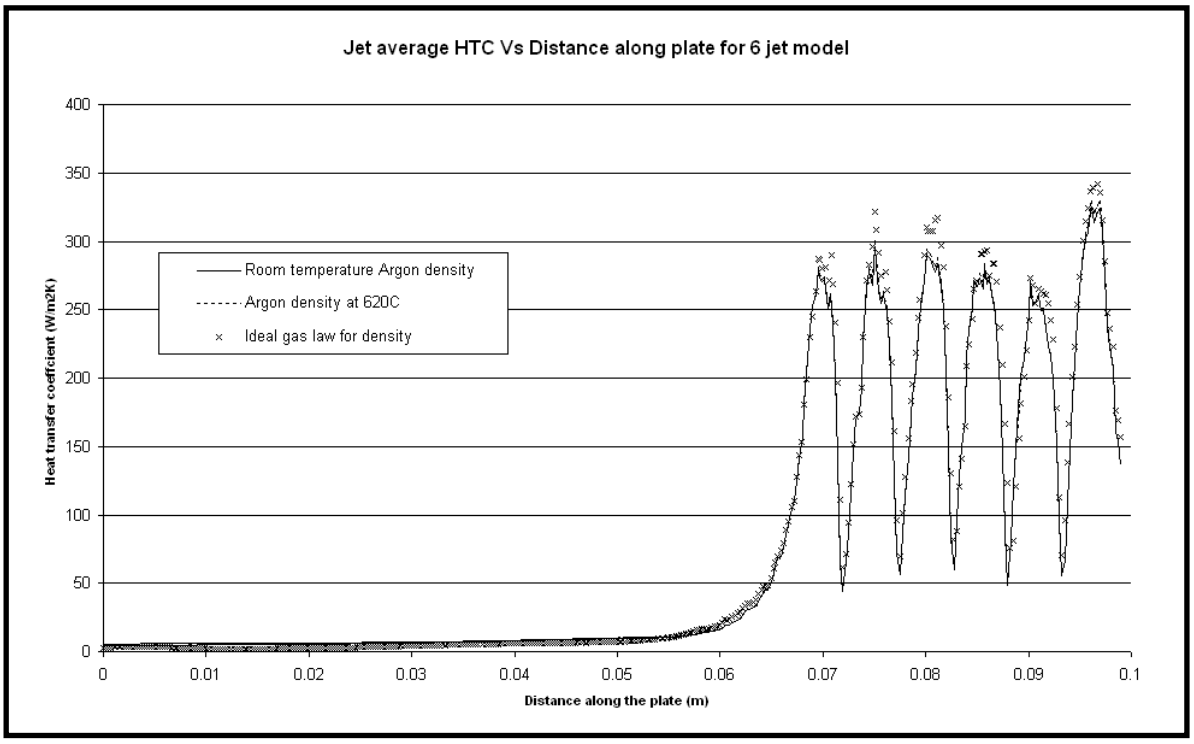


Figure 11-17 : Comparison between heat transfer coefficient plots for different argon densities

Figure 11-17 generated from the CFD analysis shows the values for the heat transfer coefficients predicted in three different Fluent simulations. The lines

represent the heat transfer coefficients across the plate in the case of high density, low density and with the ideal gas law used to account for the changing density of the argon with temperature. Noteworthy from these plots is that the data are consistent for all scenarios, showing that it is the flow rate that has the largest influence on the heat transfer coefficient. Also the difference between the heat transfer coefficient seen in the ideal gas simulation is only slightly different to that of the single densities. The reason for this is that in the regions where the maximum heat transfer exists, i.e. under the jets, the temperature of the gas is fairly uniform resulting in a consistent gas density in this region. Also, the mass flow rate remains constant in all simulations as it is a measured value from the experimental trials. Therefore changing the density in the model (between high and low values) has the effect of increasing the velocities seen in the model in order to maintain the mass flow rate with a lower density. As the same number of atoms come into contact with the plate irrespective of which density is used, the same heat transfer coefficient was achieved in both cases.

11.7.3 WHICH TURBULENCE MODEL GIVES THE BEST RESULT?

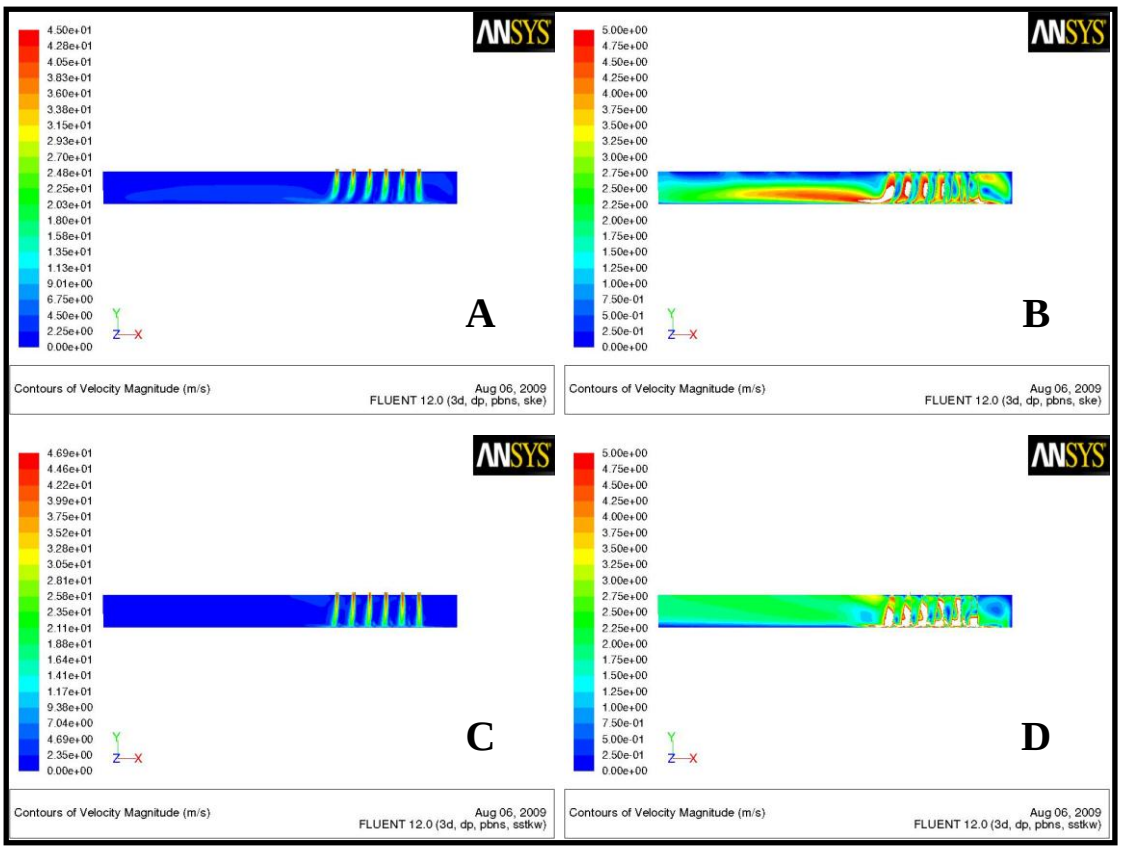


Figure 11-18 : Velocity plots for k-epsilon turbulence model (A&B) using ideal gas law, and for k-omega turbulence model (C&D) using ideal gas law. A & C show maximum velocities, B & D are scaled to show velocities below 5 ms^{-1}

The images in Figure 11-18 show the results of simulations carried out using the ideal gas law to account for the change in density of the argon as it cools on leaving on the jets. A & B are the result from a simulation using the k-epsilon turbulence model, C & D are the results using the k-omega model. There are distinct differences in the two results, with the k-omega having much more well defined cores to the jets. The central jet velocities are higher in the k-omega model and the gas outside the jet region begins to leave the plate much more quickly in the k-omega simulation. The maximum velocities are very similar at 45 and 46.9 m s^{-1} for the k-epsilon and k-omega models respectively.

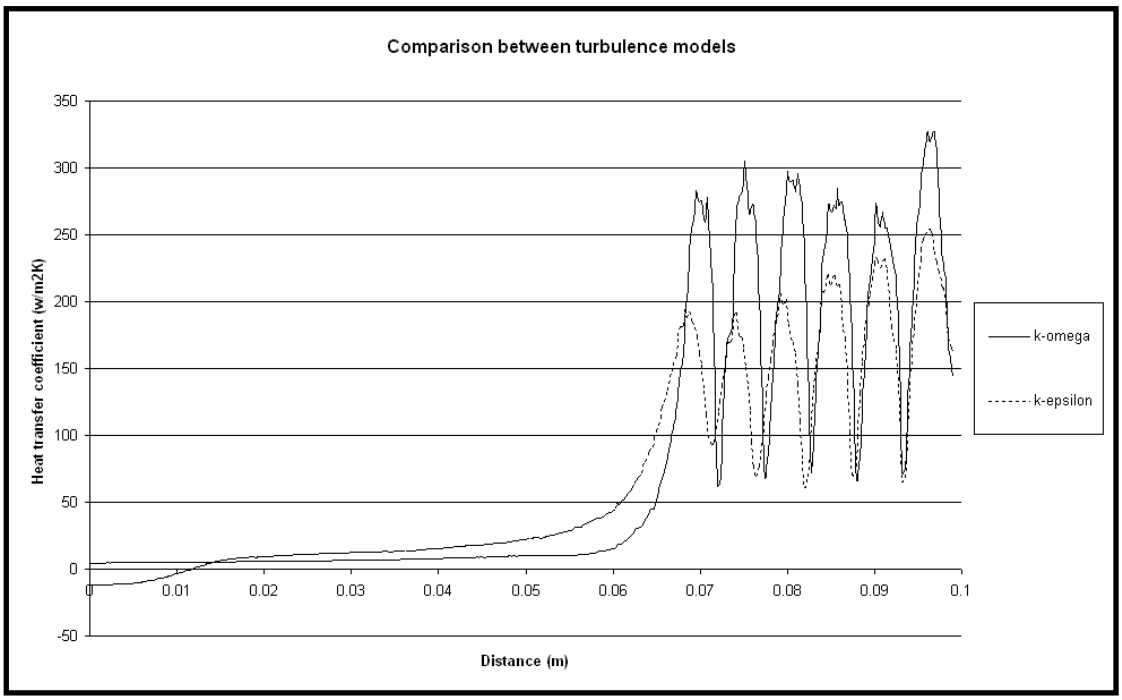


Figure 11-19 : Comparison between heat transfer coefficient plots for different turbulence models

Figure 11-19 shows the difference between the heat transfer data generated using both the k-epsilon and k-omega models. The profiles are very different with the peaks of the k-omega simulation much higher than those of k-epsilon. However, the peaks are much wider in the case of the k-epsilon. If one considers Figure 11-20 (below) it is clear that the average heat transfer coefficients for the jet regions are 20% different between the two models, with values of 118 and 99 W m^{-2} K^{-1}. The peak heat transfer coefficients are 327 and 254 W m^{-2} K^{-1} respectively, with the peak heat transfer coefficients for the jets reducing dramatically in the case of the k-epsilon model possibly due to the cross flow effect of the jets. Wang *et al* [94] also noted that the peaks shown in these heat transfer plots do not necessarily line up with the centre of the jets due to the influence of cross flow.

In the case of both turbulence models, and following conventional thought the highest heat transfer values are at the base of the jets at the stagnation point. The simulation predicts peak values of 275 – 327 W m^{-2} K^{-1} in the under head region (decreasing in magnitude towards the exhaust in agreement with the literature [89], [91], [92]), before dropping to around 5-8 W m^{-2} K^{-1} outside the head area for the k-omega model. These values are 254 – 194 W m^{-2} K^{-1} and dropping to 13 W m^{-2} K^{-1} before going negative to –12 W m^{-2} K^{-1} towards the edge of the modelled region, in the case of the k-epsilon model. The sign in this instance reflects the fact that the heat transfer is no longer from the gas to the plate, but from the plate to the gas.

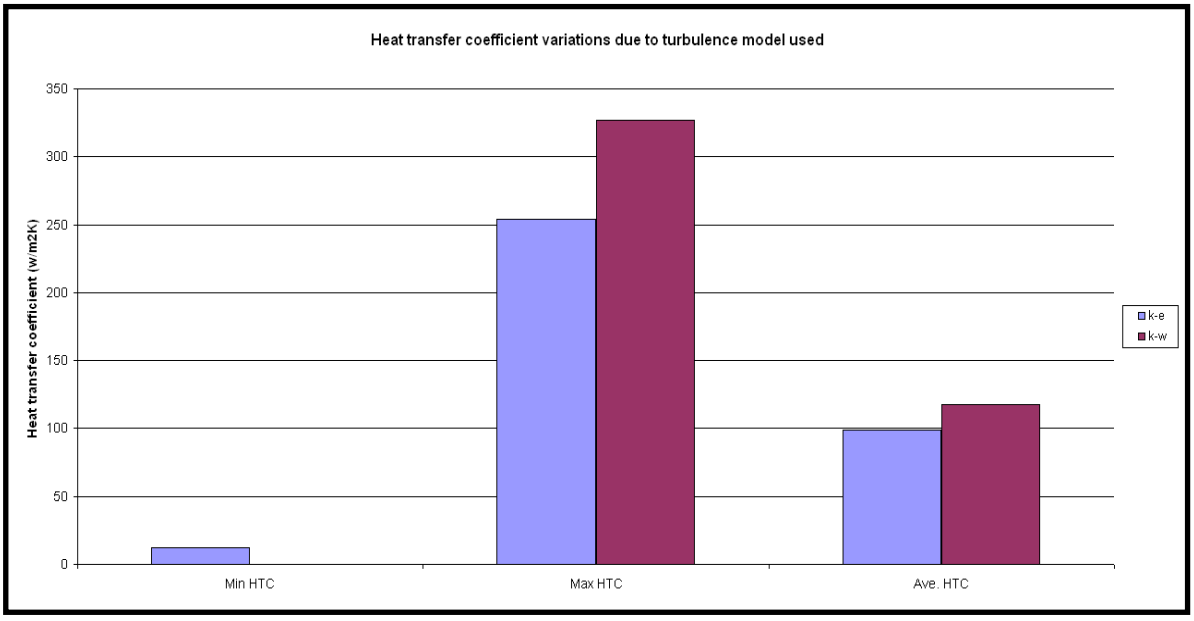


Figure 11-20 : Comparison of turbulence models

Perhaps unsurprisingly given that the k-omega turbulence model was used for these simulations the single jet argon models predicted heat transfer coefficients for the large head unit, with a jet length of 8mm and a flow rate of 100 and 140 l min^{-1} to be 276 and 397 W m^{-2} K^{-1} respectively. The 6 jet model described here had a flow rate of 120 l min^{-1} and these values correlate well with the results of the k-omega simulation. The jet average heat transfer coefficient was also very similar,

predicting a value of 118 W m^{-2} K^{-1}. A summary of the data from both single jet and multi jet models in argon for system representative flow rates is provided below (Table 11-4).

	Single 8mm jet unit cell - argon		**Multi-jet argon**	
Jet inlet temperature (K)	893	893	893	893
Jet diameter (d), (mm)	1	1	1	1
System flow rate (l min^{-1})	100	140	120	120
Turbulence model used	k-omega with SST corrections	k-omega with SST corrections	k-omega with SST corrections	k-epsilon
Peak h (W m^{-2} K^{-1})	276	397	327	254
Peak Nu	7.0	10.0	8.3	6.4
Average h (W m^{-2} K^{-1})	97	127	118	99
Average Nu	2.4	3.2	3.0	2.5

Table 11-4 : Table summarising the heat transfer data obtained from the CFD modelling. System flow rate can be converted into jet flow rate by dividing by 216 (i.e. number of jets in the large head unit). Note excellent comparison between multi-jet and single jet models (when variation in flow rate is taken into account). Gas used in the calculations is from Table 11-3.

In reality the gas temperatures measured on the plates in experimental work detailed elsewhere in this thesis were always higher than the plate temperatures in the simulations. The results for the single jet models correlate well with the literature as well as with the k-omega multi-jet simulations described in this section. The k-epsilon model also failed to fully converge to the lower residuals of below 10^{-4} for velocities, turbulence and continuity equations and a value of 10^{-6} for the energy. Instead they begin to plateau just above these values, hence choosing the k-omega turbulence model for the simulations. The k-omega turbulence model is also favoured by a number of authors modelling similar problems [127, 104].

11.8 FLOW VISUALISATION OF IMPINGING JETS

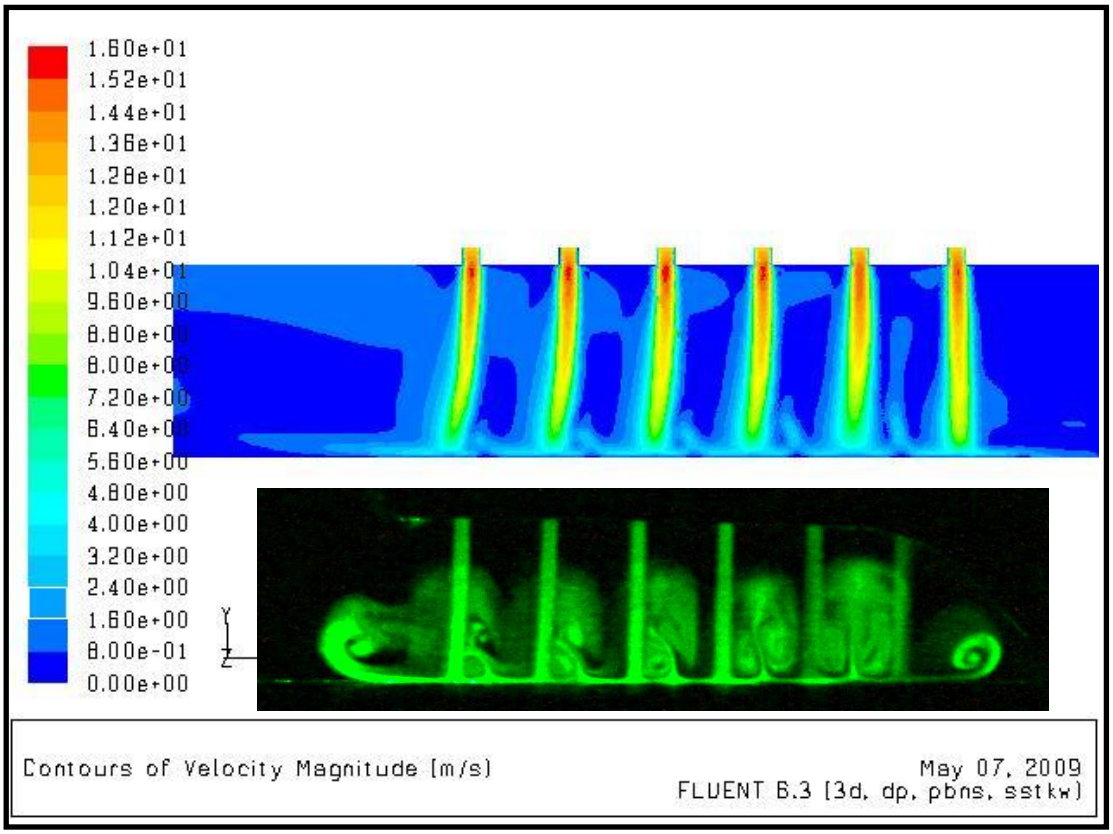


Figure 11-21 :Comparison of Fluent simulation and flow visualisation

Figure 11-21 was taken during flow visualisation experiments. A similar setup to that described by Xianchang *et al* [96] was used; room temperature compressed air with representative flow rates[§§§§] is supplied through a manual flow meter into a cylindrical plenum. This plenum was filled with smoke prior to each test run, a flow valve was opened and closed to start and stop each test. A laser light sheet was

[§§§§] The density of air at room temperature is 75% that of Argon (see Table 11-1 and Table 11-3), therefore as a flow rate of 120 l min^{-1} is used in the system (see section 9) a flow rate of 90 l min^{-1} (75%) was used for flow visualisation. By using the data in Table 11-1 and Table 11-3, and the velocities at the jets in Figure 11-18 a value of 547 for the Reynolds number is calculated for Argon at 620°C, compared to a value of 605 for room temperature air at a flow rate of 90 l min^{-1}.

used to illuminate the gas stream and a Cannon EOS 350D SLR camera was used to take images. The general shape and distribution of the gas jets is considered to be representative of that seen with argon. Figure 11-21 was taken at the beginning of the tests and shows the jets as they form very soon after impact with the plate. This initial interaction is the only time one can see the morphology of the jets using this test methodology as after only a few milliseconds the whole region is filled with air (containing smoke) and the contrast seen in this photograph is lost. When viewed in conjunction with the velocity plot from the fluent simulation, it is apparent that the general shape of the jets in the simulation appears to be representative of that seen in the flow visualisation. The jets tend to bend towards the head exit region across the plate (right to left on the images). Also the interaction between adjacent jets where a characteristic up-flow of gas is generated is well resolved in the CFD. One can see the effect of the cross-flow generated by having the largest exhaust at the front of the head unit (left most in the picture). The effect of the cross-flow is most pronounced in its influence on the up-flows; as one moves from right to left in the picture their heights reduce and they begin to collapse towards the exit. This is clearly shown both in the photographs and the CFD model. This effect of crossflow on the up-flow regions was also observed by Carcasci [105] using smoke visualisation techniques similar to that shown in Figure 11-21.

11.9 KEY OUTCOMES - VALIDITY OF THE MULTI-JET SIMULATION

The Fluent simulations suggest a peak heat transfer coefficient of 325 $W.m^{-2}.K^{-1}$ for the local heat treatment system, which gives a peak Nusselt number of 8.2. The system has a jet length to diameter ratio of 8. Therefore any comparisons with the literature should have a similar value. The majority of papers on the subject of impingement jets focus on developing correlations for turbulent air jets with high Reynolds numbers. However, some papers in the public domain do offer values for laminar air jets, for example, Gardon and Akfirat [84] suggest a peak Nusselt number of around 16 at the centre of an air slot jet impinging on a surface with a nozzle to plate spacing of 8. Also, in the paper by Livingood and Hrycak [81], a number of correlations are presented. One particular equation presented by Perry [128] offers an empirical relationship for high temperature (873K) circular air jets with a length to diameter ratio of 8, (Equation 11-9), where K = 0.1810 for an impingement angle of 90°, Nu is the Nusselt number, Re is the Reynolds number, and Pr is the Prandtl number [128].

Equation 11-9: $Nu = K\,Re^{0.7}\,Pr^{0.33}$

Using this correlation to calculate stagnation point Nusselt number and plotting against Reynolds number gives very good correlation with that calculated through the gas jet impingement modelling. Figure 11-22 shows the data calculated from Perry's equation for stagnation point Nusselt number and compares it with data from the CFD. The second set of lines (dotted) on the graph show the jet average Nusselt number calculated from the data and offered for comparison with a second correlation given in Livingood and Hrycak [81], this from Huang *et al* [129], see

Equation 11-10. Again Nu is the Nusselt number, Re is the Reynolds number, and Pr is the Prandtl number.

Equation 11-10: $Nu_{ave} = 0.0233\ Re^{0.7}\ Pr^{0.33}$

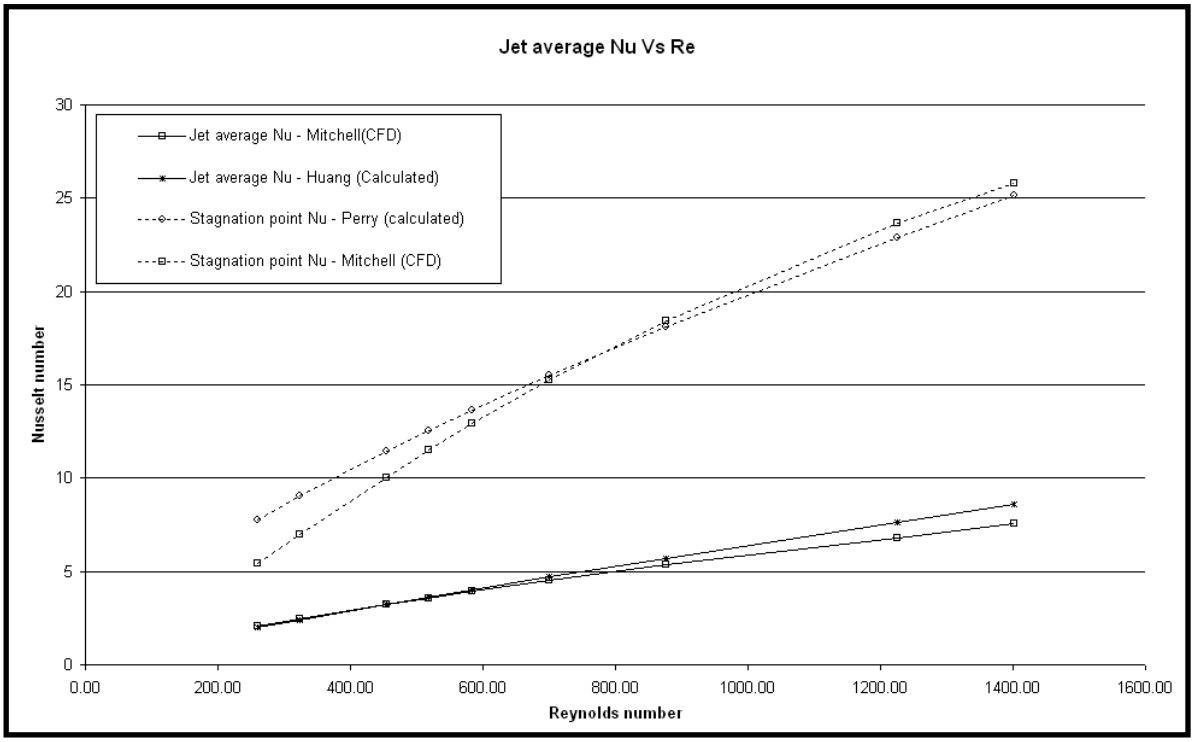


Figure 11-22 : Comparison of simulated data with empirical formulae from the literature

In the six jet simulation the peak heat transfer coefficient is in the jet furthest from the head exhaust region. This is due to the cross-flow effect deflecting the jets slightly as they interact with the plate, and each other. It is also worth noting that in the literature on impingement jets most of the data are generated from experimental results performed on large diameter jets (of the order of 10mm or greater). In the local heat treatment system the jet diameter is 1mm. Finally the data were derived from experimental work performed on jets with Reynolds number in the turbulent regime.

The average value within the heated (jet) region is shown to be 118 W m^{-2} K^{-1} from the k-omega model. However the Fluent simulation does not take into account that the jet plate will be emitting thermal radiation adding to the heating effect of the gas. Also the peak heat transfer coefficient of the jet furthest from the exhaust, region of the head unit was slightly higher than the other five jets. The reason for this is that the cross-flow generated by the exhaust gas flows towards the exhaust reduced the maximum heat transfer coefficient in each subsequent jet. This is in agreement with the observations of Bailey *et al* [89]. One can see the correlation between the reducing peak heat transfer coefficient shown in Figure 11-17, and the increased deflection of the jets in the velocity profile in Figure 11-21. Also noteworthy is that the CFD model suggests the heat transfer coefficient outside the head unit slowly reduces to a value of around 8 W m^{-2} K^{-1} along the length of plate giving an indication as to the level of heat transfer due to the exhaust gas flow.

12 MODELLING - THE FINITE ELEMENT APPROACH

12.1 EXPERIMENTAL CONFIGURATION FOR MODELLING VALIDATION

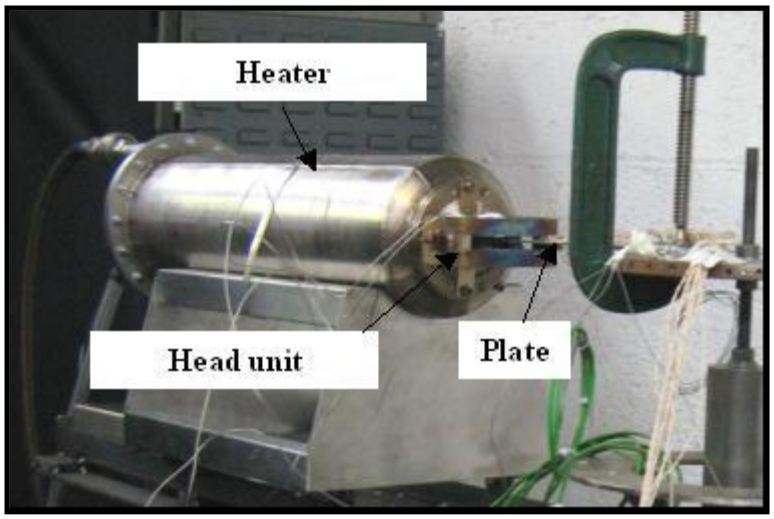


Figure 12-1 : ABAQUS modelling validation trial setup

To provide data for the validation of a finite element model experiments were performed using a plate similar to that detailed in section 10. As before the plate is heated using the local heat treatment system (positioned in the tip location) and temperatures were recorded during the heating cycle. The plate is heated in a specified region, to a depth of 20mm across the entire width of the plate. A gas temperature of 620°C is used with a flow rate of 120 l min^{-1}. Ten k-type thermocouples[*****] were positioned across the plate covering areas both within the heated zone and outside the heated zone. The end of the plate furthest from the heated zone was used to clamp the plate in position during the trials, the clamp was heavily insulated to minimise any conduction. The test setup is shown in Figure 12-1.

[*****] Thermocouples have been calibrated in the temperature range of the experimental validation.

12.2 FE MODELLING STRATEGY

To simulate the heating of the plate in Figure 12-1 a model was generated in the finite element modelling package ABAQUS. In this model a heated area is imposed on a plate with the same dimensions as the area covered by the head unit in the trial. Thermal data for the plate were entered into the modelling software and three regions on the plate identified. The region where the hot gas jets are heating the plate, the region outside the head unit where heat from the plate is

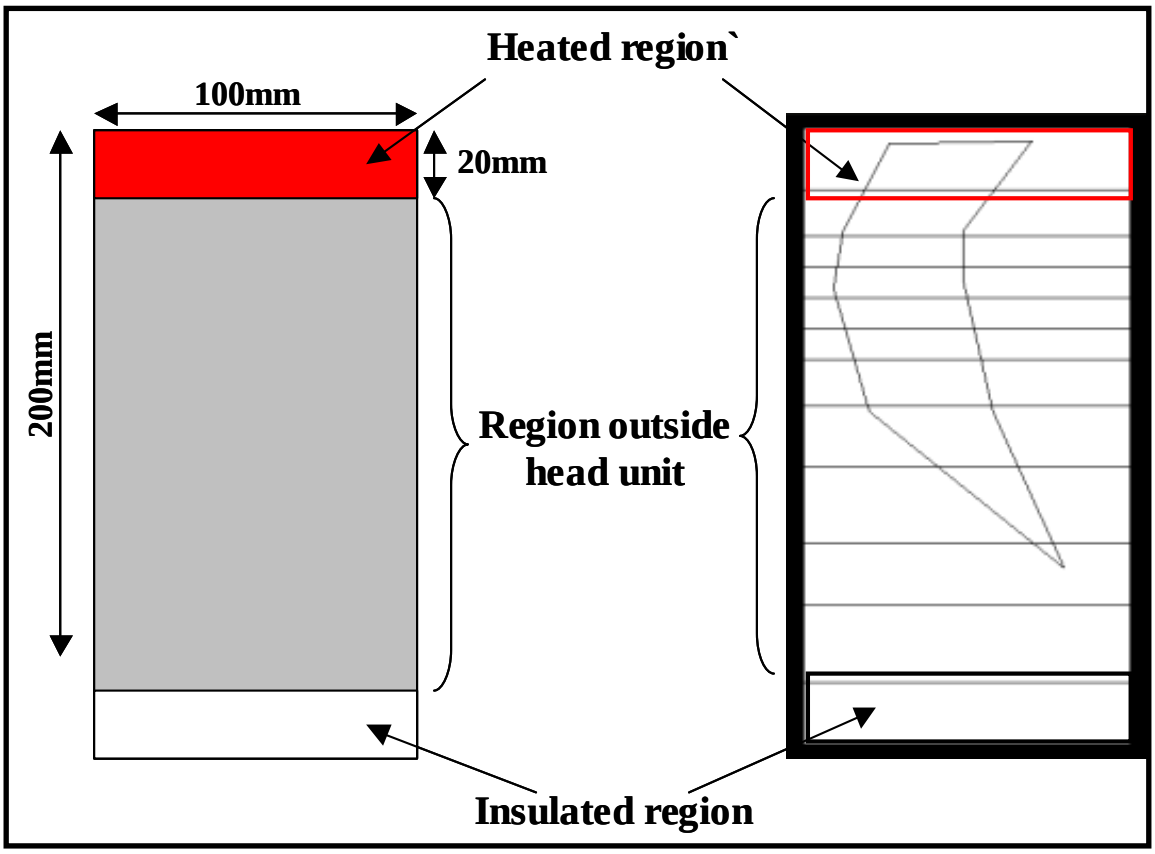


Figure 12-2 : The left hand image is a schematic diagram of the heated plate from the trials shown in Figure 12-1 with the three boundary conditions highlighted. The heated region in red, region outside head unit in grey, and insulated region in white. The right hand image is taken from the ABAQUS pre-processor and shows the plate with all the boundaries defined. The various horizontal lines represent the various regions where different film coefficients can be imposed to represent the effects of the exhaust gas flow. The polygon in the centre of the image represents the location of the thermocouples, each corner represents a node at which temperature data can be taken from the model to compare to experimental results.

transferred to the ambient environment, and finally the insulated clamp region. The model configuration is shown in Figure 12-2 (above).

The three regions had the following boundary conditions;

1. Insulated region - The clamp at the cold end of the plate is modelled as an insulated region, in the experiments the clamped region was heavily insulated to minimise any heat loss due to conduction to the clamp.

2. Region outside head unit - The rest of the plate (excluding the heated region) is assumed to transfer heat to, or be heated by the hot gas exiting the head unit and passing over the plate surface. It is therefore given a film[†††††] heat transfer coefficient and a film temperature. The losses through radiation are neglected at this stage because the plate outside the heated zone is between 373 and 673K throughout the heating cycle. It was not considered likely that significant heat would be lost through radiation at these relatively low temperatures.

3. Heated region - A second film heat transfer coefficient and film temperature to represent the heat input from the local heat treatment system is imposed. The heat transfer coefficient used at this stage is that obtained in the CFD modelling (described in section 11). In this case, the film temperature was set to follow the gas temperature recorded in the head unit (control temperature) during the

[†††††] Film is a termed used in ABAQUS and allows one to provide a temperature and heat transfer coefficient to describe the transfer of thermal energy in and out of the model. In this case it models the ambient atmospheric gases interacting with the surface of the plate outside the head unit.

experimental trials. The amplitude of the gas temperature ramp is calculated from experimental data.

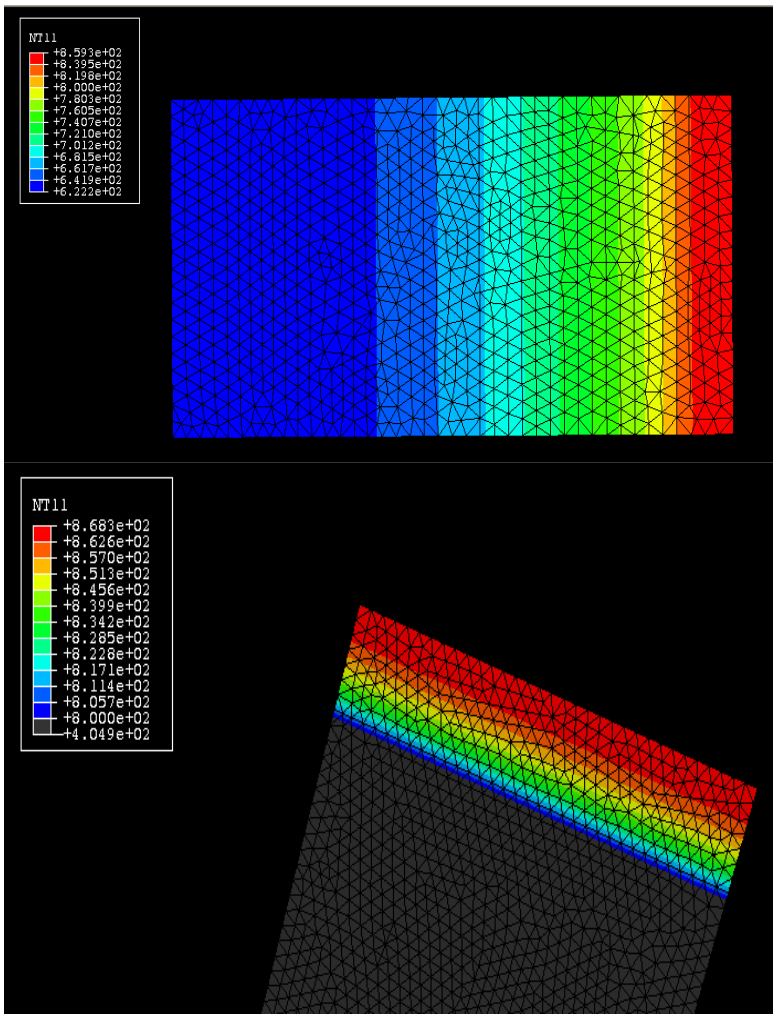
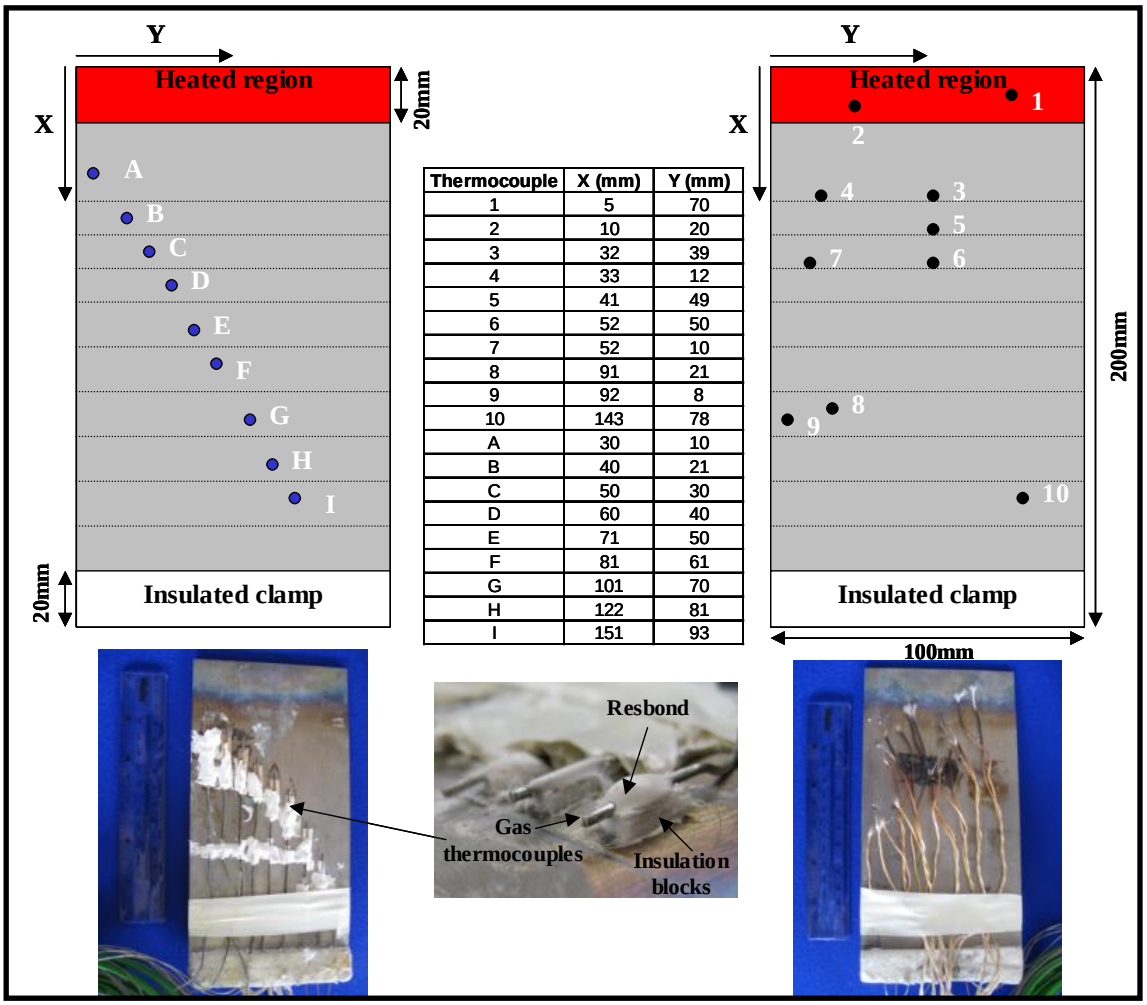


Figure 12-3 : Example of ABAQUS simulation output and mesh (element size ~3mm)

Figure 12-3 (left) shows the modelling output from the plate being heated at one end to represent the situation found when using the local heat treatment system. These images show the general trend of the isotherms in the plate from the heated region to the clamped (insulated) region. The overall temperature distribution shows a qualitative correlation with tightly packed isotherms close to the heated region becoming more spread out as one moves away. A quantative analysis of the data generated by the ABAQUS model is provided in the proceeding sections. The bottom image in Figure 12-3 shows temperatures between 868 and 800K representative of the steep temperature gradient generated when using a localised technique such as this.

12.2.1 DEVELOPING BOUNDARY CONDITIONS FOR THE ABAQUS MODEL



Thermocouple	X (mm)	Y (mm)
1	5	70
2	10	20
3	32	39
4	33	12
5	41	49
6	52	50
7	52	10
8	91	21
9	92	8
10	143	78
A	30	10
B	40	21
C	50	30
D	60	40
E	71	50
F	81	61
G	101	70
H	122	81
I	151	93

Figure 12-4 : Images showing plate setup for experimental validation of the ABAQUS modelling. The top two schematic diagrams show the position of the thermocouples on the titanium plate (also see bottom photographs). Positions of the gas thermocouples are shown in the top left image (see inset centre photograph for details of gas thermocouple positioning). Positions of the plate thermocouple locations are in the top right image.

As the gas exits the head unit region, it moves across the plate surface and the flow continues to interact with the plate. This gas also interacts and mixes with the cooler ambient air (or gas in a chamber environment). This interaction results in variations in heat transfer coefficient and gas temperature close to the plate surface.

It is clear that the temperatures achieved in the under head region are a direct result of the heating effects of the head unit and gas impingement. However, when considering temperatures further away from the heated region, the correlation becomes weaker. The temperatures achieved outside the head unit are due to a combination of conduction through the plate material and heating from the exhaust gases that pass over it on exiting the head unit. In order to address this issue in the modelling, trials to understand the temperature of the exhaust gas were performed. Figure 12-4 (above) shows examples of the thermocouple set-up used to measure gas temperature, in this experiment mineral insulated k-type thermocouples are mounted onto the plate. They are glued in position using Resbond 920^{TM} [130] on small blocks of insulation material to minimise conduction from the plate. Also important is that the gas temperature thermocouples were staggered so as to minimise their effect on gas flow in front of other thermocouples. The thermocouples were also aligned parallel to the gas flow.

The positions of the mineral insulated thermocouples were chosen to correspond with the welded thermocouples on the plate. The data generated could then be used to determine a number of zones (shown schematically and labelled A to I in Figure 12-4) with differing gas temperatures and heat transfer coefficients. This method facilitates correct understanding as to the affect due to combined heating of the exhaust gas and conduction through the plate from the heated region.

12.2.2 EXHAUST GAS TEMPERATURES

Previously, Figure 12-4 highlighted the positions of the various regions (A-I) where gas temperature was measured and the corresponding position of thermocouples (1-10). In an attempt to further understand gas flow over the plate outside the head unit some flow visualisation was performed using smoke and air at system representative flow rates (see Figure 12-7, and section 13.1.4). A laser light sheet was projected onto the gas flow to show cross-sections of the flow leaving the head unit. Together with the temperatures measured, this gave a good indication of the flow pattern and distribution of the exhaust gas.

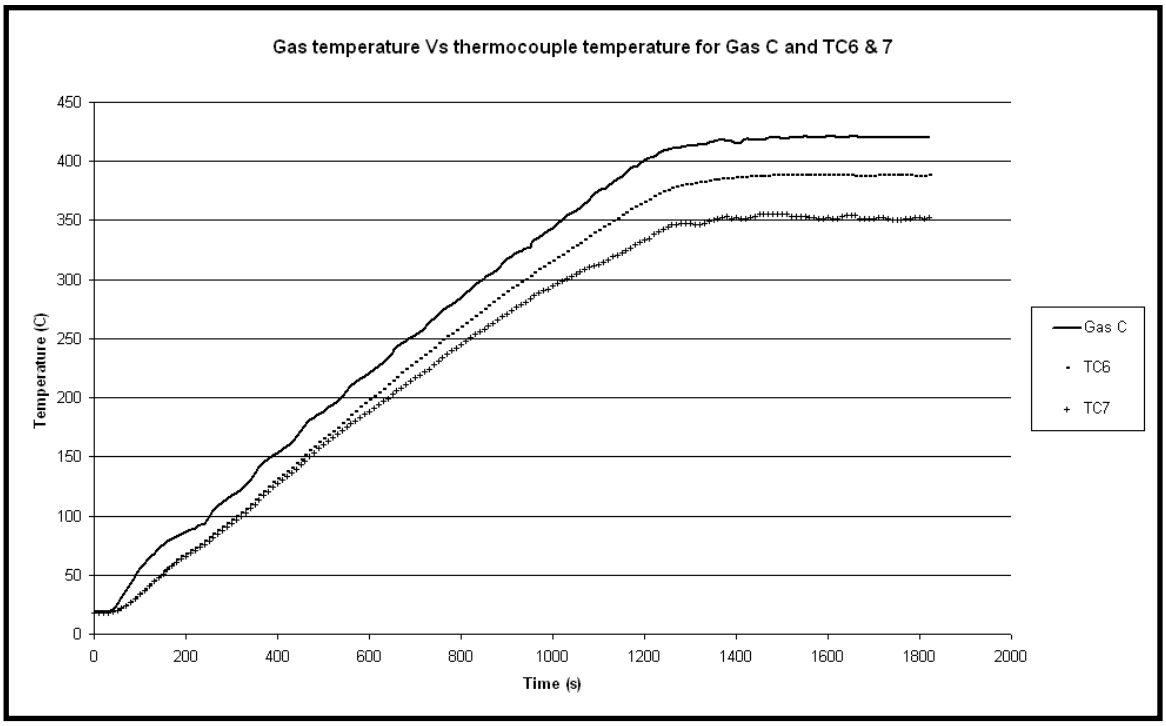


Figure 12-5 : Comparison between plate and gas temperature at TC6 and TC7

Figure 12-5 compares the temperatures of the gas measured in region C and thermocouples 6 and 7. It highlights that the gas temperature is around 40-80°C hotter than the plate temperatures in this region. The gas temperature shows little fluctuation suggesting a steady even flow past the thermocouple with minimal mixing with the ambient gas. This relationship is replicated in zones A and B but at slightly higher temperatures.

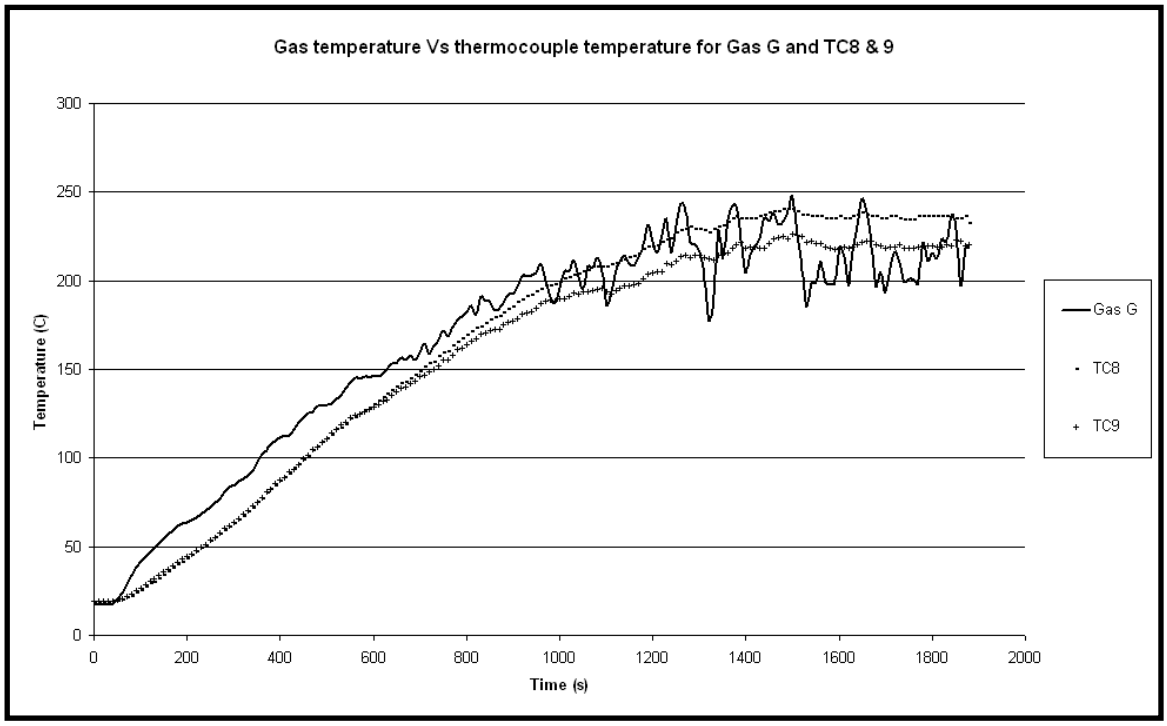


Figure 12-6 : Comparison between plate and gas temperature at TC8 and TC9

Figure 12-6 compares the temperatures between region G and thermocouples 8 and 9. In this case the gas temperature is very similar to the plate temperature and fluctuates significantly from its mean temperature. The data vary by ~75°C in the steady state 'soak' region of the cycle. The reason for this variation in gas temperature behaviour is due to the fact that the gas flow had slowed sufficiently to be mixing with the ambient gas. This resulted in lower gas temperature and the

temperatures measured in this region being erratic. Conversely the faster flow closer to the head produced a more consistent temperature is recorded due to the constant stream of hot gas displacing the cooler ambient gas. Secondly the hot argon leaving the head unit had a lower density due to its higher temperature. As a result the effects of buoyancy will cause the hotter gas to rise. When the gas has significant velocity (such as that close to the head unit) buoyancy is less pronounced due to the high levels of momentum in the gas. However as the gas slows buoyancy will begin to dominate and the hotter gas will begin to rise.

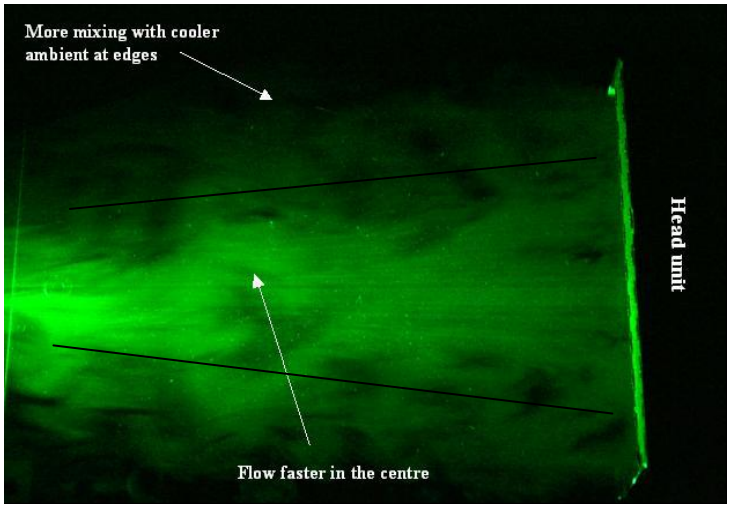


Figure 12-7 : Gas flow from tip head unit

Figure 12-7 (left) shows results from the flow visualisation exercise, this was performed with the gas at room temperature and with air and smoke. As a result the effects of buoyancy cannot be seen, but it does represent a good approximation of the flow coming out of the head unit. This allows one to assess the morphology of the gas flow and its interaction with the surroundings. Of note in this image are three main effects; firstly the central region of the gas flow has the least mixing and most constant stream highlighting that the gas here is at higher velocity. Secondly, this core of the flow (analogous to the potential core of an impinging jet) reduces in width (depicted by the black lines on the image) with distance from the head unit.

Finally the edges of the flow are slowed by friction with the ambient air causing slowing of the gas and large amounts of mixing with the ambient air.

Figure 12-7 demonstrates the basis for the relationships seen in the graphs presented previously. For example, although thermocouples 6 and 7 are the equidistant from the head unit along the plate, the temperature of thermocouple 7 is lower than 6 (Figure 12-5). This is due to its position in the region where significant mixing occurs at the edges of the flow. It can also be hypothesised that the region where the fast moving central core of gas is overcome by the mixing at the edges is where the gas temperature becomes more erratic as seen in Figure 12-6.

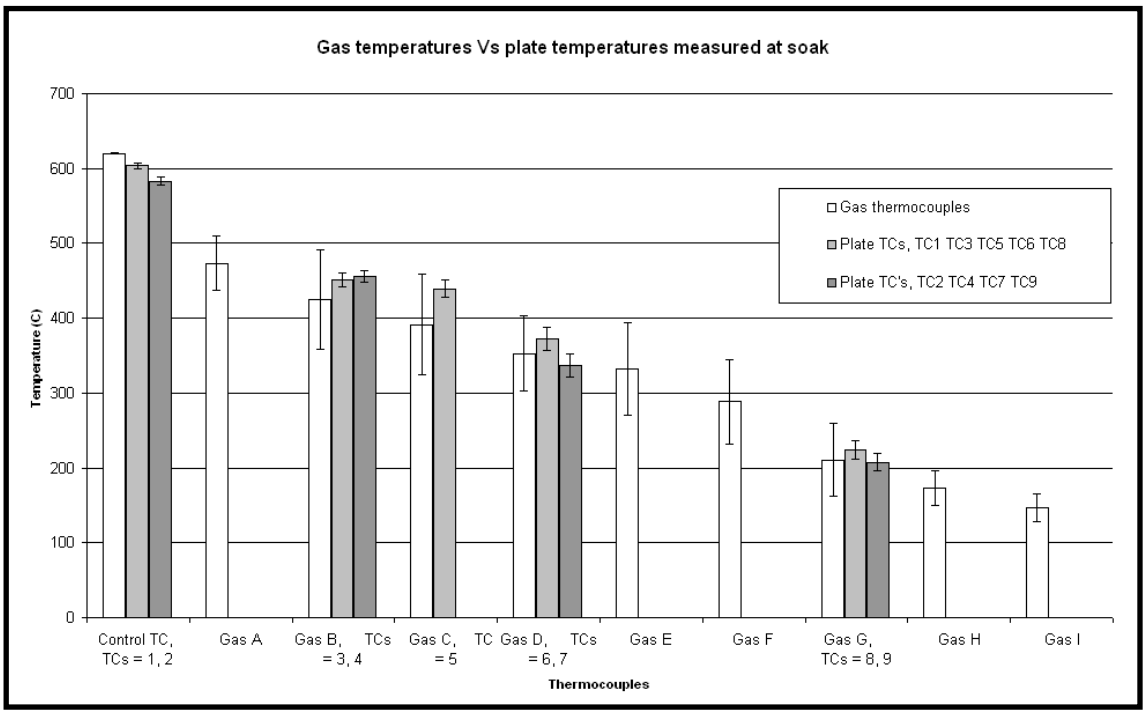


Figure 12-8 : Graph showing the variation in gas temperatures (white bars) and corresponding plate temperatures (grey bars), see Figure 12-4 for thermocouples locations. Error bars represent standard deviation of temperatures measured over a soak period. Note, thermocouple 10 data not included as it failed during testing.

Figure 12-8 shows the variation in both gas temperature and plate temperature along the plate for all thermocouples. Note the larger standard deviation in the gas temperatures due to the fluctuation shown in Figure 12-6. The temperatures are averages taken over a period of steady state in the soak region of the test, as described previously.

12.2.3 OPTIMISING THE PROCESS MODEL

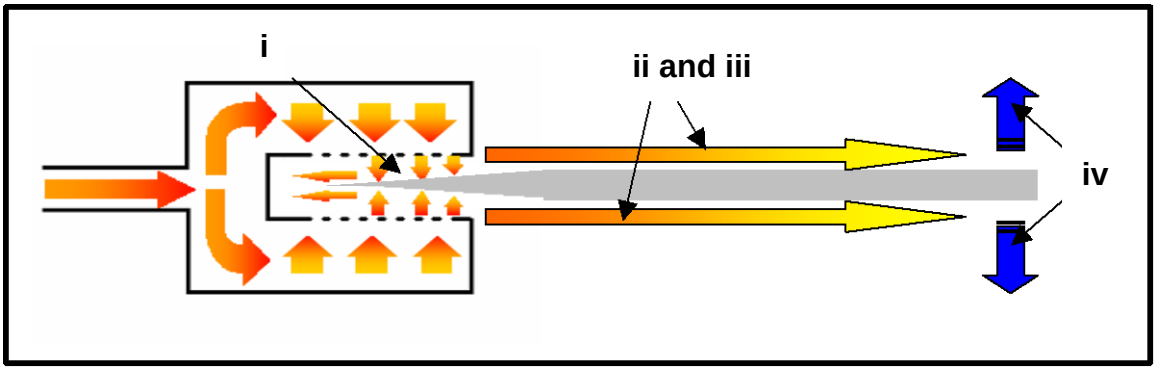


Figure 12-9 : Head and plate test piece set up, showing various regions where the plate is heated by convection.

In order to correctly model the gas jet local heat treatment system, careful consideration of the various mechanisms of heat transfer must be considered. When the plate is being heated there are a number of sources of heat flux (i - iv on Figure 12-9). Region (i), represents the heat flux from the head unit primarily comprising the jet impingement. However, the effect of radiation from the jet plate should be considered. Region (ii) immediately outside the head unit is heated by the hot exhaust gas. Region (iii) is a further region at a lower temperature heated by the exhaust gas, and region (iv) is where the plate loses heat through convection to the cooler ambient gas.

Quantifying the effect of the jet plate on heating is very difficult due to the complexity of separating the flux generated by both radiation and convection. An

estimation of the energy transferred to the component as a result of radiation from the jet plate is made below.

Radiative heating is represented by the following equation;

Equation 12-1: $q_r = \varepsilon A\sigma(T_1^4 - T_2^4)$ [75],

where q is energy emitted by the surface in Watts, A is the area of the emitting surface, σ is the Steffan-Boltzmann constant (5.67e-8 W m^{-2} K^{-4} [75]), ε is emissivity of the emitting surface, T_1 is the temperature of the emitting surface, and T_2 is the temperature of the surface being heated. In this case ε is ~0.6 [131], A is 0.002m^2 (Figure 12-2) and T_2 is 873K. In the case of T_1 some experiments have shown that in the jet plate closest to the gas inlet reaches temperatures up to 973°K[‡‡‡‡‡], as a result this value is used to represent the worst case scenario.

Therefore,

0.6 * 0.002 * 5.67e-8 * (973^4 - 873^4) = 21.5W.

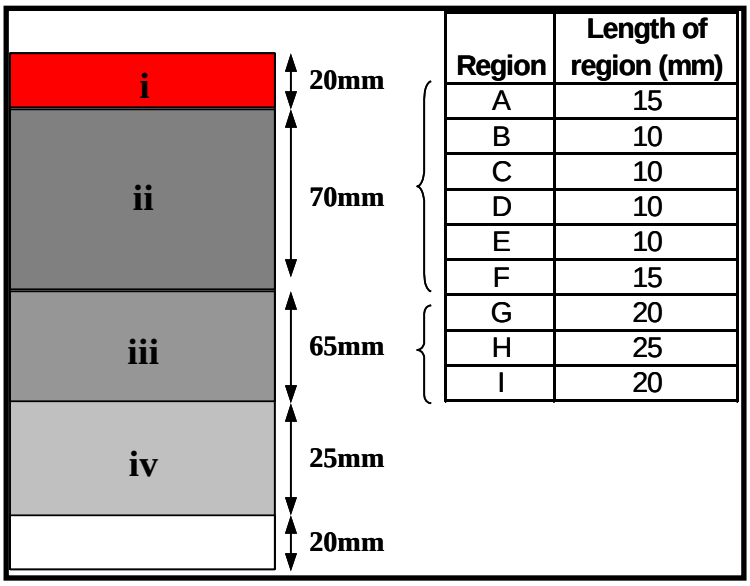
This assumes that all the energy given off by the jet plate will be transferred to the plate or component being heated. In fact, radiative heat sources emit energy in all directions, meaning that unless the target surface completely surrounds the jet plate not all the energy will be transferred [75]. Secondly, this equation assumes that there a vacuum between the heat source and the target, whereas in reality this space is filled with gas. In actual fact the gas will be heated by the radiation

---

[‡‡‡‡‡] Testing conducted on 21/05/08, Stork Cooperheat (UK) Ltd, showed the temperature of the gas within the head unit to be 700°C when a control temperature of 620°C was being used.

from the jet plate, helping to maintain gas temperature in the under head region and improve temperature uniformity. Therefore the maximum amount of heat that could be transferred to the component by radiation is 21.5W and in reality it is likely to be lower.

One of the advantages of modelling this scenario using a finite element software such as ABAQUS, is that one can impose a boundary condition in the heated region to account for both the radiation and convective heating parts of the problem. In order to establish the correct boundary condition for the model of the heated region, one must first start with the average HTC value obtained from the CFD modelling exercise, which gives a value of 118 W m^{-2} K^{-1}. To estimate the effect of radiation and incorporate this into the heat transfer coefficient used in the ABAQUS model, the following approach was taken. For this exercise region (ii) was assigned a value of 10W m^{-2} K^{-1}, and regions (iii) and (iv) a value of 8 W m^{-2} K^{-1} (see section 11.7.3).



Region	Length of region (mm)
A	15
B	10
C	10
D	10
E	10
F	15
G	20
H	25
I	20

Figure 12-10 : Schematic of regions i – iv used in the calculation of the total energy absorbed by the plate during heating. The table shows the length of the gas regions modelled in ABAQUS.

Firstly one estimates the power from the radiating jet plates as described previously (giving 21.5W), this must be doubled to account for both sides of the plate. Secondly, the plate (previously introducted in Figure 12-4) is split into four regions (see i - iv in Figure 12-10, as defined in Figure 12-9). As previously stated convective heat transfer is represented by Equation 11-1 on page 188.

Each of the regions (ii) and (iii) comprises a number of the gas zones defined previously in Figure 12-4. The energy being transferred to the plate through convection is thus calculated from experimental data for each region using the area defined in Figure 12-10, and an average of the gas temperatures from Figure 12-8[§§§§§].

Using the following equation the total energy into the plate through convective heating from the various gas regions can be calculated. (The number 2 in the following equation represents the fact that both sides are heated.)

Equation 12-2: $Q_{Total} = 2*(Q_i + Q_{ii} + Q_{iii} + Q_{iv})$,

Where,

Equation 12-3: $Q_{(x)} = A_{(x)}h_{(x)}(T_{gas}-T_{plate})$,

So,

$Q_i = 0.002 * 118 * (893 – 293) = 141.60$ W

[§§§§§] For example, region iii comprises gas zone G (length 20mm, and temperature 211°C), H (25mm, 173°C), and I (20mm, 146°C). Producing a total length of 65mm, and a mean temperature of 177°C for region iii.

Q_{ii} = 0.007 * 10 * (650 - 293) = 24.99 W

Q_{iii} = 0.0065 * 8 * (450 – 293) = 8.16 W

Q_{iv} = 0.0025 * 8 * (370 – 293) = 1.54 W

Q_{Total} = 2 * (141.60 + 24.99+ 8.16+ 1.54) = 353W

The result of this exercise is a value of 353W as the total heat transferred due to the hot gas, making the effect of radiation on heating the plate 12% of total estimated convective heat flux.

Radiative heating was incorporated into a modified heat transfer coefficient that could be used in the ABAQUS simulations. The sum of Q_i and the radiation heating value of 21.5W can be divided by product of Ai and $T_{control}$-T_{plate} (as shown below) to give a modified heat transfer coefficient was used in the model to account for radiation from the jet plate.

Equation 12-4: $Q_i+q_r = h_{mod} * A_i *(T_{control}-T_{plate})$

Equation 12-5: $h_{mod} = (Q_i+q_r) / (A_i *(T_{control}-T_{plate}))$

((0.002 * 118 * (893 – 293)) + 21.5) / (0.002 * (893-293)) = h_{mod} = 136 W m^{-2} K^{-1}

12.3 RESULTS OF PROCESS MODEL

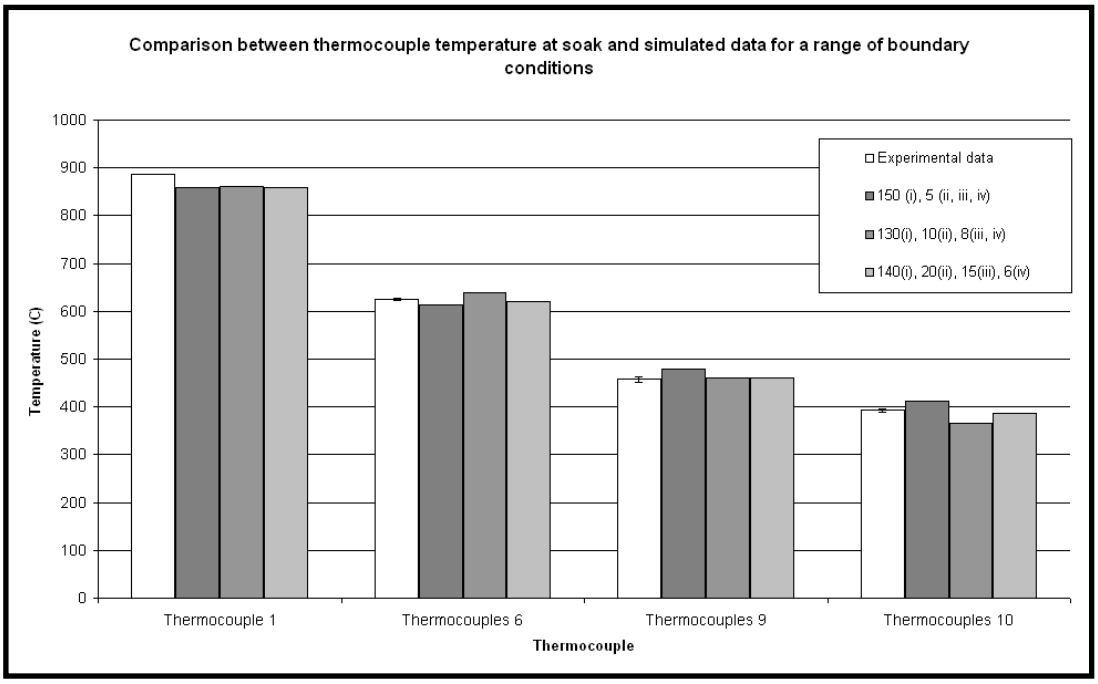


Figure 12-11 : Comparison between experimental data (white) and simulated data (grey) for thermocouples 1, 6 , 9, and 10. The error bars on the experimental data show the standard deviation of the data in soak.

The following graphs show the fit between the experimental and simulation temperatures for some of the ten thermocouples in Figure 12-4. Thermocouples 1, 6, 9 and 10 are discussed and are representative of thermocouples at various positions. For each simulation presented in this section the boundary conditions used are shown in the legends, the numbers define the heat transfer coefficients (in W m^{-2} K^{-1}). The letters in brackets relate to the relevant region in Figure 12-10. Figure 12-11 shows the correlation between the steady state temperatures achieved both experimentally and in the models with various boundary conditions. However this only provides part of the picture. The following graphs show the transient data from heating up to the soak portion of the cycle. In the following graphs, experimental data are represented by a solid line. The shapes (square,

circle and triangle) are used to represent the various boundary conditions assessed.

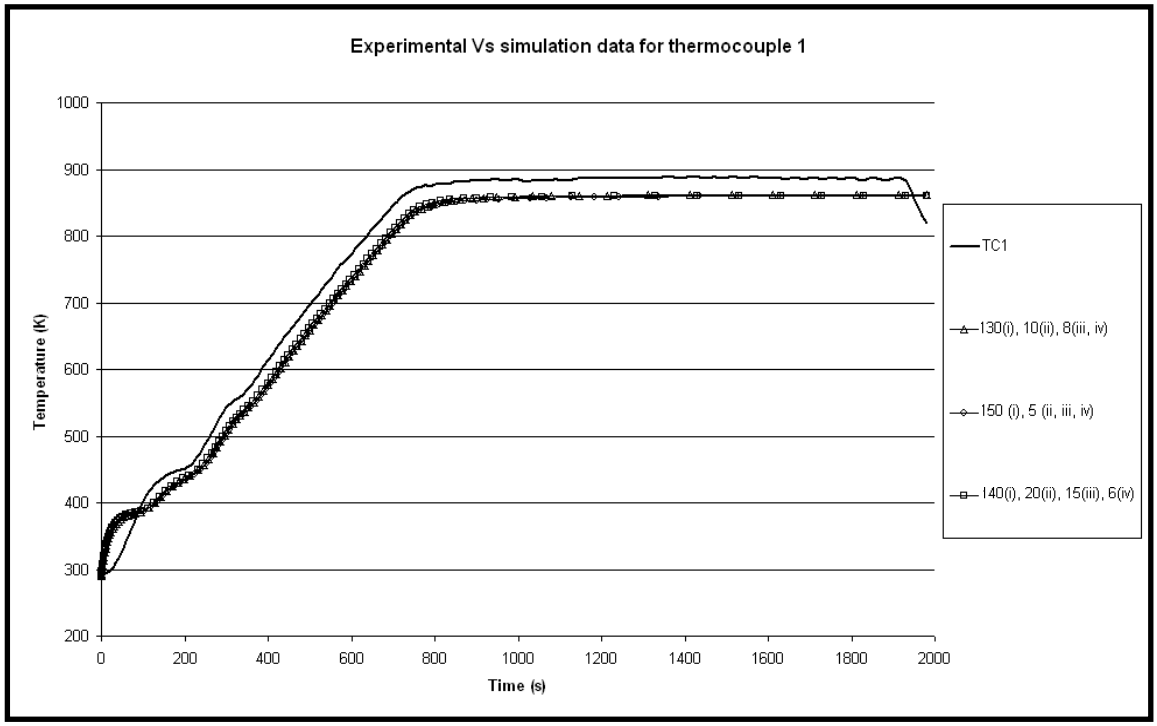


Figure 12-12 : Simulated (shapes) Vs experimental (solid line) data for thermocouple 1

Across all the graphs the best fit is found for a head heat transfer coefficient of 140 W m^{-2} K^{-1}, with heat transfer coefficients of 20, and 15 W m^{-2} K^{-1} and temperatures of 650 and 450K for the exhaust gas regions respectively. The ambient gas temperature of 370K with a heat transfer coefficient of 6 $Wm^{-2}K^{-1}$ completes the boundary conditions producing the closest fit to experimental data. All the heat transfer coefficients used gave good correlation in the under head region. In fact due to the relatively thin nature of the component being heated (i.e. 2mm) even large variations in heat transfer coefficient in the under head region have little effect on the temperatures achieved. This is due to the relatively small amount of energy required to heat the plate.

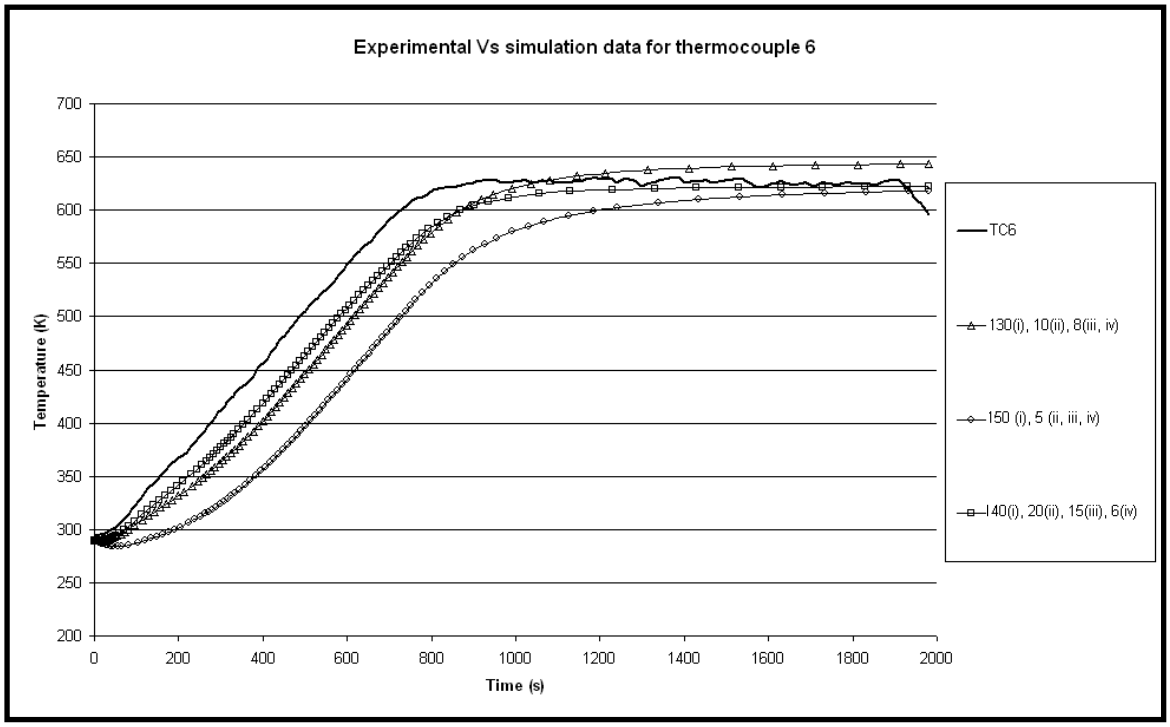


Figure 12-13 : Simulated (shapes) Vs experimental (solid line) data for thermocouple 6

The area most sensitive to the choice of boundary conditions is just outside the head unit. Due to the thin nature of the plate it is easily heated and cooled by the gas. This exhaust gas plays several roles, it not only acts to heat or cool the plate depending upon whether it is hotter or cooler, but also acts to insulate it from the cooler ambient gas further from the plate surface. As a comparison, one boundary condition for the exhaust gas region with a value of 5W m^{-2} K^{-1} and an ambient gas temperature of 370K was simulated. In Figure 12-13 (thermocouple 6) this scenario underestimates the temperatures suggesting that the heat transfer coefficient is too high, or temperature too low. However as one moves out further from the head unit through thermocouple 9 (Figure 12-14, below) and 10 (Figure 12-15, on page 234) the simulation begins to overestimate the temperatures, suggesting the heat transfer coefficient is too low or the temperature is too high.

This goes to show that including the effects of the exhaust gas outside the head unit is very important to achieve good correlation with experimental data.

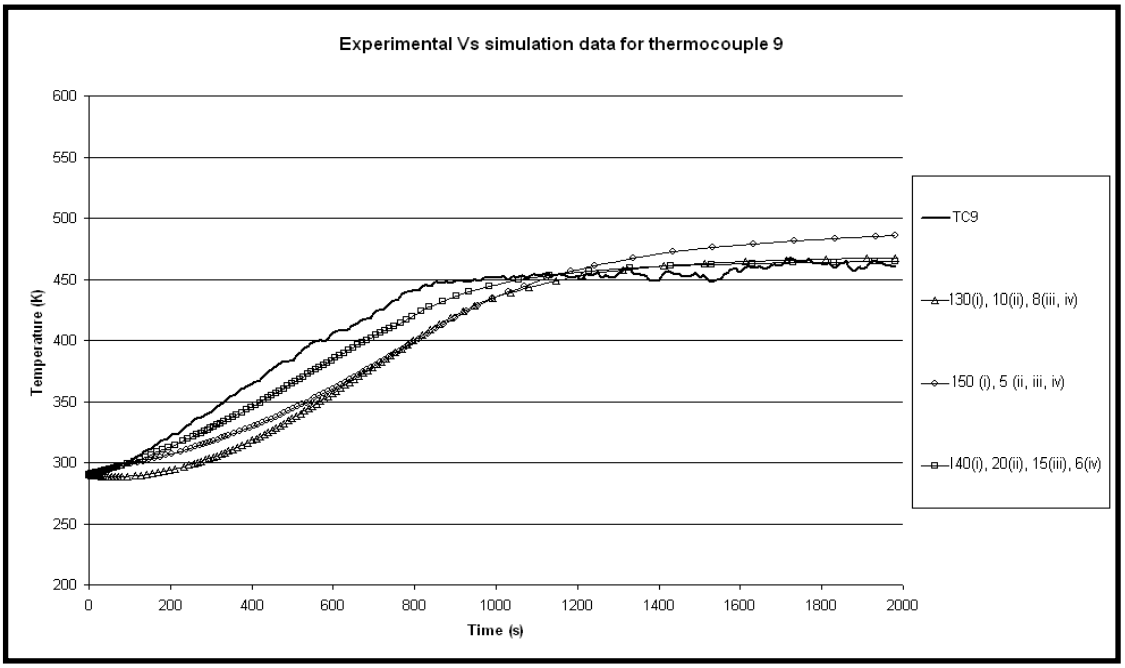


Figure 12-14 : Simulated (shapes) Vs experimental (solid line) data for thermocouple 9

As one starts to include more regions to represent the different temperatures of gas, the simulation results begin to move more closely towards the measured data. However, imposing an infinite number of exhaust gas regions outside the head unit in order to characterise these effects is not practical and it is very difficult to predict how these regions vary in position and gas temperature for different head units.

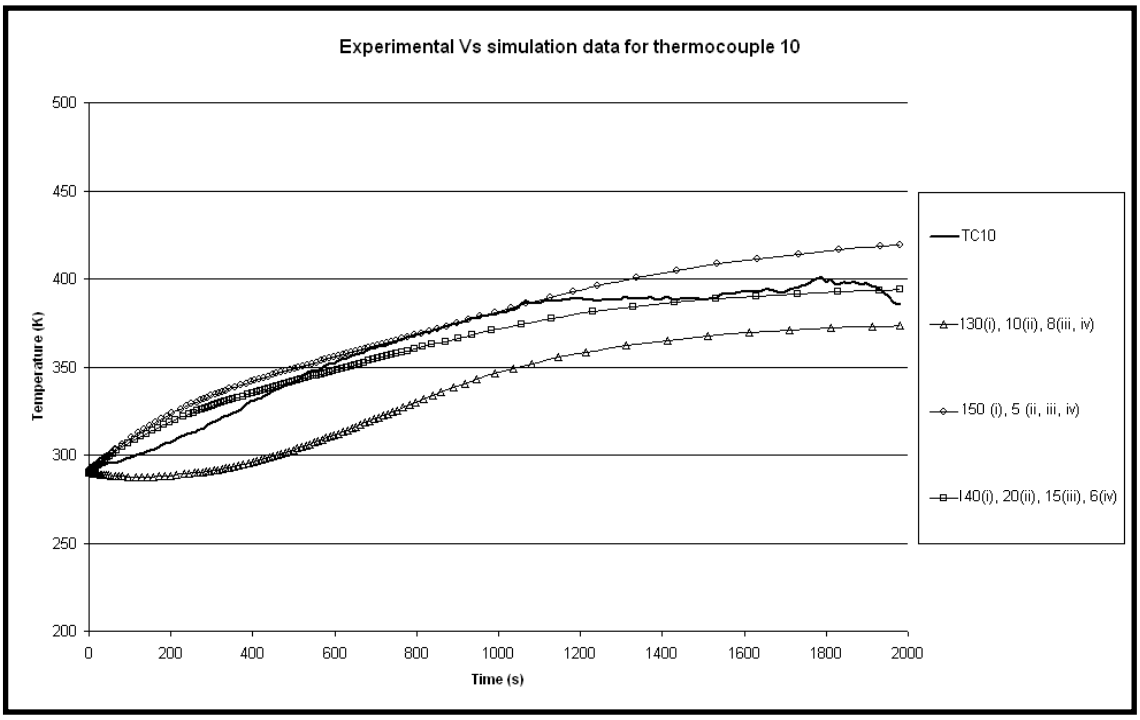


Figure 12-15 : Simulated (shapes) Vs experimental (solid line) data for thermocouple 10

12.4 DISCUSSION AND CONCLUSION OF THE INITIAL MODELLING EXERCISE

Results presented, demonstrate that this process model provides a good approximation of the local heat treatment system and its ability to heat the plate to the heat treatment temperature. The heat transfer coefficients used in this model were developed using CFD described in the previous section. It has been mentioned that it is difficult to interrogate the process model due to the geometry of the plates used in the simulations. However these are geometrically representative of the type of component this system is intended for. The simulations also highlight that the effect of exhaust gas on the plate temperatures outside the head unit is significant in the case of this particular head geometry and plate configuration. However in reality the effect of gas temperature on the temperature distribution is likely to be significantly less when there is a large heat sink close to the heated region.

The thin nature of the components intended for heat treatment mean that validating the process modelling approach on such geometry is necessary. In the case of the best correlation (i.e. 140 W m^{-2} K^{-1} (i), 20 W m^{-2} K^{-1} (ii), 15 W m^{-2} K^{-1} (iii), 6 W m^{-2} K^{-1} (iv)), the region outside the heated zone is within the correct range of heat transfer for free convection of gases (2-25 W m^{-2} K^{-1}) [132], but below those for forced convection of gases (25-250 W m^{-2} K^{-1}) [132]. This is appropriate when one considers the results of the flow visualisation, which shows the gas flowing over the surface providing slightly increased heat transfer when compared to natural convection alone. However, the head unit value can be changed significantly and

only small variations in the temperatures are seen in the simulation results. Noteworthy is that the temperature difference between the heat source temperature and plate temperature (analogous to the control offset in the system) does get very small for the higher heat transfer coefficients. The offset values seen in the simulations become much lower than that seen in testing (see Figure 10-6). As a percentage of the plate temperature this was very small making it unwise to use this as a reliable method of determining the appropriate heat transfer coefficient. The position of the control thermocouple is not guaranteed to result in a gas temperature equal to the jet exit temperature. This is an area where further investigation is needed to establish the most appropriate and repeatable position for the control thermocouple to be located. As a result of these concerns a further validation test was performed.

12.5 HEAT UP RATE ASSESSMENT

An experiment was performed in which the gas jet process was used to heat the plate as quickly as possible using the same experimental setup as in Figure 12-1. The heat transfer coefficient for the jet array region is the limiting factor to the heat up rate of the plate in this scenario. In previous experiments the control system had limited the rate at which the plate heats up by slowly raising the gas temperature and utilising a feedback loop in the control system to ensure the gas temperature (and therefore the plate) increase in temperature at a controlled and steady rate. The only difference to the setup in Figure 12-1 was that initially no plate was placed in the head unit until the gas achieved the required temperature (620°C with a flow rate of 120 l min^{-1}). The system was then held at this temperature for a period of time in order to allow the gas temperature to achieve a

steady state. Next the plate was positioned in the head unit and held there until the temperatures in the under head region had achieved a steady state value. Prior to positioning it in the head unit the plate was kept well to maintain it at close to room temperature. The graphs in Figure 12-16 and Figure 12-17 show the heat up rate from experimental trials at two under head thermocouple locations along with the results from a number of ABAQUS simulations. The thermocouples chosen for this assessment are ones positioned centrally and well within the heated zone. The reason for this was due to the rapid nature of the test (the thin plate only took 30-60 seconds to heat up). Careful alignment and checking using shims and alignment jigs is not practical. As a result the temperatures at the edges of the heated zone (close to the tightly packed isotherms) have a high likelihood of being slightly misaligned and producing significantly lower temperatures making comparison more difficult.

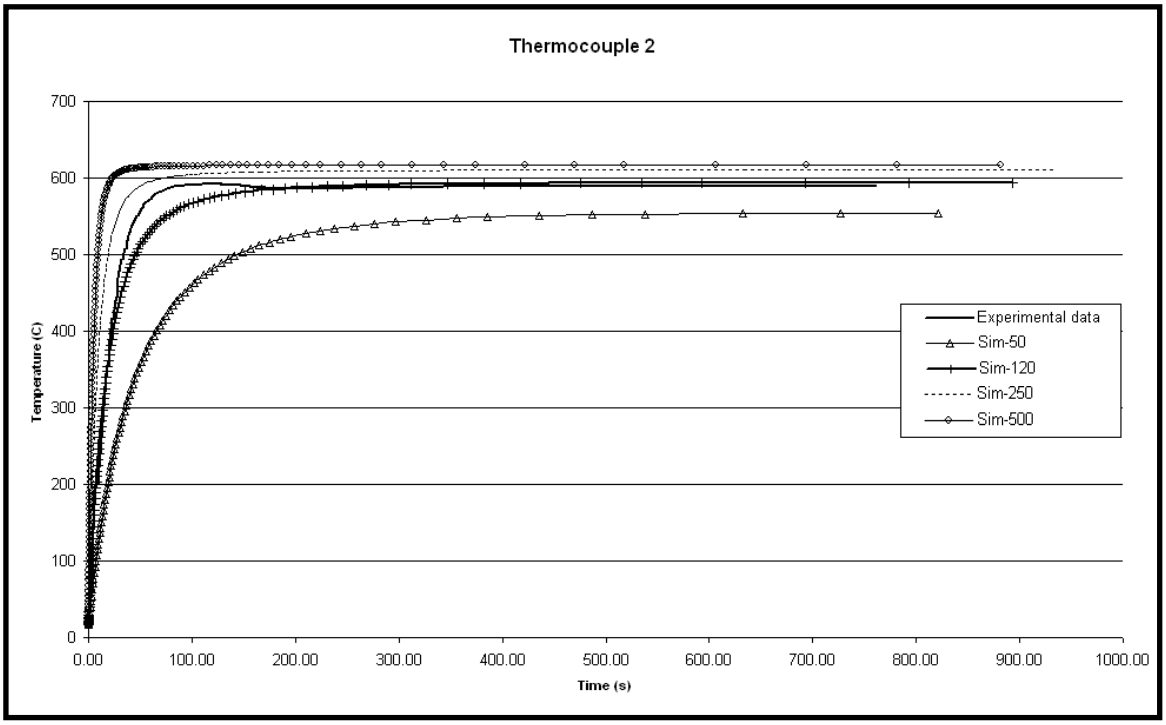


Figure 12-16 : Ramp rate comparison at thermocouple 2

Figure 12-16 highlights that for the heat transfer coefficients used in the simulation, particularly in the heating up portion of the cycle, there is strong correlation of the data with the simulation results using the Fluent derived heat transfer coefficient of 120 W m^{-2} K^{-1}. Heat transfer coefficients of 50, 250, and 500 W m^{-2} K^{-1} (i.e. <50% to around 400%) are given to highlight the relative differences. The overshoot in temperature seen in the experimental data is due to the thermal inertia in the system and the fact that the control system does not have time to react and slow down the heater to control the transition between heating and soak. This type of test is outside the intended operating window for the system; however with careful programming it may be possible to reduce this effect. Another reason for the overshoot could be a result of the flow regime over the plate surface and in the head unit. As the plate is placed in in the head unit it will disrupt the flow paths already formed, therefore it takes a few seconds before a steady state situation is reached with the plate in position.

The specific heat capacity of the material defines how much energy is required to heat the plate. For example, a material with a high heat capacity will require more joules of energy to heat it to a given temperature than a material with low specific heat capacity. A higher heat transfer coefficient provides more joules per second to a given area for a given temperature, demonstrating that the higher heat transfer coefficient will result in a shorter heat up time. (This logic was the basis for the experiments and shows that the heat up portion of the graph is very important when establishing the accuracy of the results from the Fluent modelling).

Although the fit is not perfect, the figures obtained from the Fluent simulation were in the right range. The curves for 50, 250, and 500 W m^{-2} K^{-1} show significant variations from measured data particularly during the heating.

12.6 KEY OUTCOMES

The graphs presented in this section show very good correlation to the experimental data (particularly for a heat transfer coefficient of 120 W m^{-2} K^{-1}) suggesting that the boundary conditions identified represent a good approximation of the process. As shown in section 12.3 close consideration of the heat transfer and gas temperature boundary conditions governing the exhaust gas region (i.e. regions ii, iii, iv in Figure 12-10) is important in order to replicate the temperatures outside the head unit recorded in experimental testing. The thin nature of the test piece makes heating with relatively low heat transfer coefficients possible. However, it is very important to have a good understanding of the ambient gas temperature as this has a significant effect on the temperatures achieved outside the head unit. If one chooses too low a temperature then in the simulation the plate will fail to achieve the temperature seen in reality. The effect of varying heat transfer coefficient described in section 11.3 justifies why the ramp-up region of the heat treatment cycle was important for the validation of the ABAQUS modelling. Figure 12-17 further substantiates this by highlighting that the temperature in the soak region (i.e. once the substrate is close to the gas temperature) is very insensitive to large variations in heat transfer coefficient, i.e. <10% difference between in soak temperature, under head heat transfer coefficients of 120 W m^{-2} K^{-1} and 500 W m^{-2} K^{-1}. This is particularly true in the initial

heat-up phase of the graph, before the lines (experimental data and 120 W m^{-2} K^{-1}) begin to diverge as a result of the overshoot seen experimentally.

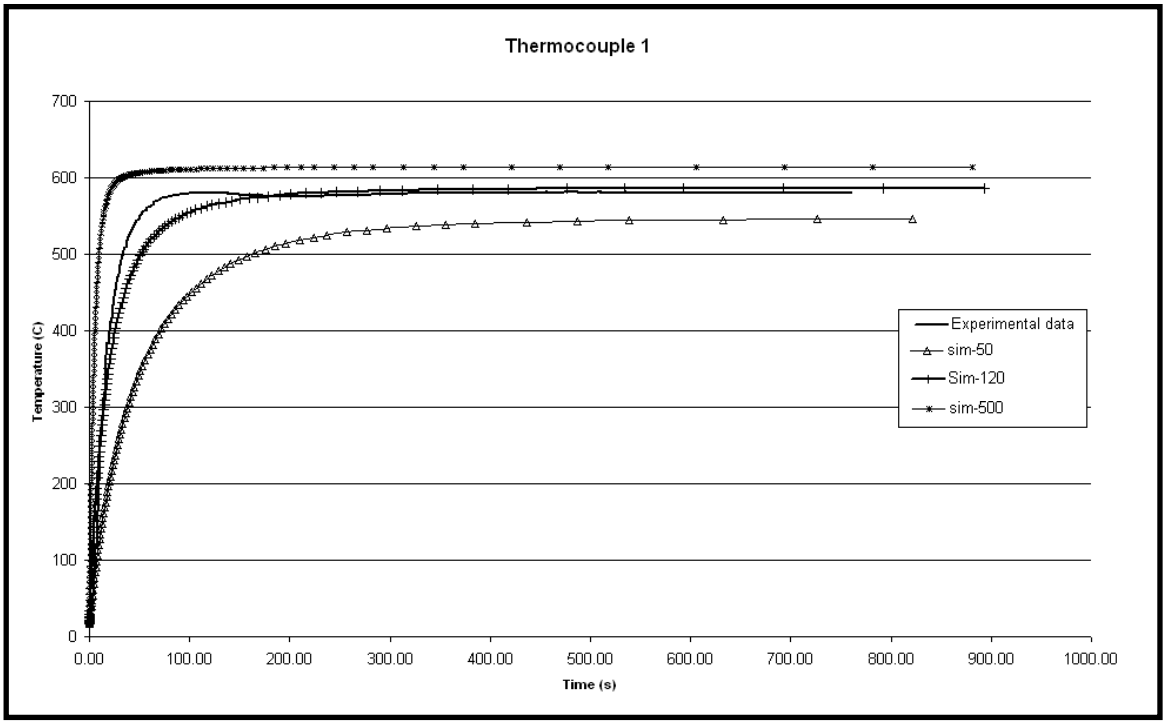


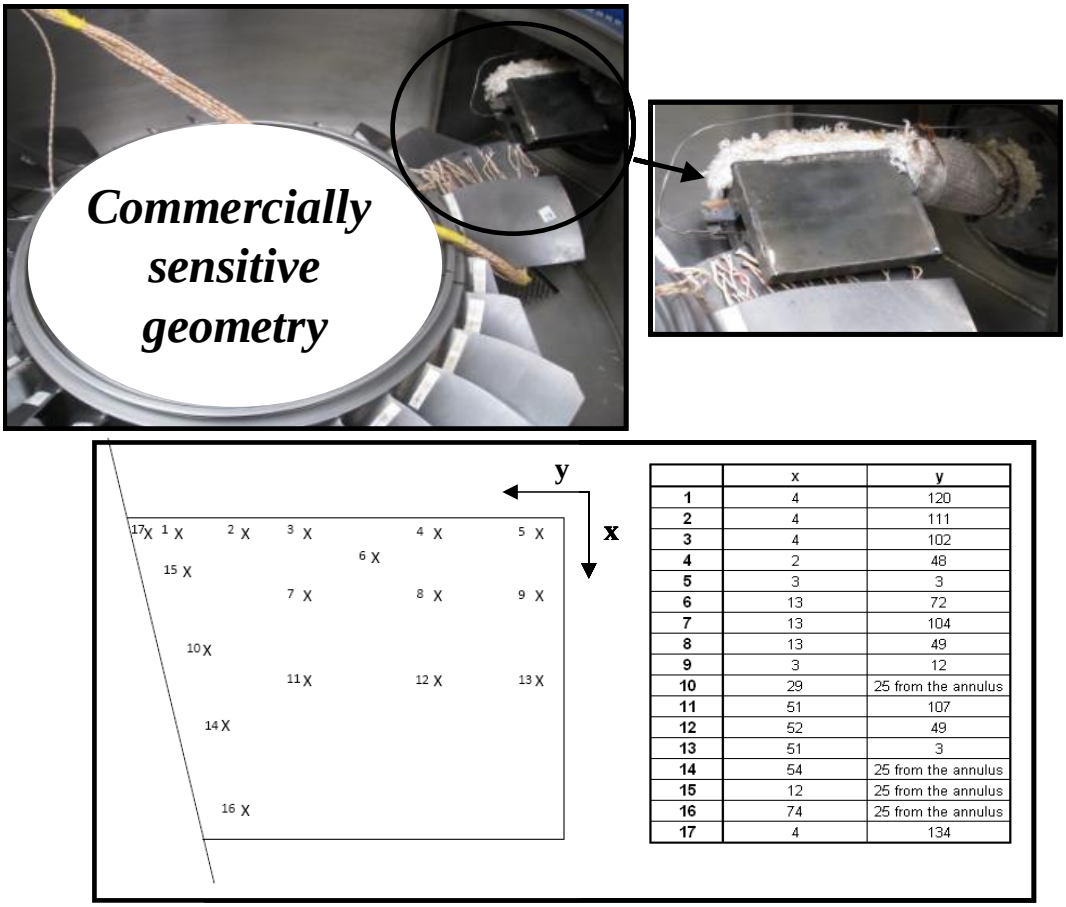
Figure 12-17 : Ramp rate comparison at thermocouple 1

12.7 USING THE PROCESS MODEL

The purpose of this exercise was to provide a tool to assess the capability of the local heat treatment system on real geometries and also to develop understanding of the physical principles that govern the process.

12.7.1 COMPONENT MODELLING – VALIDATION OF THE PROCESS MODEL

In order to test the boundary conditions a thermal validation exercise was performed on a component similar to that used in the tests described in section 9. Figure 12-18 shows the component with thermocouples positioned across regions of interest, both within the heated region and around the base of the aerofoil where



	x	y
1	4	120
2	4	111
3	4	102
4	2	48
5	3	3
6	13	72
7	13	104
8	13	49
9	3	12
10	29	25 from the annulus
11	51	107
12	52	49
13	51	3
14	54	25 from the annulus
15	12	25 from the annulus
16	74	25 from the annulus
17	4	134

Figure 12-18 : Model validation test setup (top), test piece thermocouple locations (measurements in mm)

the temperature gradient is largest. The photograph on the left in Figure 12-18 shows the component and thermocouples, and the diagram on the right shows the positions and numbers of the thermocouples used.

12.7.2 EXPERIMENTAL AND MODEL SET UP

The test piece had several areas which had been removed for previous tests and therefore CAD geometry of the test piece was produced replicating this. The affect of these regions on the temperature seen in the aerofoil of interest are likely to be very small however it is important that a representative model is produced. Detail was removed from the CAD model which significantly reduced the element count in the meshed part, therefore reducing file size and run time. The modified geometry was imported into ABAQUS finite element software and meshed using tetrahedral mesh elements with small element size on the blade being heated and a coarser mesh in the bulk of the hub section. The reason for the coarser mesh in the hub section is due to the relatively uniform temperature expected in this region and the fact that less resolution is required here for the thermal analysis. Conversely, in the

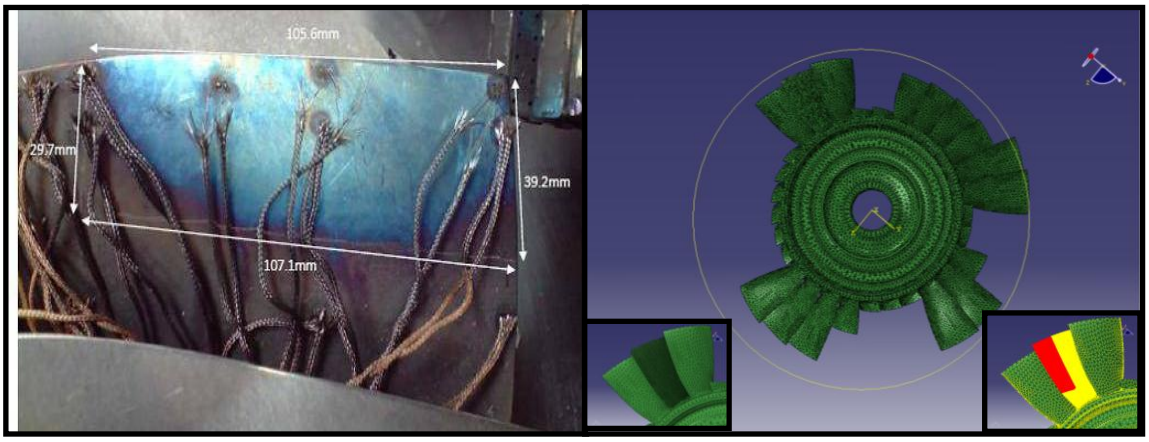


Figure 12-19 : Heated zone, test piece (left), model (right). Red zone is heated region (120 W m^{-2} K^{-1} @ 893 K), yellow and green regions ambient boundary condition (6 W m^{-2} K^{-1} @444 K)

blade steep temperature gradients exist and a large number of temperature points were needed for comparison with the thermocouple data generated in the experiment.

The leading edge head unit was used to heat the test piece with a flow rate of 120lmin^{-1} and gas temperature of 893 K. These parameters replicated those used for inputs to the CFD modelling and allowed the heat transfer coefficient defined in section 11 (120 W m^{-2}K^{-1}) to be used for the head unit boundary condition. Figure 12-19 (left) shows the area covered by the head unit in the experimental trials, and (right) the zones as transferred onto the ABAQUS model. During the heat treatment the ambient temperature was monitored using a mineral insulated thermocouple positioned within the chamber. The chamber was not purged to reduce oxygen levels but the lid was closed to replicate the thermal conditions of a full heat treatment cycle. In the ABAQUS model measurements were taken and the nodes closest to the positions of the thermocouples measured on the test piece were recorded. The temperatures at these nodes were then extracted from the post-processing software. The model was run in heat transfer mode with no distortion, therefore the nodal positions did not move relative to the heating source.

The ambient temperature in the chamber was measured as 444K and this was used along with a heat transfer coefficient of 6 W m^{-2}K^{-1} for the region outside the heated zone. No exhaust gas zones were imposed on the component as a leading edge head unit was used. Furthermore the blade has a high degree of curvature and large heat sink close to the heated zone negating the effect of any exhaust gas.

12.7.3 RESULTS

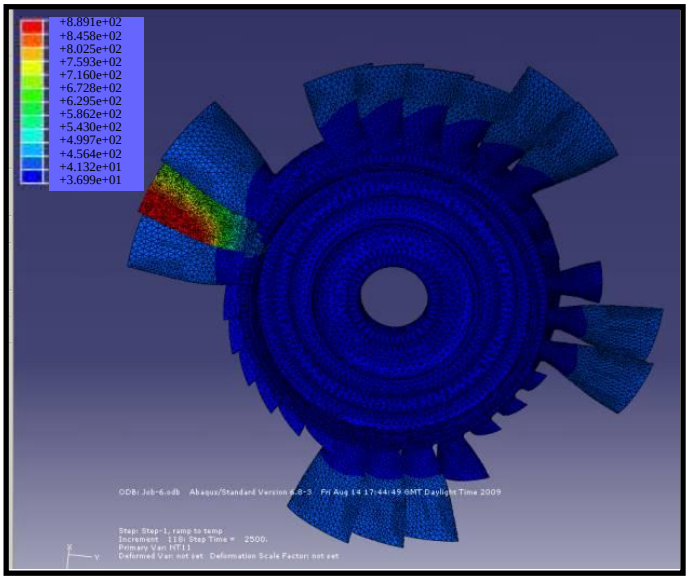


Figure 12-20 : Model output for validation exercise

Figure 12-20 shows the temperature distribution across the test piece, with the heated blade clearly evident in the top left-hand region of the image. Noteworthy are the steep temperature gradients shown on the blade surface, particularly close to the root. The temperature of all the aerofoils compared to the hub section is slightly higher, this is due to the thin sections being heated by the hot ambient gas in the chamber. Blades not being directly heated during testing reached temperatures of close to the ambient temperature after the full cycle.

Figure 12-21 (below) shows the data from the blade thermocouples plotted with the experimental data from the same thermocouples. The solid line represents the experimental data with the thick dotted line representing the simulation data. The thin dashed line shows the % error between the simulation and experimental data[******]. Only thermocouple 16 had an error of more than 10% showing excellent

[******] The error is calculated by finding the difference between the simulated and measured data and then dividing that by the experimental value and multiplying by 100 to give a percentage.

fit with the experimental data, particularly thermocouples 3-9 which were positioned in and around the heated region. Thermocouple 16 was positioned furthest from the heated zone on the aerofoil towards the trailing edge of the blade and was slightly over predicted by the ABAQUS simulation.

This exercise provides confidence in the boundary conditions derived for the gas jet processing localised heat treatment system. The temperatures extracted from the simulation match very closely those measured experimentally.

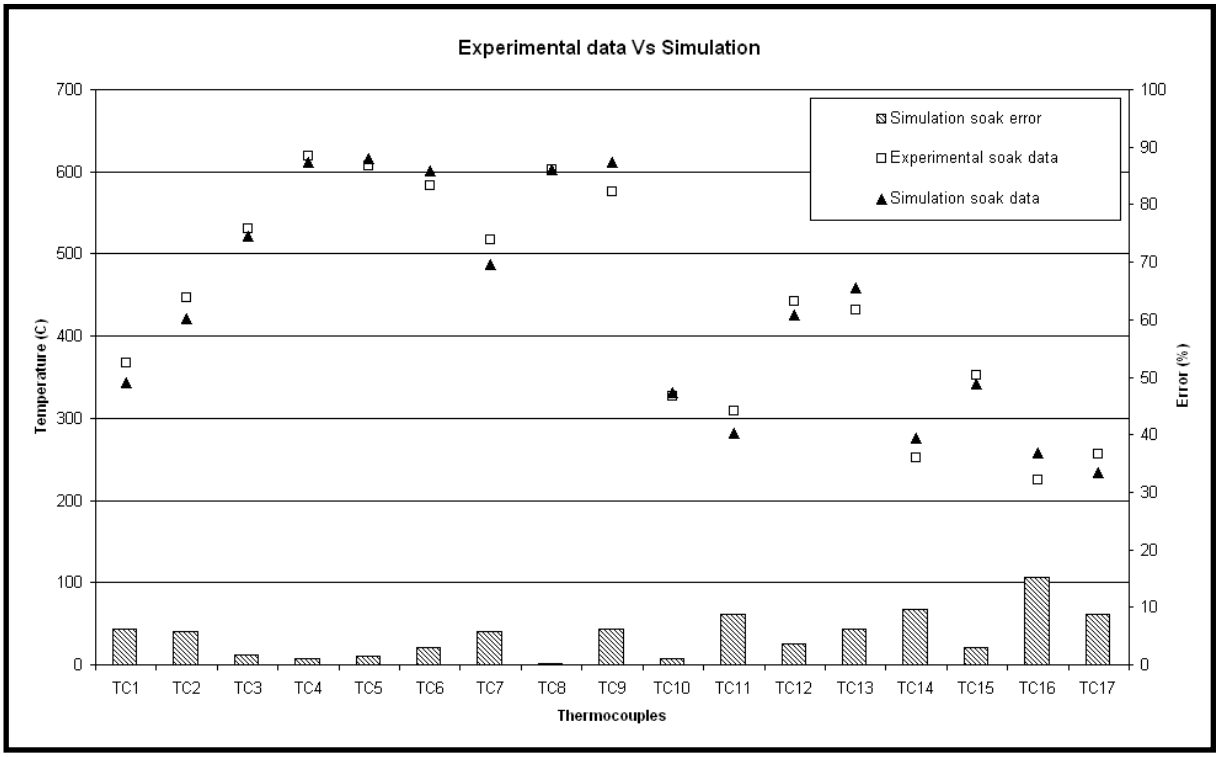


Figure 12-21 : Simulation Vs experimental data for validation

13 GENERAL DISCUSSION

'If the accomplishments of the heat treating industry in the past century could be condensed into a single sentence, it would simply be: "The art of heat treating has become the science of heat treatment." – **M. Lohrmann** [133]

13.1 GENERAL DISCUSSION : EQUIPMENT DEVELOPMENT

13.1.1 PROTOTYPE SYSTEM DESIGN

The heater unit has a basic manipulation system which allowed it to be positioned on the leading edge and tip of specific component geometry in a repeatable manner requiring only a head change between positions. The system was specified is a working prototype and only applicable to processing representative geometry hardware on a single aerofoil basis as proof of concept. The current system relies on one being able to approach and withdraw from a component in a linear motion along the heater axis centre line. In the case of the component processed in section 9 this axis is approximately parallel to the stacking axis of the aerofoil. However, if the component has a significantly varying geometry to its leading or trailing edge, this method of positioning on the repair may not be possible.

13.1.2 ATMOSPHERE QUALITY

The chamber described in this thesis constitutes a simple box structure to reduce the oxygen level in the atmosphere within which the component is processed.

13.1.2.1 Minimising alpha case

The justification for the oxygen level required for a local heat treatment system is based on the mitigation of technical risk, process timing, and the operating cost. This raises the question of what standard of system is required to achieve which technical effect? Simply building to an arbitrarily high standard of chamber locks in costs and processing time. Conversely, too low a standard may not adequately mitigate the risk of alpha case formation.

The degree of oxygen permissible in the system to generate no oxygen concentration at the surface is difficult to determine.

For risk mitigation, the purpose of the argon chamber is to provide an environment that is better than air. The decision was taken that since the component was to be etched as per processing in air, there was no justification for commissioning the design and manufacture of an integrated local convection heat treatment system with hard vacuum standard oxygen levels.

From the perspective of producing a prototype system, the processing conditions presented in this thesis are sound. Processing in an argon atmosphere with a worst-case oxygen ingress rate demonstrates the effect on the mechanical vibration response (presented later in section 13.2).

13.1.2.2 Evidence of oxidation

The purpose of equipment described in section 8 was to develop a system with the capability to process components and test pieces in a repeatable manner. The oxygen levels seen in the system were measured at between 10 and 50ppm and have produced surfaces with some level of discolouration (see Figure 13-1 and Figure 13-2). However, this is significantly more favourable than processing in air. Donachie [41] and others [49,46] have noted the significant variation that exists between the levels of alpha case seen in heat treated titanium.

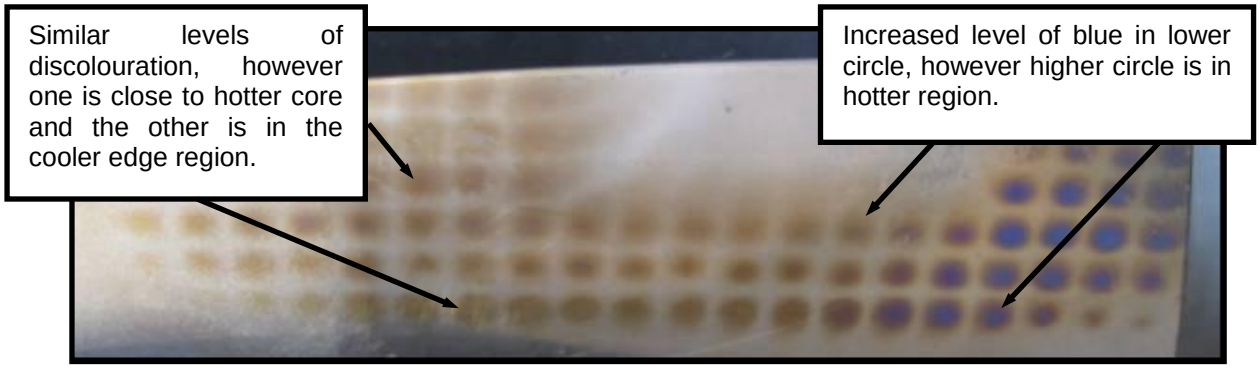


Figure 13-1 : Oxidation pattern produced after application of the local heat treatment system

Figure 13-1 shows the level of discoloration on the aerofoils processed for the HCF testing (described later) after localised heat treatment. This localised blue pattern was evident on all processed test pieces throughout this work. The silver region in the centre of these heated regions is where no gas jets are present[††††††]. Considering these test pieces, it is apparent that a significant level of oxygen is present within the system causing this level of discoloration. There are two

[††††††] Blocking jets is a design feature described previously, it is used to reduce the overall temperature distribution across the repair region by using tailored geometry jet plates

potential reasons why these areas are more oxidised; either they have more oxygen available to them and/or they are hotter. Noteworthy is the absence of a pattern towards the corner of the heated zone.

The localised nature of the blue/brown regions is not due to localised hotspots but due to the fact that these are the regions directly under the jets. They have a constant replenishment of gas (containing some oxygen) and are also the first regions to interact with gas leaving the head unit. The more silver appearance of the adjacent areas correlate with the regions of stagnant (or slower moving) flow in the regions where the interaction between adjacent jets creates an upward flow [76].

This discolouration is a result of the hot gas coming from the heater containing oxygen at a high enough level to cause localised discolouration. The pattern does not correlate with the isotherms, i.e. the hottest region is not the most blue.

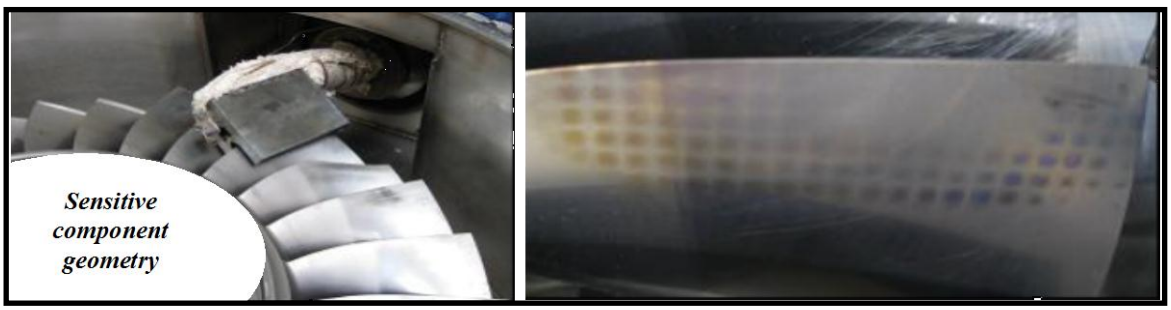


Figure 13-2 : Photographs showing the head in the leading edge position on the test pieces (left), and the resultant oxidation pattern on the test piece (right)

However the discolouration does correlate with the regions where gas is constantly supplied from the head unit, i.e. the base of the jets. The central region of the heated zone has no jets impacting on it and this is not blue in colour, in spite of it

being the hottest region (as described in section 7). Furthermore, Figure 13-1 and Figure 13-2 show no evidence to suggest that the discolouration is more evident towards the leading edge of the aerofoil and reducing in intensity as one moves into the blade chord. This is the way in which one would expect to see the pattern develop were it temperature that were driving the discolouration. In conclusion, this circular pattern is not the result of localised hotspots but a result of the process gas having a sufficient level of oxygen within it to cause discolouration. The areas containing little discolouration are the regions associated with stagnant or lower velocity flow.

13.1.3 HEAD UNIT DEVELOPMENT

The head units detailed in this thesis represent the initial attempts to design a unit for the application of the gas jet processing system. During this process much has been learned about the design and development of the head unit that must be captured as part of the capability acquisition process. Some of the key aspects of the head design are discussed below;

13.1.3.1 Jet array design

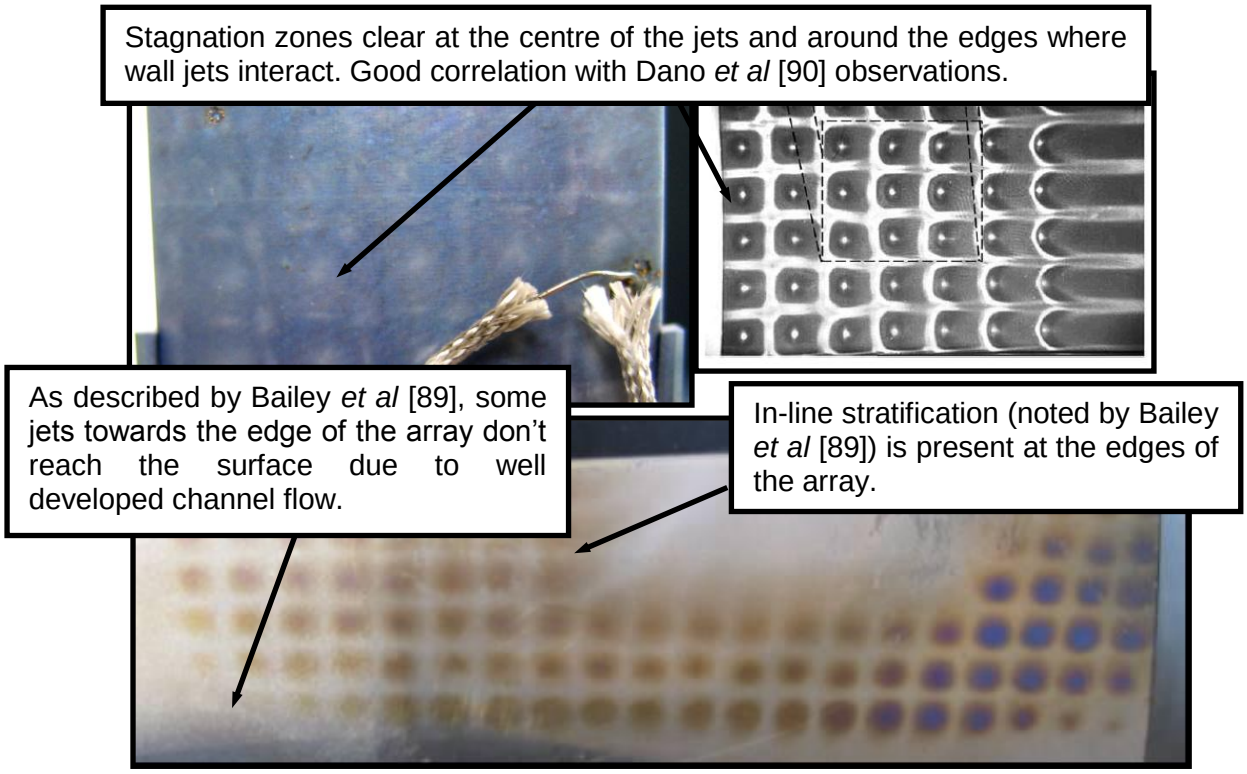


Figure 13-3 : Evidence of head jet array morphology

The top left image in Figure 13-3 shows an aerofoil test piece, heat treated using the system developed in this project. The particular head unit used in this test had just been manufactured and contained dust on the surface of the sheet metal. In

the photograph one can see the areas where this dust has been deposited by the slow moving (or stagnant) gas during processing.

As mentioned previously and documented by Martin [76] stagnation zones exist at the base of impingement jets where the gas is slowed by the component surface. Its velocity is changed through a process of deceleration in the vertical direction and acceleration in the horizontal direction. It is this change of momentum that produces the heat exchange experienced at the component surface. At this point the gas is momentarily at a very low (or zero) velocity. In the top left photograph in Figure 13-3 this moment of zero velocity is where the powder is deposited on the component surface, as the gas does not have enough momentum to continue carrying the dust particles. The second area where gas velocity drops and the same effect is noticed is at the point of interaction between adjacent wall jets. However it is worth noting that the change of velocity here is as a result of interaction between gas jets and not between gas jet and component surface, therefore there is lower heat transfer to the substrate at this point.

The bottom photograph in Figure 13-3 shows the array effects described in the literature [89], [90], [91], with the jets at the edges of the array showing the effects of crossflow and the presence of in-line stratification. Both the oxidation pattern and the dust left on the surface show that the jet array's used in these head designs have a good uniformity across the heated area.

The different flow patterns observed in Figure 13-3 are due to the different H/D ratios. The top images represent tests with low H/D ratios, for example an H/D of 3 for the experimental results using an early experimental head RPDG000187 (see

appendix 1), and an H/D of 2-4 in the case of the image from Dano *et al* [90]. Carcasci [105] notes a very similar morphology using an oil and pigment covered plate for flow visualisation. The bottom image was produced by jets with an H/D ratio of 8 (as modelled in section 11), a very similar morphology is also noted by Carcasci [105] at an H/D of 8, again using oil and pigment.

13.1.3.2 Under-head gas temperature distribution

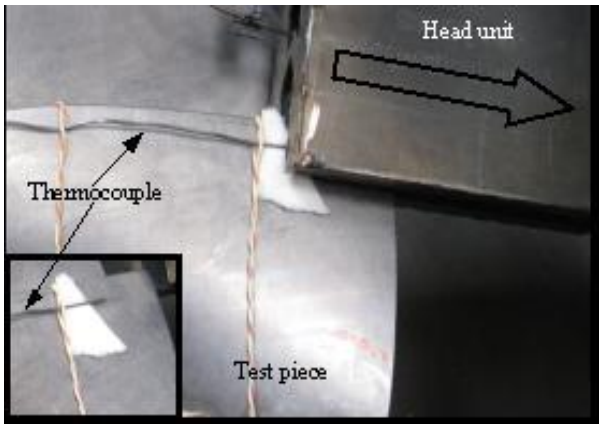


Figure 13-4 : In-head gas temperature measurement method

Figure 13-4 shows a test to establish the difference in gas temperature in the under head region. In this test a k-type mineral insulated thermocouple was placed on the surface of a test piece. The head unit was then manipulated relative to the thermocouple to position it at various

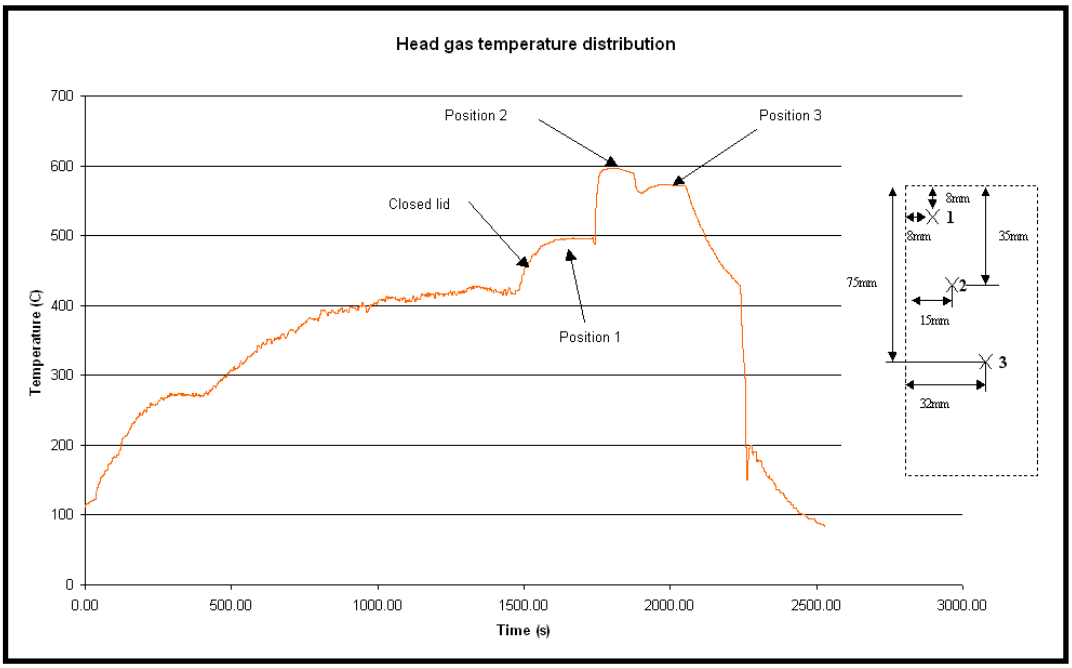


Figure 13-5 : In-head gas temperature measurement results with a control temperature of 591°C. Dotted line represents the array boundary. Flow rate used was 120 l min^{-1}.

regions around the heated zone. The thermocouple was thermally insulated from the test piece using ceramic paper. The intention with this test was to establish how much the under head temperature varied.

Figure 13-5 (above) highlights the variation in temperature with position for the test setup shown in Figure 13-4. The position within the head array is shown on the inset diagram, with the three crosses highlighting the locations plotted on the graph. The initial rise in temperature from just above 400 to 500°C is associated with the lid on the chamber being closed. This closing of the lid has the effect of increasing the localised atmosphere temperature and therefore reducing the temperature difference between the ambient and under head gas temperatures. This in turn reduces the heat loss from the under head gas and increases the temperature reading on the thermocouple. This effect is much greater at the edges of the heated area (position 1) as further under the head the gas is shielded from the cooler ambient gas. Position 2 is close to the centre of the jet array in terms of depth into the head unit (although in terms of width it is around 1/3 of the distance into the head unit). Here it is recording a temperature close to the value the hot zone of the test piece achieves in a typical cycle. The final temperature measured in the head unit is at position 3. Here the thermocouple is at the back edge of the jet array close to the final row of jets. Note that the temperature at position 3 is very close to the control temperature. In position 3 the thermocouple is closest to the location of the control thermocouples in the head unit. The gas temperature is slightly lower due to it being positioned at the edge of the array and losing temperature to the cooler gas outside the array. The temperature of the

surrounding gas at this location is higher than at position 1 as it is enclosed within the head unit and not open on two sides as with the previous examples.

The unit cell modelling approach described in section 11 could be used along with a CFD model of the head unit to better understand the variation in temperature seen in Figure 13-5. However, the inlet flow rate in these simulations was the same and therefore does not account of any variation in pressure that may exist across the array. The use of a model of the head unit without heat transfer would reduce run time and allow one to investigate the variation in pressure within the head unit. An iterative design process could then be undertaken in order to ensure a uniform velocity profile across all the jets in the array. The variation in heat transfer coefficient between the central jets and those at the edge of an array using the unit cell approach is show in Figure 11-11. A reduction of approximately 25 $Wm^{-2}K^{-1}$ is seen between the central and corner/front unit cell jets for an 8mm jet length. This is likely due to the cross flow effect seen in Figure 13-3 and described by Bailey *et al* [89].

The effect of position within the jet array on local gas temperature are clearly shown in Figure 13-5 and this has a significant impact when designing a head unit for a given application. This highlights the importance of over-sizing the head unit for a given repair application as this has the affect of shielding the central jets from the cooling effects of the surrounding ambient gas.

13.1.3.3 The use of seals and skirts in the head aperture

The design of the head aperture is critical in head design. In early design iterations (see Appendix 1, section 15) a skirt lip and insulation material was used to seal between the head and the aerofoil around the heat treatment region. This was designed to prevent the gases passing over the surface of the component outside the heated region. However, the nature of forced convection heat transfer using impingement jets requires a good flow of exhaust gases to maximise the heat transfer [93]. If a free flowing exhaust is not present then the jets are ineffective and stagnation zones form at the edges of the heated area.

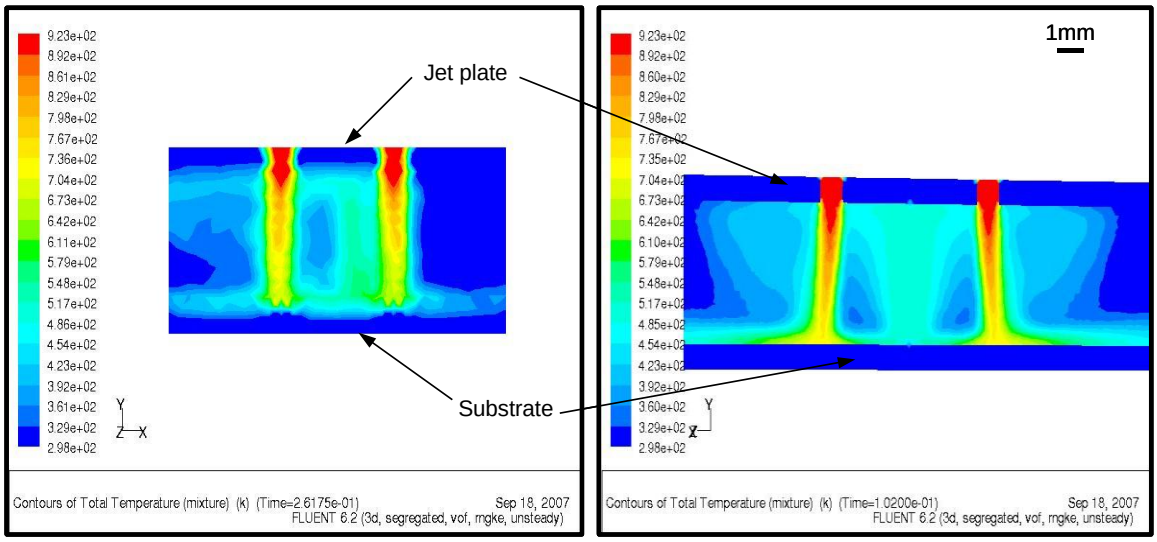


Figure 13-6 : CFD images showing effect of blocking the exhaust gas path. It is noted that the simulation on the left was produced using a significantly larger mesh size. (This was a 3D simulation using a system representative flow rate of 120 lmin$^{-1,}$ at a temperature of 620°C).

Figure 13-6 shows the temperature profile of two jets when the right hand end of the model is blocked to prevent flow of exhaust gases (left image). In the image on the right hand side the gas is free to escape at both ends of the model and this produces a more uniform heated region and allows more hot gas to be in contact with the plate.

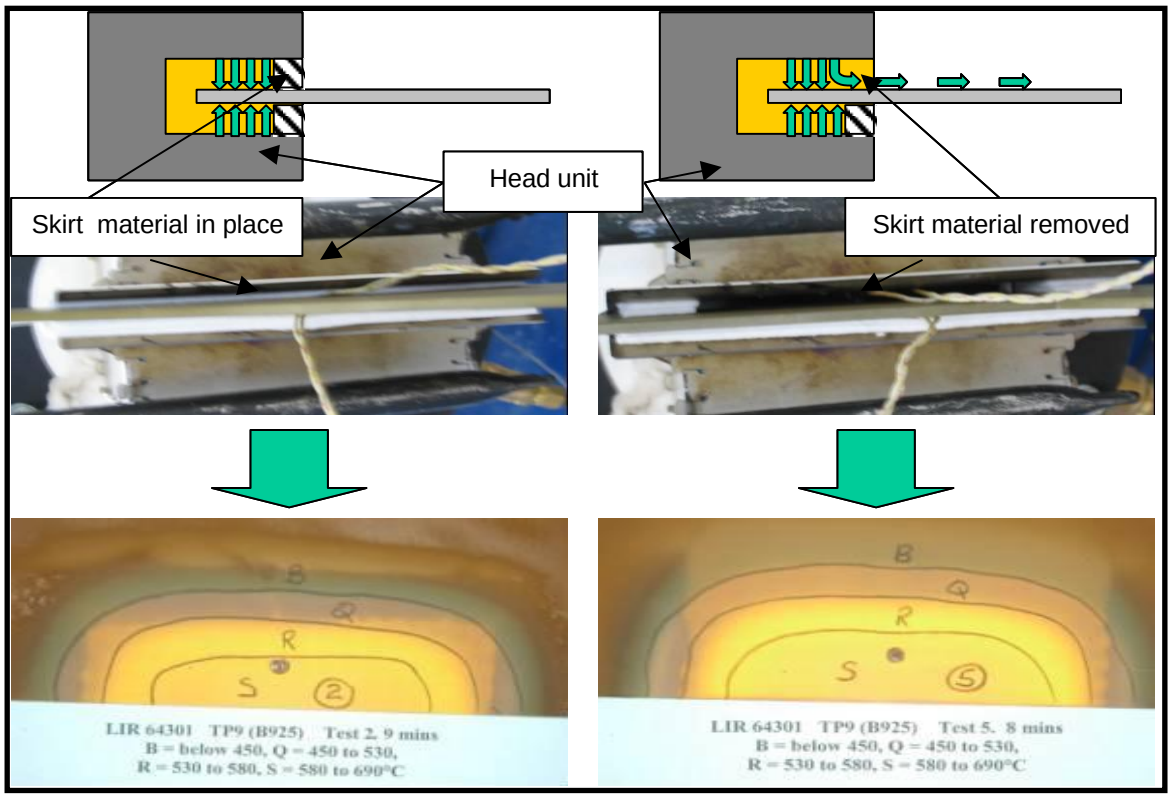


Figure 13-7 : Effect of removing skirt material. Schematic diagrams (top) in cross section showing removal of top piece of skirt material. Photograph (centre) during testing from front of head unit. Thermal painted Ti 6-4 test pieces (bottom) highlighting the effect on isotherms. Head unit used was RPDG000186.

Figure 13-7 shows two thermally painted test pieces which further substantiate this observation. The test on the left has a skirt in place round the aperture of the head unit. In the test on the right, the skirt material has been removed on the topside of the plate to provide an open exhaust for the gas post-impingement. The isotherms on the right hand plate are more spread out showing a larger overall heated region and larger hot zone in the centre. One can also see the lighter colour towards the top and central region of the heat treatment zone. This is a result of the exhaust gases heating the areas around the main target area as they pass out of the head unit to be released into the atmosphere.

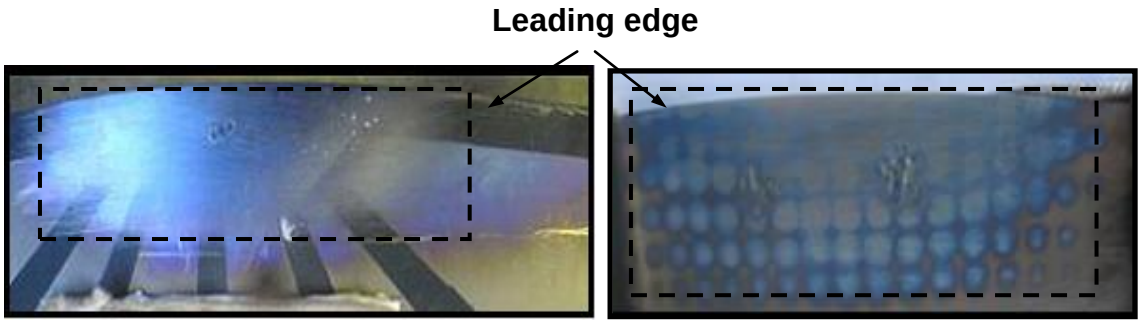


Figure 13-8 : Effect of stagnation on jet pattern, dotted line represents extent of heated zone, i.e. position of the head unit. The image on the left is from a test with no skirt material, image on the right is from a test with skirt material in position around the head aperture.

Oxidation is evident in Figure 13-8 in the locally heated region. The photograph on the right highlights that at the edges of the heated zone the temperature has been relatively low (below 400ºC) as very little discoloration has occurred. This is due to these regions having stagnated due to the lack of an open exhaust. These regions represent the highest pressure regions under the head. In some cases the central core of some impingement jets (the regions of highest velocity) have punched through this stagnant gas and impacted with the surface. Conversely the image on

the left shows a heated region with more uniform discolouration generated by a having an open exhaust.

This highlights that opening out the exhaust passage is an effective way of increasing the size of the heated region. To maintain the use of a seal (should it be required in the future), the head could be oversized to increase the heated zone and move the ineffective regions outside the desired heating zone.

13.1.4 EXHAUST GAS FLOW

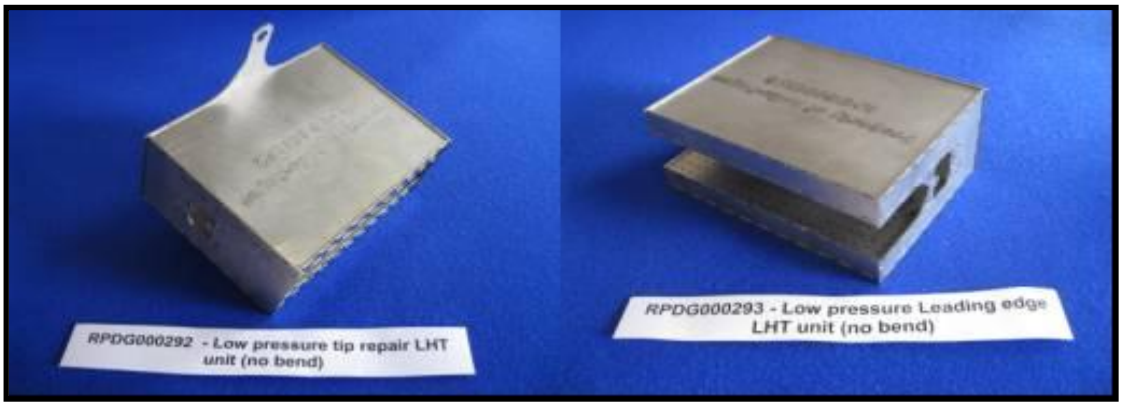


Figure 13-9 : Two generic head unit types producing different exhaust gas morphologies

Two basic head designs were presented in section 9. One targeting the leading or trailing edge, the other targeting the tip (both shown in Figure 13-9). The main difference between the head types is that one is open on three sides (leading edge head) and the other has a single outlet at the front (tip). The reason for these configurations is that in order to allow positioning on the leading edge at least two sides must be open and having the third one closed would lead to asymmetrical heating characteristics making uniform heating difficult. Also if a region in the centre of the leading edge needed heating, three open sides are required. In the case of the tip head unit having closed sides reduced the cooling effect of the

ambient gas described in the previous section (see Figure 13-5) without having to oversize the head unit too much.

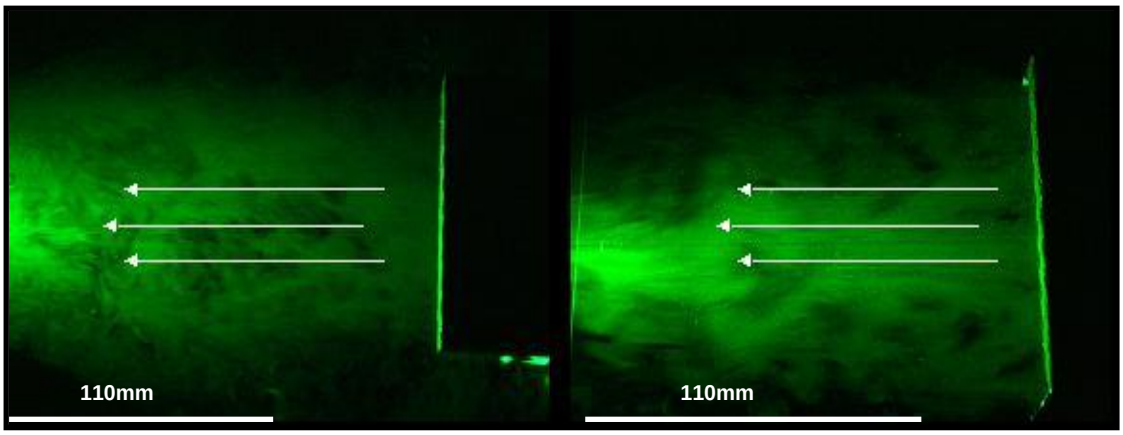


Figure 13-10 : Comparison between Tip and LE exhaust morphologies

The two designs produce very different flow patterns in their exhaust gases. The flow visualisation techniques described previously in section 11.8 were used to study the morphology of the gas exiting the different styles of head unit, the tip head unit has a very uni-directional exhaust flow shown in the right hand image of Figure 13-10 (above).

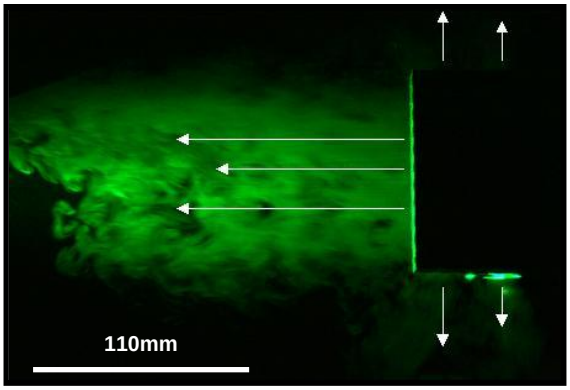


Figure 13-11 : LE exhaust gas paths

The leading edge head unit produces the flow pattern shown in Figure 13-11; here, the central flow is supplemented by perpendicular flows emanating from the sides of the head unit. These flows are from the wall jets of the jet array and out of the exhaust 'windows' at the back of the jet array. The side flows have a much lower intensity than the central front flow due

to the smaller number of jet rows in the depth direction of the array. These tests were carried out a minimum of three times in order to assess the reproducibility of the flow regime observed.

Figure 13-10 shows a comparison of the flow from a leading edge head unit (left) and a tip head unit (right). The left image shows a much slower moving gas, with more mixing evident by the existence of darker ‘pockets’ in the gas flow. The image on the right has a more well defined central core of flow with more directionality evident. The flow rate in these tests was the same, but due to the larger exhaust area the resultant mean velocity was lower in the case of the LE head. In terms of heating characteristics this will result in much cooler temperatures measured by the gas flow thermocouples (see section 12). Secondly the heat transfer is likely to be lower due to the slower exhaust gases. Finally, the lower velocity of the exhaust gas on leaving the head unit will result in buoyancy having a larger influence on the flow direction of the gas. In reality this leads to slightly lower component temperatures and larger temperature distributions, but slightly increased heat transfer coefficients due to the reduced cross-flow experienced by the individual jets.

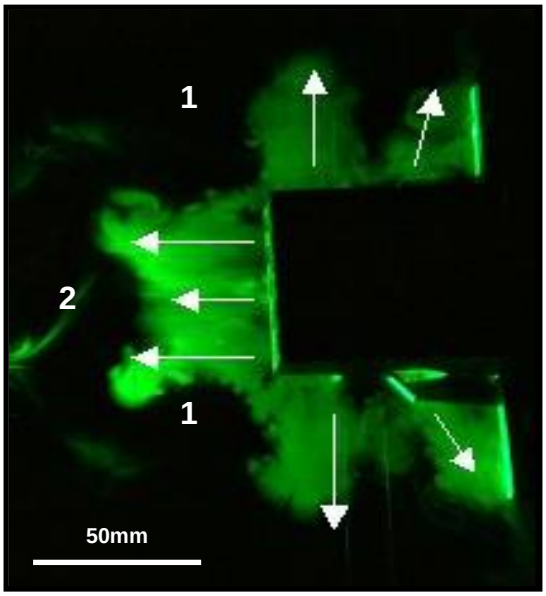


Figure 13-12 : Generic LE head exhaust morphology at the beginning of a cycle

The image in Figure 13-12 shows the early stages of the exhaust gas leaving a small leading edge head unit. The flow pattern is representative of what happens in the case of a larger leading edge head unit with higher velocities for a given flow rate. Two noteworthy regions exist which help one to understand the effects of exhaust gases on the plate/test piece temperatures. Number 1 in Figure 13-12 is the region between the two perpendicular flows emanating from the front and side of the jet array. This region contains cooler ambient and relatively stagnant gas which acts to cool the exhaust flow and slow it down due to interaction at the edges of the main flow streams. Number 2 relates to the central flow which in the case of the head units used in these trials has a curved flow front (shown by the arrows in the image). This curved flow front is due to the fact that the central jets were removed in an attempt to improve the under head temperature distribution (tailored jet plates discussed in section 7.3). Therefore less flow is present in the centre and this portion of the central core lags behind the rest as the flow forms on leaving the head unit.

The gas temperatures measured due to the different flow regimes are quite different. Generally, close to the head unit the gas temperature is slightly higher than that measured by the plate/test piece thermocouples. However, as one moves further from the head unit the temperature of the gas in the case of the leading edge head unit rapidly becomes cooler than the plate. In the case of the tip head unit the exhaust gas remains very close to the plate temperature. The heating effect of the gas in the case of the leading edge head unit configuration is much less significant. Whereas in the case of the tip head unit it has a significant effect, particularly when the plate being heated has no significant heat sink effect.

13.1.5 CONTROL THERMOCOUPLE POSITION

During much of the testing performed in the course of this doctorate the apparatus was removed and replaced between tests. A robust method of control thermocouple positioning was not developed. Once the temperatures (including distribution) had been achieved the control thermocouple was maintained in that position for the remaining tests. When the apparatus was removed and replaced every effort was taken to measure the thermocouple and its position within the head unit so that its junction was positioned centrally. Further work needs to be undertaken in the future development of this technology to establish the most appropriate way of positioning the control thermocouple. In addition a temperature survey of the under head region should be completed to identify any variations in gas temperature that may exist. It is important for material integrity that a value close to the maximum gas temperature is measured as it would be unfavourable if the control was reading a value below the maximum temperature achieved on the component.

13.1.6 POSITIONAL VARIATION

During the repeated movement and setting up of the apparatus every effort was made to carefully measure and position the test piece, however it is likely that the position of the plate relative to the head unit was not always consistent. This may result in some of the variations seen in the data in section 10 for the temperature distribution. Where a component is being heat treated careful fixture and manipulation design (such as that described in section 5) can help to eliminate some of the source of positional instability, however blade-to-blade variation in

manufactured (and particularly service run) blades may mean that some level of instability still exists.

Although positional variation can affect temperature distribution in the heated zone this is due to the tight temperature tolerances required over the heated region for high integrity repairs. This should be separated from the stand-off sensitivity discussed in relation to induction and radiant heating. Here the potential is for the heated zone of the component to be raised to a temperature significantly higher than the intended heat treatment temperature. These large variations would not simply result in the heat treatment being out of tolerance resulting in insufficient stress relief, but may also cause accelerated oxidation or microstructural change.

13.1.7 TEMPERATURE OFFSET

Offset is the difference in temperature between the control (gas) temperature and the average component temperature. Several examples of the correlation between offset and system flow rate have been shown experimentally (Figure 9-14, Figure 9-20, and Figure 10-6). The reduction in offset with increased flow rate (for a fixed jet array) is consummate with the effects of increasing heat transfer coefficient shown in Figure 12-16 and Figure 12-17. The flow rate is linked to heat transfer coefficient through Reynolds number (Equation 2-4, page 41), Nusselt number (Equation 2-5, page 42), and the relationship between the two (Equation 13-1, page 282). Increasing the flow rate for a fixed array will result in an increased Reynolds number (due to increased jet velocity) and therefore a higher heat transfer coefficient.

13.2 GENERAL DISCUSSION : PROCESS VALIDATION

It is well documented [43, 56, 57, 65, 67] that alloys such as titanium 6-4 respond well to stress relief heat treatments. With this in mind the focus of this research has been on the development of the local heat treatment system capable of maintaining a localised region at a suitable temperature. The specifics of the cycle chosen are proprietary information but fall within the ranges described in section 2.7. Such cycles represent a balancing of requirements between achieving the required level of stress relief, and minimising the level of alpha case generated in the alloy after heat treatment. Whilst it is clear from the work presented in section 9 that the thermal capabilities of the gas jet localised heat treatment system meet the target temperatures and cycles. In order to determine the ability of the process to provide sufficient stress relief, the following two-stage validation exercises were conducted;

- Firstly residual stress measurements via hole drilling were performed to determine a quantative measure for the effectiveness of the localised process.

- Secondly component high cycle fatigue testing was performed on repaired and heat treated components. The results of this were compared to unrepaired components in order to determine whether the repaired components performed comparably.

13.2.1 RESIDUAL STRESS ANALYSIS

Residual stress measurements on as-repaired aerofoils and following global heat treatment have been presented in section 7.1. To provide an indication of the residual stress reduction resulting from the local heat treatment further measurements were made on repairs processed using the equipment described in this thesis. Using the same methodology as described in section 7.1 two components were measured and the resulting data presented in Figure 13-13.

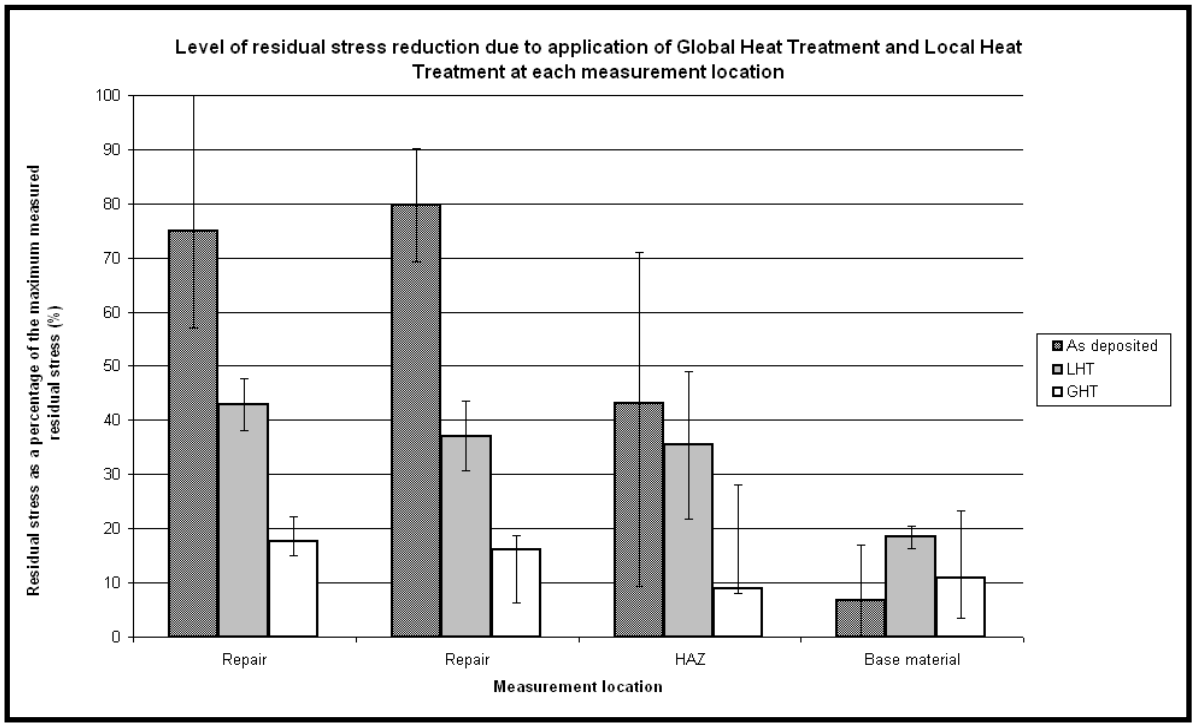


Figure 13-13 : Residual stress reduction due to LHT and conventional global heat treatment

Figure 13-13 shows the results of residual stress measurements in as-repaired (as-deposited), and repaired and heat treated test pieces. Heat treatments were completed using both localised gas jet heat treatment (LHT) and global (Vacuum furnace) heat treatment (GHT). The data presented show that both heat treatment techniques are effective at reducing the level of residual stress in the repair,

however GHT is shown to be more effective particularly in the HAZ region. This is due to the close proximity of this region to the edge of the heated zone and the fact that the surrounding material is a constraint during heat treatment. One can see that the bulk of the repair undergoes significant levels of stress relaxation resulting in ~50% of the original stress levels being relieved (slightly less than that stated in [65, 67]).

Important to note is that due to the application of the LHT process the stress field is likely to change. For example a re-distribution of the peak residual stress values may occur. The fact that the surrounding material is cool and therefore prevented from relaxing through creep during heat treatment had a significant effect on the manner of stress relief. Furthermore it was very difficult to determine whether such residual stress levels were sufficient to cause a reduction in fatigue life. Therefore, the conclusion to take from this study is that the local heat treatment system is effective at reducing the level of residual stress in the component, at the locations measured. However, in order to understand whether the local heat treatment process produced a repair with acceptable levels of residual stress in the component, high cycle fatigue testing was performed.

13.2.2 RESIDUAL STRESS FROM LOCALISED HEATING

The residual stress measurements demonstrate that holding the repaired region, the heat affected zone, and some parent material at the stress relief temperature for the required time provided some stress relief. However, there remains the question as to whether heating a localised region actually generates significant thermally induced stresses, or that the level of stress relief of the repair is sufficient to not impact fatigue life. The thermal expansion of titanium 6-4 from 20-650ºC (within the stress relief temperature range for titanium 6-4) is 9.7 x 10^{-6} mm^{-1} $°C^{-1}$ [109]. Therefore if one heats a localised region to this temperature there will be localised expansion and the hot material will be restrained by the surrounding cooler material. The hotter material will have reduced yield stress [109] and be placed in compression due to the restraint of the surrounding cooler material. If the material is put under high enough strain it will yield resulting in residual stress after cooling.

13.2.3 AEROFOIL HIGH CYCLE FATIGUE TESTING

The culmination of the system design and development came with the application of the technology on demonstration hardware (as described in section 9) to be used for component HCF testing. Prior to heat treatment of the repaired components 3 unrepaired components were heat treated and tested in HCF. Following this, a total of 15 repaired and heat treated components were tested along with 25 unrepaired (baseline) components (see Figure 13-16). Due to the sensitive nature of the data relating to the mechanical testing of these components

a brief overview of the test is provided below along with normalised data from the tests.

The purpose of testing 3 heat treated components containing no repaired region was to identify any reduction in fatigue life due to the application of the local heat treatment. The mechanical testing specialist within Rolls-Royce specified that a minimum of three aerofoils must be tested to produce a statistically significant result. Although one could not simply attribute a reduction in fatigue life to the generation of residual stress[‡‡‡‡‡] it is reasonable that any significant reduction in HCF life could be attributed to the application of local heat treatment using gas jet processing.

13.2.4 RESULTS OF HIGH CYCLE FATIGUE TESTING

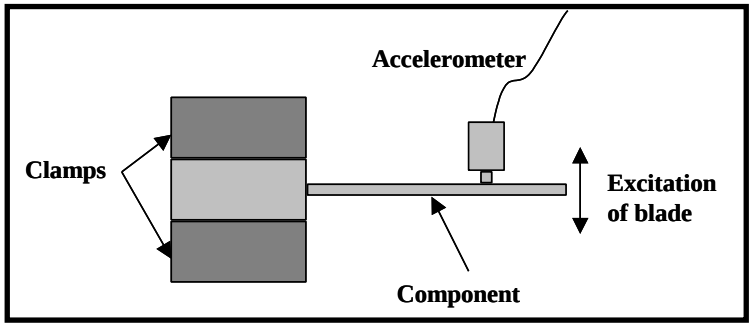


Figure 13-14 : Test configuration during high cycle fatigue blade testing

In order to fully interrogate the integrity of the component post repair, high cycle fatigue testing is often completed [10]. One advantage is that testing is performed

[‡‡‡‡‡] Many other factors may initiate fatigue failure through a variety of mechanisms. From brittle metallurgical phases such as alpha case, to geometric stress concentration factors such as scratches.

on actual blades and vibration modes can be chosen which excite the component in a manner comparable to that seen in engine running.

In an aerofoil fatigue test a blade is clamped in position using a structure sufficiently strong and rigid that its natural frequency of vibration is significantly higher than that of the blade. During the test the blade is caused to vibrate either by the use of a shaker rig, or by forced displacement of the aerofoil tip through air jets or other form of excitation. The vibrations are measured using an accelerometer, and a schematic of the test configuration is provided in Figure 13-14. A blade displays a number of resonant frequencies, which produce various bending and torsional modes (examples are provided by Rao and Gupta [134]). These modes result in regions of high stress in the component.

In order to test the repair and heat treatment a HCF test similar to that described by Richter *et al* [10] was used. In this room temperature test the blade was excited with a measured amplitude to a resonant frequency associated with the required mode shape selected (for example 1^{st} torsional, or 1^{st} bending). After a predetermined number of cycles (or time) the amplitude was increased and subjected to the same number of cycles. This was done (increasing in amplitude each time) until a drop in frequency was measured; this drop in frequency corresponded to a crack initiated by fatigue and represented the fatigue limit of the component. In the case of validation for the local heat treatment system, the length of the test (i.e. fatigue life) for unrepaired, repaired and heat treated, and heat treated only are compared. It is standard practise [10] for the mean, and maximum and minimum values of the fatigue life to be compared. In order to fully test the repair and heat treated region a mode was chosen that produced the highest peak

stress in the location of the repair and heat treated zone. This corresponded with the region shown in residual stress measurements to be the region of highest stress (see section 7.1).

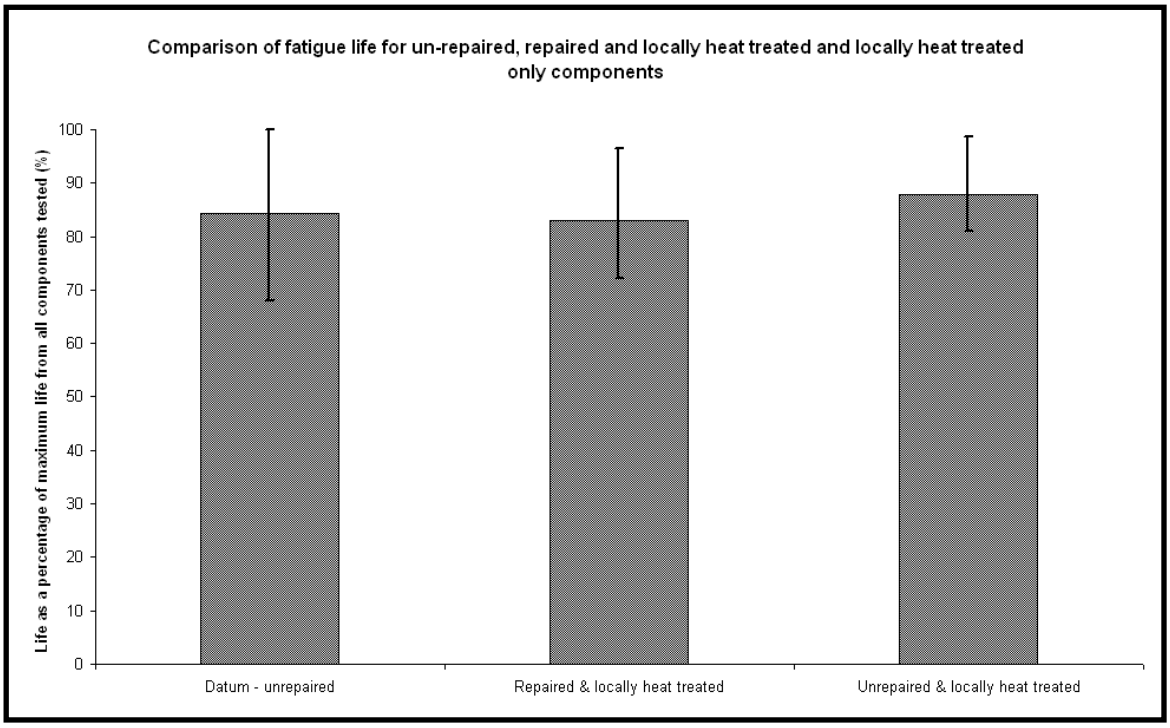


Figure 13-15 : Comparison of fatigue lives for repaired and heat treated, heat treated only, and baseline (un-repaired components)

Figure 13-15 shows the results of the fatigue testing. The y-axis represents a normalised value of fatigue life as a percentage of the maximum achieved fatigue life in all components tested. It is clear from these data that all average lives were of a similar magnitude and that critically the scatter of the heat treated components (repaired and heat treated only), are within that of the baseline test pieces. Therefore it can be said that there is no deleterious effect due to the application of the localised heat treatment process on fatigue life. This coupled with a clear reduction in residual stress produced as a result of the chosen temperature is evidence that the localised heat treatment process has been successful.

13.2.5 LOCAL HEAT TREATMENT VALIDATION

Figure 13-16 shows the development of the localised heat treatment system in order to construct and validate the system on actual components. The fatigue testing described here is the culmination of this development programme and has acted to validate the process for application to components such as those described in section 9.

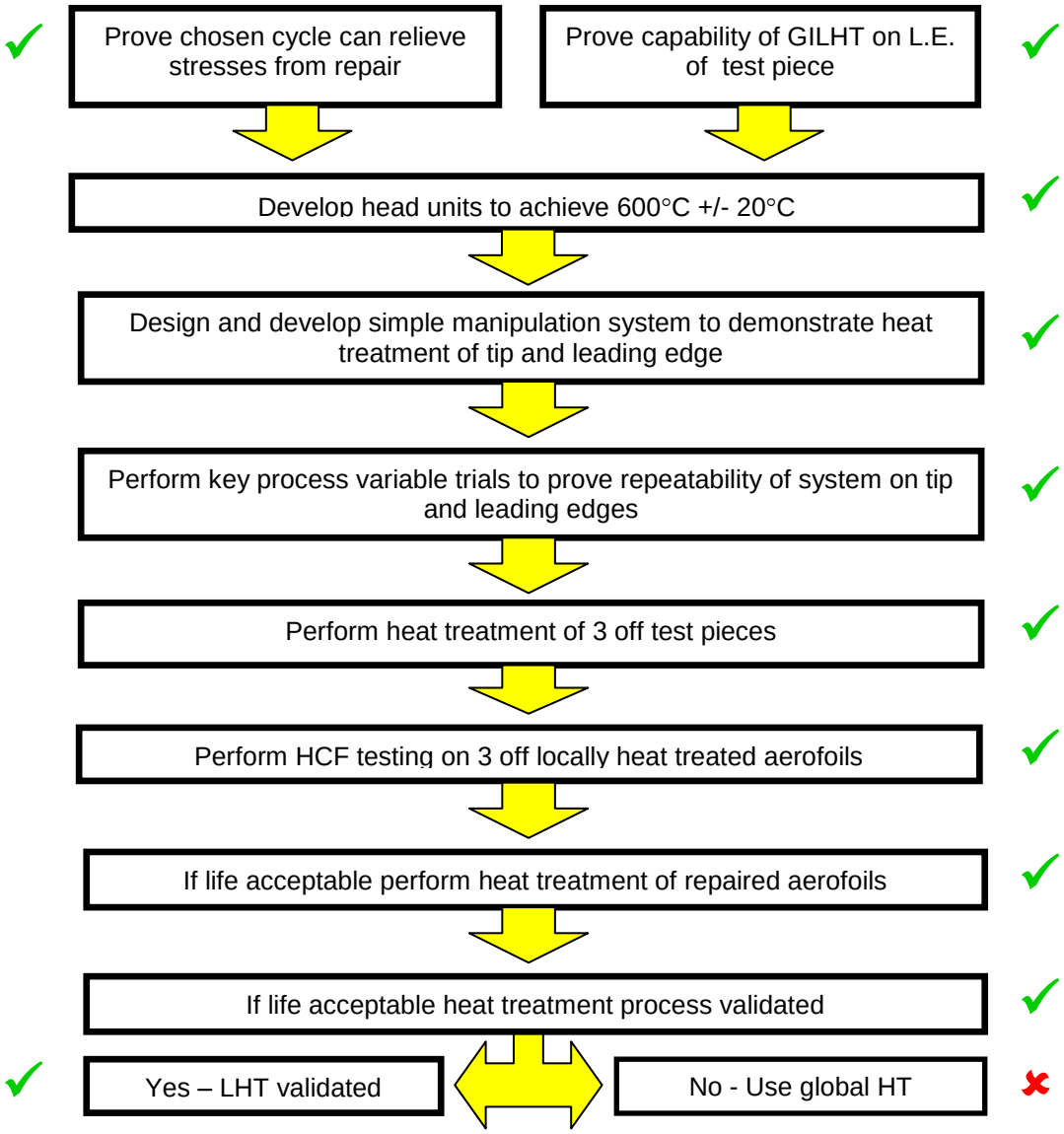


Figure 13-16 : Flow chart representing the validation of the localised heat treatment process

13.2.6 IMPLICATIONS OF MEASURED RESIDUAL STRESS TO THE APPLICATION OF THE LOCAL HEAT TREATMENT SYSTEM

The data presented in Figure 7-5 highlighted the importance of having the whole of the repaired region heated to the stress relieving temperature. Also evident is the effectiveness of the heat treatment cycle at reducing the level of residual stress within the repaired region. It also shows that even at small distances away from the repaired region (i.e. the location of the base material measurement - 7.5mm from the leading edge in Figure 7-2) the level of residual stress due to the repair is significantly lower than the deposited region. These observations have significant impact on the design and development of the gas jet local heat treatment system as they provide strong evidence to suggest that the key area to heat treat is the repair itself and that heating of large regions of the surrounding base material is not critical. Conversely the residual stress measurements taken on locally heat treated repairs showed a slight increase in residual stress in the region close to the edge of the deposit. However, the components successfully passed the high cycle fatigue validation testing showing that any issues related to insufficient heat treatment of the surrounding base material did not produce sufficient residual stress to impair component performance.

Also noteworthy is that the sensitivity of the localised heat treatment process to positional variation. Care must be taken to ensure that the whole repaired region is well within the region heated to the stress relieving temperatures. Figure 9-13, Figure 9-19, and Figure 10-10 all highlight that slight changes in position can

cause significant changes in temperature due to the tightly packed isotherms which exist at the edge of the heated zone. This is the nature of a localised heat treatment system and should be carefully considered when designing future systems.

13.3 GENERAL DISCUSSION: MODELLING

In the ABAQUS modelling of the plate a number of zones were defined to correlate with the various gas temperatures and metal thermocouple positions used in the experimental trials (see Figure 12-2, Figure 12-4, and Figure 12-10). There was the potential to vary all of these in the model in order to establish the most appropriate heat transfer coefficient. However the best correlation along the plate length was established with just four regions defined (see Figure 12-11), 1 head zone, and 3 outside the head to describe the exhaust gas flow.

The use of a number of interfacial heat transfer coefficients provided the flexibility for the regions close to the head to have values approaching forced convection (i.e. >25 W m^{-2} K^{-1}) and reducing towards values more akin to free convection (i.e. <<25 W m^{-2} K^{-1}). The higher heat transfer coefficients predicted by simulations closer to the head are consistent with the higher velocity of the flow at this region. The Fluent simulations shown in Figure 11-18 suggest a gas velocity of between 2.5 and 5 m s^{-1} close to exit of the head. The k-epsilon turbulence model also predicted a fairly gradual reduction in heat transfer coefficient as the gas exits the impingement region (although the k-omega model suggests a steeper gradient), before a significant drop in heat transfer coefficient at a distance of around 90mm from the end of the plate (see Figure 11-17). Also noteworthy is that the temperature difference between the gas and the plate is greater closer to the head (this can be seen experimentally by comparing Figure 12-5 and Figure 12-6).

In hindsight it was not necessary to define such a large number of regions in the ABAQUS model, as a good correlation was achieved with just 4 regions on a thin

plate. The finite element method provides a reasonable approximation of the heat transfer coefficients as is shown by the excellent correlation in the component modelling described in section 12.7.1. However, at the region of the component where the cross section increases (i.e. towards the root of the aerofoil) and the heat sink effect from the disc section becomes more significant, the error in the simulation appears to be larger (see TC16, TC17, TC14 on Figure 12-21). This is the type of circumstance when defining boundary conditions that more closely correlate with the effect of exhaust gas should be considered.

Considering the Fluent multi-jet simulation results in Figure 11-17 and Figure 11-19, caution is required when dealing with the heat transfer coefficients for the far field regions of the plate (i.e. away from the impingement region). Here the gas temperature is heavily dominated by the plate temperature (as can be seen in Figure 11-16). The calculation for the heat transfer coefficients given in Figure 11-17 and Figure 11-19 uses the jet exit temperature. This is not the most appropriate value as the gas cooled significantly at this point and was closer to the plate temperature or ambient air/gas. This is a limitation of using a steady state simulation such as that described, where the plate is maintained at a constant temperature. However, it is important to refer back to the modelling strategy outlined in Figure 11-1 and remember that CFD simulations are intended to provide “under head” heat transfer coefficients not far field values. Any values presented for the far field regions were simply used as starting points for further analysis in the finite element simulations. In future studies (but beyond the scope of this thesis) it is suggested that a full transient simulation of the six jet model be performed in order to further develop understanding in the far field region. This

would allow modelling of the exhaust gasses and their interaction with the component. However for the calculation of a Nusselt number and Reynolds number in these regions a more suitable characteristic length would have to be chosen as the jet diameter is not appropriate so far from the jet orifice.

13.3.1 COMPONENT MODELLING - AN ENGINEERING APPLICATION

It is relevant to consider how the model presented in section 12.7 is useful in the application of the local heat treatment and component repair in general? The answer is twofold; firstly the model allows one to visualise the temperature distribution achieved in a component by the application of the gas jet heating process. The use of thermocouples produces a discrete temperature at a specific location, whereas the model allows one to see the temperatures across the whole component. Also the model provides a quick and cost effective way in which the

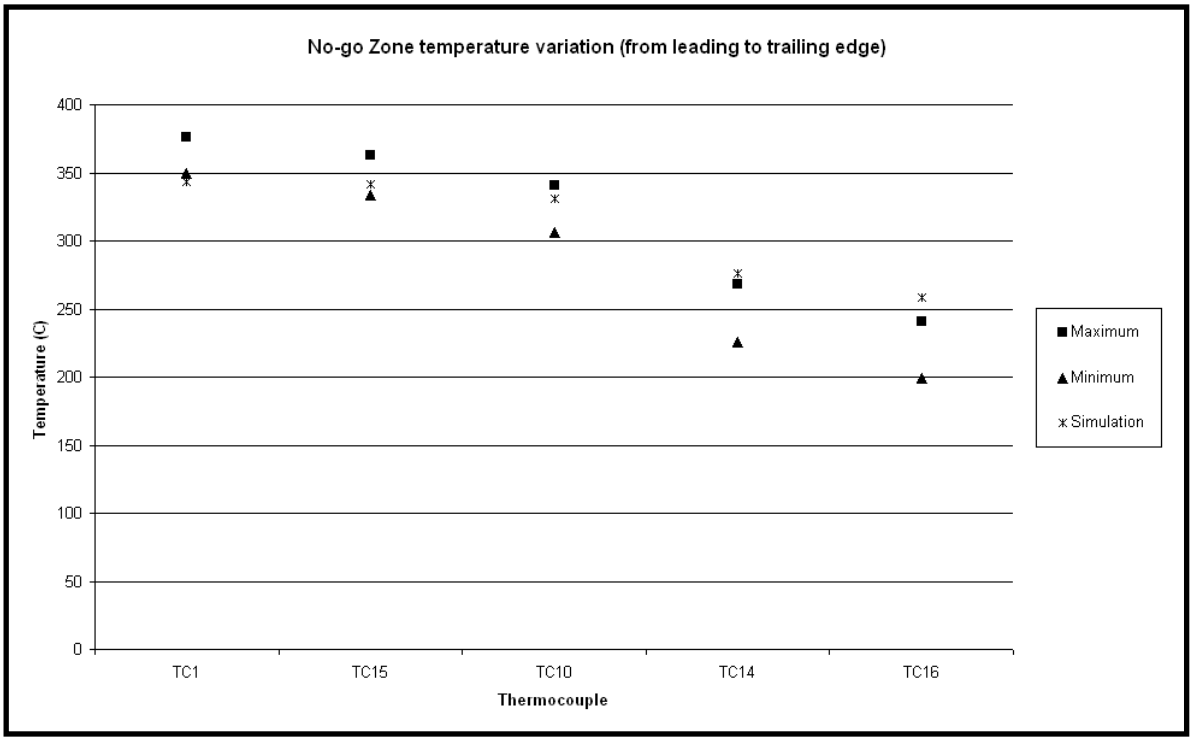


Figure 13-17 : No-go zone temperatures (simulation and experimental), for thermocouple locations reference, see Figure 12-18.

process can be optimised in order to provide the engineering solution required of the localised heat treatment. An example of this is when one considers that the component must return to service after the repair sequence. In this case one must consider the whole repair process and its effect on the component in terms of life and material integrity thus requiring one to define repair limits that do not compromise part integrity. As described in the introduction, blisks are classed as A1 critical rotating components [17] (similar to discs), and as such are subject to very strict rules governing how the component can be processed in order to maintain fatigue life. As such the heat treatment process must not affect the disc section of the blisk. Alpha case formation may directly influence the mechanical properties, and the removal of any alpha case may lead to excessive part thinning. Therefore one must define the limit to which the repair and particularly the localised heat treatment can extend down the blade to the hub.

The heat treatment region is the limiting factor in how much of the blade can be repaired and this process model can be used as a tool to define this region. Figure

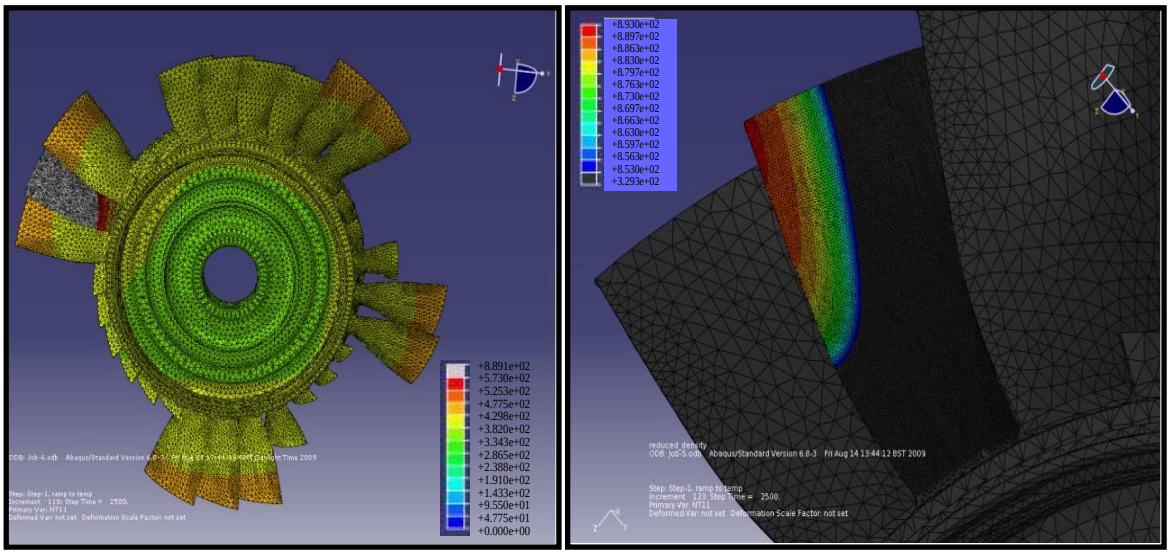


Figure 13-18 : Isotherms of interest

13-17 shows the temperatures achieved across the test piece blade at a nominal distance from the hub (this distance would be defined by the component repair and design authority). In this graph the measured temperatures are again compared with the simulation temperatures and show good correlation. This no-go zone is the region below which no heat treatment (or associated etching process) can extend. The model can therefore be used to establish how much of the leading edge, trailing edge, or tip can be heat treated by moving the heated region until these temperatures are below the value specified. The left image in Figure 13-18 shows how much of the blisk remains below 300°C, a safe limit for minimising alpha case formation. The image on the right shows how much of the component is within 40°C of the maximum temperature (equivalent to +/- 20°C – an acceptable tolerance for a localised heating process). If one wanted to shift the position of the 300°C isotherm to cover more of the blade, this could be achieved by moving the heated region further up the blade towards the tip.

13.3.2 ASSESSING CAPABILITY IN CHALLENGING APPLICATIONS

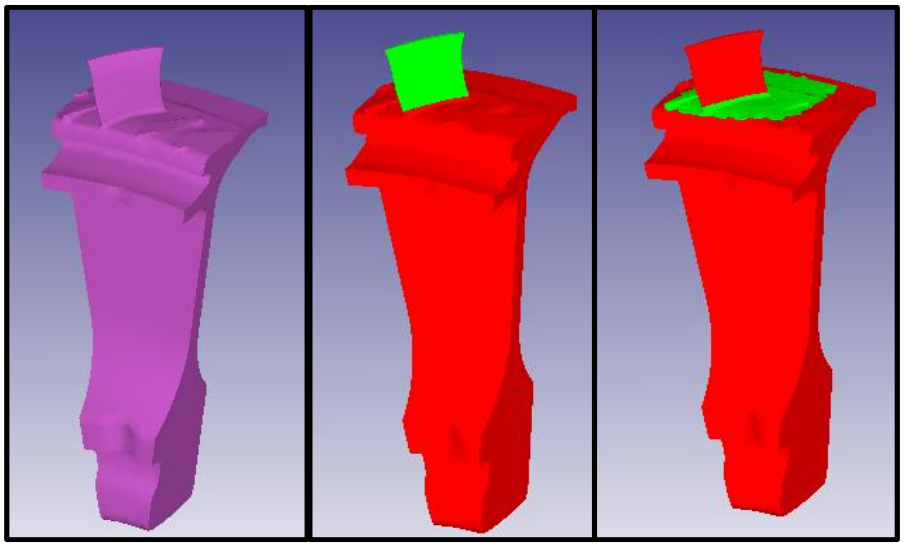


Figure 13-19 : High pressure compressor blisk geometry (far left). In the two images on the right the green highlights the two primary heat transfer regions of the model. These represent where the part is heated through convection from the hot gas. In the centre is a region to represent the gas jet array, on the far right is the exhaust gas region.

Another application where the use of the modelling strategy defined in this thesis is useful is in the assessment of the technology for application on geometries other than the ones initially intended and described. Figure 13-19 shows a component with very small blades. Blisks of this geometry are found in the high-pressure compressor region of the engine and present a very specific challenge to the application of localised heat treatment. The boundary conditions developed and validated in this thesis allow one to quickly assess the capability of the local heat treatment system in its current form on new geometries such as this.

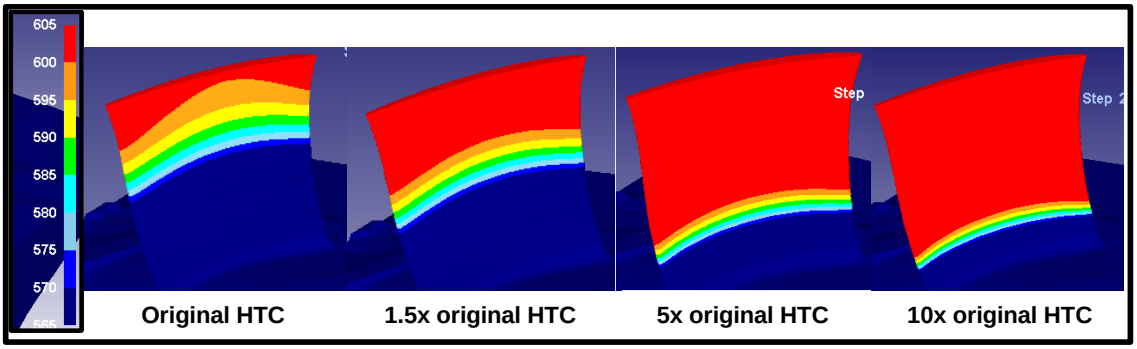


Figure 13-20 : Effect of geometry on heating requirements

Figure 13-20 shows a number of simulations performed on the smaller aerofoil blisk geometry using multiples of the heat transfer coefficients defined in the Fluent simulations (section 11). All the simulations have the heat transfer region covering the whole blade (as shown in Figure 13-19). These simulations were performed in DEFORM^{TM} finite element method (FEM) software by Goetz [135]. In the model each of the zones shown in Figure 13-19 consisted of an environmental temperature boundary condition (gas temperature) and a convention heat transfer coefficient. These simulations show that in order to increase the region on the aerofoil heated by the local heat treatment system, one must increase the heat

transfer coefficient significantly. A 1.5 times increase results in only around a quarter to half of the blade reaching above 500°C.

It is beyond the scope of this thesis to discuss in detail the results of the simulations shown in Figure 13-20, however they do provide a good indication as to the ways in which the boundary conditions defined in this work can be used to assess the capability of the technology for other applications.

The challenging application of locally heat treating small compressor aerofoils is largely due to the proximity of the heated regions to the hub, which acts as a large heat sink. The modelling performed highlights the challenges to heat treating these components and suggests that heat transfer requirements of up to 10 times (approximately 1200 W m^{-2} K^{-1}) that achieved in the GJLHT system (i.e. 120 W m^{-2} K^{-1}, from section 11) are required to heat the whole blade.

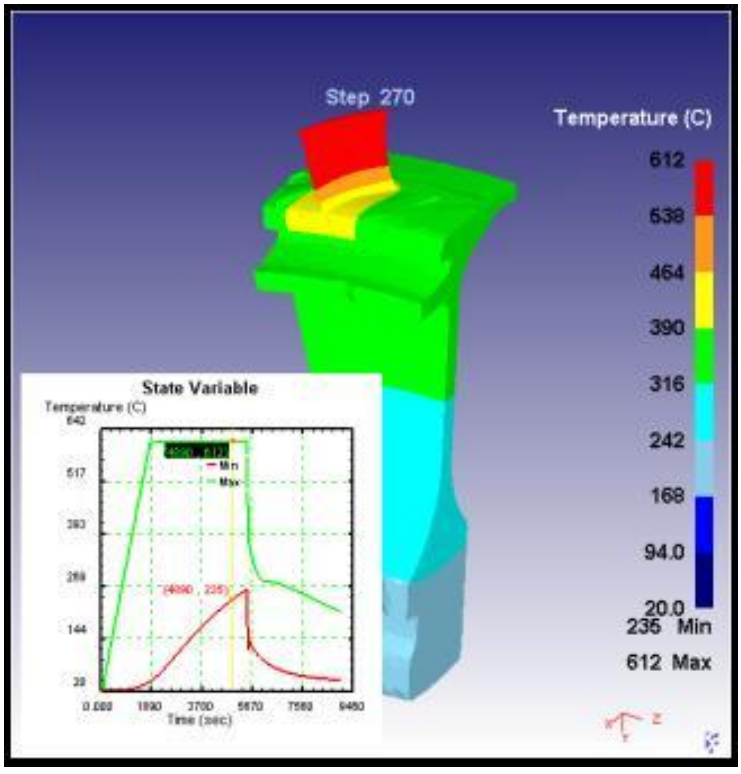


Figure 13-21 : An example of the temperature profile through the whole component from the aerofoil to hub. This was with the original heat transfer coefficient.

In order to achieve heat transfers of ten times that achieved with conventional GJLHT technology one needs much higher velocity argon gas jets. However the area to be heated is

significantly smaller than previously, meaning that a given gas flow rate (supplied by the control system) is distributed between a much smaller number of holes. It is therefore travelling faster through each jet. The following section describes how to calculate the flow rate requirements using the correlations derived through the CFD modelling (page 177) and validated through FE modelling (page 275).

Correlation for Nusselt number in impingement systems;

Equation 13-1: $Nu = y\,\mathrm{Re}^{x}$

Coefficients x and y for impinging argon jets are given in the table below (from page 195);

	y	x
Nu 5mm (ave.)	0.0594	0.6935
Nu 8mm (ave.)	0.0282	0.773
Nu 5mm	0.8544	0.4698
Nu 8mm	0.0346	0.922

We know (from pages 41 and 42, and Equation 2-4 and Equation 2-5) that;

$$Nu = \frac{hd}{k}$$

$$and,$$

$$\mathrm{Re} = \frac{Vd}{\nu}$$

$$\therefore \frac{hd}{k} = y\,\mathrm{Re}^{x}$$

(Assumptions; 1mm diameter jet, Jet-to-jet spacing is 5d (5mm))

$$V = \frac{Q}{60000N},$$

Equation 13-2:

Where Q is flow rate in $lmin^{-1}$ at room temperature (e.g. 293K) and N is the number of holes (spacing 5d), therefore the flow rate required to achieve a given heat transfer coefficient can be expressed as;

Equation 13-3:

$$\mathrm{Re} = \frac{Qd}{60000N\nu A}$$

$$\frac{hd}{k} = y\left(\frac{Qd}{60000N\nu A}\right)$$

$$Q = \frac{60000NA\nu\sqrt{\frac{hd}{ky}}}{d}$$

$$\boxed{Q = 15000N\nu\pi d\sqrt{\frac{hd}{ky}}}$$

Example calculation

In this example a small aerofoil is heated (heated area is 20mm x 20mm), if the modelling says that the area requires a 10x HTC (see Figure 13-20). What flow rate would be required?

With a 1mm hole and 5d spacing, N = 32 (16 per side), and if original HTC is 120 W $m^{-2}K^{-1}$ (from section 11)

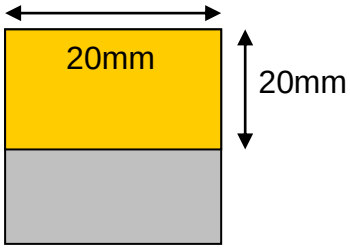
Then,

10 x 120 = 1200 W $m^{-2}K^{-1}$.

For average values with a stand-off of 8mm, x = 0.773, y = 0.0282 (see table above)

For Ar @ 620°C, Kinematic viscosity = 3.03e^{-5} m^2s^{-1}, and

Thermal conductivity = 0.0396 W $m^{-1}K^{-1}$



$$\therefore Q = 15000 * 32 * 3.03e^{-5} * \pi * 1e^{-3} * 0.773\sqrt{\frac{1200 * 1e^{-3}}{0.0396 * 0.0282}}$$ = 381.27 l min^{-1} per aerofoil to achieve 10 x HTC.

13.4 FUTURE CONSIDERATIONS

13.4.1 MULTIPLE AEROFOIL HEAT TREATMENT

It is worth noting that when this process is applied to multiple aerofoils, it may be the case that the hub will eventually soak and the temperature distribution in the aerofoils may change. This is especially true when one considers that this system is to be used in an argon chamber. The relatively high flow rates of the heater unit mean that the atmosphere in the chamber is to be largely fed by this flow. This hot gas will result in the local atmosphere temperature being significantly higher than if it was open to the 'shop floor' atmosphere. The modelling strategy described in the previous section could be used to assess the effect of heating multiple aerofoils on the temperature distribution achieve in the component as a whole.

13.4.2 USING ALTERNATIVE GASES

Argon has been chosen as the process gas for this system due to the availability of it on the shop floor and its common use as a process gas for furnaces and welding shrouds. However there are other gases, which could be used to provide heating for components using the gas jet process. A list of four common gases are given in Table 13-1. The uses of air and carbon dioxide are not considered appropriate for the heat treatment of titanium as they may lead to excessive oxidation. However the purpose of this discussion is to compare the various gases based purely on their heat carrying capacity for illustrative purposes.

	Argon [113]	Air [136]	CO_2 [136]	Helium [113]
Thermal conductivity (W $m^{-1}K^{-1}$)	0.018	0.026	0.087	0.151
Density (kg m^{-3})	1.663	1.205	1.842	0.166
Viscosity (Pa s)	2.125E-05	1.88E-05	1.16E-05	1.90E-05
Specific heat capacity (J $kg^{-1}K^{-1}$)	520.640	1005.000	5000.000	5200.000
Specific heat per unit volume (J $m^{-3}K^{-1}$)	865.824	1211.025	9210.000	863.200

Table 13-1 : Table of results for different gases at normal temperature and pressure

The first challenge to changing the gas used in the gas jet processing system is the power requirements for raising the temperature of the gas to a level required for heat treatment. The property that has the largest bearing on this is the specific heat capacity, Table 13-1 highlights that CO_2 has a specific heat capacity per unit volume 10 times that of argon. It is important to compare the per unit volume values, as in this system the flow rate is measured and controlled as a volume flow rate, not a mass flow rate. Based on the data in Table 13-1 it would require 10 times the energy to heat the gas to the same temperature. However it is noteworthy that the heater unit is currently running at around 40% power in the soak portion of a typical cycle discussed in this thesis. Also the temperature required in the heater in order to achieve around 650°C in the head unit is 1100-1200°C, largely due to the low specific heat capacity of argon. A higher specific heat capacity gas would not require such a large over heating of the gas as it would lose less temperature between the heater and the head unit.

In order to do a simple comparison between the different gases in Table 13-1 one can use Equation 2-4 from page 41 for Reynolds number, Equation 2-5 from page 42 for Nusselt number, and the relationship between the two defined previously in Equation 11-8 from page 199.

	Reynolds number	Jet average Nusselt number
Argon	462.32	3.24
Air	549.15	3.56
CO2	654.96	5.17
Helium	517.07	3.53

Table 13-2: Reynolds number variations for different gases at normal temperature and pressure

We can calculate the Reynolds numbers resulting from a jet velocity of $9.82m^{-1}s^{-1}$. Then using Equation 11-8 the jet averaged Nusselt number can be calculated from these Reynolds numbers. These values are given in Table 13-2.

The Nusselt numbers are not vastly different due to the similar nature of the Reynolds number. However Nusselt number is a ratio of the convective and conductive elements of forced convective heat transfer, therefore the fluids that are particularly good conductors will result in better heat transfer. From these Nusselt numbers, one can then calculate the heat transfer coefficient one would expect due to the different fluids by rearranging Equation 2-5 from page 42. The results of this are given in Table 13-3.

	Calculated heat transfer coefficient ($Wm^{-2}K^{-1}$)
Argon	58.26
Air	92.43
CO2	449.62
Helium	532.91

Table 13-3: Heat transfer coefficient variation for different gases at normal temperature and pressure

These data highlight a clear dependency on thermal conductivity (as a result of the Nusselt number), highlighting that if higher heat transfer coefficients are required then the use of helium would be desirable. However it is noted that the use of helium has its limitations; its metallurgical effects on titanium are unlikely to be

significant but are unknown. However due to the low molecular weight of helium, buoyancy effects are likely to be significant, particularly at high temperatures when the density reduces further. Secondly it is very difficult to contain helium meaning that any system would need to be near hermetically sealed increasing cost and complexity.

In conclusion the use of alternative gases may result in higher heat transfer coefficients being possible. However there are many considerations before these alternatives are to be embraced. In the current application of the gas jet processing system on larger aerofoils, the thin nature of these components means there is not currently the need for significantly higher heat transfer coefficients. However, as the technology is read across to other components, particularly those in closer proximity to large heat sinks, the need for higher heat transfer coefficients may increase.

14 CONCLUSIONS

The following specific conclusions can be drawn from the work in this thesis;

1. The use of inert gas jets to heat a test piece plate of uniform thickness has been shown to be a repeatable and stable process.

2. A fully functioning system capable of delivering gas at a flow rate of up to 200 $lmin^{-1}$ and a gas temperature of up to 800°C has been developed and deployed on a range of test piece geometries.

3. A number of flow rates with a range of associated gas temperatures have been tested and the correlations between flow rate, gas temperature and plate temperatures are repeatable.

4. The basis for a process model to allow exploitation of the local heat treatment system has been generated along with some developments to improve the accuracy and provide an insight into the heat transfer outside the head unit (impingement zone).

5. Due to the localised nature of the process, the isotherms at the edge of the heated zone are tightly packed resulting in a steep temperature gradient moving out from the head unit. This phenomenon will be the same for any localised heating method and is not specific to argon gas jet processing.

6. Increasing flow rate has a significant positive influence on;
    a. The temperature achievable on the component.
    b. The offset between gas temperature and component temperature.
    c. The temperature distribution across the heated region.

    This is achieved through an increase in heat transfer coefficient.

7. The positional data show the direction that has the largest effect on plate maximum temperature and heat zone distribution is that of length. This is due to the fact that changing the length position of the head unit on the plate acts to reduce the size of the heated region. Also, the tightly packed isotherms present at the edges of the heated zone result in a dramatic reduction in temperature of thermocouples for a small change in position.

8. Exhaust gas management is very important and provides thermal insulation, heating and even cooling effects of exhaust gases should be considered when designing a system such as that described in this thesis.

9. The k-omega turbulence model provided the best correlation with published data when modelling this process.

10. For laminar 5mm length argon impingement jets the equation describing the relationship between heat transfer and jet Reynolds number is $Nu = 0.1873*Re^{0.6935}$.

11. For laminar 8mm length argon impingement jets the equation describing the relationship between heat transfer and jet Reynolds number is $Nu = 0.0917*Re^{0.7746}$.

12. The jet averaged heat transfer coefficient of the argon gas jets provides a good approximation to describe the area heated by the head unit in these trials.

13. The use of gases other than argon may have the potential to increase heat transfer coefficient for a given flow gas velocity. However, there are significant other factors such as contamination and metallurgical interactions, which would have to be investigated.

14. The heating rate provides a good comparison between the measured and simulated data in the case of a finite element based approach when dealing with thin sections such as plates and aerofoils. This is due to the relatively uniform cross-sectional temperatures and rapid heating rate.

15. Jet plates can be customised and biased to account for component temperature distributions. For example, removal of jets to reduce the effect of hotspots and achieve a more uniform temperature distribution, or biasing of a jet plate to provide a higher input in one area to counteract a component heat sink effect.

16. Cooling gas can be used effectively for thermal management and to maintain the integrity of temperature sensitive regions of a component. However the use of a physical barrier to prevent the cool gas and hot gas interaction is necessary.

15 APPENDIX 1 – LOCAL HEAT TREATMENT (LHT) HEAD EVOLUTION

This section highlights some of the innovations and ideas tested during the course of the local heat treatment development.

15.1 IN-HEAD HOT SPOT

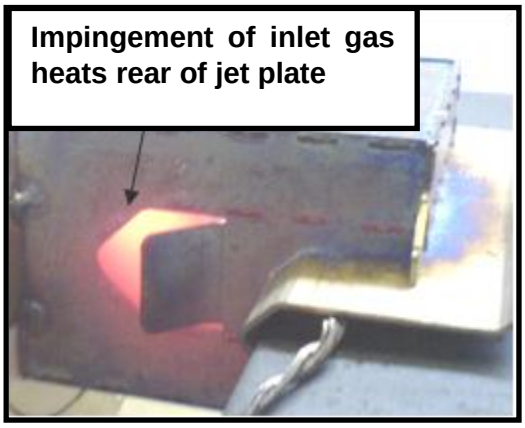


Figure 15-1 : Head unit showing location of hot zone

An improvement in the second generation heater (CES2690) to also help with in-head hotspot is the increased size of the gas inlet into the head unit. In previous heater iterations the small inlet pipe produced a high velocity gas jet that impinged on the rear of the jet plate and transferred significant heat to this portion of the head unit. Increasing the size of this inlet aperture from 12.5mm to 30mm reduced the velocity of the gas entering the head unit by a factor of 6.

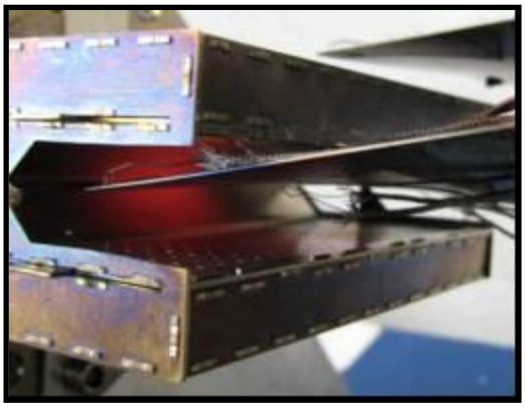
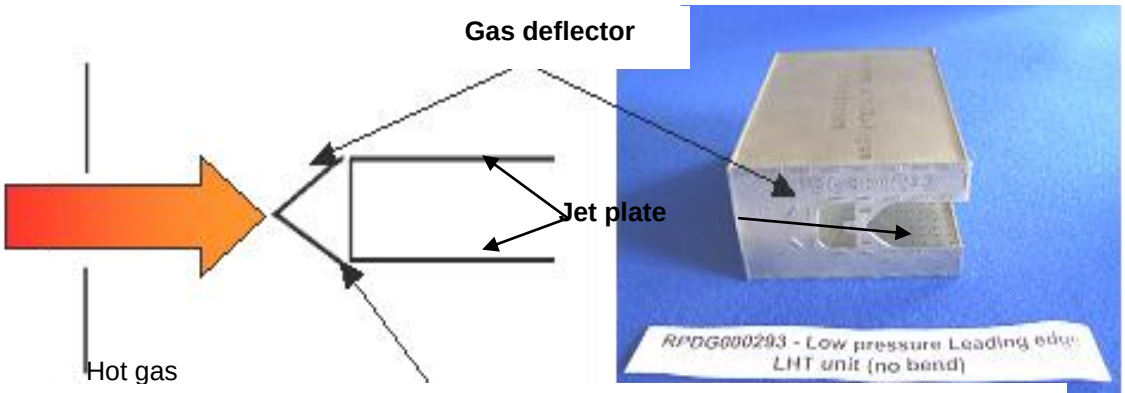


Figure 15-2 : Head unit hotspot

Hotspots appear on the rear of the jet plate within the head unit, see Figure 15-2. The effect of placing insulation on the rear portion of the jet plate was used to ascertained if there was a significant heating effect on the test piece from this region of hot material. No significant measurable

difference in the temperatures was observed on the component when compared ‘with’ and ‘without’ insulation. However, a baffle plate has been installed in later head units to reduce this hotspot and this method will be carried forward in future designs. During testing of the new ‘baffled’ heater the hotspot was visibly reduced, however it was still evident when the system was run at full operating temperature.



Gap between gas deflector and jet plate to minimise heating of the jet plate through conduction

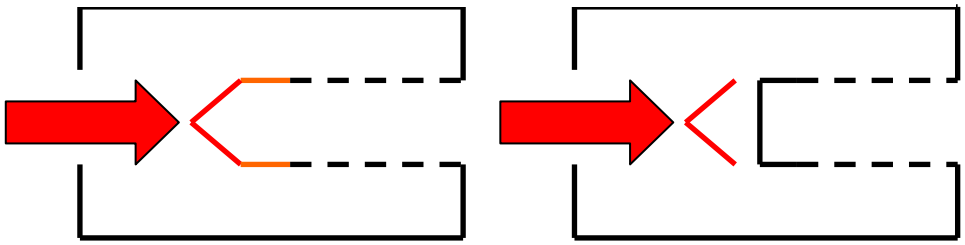


Figure 15-3 : Schematic cross section and photograph of head unit showing the deflector configuration used to reduce the hotspot (top). Comparison of baffle plate and integrated jet plate setup (bottom).

This baffle plate involves a slight redesign of the jet plate. In the original head unit design the jet plate comprised a shaped piece of C263 nickel alloy containing the jet orifices. This plate was bent into the required shape to produce an angled section where it interacted with the inlet gas entering the head unit. The shape of the jet plate is highlighted by the line of rivets visible in Figure 15-3 (below). In the baffled head unit design this plate was removed and replaced with three riveted

plates joined to create a rectangular shaped jet plate (bottom right image of Figure 15-3). A gas deflector to divert the flow of gas into the top and bottom plenum cavities of the head unit was manufactured and sits behind the revised jet plate (see Figure 15-3). This angled section is the area that has the inlet gas impinging on it as it enters the head unit and glows red (Figure 15-3). In the new baffled head unit this angled section is not part of the jet plates. As a result, this red hot spot has been significantly reduced in the new design. Although, this baffle plate shows a significant improvement, there are various methods that could be employed to reduce the effect further. These include applying localised areas of thermal barrier coating to the hottest regions, and reducing the incident angle between the inlet gas and the deflector plate.

15.2 HEAD DESIGN AND MANUFACTURE

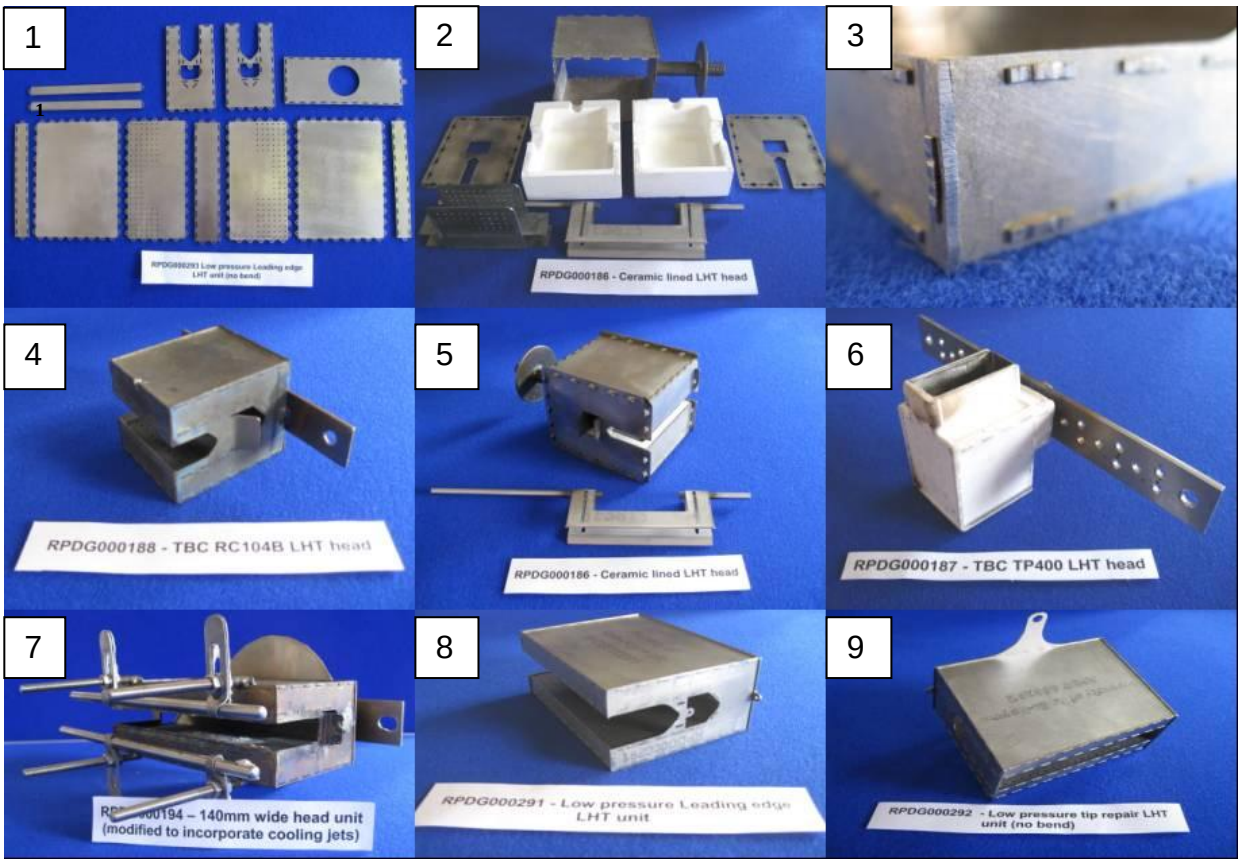


Figure 15-4 : Examples of head units produced for gas jet heating

Figure 15-4 shows a number of head units (all with a jet diameter of 1mm and jet-to-jet spacing of 5mm) for a range of component/test piece applications. The images (1-9) clockwise from top left are briefly described below to give an overview of the construction methods used;

1. The head units are laser cut from sheet metal and constructed using Rolls-Royce patented slot rivets (image 3). The head units were drawn as a two dimensional layout in AutoCAD and the file transferred to the laser to produce the parts. Once constructed these head units provide a manifold to direct gas onto the component in the form of impinging jets. The internal design of the head unit is intended to promote as uniform a flow as possible.

2. Images 2 and 5 show a composite head unit (Part no. RPDG000186), in this example a machinable ceramic central cavity is surrounded by a sheet metal skin. The ceramic section is made in two halves milled from a solid piece of low thermal conductivity (k=0.26 $Wm^{-1}K^{-1}$ at 750°C) Monalite® (Promat) material. A separate jet plate is placed in the centre of the two halves to provide the impingement jets (these could not be made from the ceramic due to its low impact strength and brittle nature, particularly in the thin sections needed for this application). This head construction approach minimised the heat loss from the head. The intention with this design was to minimise the heat loss from the gas within the head unit by reducing the temperature of the external surfaces. However when this head unit was compared with a similar unit made entirely of sheet metal, little difference in target test piece temperature was recorded. The added complexity of manufacturing a head unit in this way was not considered necessary, and as a result the decision was made to continue with sheet metal head unit.
3. Image 3 shows the rivets used to join the manifolds, this is a Rolls-Royce patented technology and produces a tight fitting joint.
4. Image 4 shows a thermal barrier coated (TBC) head (Part no. RPDG000188), the advantage of using a TBC coated head is that it is simple to produce and maintains the unit's compact nature, ensuring it fits between the blades on the blisk assembly. The use of a TBC on the inside reduces the temperature of the external surface by providing a layer of lower thermal conductivity material [137]. The lower the head outer temperature the less potential there is for heat loss through convection and conduction. The thermal barrier coating does show limited improvement; however there is a cost, effort, and time aspect to this

production approach which must be considered. The better solution appears to be the use of the machinable ceramic inserts in the head unit with a stainless steel box constructed around the outside as described in point 2.

5. Image 5 shows RPDG000186 (described above) after construction with the its mouth piece and thermocouple location tube removed and placed in front of the unit.
6. RPDG000187 was manufactured in order to test the gas jet heating concept on smaller aerofoils and test pieces for thermo-mechanical testing. In this example the head unit surrounds the test piece and heats it from both sides through gas jets with the exhaust exiting from the top and bottom of the head unit. This particular head unit also includes an external coating of TBC to minimise heat loss during testing. Although the head unit performed satisfactorily in testing it is too bulky to fit between small aerofoils on a compressor blisk. However it provided a useful test exercise and has supported subsequent work.
7. Image 7 is RPDG000194, the head unit described in section 7.4. This head unit includes the addition of cooling gas pipes to provide protection for temperature sensitive regions of the component. A more detailed description of the development of this head unit can be found in section 7.4.
8. This head unit (RPDG000291) is described in section 9.5.
9. This head unit (RPDG000292) is described in section 9.4.

16 APPENDIX 2 – KEY PROCESS PARAMETERS AND SENSITIVITY STUDY METHOD

The following pages describe the test procedure used to perform the KPV and sensitive study described in this section 9. It was written as a list of instructions to be followed and is reproduced here in that format.

16.1.1 LE KEY PROCESS VARIABLE (KPV) ANALYSIS

For the LE KPV analysis the requirement is to change the flow rate and control temperature following the plan given below in Table 16-1. The blisk and heater should be located in the neutral position. The neutral location is the position that represents the best temperature distribution for the repair. Its position should be measured before commencing with any trials. The measurement strategy is defined in on pages 305-306.

Test number	Control temperature (C)	Flow rate	Blade position	Date completed	Maximum temperature distribution
1	580	140	LE		
2	580	120	LE		
3	580	100	LE		
4	580	80	LE		
5	600	140	LE		
6	600	120	LE		
7	600	100	LE		
8	600	80	LE		
9	620	140	LE		
10	620	120	LE		
11	620	100	LE		
12	620	80	LE		

Table 16-1 : Data collection table for leading edge tests varying flow rate and control temperature

16.1.2 TIP KPV ANALYSIS

For the tip KPV analysis the requirement is to change the flow rate and control temperature following the plan given below in Table 16-2. The blisk and heater should be located in there neutral positions.

Test number	Control temperature (C)	Flow rate	Blade position	Date completed	Maximum temperature distribution
1	660	140	Tip		
2	660	120	Tip		
3	660	100	Tip		
4	660	80	Tip		
5	660	60	Tip		
6	640	140	Tip		
7	640	120	Tip		
8	640	100	Tip		
9	640	80	Tip		
10	620	140	Tip		
11	620	120	Tip		
12	620	100	Tip		
13	620	80	Tip		

Table 16-2 : Data collection table for tip tests varying flow rate and control temperature

The best methodology for performing these trials is to set up a programme (one for each control temperature (i.e. 620C, 640C, 660C)) which includes initial ramp to temperature using the optimised cycle. Following this, change the programme to ramp the control temperature to the required value (i.e. 620C, 640C, 660C) and change the flow rate through the values in the table at the end of this section. The chart below is an example to show what one should expect the resulting process chart to look like.

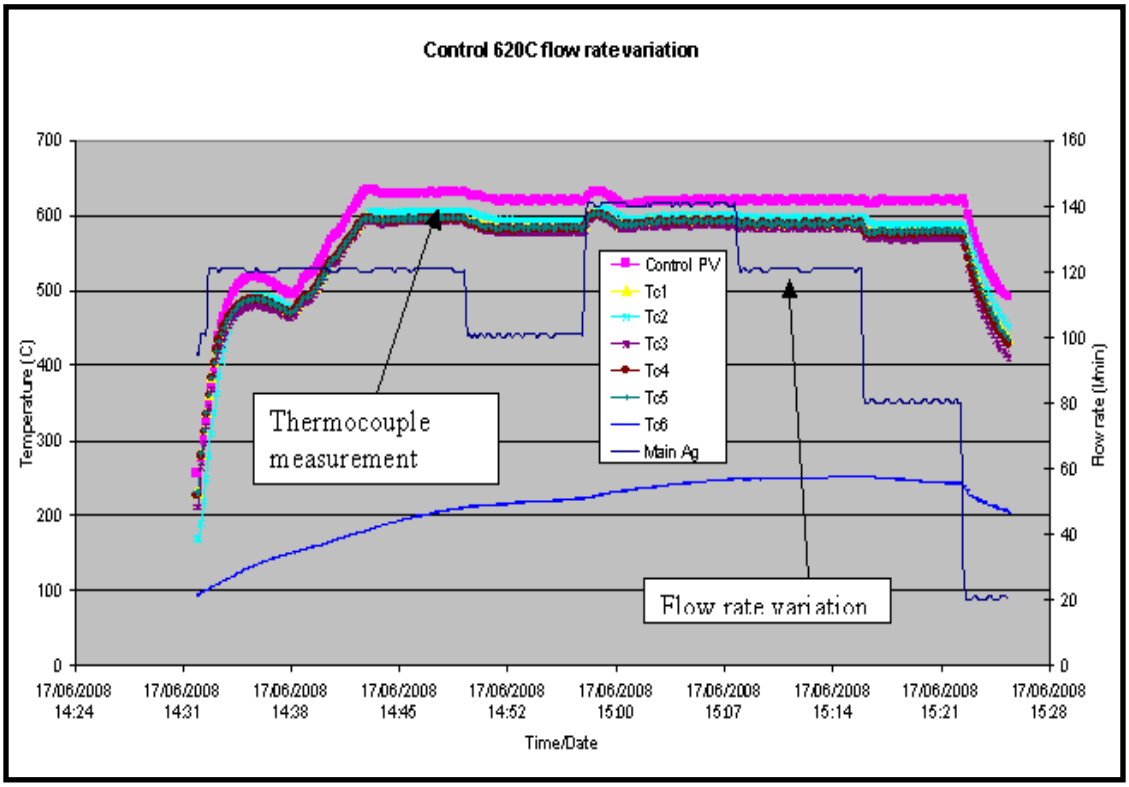


Figure 16-1: Example process chart for test to generate KPV data

16.1.3 TIP/LE PROCESS SENSITIVITY TRIALS

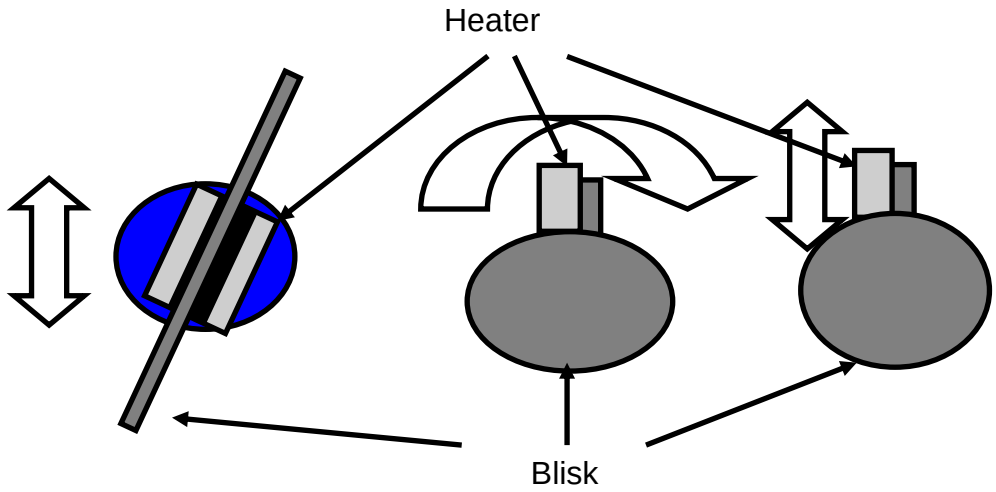


Figure 16-2 : Positional variation movements

These trials were intended to provide some information as to the effect of blade-to-blade variation on the temperature distribution seen on the aerofoil. In order to do

this the blade was moved from its neutral position to those defined by the measurements defined below and the temperature distribution produced was recorded. In these trials it was important to measure the positions and move the heater and blisk to reproduce these. The diagrams below show the three main variations of movement for the blisk and heater.

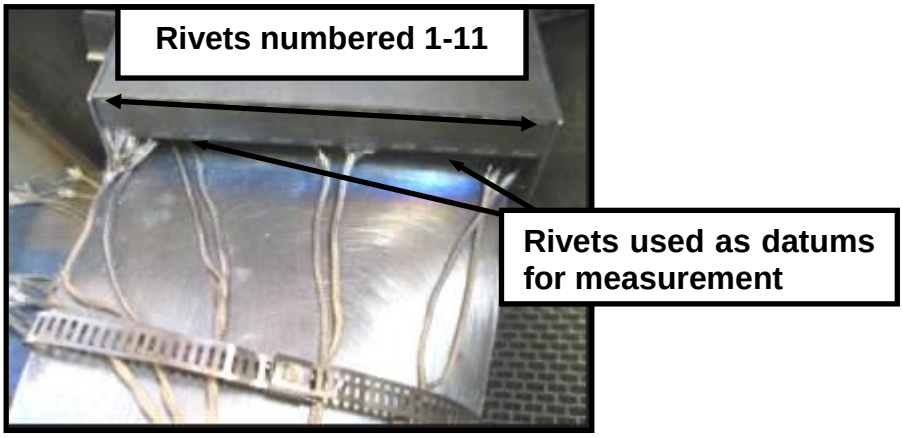


Figure 16-3 : Location of rivets for measurement location

Figure 16-3 shows the head unit positioned on the tip of an aerofoil during heat treatment, note the thermocouples (t/c's) lying on the aerofoils surface. This image is taken looking down onto the blisk showing the suction side of the aerofoil.

N.B. Note the two lines of rivets on the head unit, these are used as datums against which to take measurements to define the position of the aerofoil relative to the head unit. The rivets are numbered 1-11 from the control thermocouple end of the head unit in the direction of the arrow on the photograph.

Figure 16-4 and Figure 16-5 show how the equipment was manipulated to achieve the aerofoil positions defined in section 16.1.5. In order to achieve these measurements, the blisk was raised or lowered by rotating the support, which runs on a threaded bar.

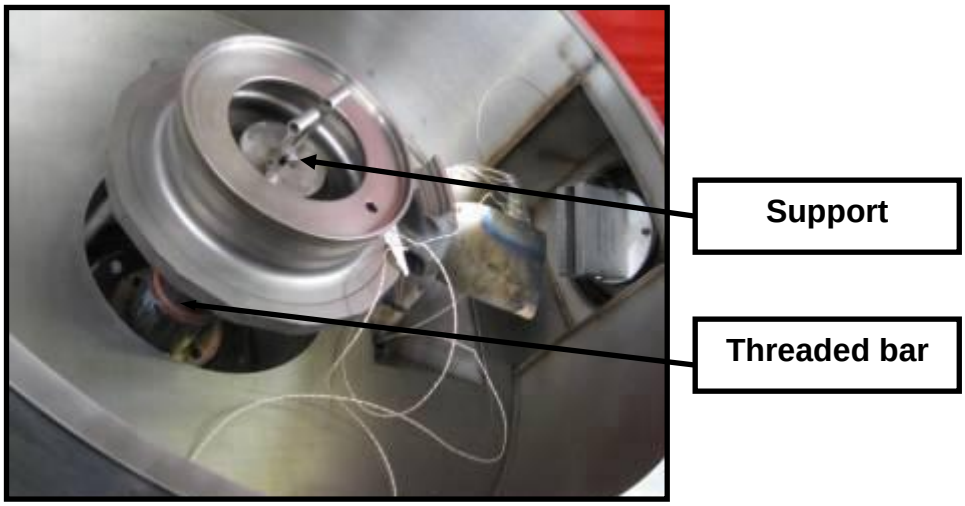


Figure 16-4 :Support structure for test piece

In order to rotate the blisk to achieve the measurements defined previously, one had to rotate the blisk using the wheel shown below (Figure 16-5) or rotate the blisk on its support fixture. The rotation on the wheel is incremented to allow

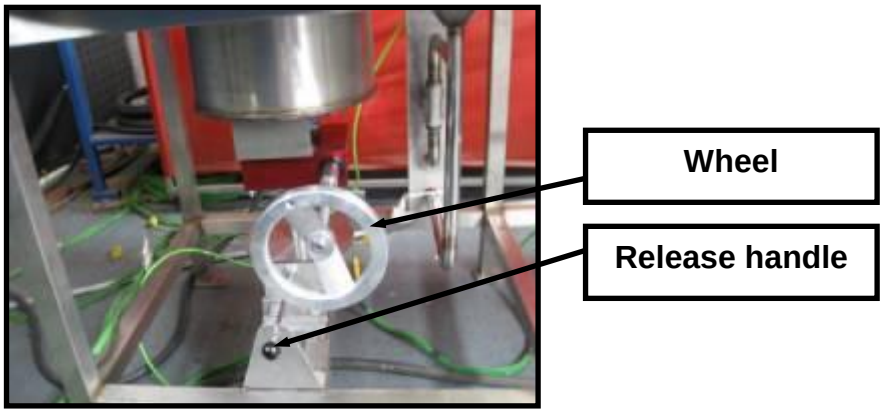


Figure 16-5 : Wheel for rotational movement

movement from blade-to-blade during a full heat treatment. However in order to rotate the blisk less than a full increment, the operator should pull the release handle and then turn the wheel.

In order to move the heater axially one must slide it on the guide rails up to the stop. The axial measurement given previously is taken between the mounting bracket and the stop shown in the photograph below.

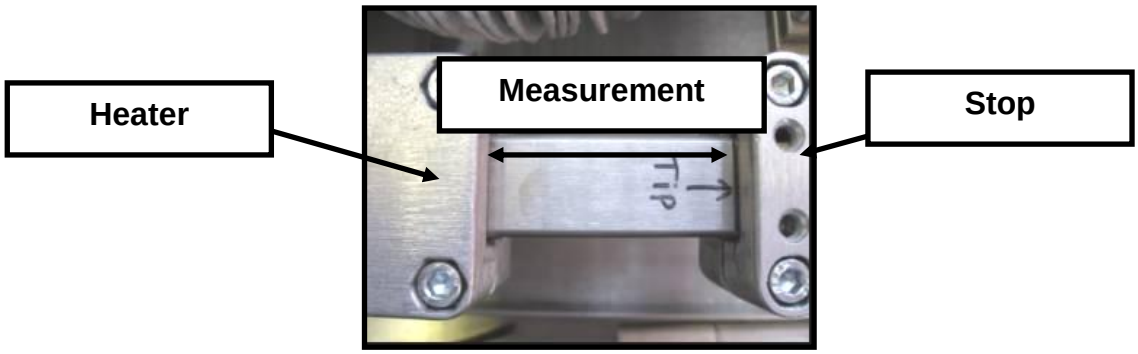


Figure 16-6 : Location for axial measurement

16.1.4 HOW TO PERFORM POSITIONAL SENSITIVITY TRIALS

The heater was placed in the neutral position at the beginning of the trial; the measurements taken at the locations defined above for this neutral position was be entered into Table 16-3. Then the position was moved to each of the eight positions defined in 16.1.6. At each of the eight positions a test was performed using first the tip, followed by the LE head units. For the tip trial a flow rate of 120l/min and a control of 630C was used, and for the leading edge trials a flow rate of 120 l/min and a control temperature of 600C. Once again the temperature distribution achieved on the blade thermocouples should be measured.

		Measurements between head and aerofoil					Maximum temperature distribution
		head to LE (1)	3rd rivet (2)	9th rivet (3)	Head to TE (4)	Date tested	
Neutral position	Tip						
	LE						
Test 1	Tip						
	LE						
Test 2	Tip						
	LE						
Test 3	Tip						
	LE						
Test 4	Tip						
	LE						
Test 5	Tip						
	LE						
Test 6	Tip						
	LE						
Test 7	Tip						
	LE						
Test 8	Tip						
	LE						

Table 16-3: Data collection table for positional variation tests varying flow rate and control temperature

Table 16-4 shows the test matrix that was completed and data was recorded in Table 16-3. The values for A and B are defined as the maximum one can manipulate the blisk in that direction without contact with the head.

16.1.5 POSITION DEFINITIONS

The following images (Figure 16-7 and Figure 16-8) shows the procedure to find the maximum and minimum position for the head unit using shims. The shim

thickness is not critical as long as once defined they are used throughout the positioning trials.

Blisk rotational movement will bring either the leading edge (anti-clockwise rotation) or trailing edge (clockwise rotation) closer to the head unit. It was separated from the head by use of the shims as shown in Figure 16-7 (below).

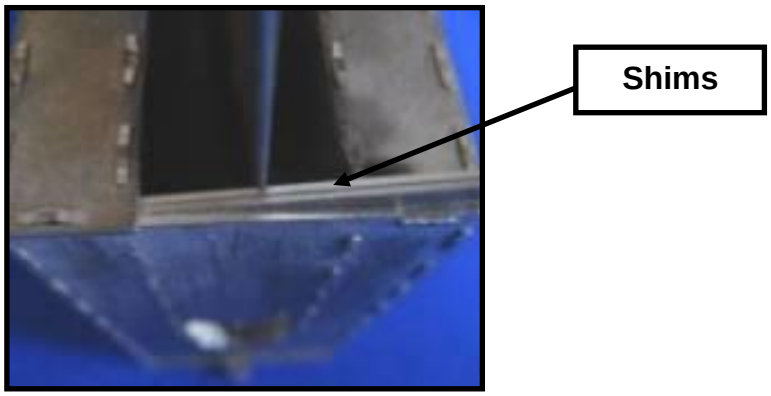


Figure 16-7 : Use if shims to vary rotational position of blade in head unit

Blisk height movement will bring either leading edge (increase height of blisk) or trailing edge (reduce height of blisk) closer to the head unit. It should be separated from the head by use of the shims as shown in the Figure 16-8 (below).

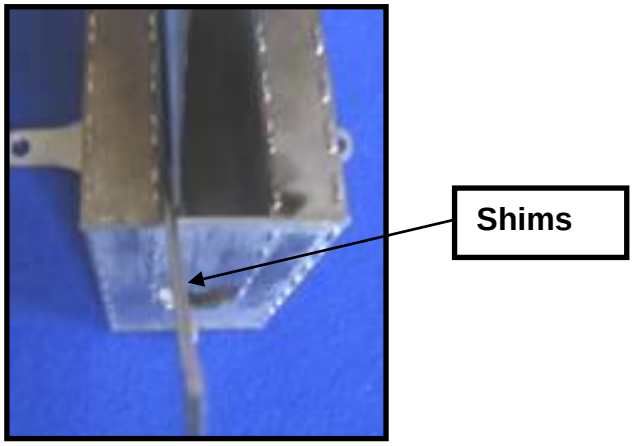


Figure 16-8 : Use of shims to vary height position of blade in head unit

16.1.6 DEFINITIONS/MATRIX FOR POSITIONAL TRIALS

Blisk rotational movement - A = Maximum rotation clockwise

B = Maximum rotation anti-clockwise

Blisk height movement - A = Maximum raised height

B = Minimum height

Heater axial movement - A = 3mm out from neutral stop position

B = 3mm in from neutral stop position

Each of the tests defined in the table below was performed with the flow rate and control temperatures given above (16.1.4). Each test has a different combination of the positions in order to test inter-relationship which may exist. Initially it was intended to rotate the heater on its axis; however this proved to be un-reliable and not repeatable. As a result the use of blade height has been chosen to capture very similar information. When the blisks were to be processed for validation testing the heater was fixed into position to prevent any rotation during heat treatment.

	Blade position		
Test no.	Rotation - blisk	Height change - blisk	Heater axial change
1	A	A	A
2	B	A	A
3	B	B	A
4	B	B	B
5	A	B	B
6	A	A	B
7	A	B	A
8	B	A	B

Table 16-4 : Test positions for each positional sensitivity trial

The main purpose of the trial described in this section assessed the risk presented by blade-to-blade variation in the blisks processed fro the validation testing (sections 9 and 13.2). The data resulting from this testing is given in section 9. However, the methodology is recorded here to allow future repeating of the testing to be performed.

16.1.7 MEASUREMENT POSITIONS

The following photographs show where to take the measurements (1-4) defined in Table 16-4 previously.

1) This measurement is taken between the inside edge of the head unit and the leading edge of the aerofoil. Because of the access issues it is important to use the base of the vernier calliper to take this particular measurement.



Figure 16-9 : Measurement position 1 at the leading edge

2) This measurement is taken at the third rivet. The base of the vernier was rested on the top of the head unit and measurement taken to the aerofoil. In order to maintain positional accuracy it is advised that the measurement probe, which exits to bottom of the vernier, should be held against the trailing edge side of the rivet.

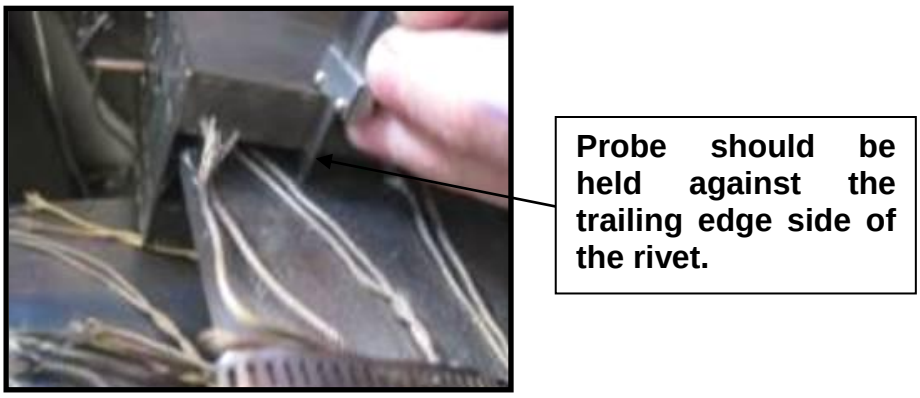


Figure 16-10 : Measurement position 2 at the 3rd rivet location

3) This measurement is as above but at the ninth rivet.



Figure 16-11 : Measurement position 3 at the 11th rivet location

4) This measurement is taken between the inside edge of the head unit and the trailing edge of the aerofoil.



Figure 16-12 : Measurement position 4 at the trailing edge

17 REFERENCES

1 **D. Clark, S. Walloe**, *Method and apparatus for the treatment of a component*, US7759614 (B2) (Patent), 2007.

2 **I. E. Mitchell, D. Clark, S. J. Tuppen**, *Gas heater*, EP2088212 (A1) (Patent), 2009

3 **I. Mitchell, D. Clark,** Localised Gas Jet Processing, In: *Gear up for the Winds of change: Heat Treating: Proceedings of the 25th ASM Heat Treating Society Conference, 14-17th September 2009, Indianapolis, USA,* ASM International, 2009, 159-166.

4 **M. Cervenka**, *The Rolls-Royce Trent Engine*, http://www.msm.cam.ac.uk/phase-trans/mphil/Trent1/sld024.htm , (accessed 20 February 2012).

5 **Rolls-Royce**, *The Jet Engine,* Key publishing, 2005.

6 **O.E. Kosing, R. Scharl, H.J. Schmuhl**, Design improvements of the EJ 200 HP Compressor. From Design Verification Engine to a Future All blisk Version*, Proceedings of ASME TURBO EXP 2001: Land, Sea and Air,* June 4-7, 2001.

7 **Rolls-Royce**, *TotalCare*®, http://www.rolls-royce.com/civil/services/totalcare/index.jsp (accessed 02/05/12)

8 **J. Rabinovich**, *Cost-Effective Repair of High-Value Parts by Ultra-low Hear PMDTM*, H&R Technology Inc., Topic: N04-025.

9 **S. Nowotny, S. Scharek, A. Schmidt**, Advanced Laser Technology Applied to Cladding and Buildup, *Welding Journal,* 2007, Vol. 86, (5), 48-51.

10 **K-H Richter, S. Orban, S. Nowotny**, Laser Cladding Of The titanium Alloy Ti6242 To Restore Damaged Blades, *Proceedings of the 23rd International Congress on Applications of Lasers and Elctro-Optics,* 2004.

11 **S. Tuppen, P.Daum, M. Rawson, K. Lucas, W. Brindley**, Development of a Laser Additive Repair Technology for High-Performance Ti-6Al-4V Blisk Aerofoils, *NATO conference,* 2009.

12 **A.P. Mackwood, R.C. Crafer**, Thermal modelling of laser welding and related processes: a literature review, *Optics & Laser Technology,* 2005, 37, 99-115.

13 **X. P. Jiang, C.-S. Man, M. J. Shepard, T. Zhai,** Effects of shot-peening and re-shot peening on four-point bend fatigue behaviour of Ti-6Al-4V, *Materials Science and Engineering A,* 480-470, 2007, 137-143.

14 **J. A. Rongong, G.T. Dunmore, L Hou**, *Initial studies into the effect that post-repair heat treatment can have on the vibration properties of visco-filled blisks*, Materials Damping Technology UTC, University of Sheffield, December 2005.

15 **N. Geffert**, *The Repair Mavens*, http://www.mtu.de/de/take-off/report/archive/1_2007/107_repair/arbeitsdateien/E_107_Repair.pdf, (Accessed 23/12/11).

16 **S. R. Thompson, J. J. Ruschau, T. Nicholas,** Influence of foreign object damage (FOD) on the fatigue life of simulated Ti-6Al-4V airfoils, *International Journal of Impact Engineering ,* 2001, vol 25, 233-250.

17 **D. Dilba**, *The Fine Art of Patching*, www.mtu.de/de/take-off/report/archive/1_2008/108_patching/arbeitsdateien/E_108_patching.pdf, (accessed 20/05/08).

18 **A. Eberlein**, *Phases of High-Tech Repair Implementation, Definition, Development, Adaption, Validation, and Qualification, in Case of Patch-Repair on Blisk Blades*, MTU Aero Engines GMBH, ISABE-2007-1102, 2007.

19 **O. Yilmaz, N. Gindy, J. Gao,** A repair and overhaul methodology for aeroengine components, *Robotics and Computer-Integrated Manufacturing,* 2010, 26, 190-201.

20 **Fraunhofer IWS,** http://www.lasertechnologies.eu/e_index.php, (accessed 28/04/12).

21 **B. Baufield, O. Van der Biest, R. Gault**, Additive Manufacture of Ti-6Al-4V components by shaped metal deposition: Microstructure and mechanical properties, *Materials and Design,* 2010, 31, (1), 5106-5111.

22 **E. Brandl, V. Michailov, B. Viehweger, C. Leyens**, Deposition of Ti-6Al-4V using laser wire, part 1: Microstructural properties of single beads, *Surface and Coatings Technology,* 2011, 206, (6), 1120-1129.

23 **G. Lewis, E. Schlienger,** Practical considerations and capabilities for laser assisted direct metal deposition, *Materials and Design,* 2000, 21, (4), 417-423.

24 **R. Moat, A.Pinkerton, L. Li, P.Withers, M. Pruess,** Residual stresses in laser direct metal deposited Waspaloy, *Materials Science and Engineering A,* 2011, 528, (6), 2288-2298.

25 **P. Passey**, Reliability of Compressor Aerofoils, *Prog. Aerospace Sci.,* 1976, 17, 67-92.

26 **E.Brinksmeier, J. T. Cammett, W. Konig, P. Leskover, J. Peters, H. K. Tonshoff**, Residual Stresses – Measurement and Causes in Machining Processes, *Annals of the CIRP,* 1982, 3.

27 **A. Ginting, M. Nouari,** Surface integrity of dry machined titanium alloys, *International Journal of Machine Tools and Manufacture,* 2009, 49, (3-4), 325-332.

28 **I. Polmear**, *Light alloys*, 4th Edition, Butterworth-Heinemann, 2006,

29 **J.C. Anderson, K.D. Leaver, R.D. Rawlings, J.M. Alexander**, *Materials Science*, 4th Edition, Cheltenham, Stanley Thrones, 1990.

30 **W. D. Callister, Jr.** *Materials Science and Engineering and introduction*, 6th Edition, Wiley, 2003.

31 **M.J.Donachie**, *Titanium a technical guide*, 2nd Edition, ASM International, 2000.

32 **K.H. Matucha,** *Materials Science and Technology, Volume 8; Structure and Properties of Nonferrous Alloys*, Wiley-VCH, 1995.

33 **D. A. Porter, K. E. Easterling**, *Phase Transformations in Metals and Alloys*, 2nd Edition, Nelson Thornes, 2001.

34 **G. Lütjering**, Influence of processing on microstructure and mechanical properties of (α+β) titanium alloys, *Materials Science and Engineering,* 1998, A243, (1-2), 32-45.

35 **K. Kubiak, J. Sieniawski,** Development or the microstructure and fatigue strength of two phase titanium alloys in the processes of forging and heat treatment, *Journal of Materials Processing Technology,* 1998, 78, (1), 117-121.

36 **E.Brandl, A. Schoberth, C. Leyens**, Morphology, microstructure, and hardness of titanium (Ti-6Al-4V) blocks deposited by wire-feed layer manufacture (ALM), *Materials Science and Engineering A*, 2012, 532, 295-307.

37 **M. N. Ahsan, A. J. Pinkerton, R. J. Moat, J. Shackleton,** A comparative study of the laser direct metal deposition characteristics using gas and plasma-atomised Ti-6Al-4V powders, *Materials Science and Engineering A,* 2011, 528, (25-26), 7648-7657.

38 **D. Ulutan, T. Ozel,** Machining induced surface integrity in titanium and nickel alloys: A review, *International Journal of Machine Tools and Manufacture*, 2011, 51, (3), 250-280.

39 **B. Griffiths,** *Manufacturing Surface Technology – Surface Integrity & Functional Performance, (Manufacturing Engineering Modular Series)*, Penton Press, 2000.

40 **C. H. Che-Haron, A.Jawaid**, The effect of machining on surface integrity of titanium alloy Ti-6% Al-4% V, *Journal of Materials Processing Technology*, 2005, 166, (2), 188-192.

41 **J. Donachie Jr**, Heat treating titanium and its alloys, *Heat treating progress*, 2001, 1, (1), 47-57.

42 **C. Jones**, Titanium specialist (Rolls-Royce plc), Personnel communication, 05/05/07.

43 **J.A.Burger, D.K. Hanink**, *Heat Treating titanium and Its Alloys*, The Heat Treating Source Book, American Society for Metals, 1986.

44 **H. Fukai, H. Iizumi, K-n. Minakawa, C. Ouchi**, The effects of the Oxygen-enriched Surface Layer on Mechanical Properties of $\alpha+\beta$ Type titanium Alloys, *ISIJ International,* 2005, 45, (1), 133-141.

45 **M.R. Bache, W.J. Evans, M. McElhone**, The effects of environment and internal oxygen on fatigue crack propagation in Ti-6Al-4V, *Materials Science and Engineering: A,* 1997, 234-236, 918-922.

46 **D. Jordan**, Study of Alpha Case Formation on Heat Treated Ti-6-4 Alloy, *Heat Treating Progress*, 2008, 8(3), 45-47.

47 **S.Zabler**, Interstitial Oxygen diffusion hardening – A practical route for the surface protection of titanium, *Materials Characterization*, 62, 2001, 1205-1213.

48 **Air liquide**, *Argon Material Data Safety Sheet*, http://alphagaz.airliquide.com/Specialty_Gas_US/Argon.pdf, accessed 21/05/12.

49 **D.D. Harwig, C. Fountain, W. Ittiwattana and H. Castner**, AMS Welding research, *Welding journal, November 2000, 79 (11)*.

50 **I. A. Menzies, K. N. Strafford,** Studies of the oxidation of titanium in carbon dioxide – I. Characteristics within the reaction temperature range 675-800C, *Corrosion Science, 1975, 15, 69-90.*

51 **L. I. Sokol'skaya**, *Gases In Light Metals*, Pergamon Press, 1961.

52 **M. Lazar, R. Edwards,** The Theory and Economics of Atmosphere Selection, *Heat Treating Progress,* 2005, 5, (1), 53-56.

53 **R. J. Fradette**, *Operating a Vacuum Furnace Under Humid Conditions*, Vacuum Furnace Reference Series, Solar Manufacturing Inc., Number 3, Revision 9/11, 2011, http://www.solarmfg.com/wp-content/uploads/2011/01/Op-Vac-Furn-Humid.pdf (accessed 02/03/06).

54 **C. L. Briant, Z. F. Wang, N. Chollocoop**, Hydrogen Embrittlement of Commercial Purity Titanium, *Corrosion Science,* 2002, 44, (8), 1875-1888.

55 **E. W. Collins**, *Titanium Alloys*, Material Properties Handbook, ASM International, 1994.

56 **P. S. Gupton**, *The Heat Treating Source Book – A Collection of Outstanding Articles from the Technical Literature*, Metals Progress, American Society for Metals, Ohio, 1967.

57 **L. Wagner, C. Gerdes, G. Lutjering,** Influence of Surface Treatment on Fatigue Strength of Ti-6Al-4V, Titanium-Science and Technology Vol. 4, Munich, Sept 1984.

58 **J. Ding, P. Colegrove, J. Mehnen, S. Ganguly, P. M. Sequeira Almeida, F. Wang, S. Williams**, Thermo-mechanical analysis of Wire and Arc Additive Layer Manufacturing process on large multi-layer parts, *Computational Materials Science*, 2011 , 50, (12), 3315-3322.

59 **R . H. Leggatt**, Residual Stresses in welded structures, *International Journal of Pressure Vessels and Piping*, 2008, 85, (3), 144-151.

60 **F. Liu, X. Xin, G. Yang, M. Song, J. Chen, W. Huang**, Microstructure and residual stress of laser rapid formed Inconel 718 nickel-base superalloy, *Optics and Laser Technology*, 2011, 43, (1), 208-213.

61 **D. Radaj**, *Welding Residual Stresses and Distortion Calculation and Measurement*, Revised Edition, DVS Verlag, 2003.

62 **W. L. Williams**, Development of Structural Titanium Alloys for Marine Applications, *Ocean Engineering, 1969, 1, (4), 375-378.*

63 **P. Prevey, D. Hornbach, P. Mason**, Thermal Residual Stress Relaxation and Distortion in Surface Enhanced Gas Turbine Engine Components, *Proceedings of the 17th Heat Treating*

Society Conference and exposition and the 1st International Induction Heat Treating Symposium, 1998.

64 **J. E. Wyatt, J. T. Berry,** A new technique for the determination of superficial residual stresses associated with machining and other manufacturing processes, *Journal of Materials Processing Technology*, 2006, 171, (1), 132-140.

65 *Volume 4: Heat treating*, ASM Handbook, 9th Edition, ASM International, 1991, 2050.

66 **F. Li, J.W. Brooks, X.P. Fu, T.A. Dean**, High temperature Stress Relaxation of a Ti-6Al-4V Alloy, *titanium '95; Science and Technology*, 1995.

67 **B.R. Sridhar, G. Devananda, K. Ramachandra, Ramaraja Bhat,** Effect of machining parameters and heat treatment on the residual stress distribution in titanium alloy IMI-834, *Journal of Materials Processing Technology, 2003, 139, (1-3), 628-634.*

68 **A.Majorell, S. Srivatsa, R. C. Picu**, Mechanical behaviour of Ti-6Al-4V at high and moderate temperatures – Part I: Experimental results, *Materials Science and Engineering A*, 2002, 326, (2), 297 – 305.

69 **W. Summer**, *Ultra-violet and Infra-red Engineering*, Sir Isaac Pitman & Sons, 1962

70 **P. Smith, D. Clark,** MTL 50353, Rolls-Royce, March 2005.

71 **N. Lowerie (ed)**, Surface Treatment of titanium Designers and Users Handbook, *The titanium information group*, 2006.

72 **V. Rudnev, D. Loveless, R. Cook, M. Black**, *Handbook of Induction Heating*, CRC Press, 2003.

73 **J. Davies, P. Simpson**, *Induction Heating Handbook*, London, McGraw-Hill Book Company (UK) Ltd, 1979.

74 **J. L. Myers, T.F. Broderick**, *Localized heat treating apparatus for blisk aerofoils*, US 2008/0099465 A1, 2006.

75 **F. P. Incropera, D.P. DeWitt**, *Introduction To Heat Transfer*, Fourth Edition, Willey, 2001.

76 **H. Martin**, Heat and Mass Transfer between Impinging Gas Jets and Solid Surfaces, *Advances in Heat Transfer,* 1977, 13, 1-60.

77 **A. Sarkar, N. Nitin, M.V.Karwe, R.P. Singh**, Fluid Flow and Heat Transfer in Air Jet Impingement in Food Processing, *Journal of Food Science,* 2004, 69, (4), 113-122.

78 **W. B. Wright**, An evaluation of Jet Impingement Heat Transfer Correlations for Piccolo Tube Application, National Aeronautics and Space Administration, *42nd Aerospace Sciences Meeting and Exhibit sponsoured by the American Institute of Aeronautics and Astronautics*, Reno, Nevada, 2004.

79 **K. Jambunathan, E. Lai, M. A. Moss, B. L. Button,** A review of heat transfer data for single circular jet impingement, *Int. J. Heat and Fluid Flow,* 1992, 13, (2), 106-115.

80 **R.J.Goldstein,** E. R. G. Eckert, W. E.Ibele, S. V. Patankar, T. W. Simon, T.H. Kuehn, P.J Strykowski, K. K. Tamma, A. Bar-Cohen, J. V. R Heberlein, J. H. Davidson, J. Bischof, F.A. Kulacki, U. Kortshagen, S. Garrick, V. Srinivasan, Heat transfer – a review of 2002 literature, *International Journal of Heat and Mass Transfer*, 2005, 48, (5), 819-927.

81 **J. Livingood, P. Hrycak**, *Impingement Heat Transfer From Turbulent Air Jets To Flat Plates – A Literature Survey*, Lewis Research Center, Cleveland, NASA Technical Memorandum, May 1973.

82 **R. Viskanta**, Heat Transfer to Impinging Isothermal Gas and Flame Jets, *Experimental Thermal and Fluid Science,* 1993, 6, (2), 111-134.

83 **H. M.Hofmann, M. Kind, H.Martin**, Measurements on steady state heat transfer and flow structure and new correlations for heat and mass transfer in submerged impinging jets, *International Journal of Heat and Mass Transfer*, 50, 2007, 3957-3965.

84 **R. Gardon, C. J. Akfirat**, The Role of Turbulence in Determining The Heat Transfer Characteristics of Impinging Jets, *International Journal of Heat and Mass Transfer,* 1965, 8, (10), 1261-1272.

85 **S. Corrsin**, *Investigation of flow in an axially symmetrical jet of air*, NACA Wartime Reports, series WR-94 (1943).

86 **D.W. Colucci, R. Viskanta,** Effect of Nozzle Geometry on Local Convective Heat Transfer to a Confined Impinging Air Jet, *Experimental Thermal and Fluid Science,* 1996, 13, (1), 71-80.

87 **D.Hee Lee, J. Song, M. Chan Jo**, The Effects of Nozzle Diameter on Impinging Jet Heat Transfer and Fluid Flow, *Journal of Heat Transfer,* 2004, 126, (4), 554-558.

88 **C. Glynn, T. O'Donovan, D. Murray**, Jet Impingement Cooling, Department of Mechanical and Manufacturing Engineering, Trinity College Dublin, http://home.eps.hw.ac.uk/~tso1/Papers/417.pdf (accessed 03/09/08).

89 **J.C. Bailey, R.S. Bunker**, Local Heat Transfer and Flow Distributions for Impinging Jet Arrays of Dense and Sparse Extent, *Proceedings of 2002 IGTI International Gas Turbine Conference and Exposition*, June 3-6, Amsterdam, 2002, 855-864.

90 **B. P. E. Dano, J. A. Liburdy, K. Kanokjaruvijit,** Flow Characteristics and Heat Transfer Performances of a Semi-Confined Impinging Array of Jets: Effect of Nozzle Geometry, *International Journal of Heat and Mass Transfer,* 2005, 48 (2-3), 691-701.

91 **M. Goodro, J. Park, P. Ligrani, M. Fox, H-K. Moon**, Effects of Mach number and Reynolds number on jet array impingement heat transfer, International Journal of Heat and Mass Transfer, 2007, 50, (1-2), 367-380.

92 **J. O'Grady**, *Jet Impingement Cooling of Turbine Blades by Forced Convection*, MAE 221A Heat Transfer, University of California, San Diego, December 2007, http://courses.ucsd.edu/rherz/mae221a/reports/OGrady_221A_F07.pdf (accessed 03/05/12).

93 **Han, Je-Chin**, *Gas Turbine Heat Transfer and Cooling Technology*, New York: Taylor and Francis, 2000.

94 **T. Wang, M. Lin, R. Bunker**, Flow and heat transfer of confined impingement jets cooling using a 3-D transient liquid crystal scheme, *International Journal of Heat and Mass Transfer*, 48, 2005, 4887-4903.

95 **A. Dahlquist**, *Axial Gas Turbine Blade Cooling with Impingement/Film-Cooling*, Lund University, MVK160, 2008.

96 **L.Xianchang, J. L. Gaddis, T. Wang**, Multiple patterns and heat transfer in confined jet impingement, *International Journal of Heat and Fluid Flow*, 26, 2005, 746-754.

97 **B. E. Launder, D. B. Spalding**, The numerical computation of turbulent flows, *Computer Methods in Applied Mechanics and Engineering*, 3, 1974, 269-289.

98 **D. C. Wilcox**, Turbulence Modelling for CFD, *DCW Industries*, 2006, USA.

99 **M. F. Koseoglu, S. Baskaya**, The role of jet inlet geometry in impinging jet heat transfer, modelling and experiments, *International Journal of Thermal Sciences*, 49, 2010, 1417-1426.

100 **M. F. Koseoglu, S. Baskaya**, The effect of flow field and turbulence on heat transfer characteristics of confined circular and elliptic impinging jets, *International Journal of Thermal Sciences*, 47, 2008, 1332-1346.

101 **M. Behnia, S. Perneix, P. A. Durbin**, Prediction of heat transfer in an axisymmetric turbulent jet impinging on a flat plate, *International Journal of Heat and Mass Transfer*, 41, (12), 1998, 1845-1855.

102 **M. Angioletti, E. Nino, G. Ruocco**, CFD turbulent modelling of jet impingement and its validation by particle image velocimetry and mass transfer measurements, *International Journal of Thermal Sciences*, 44, 2005, 349-356.

103 **B. Sagot, G. Antonini, A. Christgen, F. Buron**, Jet impingement heat transfer on a flat plate at a constant wall temperature, *International Journal of Thermal Sciences*, 47, 2008, 1610-1619.

104 **K. Funazaki, K. Hachiya,** Systematic Numerical Studies on Heat Transfer and Aerodynamic Characteristics of Impingement Cooling Devices Combined with Pins, *Proceedings of ASME Turbo Expo 2003,* June 16-19, Atlanta, Georgia, USA, 2003.

105 **C. Carcasci**, An experimental investigation on air impinging jets using visualisation methods, *Int. J. Sci.,* 38, 1999, 808-818.

106 **A. Sarkar**, R. P. Singh, Air impingement technology for food processing: visualization studies, *Lebensm.-Wiss. U.-Technol*. 37, 2004, 873-879.

107 **ASM Aerospace Specification Metals Inc**., Aerospace Specification Metals ASM specification for titanium Ti-6Al-6V (Grade 5), Annealed, http://asm.matweb.com/search/SpecificMaterial.asp?bassnum=MTP641 (accessed 03/05/12).

108 **M. Ashby, D. Jones**, Engineering Materials 2, 2nd Edition, Butterwoth Heinemann, Oxford UK, 2001.

109 **TIMET Corporation**, Timetal ® 6-4, 6-4 ELI & 6-4-.1Ru – Medium to high strength general-purpose alloys, *TIMET, USA, 2000.*

110 **M. Necati Ozisik,** *Heat Transfer A Basic Approach*, McGraw-Hill International Editions, Mechanical Engineering Series, 1985, 2.

111 **J. Carvill**, *Mechanical Engineer's Data Handbook*, 1st edition, Butterworth-Heinemann, Oxford, 2001.

112 **E. W. Lemmon, R.T. Jacobsen**, Viscosity and Thermal Conductivity Equations for Nitrogen, Oxygen, Argon and Air, *International Journal of Thermophysics,* 2004, 25, (1), 21-69.

113 **G. A. Cook (editor),** *Argon Helium and the Rare Gases The elements of the Helium Group, Vol. 1 : History, Occurrence, and properties*, Interscience publishers, 1961.

114 **F. Din**, *Thermodynamic Functions of Gases, Volume 2: Air, Acetylene, Ethylene, Propane and Argon*, Butterworth scientific publications, 1965.

115 **J.C. Mankins**, Technology readiness and risk assessments: A new approach, *Acta Astronautica,* 2009, 65, (9-10), 1208-1215.

116 **J.C. Mankins**, Technology readiness assessments: A retrospective, *Acta Astronautica,* 2009, 65, (9-10), 1216-1223.

117 Internal report, Rolls-Royce, 2005.

118 **N. T. P. L**, *Certificate of Calibration*, Certification no. 06-10-18, Reference no. 26846, 2006.

119 **I. Mitchell**, *Specification for argon Heater*, MTL50391, (internal Rolls-Royce report).

120 **A. Volbrecht**, Guidelines for Good Thermocouple Practice, *Heating Progress,* 2007, 7, (3),48-51.

121 **P. V. Grant, J.D. Lord, P. S. Whitehead,** The Measurement of Residual Stresses by the Incremental Hole Drilling Technique, *Measurement Good Practice Guide No. 53,* National Physical Laboratory, 2002, ISSN 1368-6550.

122 **N. B. Jenkins**, Internal Rolls-Royce Report, DNS72767,

123 **N.A. Walker,** Internal Rolls-Royce Report, MEG034186.

124 **H. Dong, X. Y. Li**, Oxygen boost diffusion for the deep-case hardening of titanium alloys, *Materials Science and Engineering,* 2000, 280, (2), 303-310.

125 **I. Mitchell**, EngD student, Internal Rolls-Royce communication, 23/05/06.

126 **N.Zuckerman, N.Lior,** Jet ImpingementHeat Transfer: Physics, Correlations, and Numerical Modeling, *Advances in Heat Transfer*, 2006, 39, 565-631.

127 **B.Sagot, G. Antonini, A. Christgen, F. Buron,** Jet impingement heat transfer on a flat plate at a constant wall temperature, *International Journal of Thermal Sciences,* 2008, 47, 1610-1619.

128 **Perry, K.P,** Heat Transfer by Convection from a Hot Gas Jet to a Plane Surface, *Proc.Inst. Mech. Eng., 168 (30), 1954, 775-780.*

129 **Huang, G. C,** Investigations of Heat-Transfer Coefficients for Air Flow Through Round Jets Impinging Normal to a Heat-Transfer Surface, *J. Heat Transfer, 1963, 85, (3).*

130 **Cotronics Corp**, *Electrically resistive adhesives*, http://www.cotronics.com/catalog/29%20%20919%20%20920.pdf, (accessed 02/05/12).

131 **Titanium Metal Corporation**, *Properties and Processing of TIMETAL® 6-4*, Titanium Metals Corporation, USA, 1998.

132 **Y. Cengel, M. Boles**, *Thermodynamics An Engineering Approach*, Third Edition, WCB McGraw-Hill, 1998, 108-109.

133 **M. Lohrmann, D.H. Herring,** Heat Treating Challenges in the 21st Century, *Heat Treating progress,* 1, (2), 2001.

134 **J. S. Rao, K. Gupta**, *Introductory Course On Theory and Practice of Mechanical Vibrations, New Age International*, 2nd Edition, 1999, ISBN 8122412157, 477-480.

135 **R. Goetz**, Internal Rolls-Royce report, RET101098, August 2009.

136 http://www.engineeringtoolbox.com/air-properties-d_156.html, (accessed 13/05/12).

137 **R. C. Reed**, *The Superalloys fundamentals and Applications*, Cambridge University Press, 2006.